



University
of Glasgow

Rampurawala, Abdul Moosa (2005) *Aeroelastic analysis of aircraft with control surfaces using CFD*. PhD thesis.

<http://theses.gla.ac.uk/5499/>

Copyright and moral rights for this thesis are retained by the author

A copy can be downloaded for personal non-commercial research or study, without prior permission or charge

This thesis cannot be reproduced or quoted extensively from without first obtaining permission in writing from the Author

The content must not be changed in any way or sold commercially in any format or medium without the formal permission of the Author

When referring to this work, full bibliographic details including the author, title, awarding institution and date of the thesis must be given

Aeroelastic Analysis of Aircraft with Control Surfaces Using CFD

by

Abdul Moosa Rampurawala
M.Sc.[Aerospace], University of Glasgow, Glasgow 2002
B.E.[Aeronautics], University of Madras, Madras 2000

Thesis submitted to the Faculty of Engineering, in fulfillment of the
requirements for the Doctor of Philosophy at the University of Glasgow

University of Glasgow
Faculty of Engineering
Department of Aerospace Engineering
©November 2005 Abdul M Rampurawala

Abstract

An instability in flight due to the interaction of the aerodynamic, elastic and inertial forces could prove catastrophic. Hence due importance is given to the aeroelastic analysis of the aircraft in the design stage. Until the advent of modern computers the only tools available to perform this kind of analysis were analytical and wind tunnel based. There are only some situations where the analytical tools are predictive and the experimental investigations can be expensive. However with the introduction of high speed computers a new tool was made available to the aeroelastician to accurately predict instabilities. Coupled linear structural and aerodynamic models started to be used in industry in the 1960's and are still the norm. Though there exist research codes based on CFD level aerodynamics that have excellent aeroelastic capabilities the usage in the industry is limited due to their high computational cost and slow turnaround times. In recent times the research codes have developed exciting capabilities and can accurately predict instabilities in the nonlinear transonic flow regimes. However these developments have been limited to fairly simple geometries and most of the codes still struggle to cope with anything more complex than a wing. Sources of instabilities within the flight envelope are usually the secondary components like control surfaces and stores. The ability to predict instabilities due to control surfaces using CFD based aeroelasticity is a challenge and forms the theme of this thesis. The buzz phenomena occurs on spring loaded control surfaces due to the interaction of the flap rotation mode and the shock motion. For the simulation of control surface buzz accurate prediction of the shock location and the shock strength is essential and this is currently achieved using Euler and RANS based CFD analysis. To calculate the motion of the control surface only the flap rotation mode needs to be modelled. In the current work the CFD solver is coupled with a modal based FEM solver. The multi-level hierarchical blending transformation methodology is applied for the aeroelastic analysis of complex geometries. The methodology is used for the treatment of blended control surfaces and the effect of the blending on the aero-structural response is measured. Forced flap oscillations of a Supersonic Transport (SST) configuration are simulated and the dynamic deformation of the wing and the unsteady pressure due to the forced oscillations are validated against experiments. Transonic buzz on a trailing edge flap is investigated on the Supersonic Transport configuration using the RANS and the Euler equations. Characteristics associated with a buzz instability are reproduced computationally and the effect of the flap on the wing flutter is measured. Finally aeroelastic simulations are performed on the Hawk aircraft. The combat flap configuration of the Hawk aircraft is investigated using CFD and the effect of the flap on wing flutter is assessed. The aeroelastic response of the rudder at supersonic freestream Mach numbers is studied. The importance of aerodynamic interference on the aeroelastic behaviour is assessed.

Acknowledgements

I am grateful to BAE SYSTEMS for funding this work as part of the programme of the Partnership for Unsteady Methods in Aerodynamics (PUMA) Defence and Aerospace Research Partnership (DARP). Support from an Overseas Research Students Award Scheme (ORSAS) and the University of Liverpool is acknowledged. This work would not be possible without the generous aid of these agencies.

I would like to thank my supervisor Professor Ken Badcock for his support, encouragement and able guidance over the past 4 years that made my graduate studies exciting and fulfilling. His guidance extended beyond academics and his wisdom will be warmly remembered. I would also like to thank Dr. George Barakos for his prompt help with myriad of things that only he could deal with. His knowledge and enthusiasm is something one can only aspire for.

My colleagues at the CFD Laboratory will be fondly remembered for their friendliness and for maintaining a cordial environment. All of them have contributed in their own way into making this work possible. My former colleague Dr. Punit Nayyar merits a special thanks for his many contributions and his helping nature.

I am indebted to Mr. Chris Denley of BAE SYSTEMS, Brough for his help with the Hawk structural models and his valuable suggestions for the thesis. I would also like convey thanks to Dr. Masato Tamayama of Japan Aerospace Exploration Agency for providing the experimental data on the Supersonic Transport test case.

Finally I owe a debt of gratitude to my parents Moosa and Ajab Rampurawala for their moral support and encouragement through out my years as a student.

Contents

1	Introduction	1
1.1	Aircraft Aeroelastic Instabilities	1
1.2	Flutter Analysis Techniques	4
1.3	CFD Based Analysis of Control Surfaces	6
1.4	Thesis Organisation	7
2	Computational Aeroelasticity Methodology	9
2.1	Introduction	9
2.2	Flow Solver	9
2.2.1	Non-dimensional form	10
2.2.2	Reynolds-averaged form	12
2.2.3	Curvilinear form	13
2.2.4	Steady State Solver	14
2.2.5	Unsteady Solver	16
2.3	Mesh Movement	17
2.3.1	Transfinite Interpolation	17
	TFI of Block Edges	18
	TFI of Block Faces	18
	TFI of Block Volumes	20
2.3.2	Geometric Conservation Law	22
2.4	Structural Solver	23
2.5	Sequencing of Structural and Fluid Solvers	24
3	Transformation Methodology	26
3.1	Introduction	26
3.2	Requirements of a Transformation Scheme	26
3.2.1	Grid Smoothness	27
3.2.2	Accurate Information Transfer	27
3.2.3	Sparse Structural Models	29
3.2.4	Complex Geometries	29
3.2.5	Memory Requirements	29
3.2.6	Conservation of Energy	29
3.3	Interpolation Schemes	30
3.3.1	Infinite Plate Spline	30

3.3.2	Finite Plate Spline	30
3.3.3	Inverse Isoparametric Mapping	31
3.3.4	Boundary Element Method	33
3.4	The Constant Volume Tetrahedron	34
3.4.1	Selection of the Structural Elements	36
3.4.2	1D Constant Volume Tetrahedron	37
3.5	Full Aircraft Transformation	39
3.6	Control Surface Transformation	43
3.6.1	Transpiration	43
3.6.2	Rigid blending	44
3.6.3	Multilevel blending	45
3.6.4	Chimera grids	45
3.6.5	Virtual zones	45
3.6.6	Gap blocks	46
3.7	Assessment of Control Surface Treatments	46
3.7.1	Control Surface Transformation-Rudder	46
3.7.2	Comparison of Flaps with Blended and Free Edges	50
3.8	Multi-component Test Case	52
4	Validation for Forced Flap Motions	56
4.1	Introduction	56
4.2	The Experimental Models	58
4.2.1	The BACT Wing	58
4.2.2	The NAL SST Arrow Wing	60
4.3	Aeroelastic Modelling	61
4.3.1	Flap Grid Treatment	62
4.3.2	CFD Grids	63
The BACT Wing	63	
NAL SST Arrow Wing	63	
4.4	BACT Results	64
4.5	SST Results	64
4.6	Conclusion	66
5	Control Surface Instability	80
5.1	Introduction	80
5.1.1	Test Case Description	81
5.1.2	The Structural Model	82
5.1.3	CFD Grids	82
5.2	Results and Discussions	84
5.2.1	Grid and time-step refinement study	84
5.2.2	Dependence of buzz on flap blending	84
5.2.3	Dependence of buzz on the initial impulse	86
5.2.4	Dependence of buzz amplitude and frequency on Reynolds numbers	91

5.2.5	Dependence of buzz amplitude on structural damping	99
5.2.6	Linear and CFD based flutter results for Model1 and Model2	99
5.3	Limitation of Linear Aerodynamics	102
5.4	Conclusions	104
6	The Hawk Aircraft¹	106
6.1	Overview	106
6.2	The Hawk Wing	107
6.2.1	CFD Setup	107
6.2.2	The Structural Model	108
6.2.3	Results	109
6.3	Wing with Flap	112
6.3.1	CFD Setup	114
6.3.2	Structural Model	115
6.3.3	Results	118
6.4	Rudder Cases	119
6.4.1	CFD Setup	124
Body-Fin-Rudder Case	124	
Body-Fin-Rudder-Tail Case	125	
Body-Fin-Wing-Rudder-Tail Case	125	
6.4.2	The Structural Model	126
Mirroring of Modes	128	
6.4.3	The Complete Hawk Model	130
6.4.4	Results and Discussions	130
Steady Results	130	
Dynamic Results	132	
6.5	Conclusions	133
7	Conclusions	143
7.1	Treatment of Control Surfaces	143
7.2	Buzz Instability	143
7.3	Instability on Complex Geometry	144
7.4	CFD in Industry	145
7.5	Future Work	145
Bibliography		147

Chapter 1

Introduction

1.1 Aircraft Aeroelastic Instabilities

Aerodynamic forces act on the aircraft structure which, being flexible, deforms. The interaction of the aerodynamic forces with the flexible structure is termed aeroelasticity. Figure 1.1 shows the classical Collar's triangle whose three vertices are aerodynamic, elastic and inertial forces. The interaction of the aerodynamic and elastic forces result in static deformations. The interaction of all the three forces give rise to dynamic instabilities and is shown in the centre of the triangle. The interaction of inertial and aerodynamic forces are usually associated with flight mechanics problems, whereas the study of the interaction of the elastic and the inertial forces is known as structural dynamics. The classical Collar's triangle has been extended to include heating effects at high Mach numbers and the effect of control systems, termed aeroservoelasticity.

Aeroelastic instabilities are classified either as static or dynamic. As mentioned earlier the static instability arises due to the interaction of the aerodynamic forces and the elastic restoring forces of the structure. The inertial forces due to motion of the structure are not involved and hence deformation is independent of time. Static deformations are of concern as these change the lift distribution over the wing which is important for performance and flight mechanics of the aircraft. Usually elastic restoring forces and the aerodynamic loads acting on the structure are in equilibrium. However at certain values of freestream velocity the elastic restoring forces of the structure are less than the aerodynamic loads, leading to a catastrophic failure known as divergence.

Aircraft components, including the lifting surfaces, are manufactured to have minimal structural weight, making them light and flexible. In modern aircraft the need to increase the range and fuel economy necessitates lighter structures. In military aircraft the extreme operational conditions due to rapid combat manoeuvres make the static deformations large enough to have an impact on the aerodynamics of the aircraft. Apart from the loss of aerodynamic attributes there is a risk of catastrophic failure due to static wing divergence. During the design process static corrections are usually added to computed aerodynamic forces on the rigid wing to take into account the static deformations [1].

Potential dynamic instabilities are more numerous than static ones, and they involve coupling of all the three forces of the Collar's triangle. Wing flutter is probably the most commonly known and studied of all the dynamic aeroelastic phenomena. All flexible wings twist and bend under

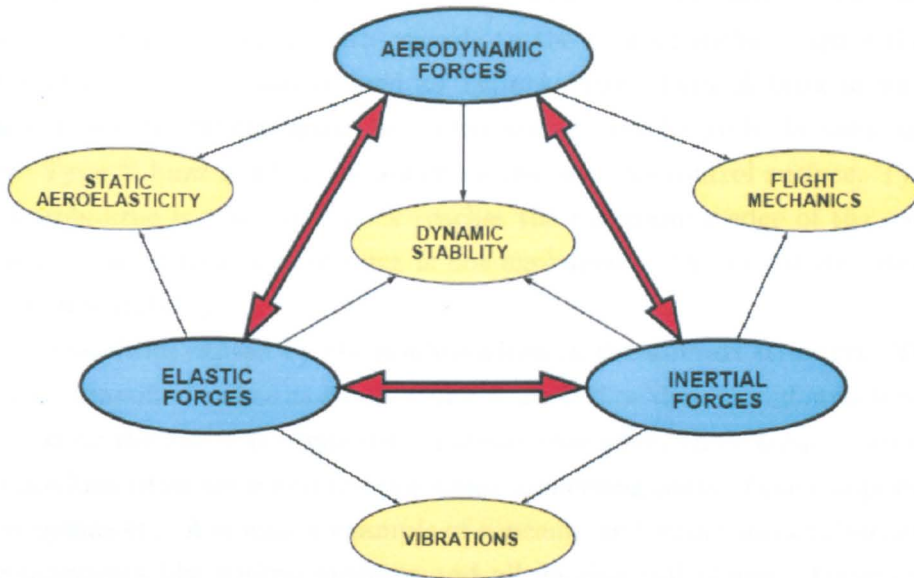


Figure 1.1: The Collar's Aeroelasticity Triangle

applied aerodynamic forces. The aerodynamic loads deform the structure which in turn changes the aerodynamic loads due to the change in the wing geometry. This feedback process between the flow and the structure can result in a self excited system. If the wing twists and bends in a certain manner the unsteady aerodynamic loads start feeding the elastic motion of the wing causing the amplitudes to grow, eventually leading to structural failure or LCO. The classical wing bending-torsion flutter involves the coupling of the bending and the torsional modes driven by the unsteady aerodynamics.

Buffet and control surface buzz are a class of aeroelastic instabilities that are driven by nonlinearities in the aerodynamics. Modern fighter aircraft carry out high angle of attack manoeuvres extending the flight envelope to stall and post stall regimes [2]. At high angles of attack slender wing geometries like strakes, leading edge extensions and the wing leading edge generate strong vortices which increase the performance of the wing. However these vortices burst over the wing surface resulting in a wake with high turbulent intensities. Buffeting involves oscillations of the aircraft component lying in the turbulent wake of an upstream component or a broken vortex. Though not catastrophic these increase the structural fatigue and maintenance costs. Some of the examples of buffeting are fin buffet for fighter aircraft, and tailplane buffet.

Control surface buzz is a Limit Cycle Oscillation (LCO) type of aeroelastic instability observed on trailing edge control surfaces. The oscillations are brought about by the interaction of the shock, the boundary layer and the control surface rotation mode. Buzz is usually observed between Mach numbers 0.9 to 1.4 depending on wing profile, angle of attack and the chord-wise location of the control surface hinge. There are two main types of buzz mechanism. The first is a buffeting type where the shock interacts with the boundary layer causing the flow to separate ahead of the hinge. The separated flow interacts with the control surface resulting in LCO. This type of buzz was termed as classical buzz by Bendiksen [3]. The second type of buzz is purely due to the oscillation of the shock over the control surface and does not involve separation. This

is termed as nonclassical buzz in [3]. An earlier classification of buzz by Lambourne [4] was based on the location of the shock with regards to the control surface. Buzz due to a shock located upstream of the hinge was termed as Type A buzz. Type A buzz inevitably involves separation as source of unsteadiness on the control surface and hence is the same as Bendiksen's classical buzz. Type B buzz is when the shock moves over the control surface. Type C buzz as classified by Lambourne is when the shock reaches the trailing edge of the control surface. The exact mechanism of this type of buzz is not explained in the literature. Buzz is a single degree of freedom instability.

There are instabilities caused by the nonlinearities in the aircraft structure. The structural nonlinearities are classified either as local or distributed. The distributed structural nonlinearities are governed by the elastodynamic deformations that effect the complete aircraft. Local or concentrated nonlinearities are found at hinges and connecting parts of the component interfaces like wings and pylons etc. A common example of concentrated structural nonlinearity is freeplay on aircraft components like control surfaces and all moving tail planes. These can arise from worn hinges of control surfaces and loose control linkages [5]. Freeplay of control surfaces can cause a low amplitude LCO to ensue in flight. LCO due to freeplay occurs at flight speeds lower than the flutter velocity however it has been shown that control surface freeplay can significantly change the flutter characteristics of the wing [6].

The first instance of a catastrophic aeroelastic instability is older than the first powered flight itself. The Langley Monoplane was suspected to have been the first victim. In December 1903, a few days before the famous flight of the Wright brothers, Langley attempted his second catapulted flight of his tandem monoplane. The attempt was unsuccessful due to the collapse of the rear wing and tail [7]. It was conjectured in a paper by Hill [8] that a torsional divergence was probably the cause of the failure as a lack of torsional rigidity was observed in the prototype. It has been acknowledged that if it was not for aeroelasticity Langley might have been the first to have a powered flight. Over the years there have been numerous aeroelastic incidents and resulting fatalities. Many of the incidents arose during the flight testing of the prototypes and are not necessarily reported in the public domain. The first documented flutter study was by Lanchester and Birstow [9, 10] on the Handley Page 0/400 WW1 bomber. As the understanding of the aeroelastics increased there were preventive measures taken to avoid flutter. However with the rapid increase in performance and streamlining of structures, there was also an increase in the number of incidents [11]. In Germany there was a dramatic increase in the number of aircraft development projects around 1933, and during the period to 1945 there were 146 flutter incidents leading to 24 crashes [12]. Around that time in Britain a comprehensive report on air accidents [13] by the Aircraft Research Council summarised 50 detailed flutter investigations [7]. In the 1950s after the war there was a range of prototypes under development in Britain but the number of reported incidents steadily reduced [14]. There were 24 reported incidents between 1952 and 1954 as compared to 15 between 1954 and 1960 [11]. According to Templeton [15] the developments that had reduced incidents in Britain were improvements in the calculation of aerodynamic forces, high speed computational aids, experimental techniques for flutter model, ground resonance and flight flutter testing [11]. The aircraft development program in the U.S. after WW2 accelerated with the onset of the cold war and along with the high speed military aircraft came the problems related to transonic aeroelasticity. This is indicated in a survey

of flutter encounters compiled by the NACA subcommittee on Vibration and Flutter [16] for military aircraft between the years 1947 and 1956. Garrick notes that 21 of the listed incidents involved transonic control surface buzz for which no adequate theory or basic understanding was available for guiding design [7]. It is also interesting to note that if tabs are considered as control surfaces then all but 10 incidents involved control surfaces. He also mentions that all of the 7 wing flutter incidents involved externally mounted stores including pylon mounted power plants. In Britain the reduction in flutter incidents continued and there were only 7 mild flutter cases reported between the years 1960 and 1972 [17]. According to Keynes [11] this trend has continued in Britain to the present time with the majority of the flutter incidents reported during the flight testing of prototypes. He however cautions that this trend should in no way be taken as a sign that the flutter problem is “solved”. Some of the reasons he cites for this are the lack of truly accurate tools available, the reduced stiffness of the aircraft due to the weight optimisation of the structures and the servicing of the flight control system during the lifetime of the aircraft which changes the aeroelastic characteristics. There have been a number of flutter related crashes in recent times that substantiate these points. To cite a few, there was a fatal accident of the Shorts Tucano aircraft during a flight test due to the flutter involving the rear fuselage torsional mode and the rudder rotation mode [11], a fatal crash of the Taiwanese Chiang-kuo fighter aircraft in 1995 due to transonic flutter of the wings, and finally the American F-117A “Stealth” bomber which crashed in an airshow in Baltimore in September 1997. The crash was attributed to the flutter of the aileron/flaperon causing structural failure [18].

1.2 Flutter Analysis Techniques

The first major development in the understanding of flutter came in 1916 during the World War 1 [7]. Lanchester, a British aircraft engineer, investigated violent antisymmetric oscillations of the fuselage and tail of the Handley Page 0/400 biplane bomber. The portside and starboard side elevators were independently connected to the control stick through cables. Lanchester’s solution was to connect the elevators to each other with a torque tube so that they could not oscillate independently [9]. As the oscillations were antisymmetric the torque tube eliminated the relative oscillations between the elevators. A paper by Bairstow based on this investigation [10] provides the first analytical treatment of flutter [7].

Another important milestone in the analysis of flutter on aircraft was realised by von Baumhauer and Koning in the early 1930s. In a systematic study of the wing bending combined with aileron rotation flutter they found that by mass balancing the control surfaces, flutter could be completely eliminated [19]. This was an important realisation as now the basic mechanism of flutter was just beginning to be understood. From this study it was found that adding and removing mass could increase the speed at which control surface flutter occurs and hence the concept of decoupling the modes of vibration of aircraft was discovered.

In 1928 Frazer and Duncan published a comprehensive monograph on the flutter phenomenon [20] which was often referred to in Britain as “The Flutter Bible” [7]. Simplified wind tunnel models were used to study flutter and detailed recommendations were made for aircraft design. The concept of semi-rigid modes where it is assumed that the deformation at a wing section is independent of the load distribution on the wing was introduced for the first time. This greatly

simplified the theoretical analysis of flutter.

An important report on the theoretical treatment of flutter was published by Theodorsen in 1934 [21] where he outlined a method for calculating the flutter characteristics of an aerofoil with 2 or 3 degrees of freedom. Theodorsen's theory represented the simplest exact theory for the idealised flat plate aerofoil and has been used in the development of Strip theory [7]. Theodorsen and Garrick [22] developed numerous applications and trend studies of exact theory yielding insights into effects of individual parameters like centre of mass, elastic axis, moment of inertia, mass ratio, aileron hinge location and bending-torsion frequency ratio. This method remained a mainstay for flutter prediction for aircraft in the U.S. until the advance of computers in the 1970s [23]. Smilg and Wasserman [24] wrote a comprehensive document based on Theodorsen's theory containing tables for unsteady aerodynamic coefficients and tables on control surface aerodynamic balance. This document became a flutter handbook in the American aircraft industry for several years [7, 23].

The advent of computers in the 1970s greatly influenced the analysis and prediction of aeroelastic instabilities. Problems involving large matrices could now be solved in a matter of minutes. A significant advancement in the field of computational aeroelastic analysis came with the development of the Doublet Lattice method by Albano and Rodden for subsonic flows [25]. Since this method was introduced in 1970, it has been continuously refined and enhanced [26, 27, 28] and has become the mainstay of flutter calculation for production level flutter clearance. Due to its widespread use and understanding of the method it has also become a standard by which other unsteady methods, including CFD based methods, are judged [29].

For supersonic aeroelastic analysis there has not been any robust linear method developed comparable to the Doublet Lattice Method for subsonic flows until the recent development of the Harmonic Gradient Method by Chen and Liu [30] in 1985. This method was motivated by the aeroelastic requirements of fighter aircraft, and is now widely used in the industry. It has been incorporated in commercial codes like **Nastran** and **ZERO**.

The linear methods have proved dependable and robust for production flutter clearance. However there is still a range of Mach numbers where the results from the linear methods are potentially inaccurate and misleading. Between the Mach numbers 0.8 and 1.2 the flow is nonlinear and difficult to analyse. In this region linear methods cannot be considered to be valid due to the presence of moving shocks on the lifting surfaces which cannot be predicted by linear aerodynamic theory. CFD based time marching aeroelastic analysis is currently one of the few options available to analyse aeroelastics in transonic flow. One of the first CFD based studies was by Borland and Rizetta on a uniform planform wing of constant parabolic cross section using the transonic small disturbance equations [31]. Reference [32] gives an interesting account of the growth of CFD for aeroelastic predictions at one of the world's leading aircraft manufacturers. From 1973 to 1983, panel methods that could model a complex geometry were the important aeroelastic tools. Between 1983 and 1993 the nonlinear potential flow/coupled boundary layer and Euler codes found use in industry, and from 1993 onwards RANS based codes have also started to be used increasingly [32]. Although there has been steady progress in the development of CFD based methods over the years it has not been used as a production tool mainly because of the problems associated with the computational time, grid generation and validation of the methods.

1.3 CFD Based Analysis of Control Surfaces

The motivation for the current work comes from a desire to investigate nonlinearities in the aeroelastic behaviour of complex configurations. Just about half of the recorded flutter incidents on military aircraft in the decade 1947 to 1956 are control surface related including control surface buzz. Modern military aircraft are designed to withstand load factors of several gs . The strength considerations for the structure to withstand these kind of loads results in stiff wing structures which will have flutter velocities exceeding the required 15 % flutter speed margin. Hence flutter on a idealised clean wing is not usually a concern for modern military aircraft [29]. Nevertheless auxiliary components like stores, pylons and control surfaces which are installed on aircraft are possible sources of transonic instabilities. Control surfaces on modern concepts for Supersonic Transport (SST) aircraft are proposed to have simple mechanical spring loaded fixtures instead of the complex irreversible hydraulics due to the lack of space in the trailing edges of the thin supersonic wing profiles [33] making transonic buzz a possibility. Another problem associated to trailing edge control surfaces is that of aileron reversal which has implications on the wing design [34]. It is stated in reference [35] that in the case of a SST at Mach 1 the effectiveness of the aileron is reduced to zero.

Before the advent of supersonic aircraft, Theodersen's analytical flutter solution for a 2D aerofoil with a trailing edge control surface [21] was the main analytical method used for control surface flutter. However as the aircraft flew faster compressibility effects came into play. Buzz was a major concern before the advent of hydraulics in the actuators for control surfaces. One of the earliest 2D simulations of transonic buzz was performed by Steger [36] on the NACA 65-213 aerofoil. A detailed investigation of "nonclassical" Type B buzz was carried out by Bendiksen [3].

The earliest 3D buzz simulations on the National Aerospace Plane (NASP) were performed by Pak and Baker [37] using a transonic small disturbance code CAPTSDv and the RANS code CFL3D. Recently 3D buzz simulation was performed on the SST configuration using an implicit multiblock code with thin layer Navier-Stokes approximation [38].

Forced flap oscillations of a trailing edge control surface have been investigated in a number of computational studies. Unsteady pressure has been validated with experimental values in most of these studies. One of the earliest studies was by Bharadvaj [39] on an F5 fighter aircraft wing and a High Aspect Ratio Wing (HARW) using a transonic unsteady full potential aeroelastic code. The control surface treatment in this study was a transpiration type where the deflection is brought about by the modification of the boundary conditions. A similar study was performed on the F5 wing and a clipped delta wing by Obayashi and Guruswamy using the RANS equations in the code ENSAERO [40]. The control surface treatment was through the introduction of gaps between the flap edges and the wing, shearing the grid in these gaps. A further improvement in this code was brought about by introducing virtual zones in the gaps. These virtual zones act as an interface between the moving flap blocks and the stationary wing blocks [41]. Schuster performed validation of the forced flap oscillations of the Benchmark Active Control Technology (BACT) wing using the RANS codes ENS3DAE and CFL3DAE [42]. The control surface edges in this study were blended with the wing edges. Studies on the forced flap oscillations were also performed by Cole *et al.* [43] using the STARS suite of codes developed at

NASA. The control surface is treated using transpiration methods. In all of the above studies the wing is assumed to be rigid. A forced flap oscillation study on a flexible wing, similar to the study in the current work, was performed by Utaka and Nakamichi using the Euler equations [44]. A Chimera grid approach is used to model the moving control surface in this study.

There have been a number of studies performed on the forced flap oscillations using linear panel methods. The treatment of control surfaces in panel methods is comparatively simple as the wings and control surfaces are modelled as 2D plates. Liu *et al.* [45] performed forced flap oscillation studies on the F-18 Wing and the British Aerospace Corporation fin in the supersonic flow using the ZONA51C code. Rowe *et al.* [46] developed a code, based on vortex-lattice technique, specifically to predict the aerodynamic loads due to control surface motions in subsonic flows. Recently Roughen *et al.* [47] presented results on the forced oscillations of the flap on the Benchmark Active Control Technology wing using a Doublet Lattice Method code NK5.

1.4 Thesis Organisation

The aeroelastic methodologies developed in this thesis and its application on a number of test cases has shown that CFD can be used to predict aeroelastic response due to control surfaces on complex 3D configurations. The validation of the CFD results against experiments of the wing deformations due to control surface oscillations in Chapter 4 is one of the first. The work in this thesis also aims to investigate the aeroelastic instabilities associated with a trailing edge control surface using CFD. Control surface buzz is the main instability of interest and a methodology is developed to enable a CFD based analysis. The effect of the control surface on the flutter boundary is also assessed. Before investigating these instabilities the feasibility of the proposed control surface treatment is assessed and is validated on a forced flap oscillation test case.

The thesis is divided into five main chapters. Chapter 2 describes the basic formulation of the flow solver PMB, which is the CFD tool used for this work. The description of the CFD code is provided along with the methodology employed for mesh movement and a description of the modal FEM solver. The method of coupling the flow and structural solver is also described here. Chapter 3 examines the issue of transfer of information between the structural and fluid grids. A brief introduction of available techniques before the detailed description of the technique developed is given. An assessment of the blended flap and flap with free edges is also presented. Chapter 4 is the validation study of the forced flap motion on a flexible SST configuration. A technique for implementing forced motions on a component, a trailing edge flap in this case, is described here. Chapter 5 contains an investigation of control surface buzz on the SST configuration. Buzz characteristics observed in the experiments are reproduced computationally. Aeroelastic analysis of the Hawk aircraft is the topic of Chapter 6. A Study of the effects of the control surfaces on the aeroelastic behaviour of the wing and a 3D investigation of the fin-rudder buzz observed in flight tests are reported in this chapter. It is noted here that due to the proprietary nature of the work the scales on all plots and figures in Chapter 6 have been blanked. However there is no validation against experiments performed in this chapter with most of the plots being qualitative in nature. The comparison of the flutter boundaries in Chapter 6 using linear and CFD methods serve to establish the qualitative differences in the behaviour

of the instability boundary at transonic Mach numbers. Finally conclusions regarding the work presented and recommendations for future work are given in Chapter 7.

Chapter 2

Computational Aeroelasticity Methodology

2.1 Introduction

The Parallel Multiblock code (PMB) is the primary simulation tool used for the nonlinear time-marching simulations in the current work. The main requirements of the solver for the work carried out in this thesis is the ability to accurately determine the unsteady flow in the highly nonlinear transonic regime, a robust and accurate intergrid transformation scheme for the transfer of information between the structural and the fluid grids and the ability to perform aeroelastic simulations on complex geometries. PMB is a research code developed at the University of Glasgow which has been validated for a range of aerodynamic and aeroelastic problems. Some of the challenging validation cases include transonic buffet studies, transonic cavity flows, vortical flows, an aerospike in supersonic flow, synthetic jets, rotorcraft simulations and aeroelastic instabilities over complex geometries. Most of the validation of PMB has been documented in the literature and a description of the flow solver is provided in Badcock *et al.* [48]. The transformation scheme used here is called the Constant Volume Tetrahedron (CVT) developed at the University of Glasgow and has been extensively tested for a number of test cases [49] and compared with other transformation schemes [50]. CVT scheme can be used with structural models consisting 1D elements and for complex geometries like complete aircraft [51] making it appropriate for use on the test cases considered in this work. The current chapter summarises the aspects of PMB that are relevant to the work undertaken in this thesis. This includes a description of the steady and unsteady methodology of the flow solver, the mesh movement algorithm and the structural solver. The transformation scheme that couples the flow and structural solvers requires a more detailed discussion and forms the topic of Chapter 3.

2.2 Flow Solver

The three-dimensional flow model equations are presented here in conservative form. A full derivation from first principles can be found in numerous fluid dynamics text books such as Anderson [52]. The following description is summarised from the theory guide of the 2D version of PMB [53] and subsequently rewritten for 3D [54].

2.2.1 Non-dimensional form

In a three-dimensional Cartesian coordinate system, the non-dimensional form of the equations may be written as

$$\frac{\partial \mathbf{W}}{\partial t} + \frac{\partial(\mathbf{F}^i - \mathbf{F}^v)}{\partial x} + \frac{\partial(\mathbf{G}^i - \mathbf{G}^v)}{\partial y} + \frac{\partial(\mathbf{H}^i - \mathbf{H}^v)}{\partial z} = 0 \quad (2.1)$$

Here \mathbf{W} is the vector of conserved flow variables and is sometimes referred to as the solution vector. It can be written as

$$\mathbf{W} = \begin{pmatrix} \rho \\ \rho u \\ \rho v \\ \rho w \\ \rho E \end{pmatrix} \quad (2.2)$$

where ρ is the density, u , v and w are the components of velocity given by the Cartesian velocity vector $\mathbf{U} = (u, v, w)$ and E is the total energy per unit mass.

When deriving the Navier-Stokes equations, the conservative form is obtained using a control volume that is fixed in space. We consider the flux of energy, mass and momentum into and out of the control volume. The flux vectors \mathbf{F} , \mathbf{G} , and \mathbf{H} consist of inviscid (i) and viscous (v) diffusive parts. These are written in full as

$$\begin{aligned} \mathbf{F}^i &= \begin{pmatrix} \rho u \\ \rho u^2 + p \\ \rho uv \\ \rho uw \\ \rho uH \end{pmatrix} \\ \mathbf{G}^i &= \begin{pmatrix} \rho v \\ \rho vu \\ \rho v^2 + p \\ \rho vw \\ \rho vH \end{pmatrix} \\ \mathbf{H}^i &= \begin{pmatrix} \rho w \\ \rho wu \\ \rho wv \\ \rho w^2 + p \\ \rho wH \end{pmatrix} \end{aligned} \quad (2.3)$$

$$\begin{aligned}
\mathbf{F}^\nu &= \frac{1}{Re} \begin{pmatrix} 0 \\ \tau_{xx} \\ \tau_{xy} \\ \tau_{xz} \\ u\tau_{xx} + v\tau_{xy} + w\tau_{xz} + q_x \end{pmatrix} \\
\mathbf{G}^\nu &= \frac{1}{Re} \begin{pmatrix} 0 \\ \tau_{xy} \\ \tau_{yy} \\ \tau_{yz} \\ u\tau_{xy} + v\tau_{yy} + w\tau_{yz} + q_y \end{pmatrix} \\
\mathbf{H}^\nu &= \frac{1}{Re} \begin{pmatrix} 0 \\ \tau_{xz} \\ \tau_{yz} \\ \tau_{zz} \\ u\tau_{xz} + v\tau_{yz} + w\tau_{zz} + q_z \end{pmatrix}
\end{aligned} \tag{2.4}$$

The stress tensor components are written as

$$\begin{aligned}
\tau_{xx} &= -\mu \left(2 \frac{\partial u}{\partial x} - \frac{2}{3} \left(\frac{\partial u}{\partial x} + \frac{\partial v}{\partial y} + \frac{\partial w}{\partial z} \right) \right) \\
\tau_{yy} &= -\mu \left(2 \frac{\partial v}{\partial y} - \frac{2}{3} \left(\frac{\partial u}{\partial x} + \frac{\partial v}{\partial y} + \frac{\partial w}{\partial z} \right) \right) \\
\tau_{zz} &= -\mu \left(2 \frac{\partial w}{\partial z} - \frac{2}{3} \left(\frac{\partial u}{\partial x} + \frac{\partial v}{\partial y} + \frac{\partial w}{\partial z} \right) \right) \\
\tau_{xy} &= -\mu \left(\frac{\partial u}{\partial y} + \frac{\partial v}{\partial x} \right) \\
\tau_{xz} &= -\mu \left(\frac{\partial u}{\partial z} + \frac{\partial w}{\partial x} \right) \\
\tau_{yz} &= -\mu \left(\frac{\partial v}{\partial z} + \frac{\partial w}{\partial y} \right)
\end{aligned} \tag{2.5}$$

and the heat flux vector components are written as

$$\begin{aligned}
q_x &= -\frac{1}{(\gamma - 1)M_\infty^2} \frac{\mu}{Pr} \frac{\partial T}{\partial x} \\
q_y &= -\frac{1}{(\gamma - 1)M_\infty^2} \frac{\mu}{Pr} \frac{\partial T}{\partial y} \\
q_z &= -\frac{1}{(\gamma - 1)M_\infty^2} \frac{\mu}{Pr} \frac{\partial T}{\partial z}
\end{aligned} \tag{2.6}$$

Here γ is the specific heat ratio, Pr is the laminar Prandtl number, T is the static temperature and M_∞ and Re are the freestream Mach number and Reynolds number, respectively. The various flow quantities are related to each other by the perfect gas relations

$$\begin{aligned}
H &= E + \frac{p}{\rho} \\
E &= e + \frac{1}{2} (u^2 + v^2) \\
p &= (\gamma - 1) \rho e \\
\frac{p}{\rho} &= \frac{T}{\gamma M_\infty^2}
\end{aligned} \tag{2.7}$$

Finally, the laminar viscosity μ is evaluated using Sutherland's law,

$$\frac{\mu}{\mu_0} = \left(\frac{T}{T_0}\right)^{3/2} \frac{T_0 + 110}{T + 110} \quad (2.8)$$

where μ_0 is a reference viscosity at a reference temperature T_0 . These can be taken as $\mu_0 = 1.7894 \times 10^{-5}$ kg/(m.s) with $T_0 = 288.16$ K. All quantities have been non-dimensionalised as follows

$$x = \frac{x^*}{L^*}, \quad y = \frac{y^*}{L^*}, \quad t = \frac{t^*}{L^*/V_\infty^*},$$

$$u = \frac{u^*}{V_\infty^*}, \quad v = \frac{v^*}{V_\infty^*}, \quad \mu = \frac{\mu^*}{\mu_\infty^*},$$

$$\rho = \frac{\rho^*}{\rho_\infty^*}, \quad p = \frac{p^*}{\rho_\infty^* V_\infty^{*2}}, \quad T = \frac{T^*}{T_\infty^*}, \quad e = \frac{e^*}{V_\infty^{*2}} \quad (2.9)$$

2.2.2 Reynolds-averaged form

Turbulence can be studied by solving the full N-S equations (called Direct Numerical Simulation - DNS). However these calculations are very large and are currently only possible when examining Reynolds numbers several orders less than those encountered by aircraft [55]. Rather than attempt to solve the time evolution of the conserved variables, a somewhat less ambitious approach is to calculate the Reynolds averaged form. This form of the Navier-Stokes equations permits turbulent flow to be considered at high Reynolds' numbers. The derivation of the equations can be found in Anderson [52]. Here it is noted that fundamental to this approach is the consideration of the flow variables as consisting of two components, a time averaged component and a turbulent fluctuation. For example, the density, pressure and velocity components are decomposed as

$$\rho = \bar{\rho} + \rho', \quad P = \bar{P} + P', \quad u = \bar{u} + u', \quad v = \bar{v} + v', \quad w = \bar{w} + w'.$$

The quantities k (the turbulent kinetic energy), μ_T (the eddy viscosity) and Pr_T (the turbulent Prandtl number) are introduced via the Boussinesq assumption in an attempt to model the Reynolds' stress terms arising from the averaging. The Reynolds-averaged form of the Navier-Stokes equations are identical to those presented above differing in the stress tensor and heat flux vector components shown. The variables should be considered as mean flow quantities (superscripts are dropped for clarity). The turbulent nature of the flow is modelled via the eddy viscosity μ_T and the turbulent kinetic energy k and a closure hypothesis or turbulence model, for example the Spalart-Allmaras model , the $k - \omega$ model , or the Shear Stress Tensor model,

leading to modified terms

$$\begin{aligned}
\tau_{xx} &= -(\mu + \mu_T) \left(2 \frac{\partial u}{\partial x} - \frac{2}{3} \left(\frac{\partial u}{\partial x} + \frac{\partial v}{\partial y} + \frac{\partial w}{\partial z} \right) \right) + \frac{2}{3} \rho k \\
\tau_{yy} &= -(\mu + \mu_T) \left(2 \frac{\partial v}{\partial y} - \frac{2}{3} \left(\frac{\partial u}{\partial x} + \frac{\partial v}{\partial y} + \frac{\partial w}{\partial z} \right) \right) + \frac{2}{3} \rho k \\
\tau_{zz} &= -(\mu + \mu_T) \left(2 \frac{\partial w}{\partial z} - \frac{2}{3} \left(\frac{\partial u}{\partial x} + \frac{\partial v}{\partial y} + \frac{\partial w}{\partial z} \right) \right) + \frac{2}{3} \rho k \\
\tau_{xy} &= -(\mu + \mu_T) \left(\frac{\partial u}{\partial y} + \frac{\partial v}{\partial x} \right) \\
\tau_{xz} &= -(\mu + \mu_T) \left(\frac{\partial u}{\partial z} + \frac{\partial w}{\partial x} \right) \\
\tau_{yz} &= -(\mu + \mu_T) \left(\frac{\partial v}{\partial z} + \frac{\partial w}{\partial y} \right)
\end{aligned} \tag{2.10}$$

$$\begin{aligned}
q_x &= -\frac{1}{(\gamma - 1) M_\infty^2} \left(\frac{\mu}{Pr} + \frac{\mu_T}{Pr_T} \right) \frac{\partial T}{\partial x} \\
q_y &= -\frac{1}{(\gamma - 1) M_\infty^2} \left(\frac{\mu}{Pr} + \frac{\mu_T}{Pr_T} \right) \frac{\partial T}{\partial y} \\
q_z &= -\frac{1}{(\gamma - 1) M_\infty^2} \left(\frac{\mu}{Pr} + \frac{\mu_T}{Pr_T} \right) \frac{\partial T}{\partial z}
\end{aligned} \tag{2.11}$$

2.2.3 Curvilinear form

The model equations are written in curvilinear form to facilitate use on grids of arbitrary local orientation and density. A transformation from the Cartesian co-ordinate system to the local coordinate system is introduced as

$$\begin{aligned}
\xi &= \xi(x, y, z) \\
\eta &= \eta(x, y, z) \\
\zeta &= \zeta(x, y, z) \\
t &= t
\end{aligned}$$

The Jacobian determinant of the transformation is given by

$$J = \frac{\partial(\xi, \eta, \zeta)}{\partial(x, y, z)}$$

The Equation 2.1 can then be written as

$$\frac{\partial \hat{\mathbf{W}}}{\partial t} + \frac{\partial(\hat{\mathbf{F}}^i - \hat{\mathbf{F}}^v)}{\partial \xi} + \frac{\partial(\hat{\mathbf{G}}^i - \hat{\mathbf{G}}^v)}{\partial \eta} + \frac{\partial(\hat{\mathbf{H}}^i - \hat{\mathbf{H}}^v)}{\partial \zeta} = 0 \tag{2.12}$$

where

$$\begin{aligned}
\hat{\mathbf{W}} &= \frac{\mathbf{W}}{J} \\
\hat{\mathbf{F}}^i &= \frac{1}{J} (\xi_x \mathbf{F}^i + \xi_y \mathbf{G}^i + \xi_z \mathbf{H}^i) \\
\hat{\mathbf{G}}^i &= \frac{1}{J} (\eta_x \mathbf{F}^i + \eta_y \mathbf{G}^i + \eta_z \mathbf{H}^i) \\
\hat{\mathbf{H}}^i &= \frac{1}{J} (\zeta_x \mathbf{F}^i + \zeta_y \mathbf{G}^i + \zeta_z \mathbf{H}^i) \\
\hat{\mathbf{F}}^v &= \frac{1}{J} (\xi_x \mathbf{F}^v + \xi_y \mathbf{G}^v + \xi_z \mathbf{H}^v) \\
\hat{\mathbf{G}}^v &= \frac{1}{J} (\eta_x \mathbf{F}^v + \eta_y \mathbf{G}^v + \eta_z \mathbf{H}^v) \\
\hat{\mathbf{H}}^v &= \frac{1}{J} (\zeta_x \mathbf{F}^v + \zeta_y \mathbf{G}^v + \zeta_z \mathbf{H}^v)
\end{aligned} \tag{2.13}$$

The expressions for the inviscid fluxes can be simplified by defining

$$\begin{aligned}
U &= \xi_x u + \xi_y v + \xi_z w \\
V &= \eta_x u + \eta_y v + \eta_z w \\
W &= \zeta_x u + \zeta_y v + \zeta_z w
\end{aligned} \tag{2.14}$$

The inviscid fluxes can then be written as

$$\begin{aligned}
\hat{\mathbf{F}}^i &= \begin{pmatrix} \rho U \\ \rho u U + \xi_x p \\ \rho v U + \xi_y p \\ \rho w U + \xi_z p \\ \rho U H \end{pmatrix} \\
\hat{\mathbf{G}}^i &= \begin{pmatrix} \rho V \\ \rho u V + \eta_x p \\ \rho v V + \eta_y p \\ \rho w V + \eta_z p \\ \rho V H \end{pmatrix} \\
\hat{\mathbf{H}}^i &= \begin{pmatrix} \rho W \\ \rho u W + \zeta_x p \\ \rho v W + \zeta_y p \\ \rho w W + \zeta_z p \\ \rho W H \end{pmatrix}
\end{aligned} \tag{2.15}$$

The derivative terms found in the viscous fluxes are evaluated using the chain rule, for example

$$\frac{\partial u}{\partial x} = \xi_x \frac{\partial u}{\partial \xi} + \eta_x \frac{\partial u}{\partial \eta} + \zeta_x \frac{\partial u}{\partial \zeta}$$

2.2.4 Steady State Solver

The spatial discretisation of Equation 2.12 leads to a set of ordinary differential equations in time,

$$\frac{d}{dt} (\mathbf{W}_{i,j,k} V_{i,j,k}) = -\mathbf{R}_{i,j,k}(\mathbf{W}) \quad (2.16)$$

where \mathbf{W} and \mathbf{R} are the vectors of cell conserved variables and residuals respectively. The convective terms are discretised using Osher's approximate Riemann solver (Osher et al. [56]). MUSCL variable extrapolation is used to provide second-order accuracy with the Van Albada limiter to prevent spurious oscillations around shock waves. Boundary conditions are set by using ghost cells on the exterior of the computational domain. In the far field ghost cells are set at the freestream conditions. At solid boundaries the no-slip condition is set for viscous flows, or ghost values are extrapolated from the interior (ensuring the normal component of the velocity on the solid wall is zero) for inviscid flow.

The integration in time of Equation 2.16 to a steady-state solution is performed using an implicit time-marching scheme given by

$$\frac{\mathbf{W}_{i,j,k}^{n+1} - \mathbf{W}_{i,j,k}^n}{\Delta t} = -\frac{1}{V_{i,j,k}} \mathbf{R}_{i,j,k}(\mathbf{W}_{i,j,k}^{n+1}) \quad (2.17)$$

where $n + 1$ denotes the solution values at time $(n + 1) * \Delta t$. Equation 2.17 represents a system of non-linear algebraic equations and to simplify the solution procedure, the flux residual $\mathbf{R}_{i,j,k}(\mathbf{W}_{i,j,k}^{n+1})$ is linearised in time

$$\begin{aligned} \mathbf{R}_{i,j,k}(\mathbf{W}^{n+1}) &= \mathbf{R}_{i,j,k}(\mathbf{W}^n) + \frac{\partial \mathbf{R}_{i,j,k}}{\partial t} \Delta t + O(\Delta t^2) \\ &\approx \mathbf{R}_{i,j,k}^n(\mathbf{W}^n) + \frac{\partial \mathbf{R}_{i,j,k}}{\partial \mathbf{W}} \frac{\partial \mathbf{W}}{\partial t} \Delta t \\ &\approx \mathbf{R}_{i,j,k}^n(\mathbf{W}^n) + \frac{\partial \mathbf{R}_{i,j,k}}{\partial \mathbf{W}} \Delta \mathbf{W} \end{aligned} \quad (2.18)$$

where $\Delta \mathbf{W} = \mathbf{W}^{n+1} - \mathbf{W}^n$. Equation 2.17 now becomes the following linear system

$$\left[\frac{V_{i,j,k}}{\Delta t} \mathbf{I} + \frac{\partial \mathbf{R}_{i,j,k}}{\partial \mathbf{W}} \right] \Delta \mathbf{W} = -\mathbf{R}_{i,j,k}^n(\mathbf{W}^n) \quad (2.19)$$

The number of operations required in a direct method to solve a linear system of \mathcal{N} equations is \mathcal{N}^3 , which becomes prohibitive when the total number of equations \mathcal{N} becomes large.

On the other hand, iterative techniques such as Krylov methods are capable of solving large systems of equations more efficiently in terms of time and memory if the system is sparse. Krylov methods find an approximation to the solution of a linear system by minimising a suitable residual error function in a finite-dimensional space of potential solution vectors. Several algorithms, such as BiCG, CGSTAB, CGS and GMRES, have been tested (see Badcock *et al.* [57]) and it was concluded that the choice of method is not as crucial as the preconditioning. The current results use a Generalised Conjugate Gradient method - see Axelsson [58].

The preconditioning strategy is based on a Block Incomplete Lower-Upper (BILU) factorisation (Axelsson [58]). The sparsity pattern of the Lower and Upper matrices is defined to reflect the sparsity of the unfactored matrix for simplicity. Furthermore the BILU factorisation is decoupled between blocks to improve parallel efficiency and this approach does not seem to have a major impact on the effectiveness of the preconditioner as the number of blocks increases.

The formulation used has an approximate Jacobian Matrix with a reduced number of non-zero entries per row. This has several advantages. First, the memory requirements are lowered. Secondly, the resolution of the linear system by the GCG method is faster in terms of CPU-time since all the matrix-vector multiplications involved require lower operation counts. Finally, the linear system is easier to solve since the approximate Jacobian matrix is more diagonally dominant. A full discussion of the Jacobian formulation is given in Cantariti *et al.* [59].

The steady state solver for the turbulence equations is formulated and solved in an identical manner to that already described for the mean flow. The eddy-viscosity is calculated from the latest values of k and ω (for example) and is used to advance the mean flow solution, and then this new solution is used to update the turbulence solution, freezing the mean flow values. An approximate Jacobian is used for the source term by only taking into account the contribution of the dissipation terms $\hat{\mathbf{D}}_k$ and $\hat{\mathbf{D}}_\omega$ i.e. no account of the production terms is taken on the left hand side of the system. This approach has a stability advantage as described in Wilcox [55].

2.2.5 Unsteady Solver

The formulation is described for the turbulent case. The laminar and inviscid cases represent a simplification of this. The presentation follows that of reference [54].

Following the pseudo-time formulation (Jameson [60]), the updated mean flow solution is calculated by solving the steady state problems

$$\mathbf{R}_{i,j,k}^* = \frac{3\mathbf{w}_{i,j,k}^{n+1} - 4\mathbf{w}_{i,j,k}^n + \mathbf{w}_{i,j,k}^{n-1}}{2\Delta t} + \mathbf{R}_{i,j,k}(\tilde{\mathbf{w}}_{i,j,k}^{k_m}, \tilde{\mathbf{q}}_{i,j,k}^{k_t}) = 0 \quad (2.20)$$

$$\mathbf{Q}_{i,j,k}^* = \frac{3\mathbf{q}_{i,j,k}^{n+1} - 4\mathbf{q}_{i,j,k}^n + \mathbf{q}_{i,j,k}^{n-1}}{2\Delta t} + \mathbf{Q}_{i,j}(\tilde{\mathbf{w}}_{i,j,k}^{l_m}, \tilde{\mathbf{q}}_{i,j,k}^{l_t}) = 0. \quad (2.21)$$

Here k_m, k_t, l_m and l_t give the time level of the variables used in the spatial discretisation. Since grid deformation is required, time varying areas are required in the expression for the real time derivative in equations 2.20 and 2.21. If $k_m = k_t = l_m = l_t = n + 1$ then the mean and turbulent quantities are advanced in real time in a fully coupled manner. However, if $k_m = l_m = l_t = n + 1$

and $k_t = n$ then the equations are advanced in sequence in real time, i.e. the mean flow is updated using frozen turbulence values, and then the turbulent values are updated using the latest mean flow solution. This has the advantage that the only modification, when compared with the laminar case, to the discretisation of the mean flow equations is the addition of the eddy viscosity from the previous time step. The turbulence model only influences the mean flow solution through the eddy viscosity and so any two equation model can be used without modifying the mean flow solver. Hence, the implementation is simplified by using a sequenced solution in real time. However, the uncoupling could adversely effect the stability and accuracy of the real time stepping, with the likely consequence of limiting the size of the real time step that can be used.

Equations (2.20) and (2.21) represent a coupled nonlinear system of equations. These can be solved by introducing an iteration through *pseudo time* τ to the steady state, as given by

$$\frac{\mathbf{w}_{i,j}^{n+1,m+1} - \mathbf{w}_{i,j}^{n+1,m}}{\Delta\tau} + \frac{3\mathbf{w}_{i,j}^{k_m} - 4\mathbf{w}_{i,j}^n + \mathbf{w}_{i,j}^{n-1}}{2\Delta t} + \mathbf{R}_{i,j}(\tilde{\mathbf{w}}_{i,j}^{k_m}, \tilde{\mathbf{q}}_{i,j}^{k_t}) = 0 \quad (2.22)$$

$$\frac{\mathbf{q}_{i,j}^{n+1,m+1} - \mathbf{q}_{i,j}^{n+1,m}}{\Delta\tau} + \frac{3\mathbf{q}_{i,j}^{l_t} - 4\mathbf{q}_{i,j}^n + \mathbf{q}_{i,j}^{n-1}}{2\Delta t} + \mathbf{Q}_{i,j}(\tilde{\mathbf{w}}_{i,j}^{l_m}, \tilde{\mathbf{q}}_{i,j}^{l_t}) = 0 \quad (2.23)$$

where the m -th pseudo-time iterate at the $n+1$ th real time step are denoted by $\mathbf{w}^{n+1,m}$ and $\mathbf{q}^{n+1,m}$ respectively. The iteration scheme used only effects the efficiency of the method and hence we can sequence the solution in pseudo time without compromising accuracy. For example, using explicit time stepping we can calculate $\mathbf{w}^{n+1,m+1}$ using $k_m = n+1, m$ and $k_t = n+1, m$ and $\mathbf{q}^{n+1,m+1}$ using $l_m = n+1, m+1$ and $l_t = n+1, m$. For implicit time stepping in pseudo time we can use $k_m = l_m = l_t = n+1, m+1$ and $k_t = n+1, m$. In both of these cases the solution of the equations is decoupled by freezing values but at convergence the real time stepping proceeds with no sequencing error. It is easy to recover a solution which is sequenced in real time from this formulation by setting $k_t = n$ throughout the calculation of the pseudo steady state. This facilitates a comparison of the current pseudo time sequencing with the more common real time sequencing. In the code the pseudo steady-state problems are solved using the implicit steady state solver described in detail in Section 2.2.4.

2.3 Mesh Movement

2.3.1 Transfinite Interpolation

The deformation of the volume grid is performed in the PMB code using Transfinite Interpolation (TFI). TFI is an algebraic method of grid deformation that is computationally inexpensive as well as easy to implement. Currently the grid deformation is performed only in the blocks containing moving solid surfaces and the rest of the blocks are held rigid. The TFI of the nodes contained in a block is performed in 3 steps. In the first step the nodes of the block edges are interpolated linearly to adjust to the deformation of the block corners. In the second step the nodes of the block faces are interpolated using TFI to adjust to the deformation of the block

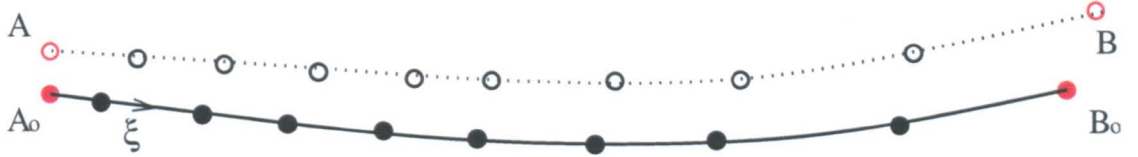


Figure 2.1: Displacement of a block edge

edges brought about in step 1. Finally the nodes in the interior of the block, the volume nodes, are interpolated using TFI to adjust to the deformation of the block faces. The presentation follows reference [61].

TFI of Block Edges

Figure 2.3.1 shows an edge of a moving block with end points A_0 and B_0 displaced by dA and dB respectively. The deformation of the interior nodes of the edge are interpolated using the deformation of the end points. The position and deformation vectors of the nodes of the edge are denoted by,

$$\mathbf{x} = \begin{bmatrix} x(\xi) \\ y(\xi) \\ z(\xi) \end{bmatrix}, \quad d\mathbf{x} = \begin{bmatrix} dx(\xi) \\ dy(\xi) \\ dz(\xi) \end{bmatrix} \quad (2.24)$$

As the values of the displaced block corners are known the displacements of the end points are calculated by,

$$dA = A - A_0, \quad dB = B - B_0$$

The linear interpolation on the nodes of the edge is then given by the equation,

$$d\mathbf{x}(\xi) = dA(1 - s(\xi)) + dBs(\xi) \quad (2.25)$$

where,

$$s(\xi) = \frac{\text{Length from } A_0 \text{ to } x_0(\xi)}{\text{Length of the curve } A_0 \text{ to } B_0}$$

The coordinates of the new grid points are obtained as

$$\mathbf{x}(\xi) = \mathbf{x}_0(\xi) + d\mathbf{x}(\xi)$$

TFI of Block Faces

After the nodes on the block edges are interpolated following the displaced block vertices, the interior nodes of the block faces are interpolated next. Consider a block face made up of 4 curves C1, C2, C3 and C4 as shown in Figure 2.2. The nodes on the edge curves have already been interpolated in the previous step. The position vector and the deformation vector of the nodes on the face are denoted by,

$$\mathbf{x} = \begin{bmatrix} x(\xi, \eta) \\ y(\xi, \eta) \\ z(\xi, \eta) \end{bmatrix}, \quad d\mathbf{x} = \begin{bmatrix} dx(\xi, \eta) \\ dy(\xi, \eta) \\ dz(\xi, \eta) \end{bmatrix} \quad (2.26)$$

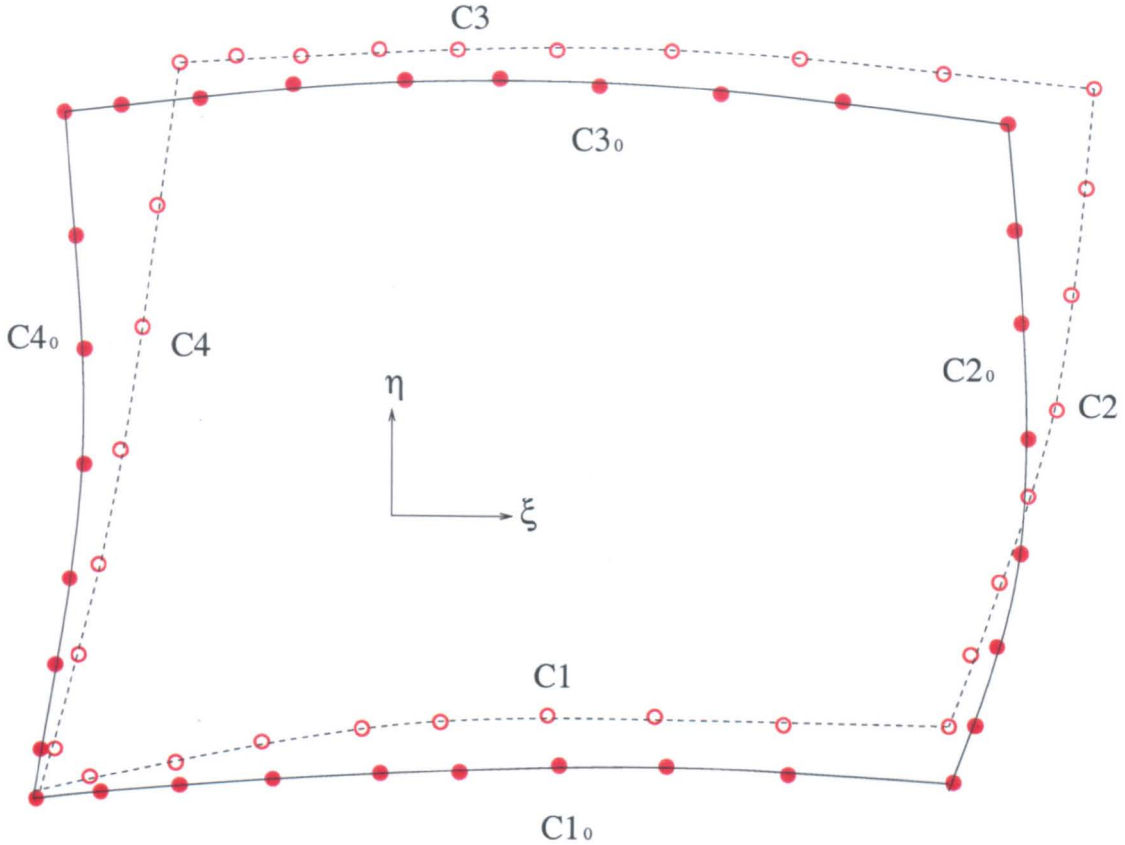


Figure 2.2: The edges of a block face.

As the values of the displaced block edges are known the displacements of the nodes of the edges are calculated as,

$$d\mathbf{C1} = \mathbf{C1} - \mathbf{C1}_0$$

$$d\mathbf{C2} = \mathbf{C2} - \mathbf{C2}_0$$

$$d\mathbf{C3} = \mathbf{C3} - \mathbf{C3}_0$$

$$d\mathbf{C4} = \mathbf{C4} - \mathbf{C4}_0$$

where \mathbf{C}_0 and \mathbf{C} are the old and new positions of the edges. The displacements of the interior nodes are then calculated as,

$$d\mathbf{x}(\xi, \eta) = \mathbf{f}_1(\xi, \eta) + \mathbf{f}_2(\xi, \eta) \quad (2.27)$$

where,

$$\mathbf{f}_1(\xi, \eta) = (1 - \psi_1(\xi))d\mathbf{C4}(\eta) + \psi_1(\xi)d\mathbf{C2}(\eta) \quad (2.28)$$

$$\mathbf{f}_2(\xi, \eta) = \phi_1(\eta)[d\mathbf{C1}(\xi) - \mathbf{f}_1(\xi, 0)] + (1 - \phi_1(\eta))[d\mathbf{C3}(\xi) - \mathbf{f}_1(\xi, 1)] \quad (2.29)$$

ψ and ϕ are known as the blending functions in ξ and η directions respectively. These are calculated as

$$\begin{aligned} \psi_1(\xi, \eta) &= \left[1 - \left[\frac{s_2(\eta) + s_4(\eta)}{2}\right]\right] s_1(\xi) + \left[\frac{s_2(\eta) + s_4(\eta)}{2}\right] s_3(\xi) \\ \phi_1(\xi, \eta) &= \left[1 - \left[\frac{s_1(\xi) + s_3(\xi)}{2}\right]\right] s_2(\eta) + \left[\frac{s_1(\eta) + s_3(\eta)}{2}\right] s_4(\eta) \end{aligned}$$

where $s_1(\xi)$, $s_2(\eta)$, $s_3(\xi)$ and $s_4(\eta)$ are the length ratios along curves **C1**, **C2**, **C3**, and **C4**. These are calculated as

$$\begin{aligned} s_1(\xi) &= \frac{\text{Length to } \mathbf{x}(\xi, 0)}{\text{Length of the curve } \mathbf{C1}} \\ s_2(\eta) &= \frac{\text{Length to } \mathbf{x}(1, \eta)}{\text{Length of the curve } \mathbf{C2}} \\ s_3(\xi) &= \frac{\text{Length to } \mathbf{x}(\xi, 1)}{\text{Length of the curve } \mathbf{C3}} \\ s_4(\eta) &= \frac{\text{Length to } \mathbf{x}(0, \eta)}{\text{Length of the curve } \mathbf{C4}} \end{aligned} \quad (2.30)$$

The new locations of the interior nodes on the block face are given by,

$$\mathbf{x}(\xi, \eta) = \mathbf{x}_0(\xi, \eta) + d\mathbf{x}(\xi, \eta)$$

TFI of Block Volumes

Interpolation of the interior nodes of the block forms the final step of the TFI methodology. The interpolated nodes on the block faces now act as the endpoints for the nodes lying in the interior of the block. The position vector and the deformation vector of the nodes on the face are denoted by,

$$\mathbf{x} = \begin{bmatrix} x(\xi, \eta, \zeta) \\ y(\xi, \eta, \zeta) \\ z(\xi, \eta, \zeta) \end{bmatrix}, \quad d\mathbf{x} = \begin{bmatrix} dx(\xi, \eta, \zeta) \\ dy(\xi, \eta, \zeta) \\ dz(\xi, \eta, \zeta) \end{bmatrix} \quad (2.31)$$

The volume block is bounded by 6 rectangular faces **F1**, **F2**, **F3**, **F4**, **F5** and **F6** shown in Figure 2.3. Each face is made up of 4 edges, which are shown in Figure 2.4.

$$\begin{aligned} \mathbf{F1} &\rightarrow (\mathbf{C1}, \mathbf{C5}, \mathbf{C4}, \mathbf{C8}) \\ \mathbf{F2} &\rightarrow (\mathbf{C5}, \mathbf{C10}, \mathbf{C6}, \mathbf{C11}) \\ \mathbf{F3} &\rightarrow (\mathbf{C2}, \mathbf{C6}, \mathbf{C3}, \mathbf{C7}) \\ \mathbf{F4} &\rightarrow (\mathbf{C9}, \mathbf{C7}, \mathbf{C12}, \mathbf{C8}) \\ \mathbf{F5} &\rightarrow (\mathbf{C1}, \mathbf{C10}, \mathbf{C2}, \mathbf{C9}) \\ \mathbf{F6} &\rightarrow (\mathbf{C4}, \mathbf{C11}, \mathbf{C3}, \mathbf{C12}) \end{aligned}$$

The final deformation of the interior nodes is given by,

$$d\mathbf{x}(\xi, \eta, \zeta) = \mathbf{f}_1(\xi, \eta, \zeta) + \mathbf{f}_2(\xi, \eta, \zeta) + \mathbf{f}_3(\xi, \eta, \zeta) \quad (2.32)$$

and the functions \mathbf{f}_1 , \mathbf{f}_2 and \mathbf{f}_3 are given by,

$$\mathbf{f}_1(\xi, \eta, \zeta) = [1 - \psi]d\mathbf{F4} + \psi d\mathbf{F2} \quad (2.33)$$

$$\mathbf{f}_2(\xi, \eta, \zeta) = [1 - \phi][d\mathbf{F5} - \mathbf{f}_1(\xi, 0, \zeta)] + \phi[d\mathbf{F6} - \mathbf{f}_1(\xi, 1, \zeta)] \quad (2.34)$$

$$\mathbf{f}_3(\xi, \eta, \zeta) = [1 - \omega][d\mathbf{F1} - \mathbf{f}_2(\xi, \eta, 0)] + \omega[d\mathbf{F3} - \mathbf{f}_2(\xi, \eta, 1)] \quad (2.35)$$

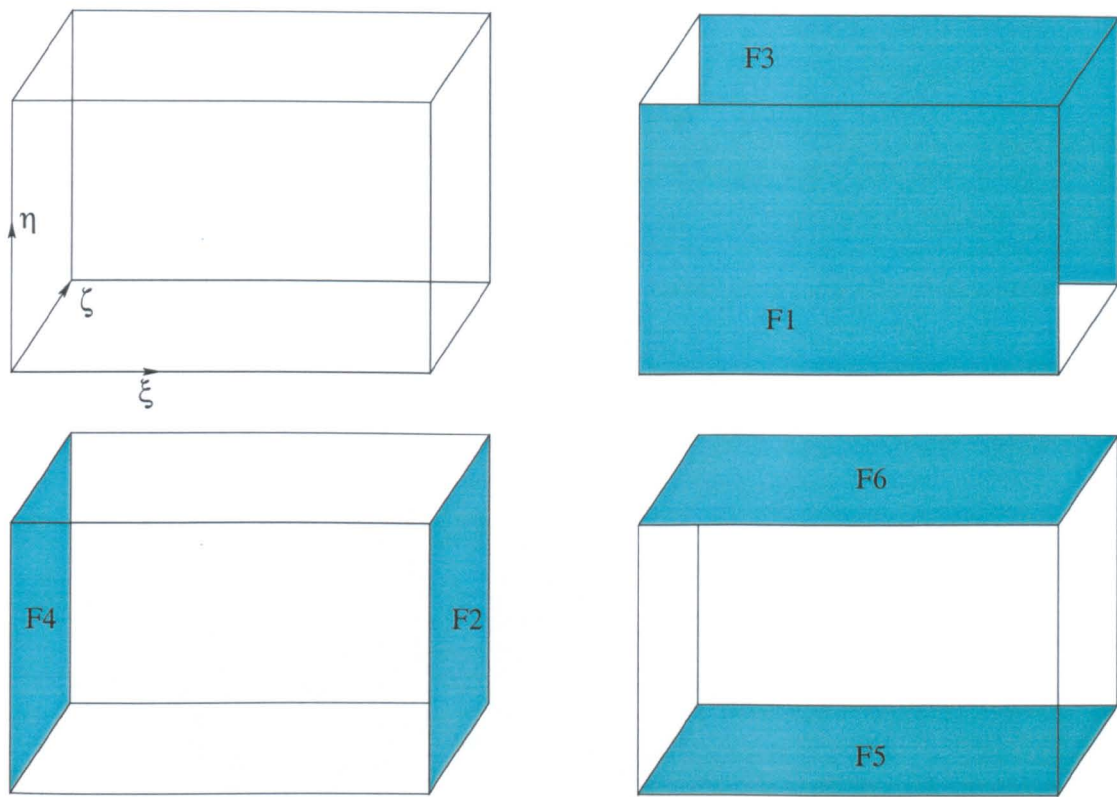


Figure 2.3: The faces of the volume block.

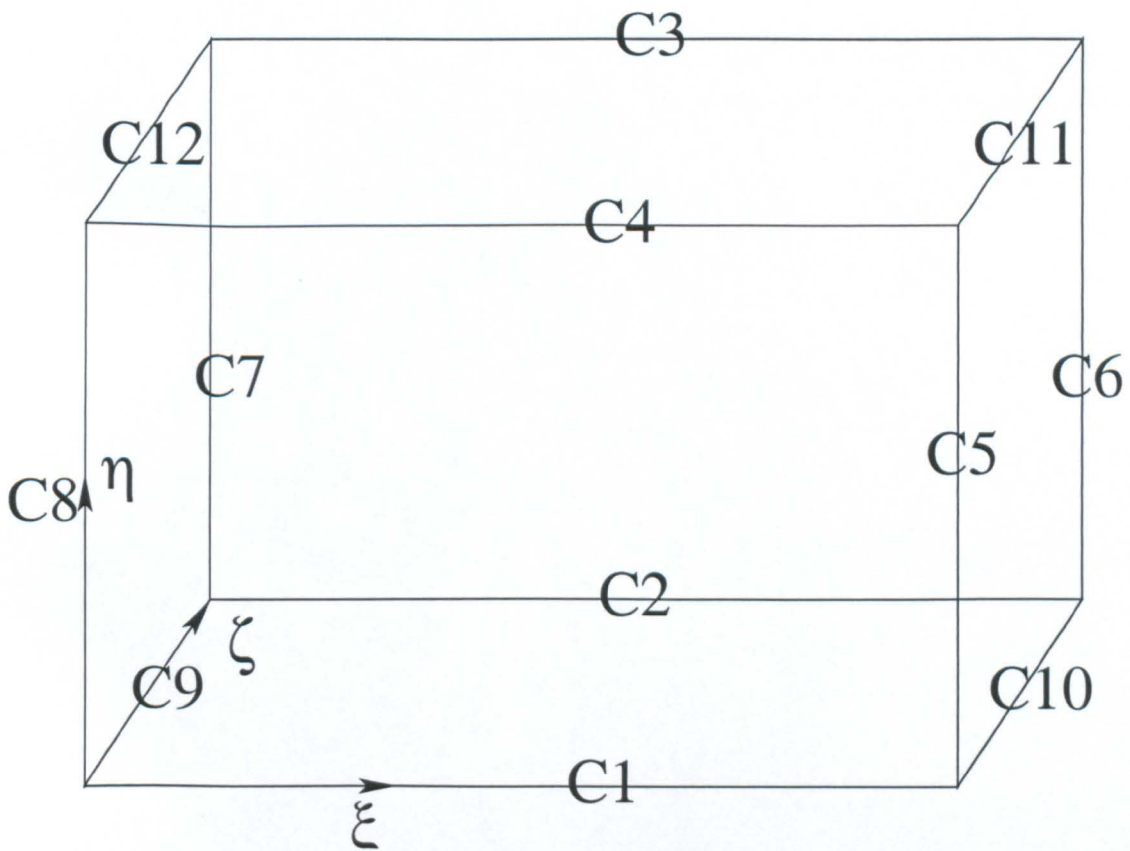


Figure 2.4: The edges of the volume block.

The functions ψ , ϕ and ω are the blending functions in the ξ , η and ζ directions respectively and are calculated from

$$\begin{aligned}\psi &= [1 - s_\eta][1 - s_\zeta]s_1 + [1 - s_\eta][s_\zeta]s_2 + [s_\eta][1 - s_\zeta]s_3 + [s_\eta][s_\zeta]s_4 \\ \phi &= [1 - s_\zeta][1 - s_\xi]s_5 + [1 - s_\zeta][s_\xi]s_6 + [s_\zeta][1 - s_\xi]s_7 + [s_\zeta][s_\xi]s_8 \\ \omega &= [1 - s_\xi][1 - s_\eta]s_9 + [1 - s_\xi][s_\eta]s_{10} + [s_\xi][1 - s_\eta]s_{11} + [s_\xi][s_\eta]s_{12}\end{aligned}$$

where,

$$\begin{aligned}s_\xi &= \frac{s_1 + s_2 + s_3 + s_4}{4} \\ s_\eta &= \frac{s_5 + s_6 + s_7 + s_8}{4} \\ s_\zeta &= \frac{s_9 + s_{10} + s_{11} + s_{12}}{4}\end{aligned}$$

with s_i calculated from Equation 2.30.

2.3.2 Geometric Conservation Law

In an unsteady simulation that involves the local deformation of the CFD grid the cell volumes of the grid vary with time. For the scheme to be conservative it is important that the time variation of the volumes is consistent with the mesh speeds. The Geometrical Conservation Law (GCL) is derived from a volume continuity equation and is stated as

$$\frac{\partial}{\partial t} \int_{\Omega} dV - \oint_{\partial \Sigma} \mathbf{v} \cdot \mathbf{n} d\Sigma = 0 \quad (2.36)$$

where V is the cell area, \mathbf{v} is the grid speed, \mathbf{n} is the normal area vector and $\partial \Sigma$ is the boundary surface of the control volume Ω . The second order time discretisation used for the flow equations is used to discretise equation 2.36,

$$\frac{3V_{i,j}^{n+1} - 4V_{i,j}^n + V_{i,j}^{n-1}}{2\Delta t} - \oint_{\partial \Sigma} \mathbf{v} \cdot \mathbf{n} d\Sigma = 0 \quad (2.37)$$

The control volume at the next time level is then given by

$$V_{i,j}^{n+1} = \frac{4V_{i,j}^n - V_{i,j}^{n-1}}{3} + 2\Delta t \oint_{\partial \Sigma} \mathbf{v} \cdot \mathbf{n} d\Sigma \quad (2.38)$$

The rate of the area traversed by the cell boundaries is given by

$$\oint_{\partial \Sigma} \mathbf{v} \cdot \mathbf{n} d\Sigma = (\xi_t)_{i+\frac{1}{2},j,k} - (\xi_t)_{i-\frac{1}{2},j,k} + (\eta_t)_{i,j+\frac{1}{2},k} - (\eta_t)_{i,j-\frac{1}{2},k} + (\zeta_t)_{i,j,k+\frac{1}{2}} - (\zeta_t)_{i,j,k-\frac{1}{2}} \quad (2.39)$$

and

$$\xi_t = -(\xi_x x_t + \xi_y y_t) \quad (2.40)$$

$$\eta_t = -(\eta_x x_t + \eta_y y_t) \quad (2.41)$$

Here x_t and y_t are the grid velocities. It can be seen that as V^{n+1} is numerically obtained from ξ_t and η_t rather than analytically from the updated nodal positions. The importance of maintaining the consistency between the integrated cell volumes and the flow equations is discussed in [62].

2.4 Structural Solver

Finite Element Method (FEM) solvers enable the static and dynamic modelling of aircraft structures. For the prediction of aeroelastic instabilities the structure is here assumed to be linear. Structural nonlinearities like structural freeplay, change of stiffness due to static loading of the structure and internal damping are neglected. This approximation of linear structural behaviour allows the N degree of freedom elastic equilibrium equation to be written as a second order linear ordinary differential equation

$$\mathbf{M}\ddot{\mathbf{x}} + \mathbf{C}\dot{\mathbf{x}} + \mathbf{K}\mathbf{x} = \mathbf{f} \quad (2.42)$$

where \mathbf{M} is the mass, \mathbf{C} the viscous damping and \mathbf{K} the stiffness matrices of size $N \times N$. Here \mathbf{x} and \mathbf{f} are the time dependent displacements and the external force vectors of size N . As the structure is linear the deformation can be calculated as a summation of pre calculated natural modes. In PMB a modal FEM solver is incorporated into the code and the mode shapes and natural frequencies are pre calculated using a commercial FEM package, and given as input. For problems where aeroelastic instabilities are not due to structural nonlinearities a modal model of the structure can be used to calculate the structural response. The basic assumption is that the structure oscillates in distinct natural modes of vibration. As the modes are calculated only once before starting the coupled aeroelastic calculations the actual cost of obtaining the structural response (Equation 2.51) is small as compared to the cost of solving the CFD equations. The undamped modes are a useful basis set for even the damped system. Moreover, at the buzz/flutter condition, aerodynamic damping is zero and structural (hysteretic) damping is very small for modern aircraft. The effect of adding damping is investigated in Chapter 5. The mode shapes of a linear structural system can be calculated by determining the undamped free vibration characteristics of the Equation 2.42 which is rewritten as

$$\mathbf{M}\ddot{\mathbf{x}} + \mathbf{K}\mathbf{x} = 0 \quad (2.43)$$

Assuming that the motion of the structure is sinusoidal and that the whole structure oscillates with a single frequency for each mode then

$$\mathbf{x}(t) = \mathbf{x}e^{i\omega t} \quad (2.44)$$

where \mathbf{x} is the vector of time independent amplitude of the mode with frequency ω , hence

$$\ddot{\mathbf{x}} = -\omega^2 \mathbf{x}e^{i\omega t} \quad (2.45)$$

Substituting \mathbf{x} and $\ddot{\mathbf{x}}$ in Equation 2.43

$$(\mathbf{K} - \omega^2 \mathbf{M})\mathbf{x}e^{i\omega t} = 0 \quad (2.46)$$

The frequencies ω can be obtained by solving the determinant

$$|\mathbf{K} - \omega^2 \mathbf{M}| = 0 \quad (2.47)$$

The solution of Equation 2.47 gives N values of ω_i , which are the natural frequencies of vibration. The i^{th} natural frequency ω_i is substituted in Equation 2.43 to obtain the corresponding mode

shape Φ_i . The mode shapes are mass generalised before they are used for aeroelastic calculations. Mass generalisation is performed thus

$$\Phi_i = m_i^{-1/2} \Phi_i^{mass} \quad (2.48)$$

where m_i is the generalised mass of the i^{th} mode and Φ_i^{mass} is the non mass generalised mode shape. The generalised masses are obtained from the orthogonality property of the modal system which states that

$$\Phi_i^{massT} \mathbf{M} \Phi_i^{mass} = m_i \quad (2.49)$$

The mass generalised mode shape hence have the property of

$$\Phi^T \mathbf{M} \Phi = \mathbf{I} \quad (2.50)$$

Reformulating Equation 2.42 in the modal form, it can be rewritten as

$$\ddot{\eta}_i + C_i \dot{\eta}_i + \omega_i^2 \eta_i = \Phi_i F_s \quad (2.51)$$

where η_i is known as the generalised coordinate and F_s is the total force acting on the structure. C_i is an empirically obtained value of structural damping. Equation 2.51 can be solved for η_i using one of the Runge-Kutta schemes. The deformation at the given time step for a problem with p modes is given by

$$\mathbf{x} = \sum_{i=1}^p \Phi_i \eta_i \quad (2.52)$$

2.5 Sequencing of Structural and Fluid Solvers

PMB employs a loosely coupled approach for calculating aeroelastic response. The CFD solver calculates the aerodynamic forces on the body. These forces are then transferred to the structural model through a transformation scheme. The FEM solver calculates the deformation on the structural grid which is then transferred back to the fluid grid. Ideally for a coupled dynamic calculation the fluid and the structural equations need to be solved simultaneously and progress together in time. However such a fluid-structure formulation is complex and poses numerical difficulties. The structural equations are in Lagrangian or material coordinates where the grid nodes move as the solution progresses, whereas the fluid equations are in Eulerian or space coordinates where the flow moves through the stationary grid. The combined formulation is usually referred to as Arbitrary Lagrangian Eulerian (ALE) formulation.

In a loosely coupled approach to solve the structural equations the value of the force is required at time levels n and $n + 1$. The PMB code uses Jameson's [60] dual time stepping scheme for time marching calculations. Here the unsteady problem is reformulated as a modified steady state problem with each iteration in pseudo time solved as a steady state problem until convergence. This allows for the coupling of the structural equations within the pseudo time loop. To solve Equation 2.51 an estimate of F_s is required at time level $n + 1$. The sequencing in a dynamic calculation is performed as follows:

- An estimate of the force at $n + 1$ real time and m^{th} pseudo time level $F_f^{n+1,m}$ is calculated on the fluid surface.

- This is transferred on to the surface grid using the intergrid transformation scheme to get $F_s^{n+1,m}$.
- The structural solution from Equation 2.51 is obtained using the transferred force $\mathbf{x}^{n+1,m} = \sum_{i=1}^p \Phi_i \eta_i^{n+1,m}$. Here the value of the force at $n + 1$ time level is estimated with the force value at $n + 1, m$.
- Interpolate the deformations back to the fluid grid using the transformation scheme.
- increment m and continue until converged

At convergence both structural and fluid solutions progress forward in real time together.

Chapter 3

Transformation Methodology

3.1 Introduction

Computational Aeroelasticity involves the coupled solution of aerodynamic and structural equations to obtain the aeroelastic response. These equations are usually solved on separate grids and the coupling takes place through an inter-grid transformation scheme. The unsteady aerodynamic solver calculates the flow variables like force and pressure on the aerodynamic grid. The calculated force values over the wetted body are interpolated onto the structural grid. The interpolated forces are input for the structural solver which calculates the deformation on the structural grid. This deformation is then transferred to the aerodynamic grid once again using the inter-grid transformation, to give a new geometry for the aerodynamic solver. Figure 3.1 shows a typical simulation cycle. The aerodynamic methods used for the analysis can range from linear panel methods like the doublet lattice method to advance RANS solvers. Similarly the method for solving structural equations can either be a modal based solver on simplified or detailed geometry, or can involve a nonlinear FEM solution on a detailed structure.

The transformation scheme that couples the aerodynamic and structural solver has to conform to the requirements of the solvers. For example the doublet lattice method uses 2D panels to calculate the aerodynamics and can be coupled with a structural solver using a simplified structural grid through a 2D interpolation scheme like the Infinite Plate Spline or Isoparametric Mapping without a loss of accuracy. This is facilitated by the fact that structural and aerodynamic grid points for such a case lie on the same surface allowing simple interpolation between the grid points. However for more advanced Euler and RANS based CFD solvers that model aerodynamics on the detailed geometry, a 3D interpolation scheme is essential. There are a number of papers in the literature that discuss and compare the various transformation schemes [63, 64, 65, 66]. For the sake of completeness a brief description of some of the more popular schemes is given in Section 3.3.

3.2 Requirements of a Transformation Scheme

In a computational aeroelastic calculation the transformation scheme plays a vital role as it links the different physical models to obtain a coupled response. The task is further complicated by the requirement to maintain grid fidelity (smoothness) in CFD based simulations and the simplification of the structural models that are commonly used [67]. Taking into consideration

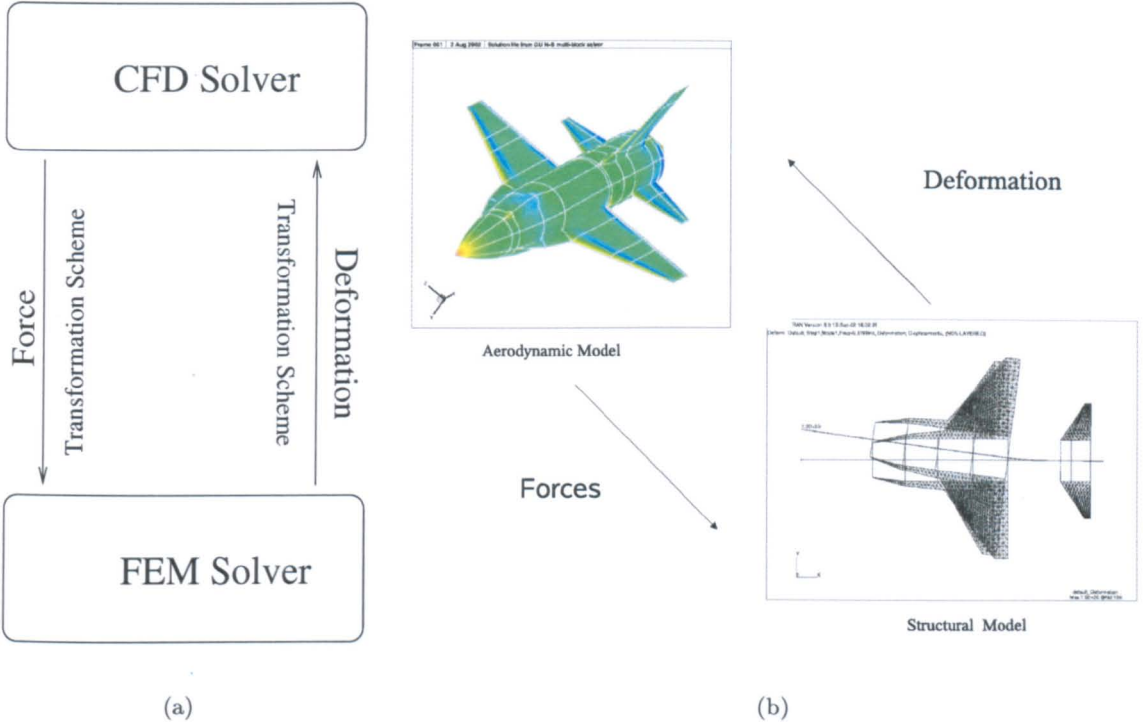


Figure 3.1: A typical cycle for coupled aeroelastic simulations.

the needs of high fidelity CFD based simulations on complex configurations there are certain requirements for a transformation scheme that need to be fulfilled to enable robust and accurate aeroelastic simulations.

3.2.1 Grid Smoothness

This is one of the basic requirements for all transformation schemes. The deformation transferred from the structural grid to the aerodynamic surface grid should be as smooth as possible. This is important as surface distortions introduced on account of inaccurate transformation can lead to spurious flow behaviour in RANS based simulations. The distortions could lead to premature separation. In cases where there are discontinuities in the structural deformation, for example the intersection between components like wing and fuselage which deform in different planes, the scheme should be able to blend this discontinuity when transferring the information to the aerodynamic grid.

3.2.2 Accurate Information Transfer

A preferred property in a transformation scheme is the ability to accurately resolve the rigid body rotational modes with minimal distortion of the cross-section of the body. Most of the 2D interpolation schemes are unable to do this. Figure 3.2 shows a circle driven by a rigid bar. It can be seen that circle loses its shape when the bar is rotated when using the IPS scheme. A discussion on this property is given in references [49, 50].

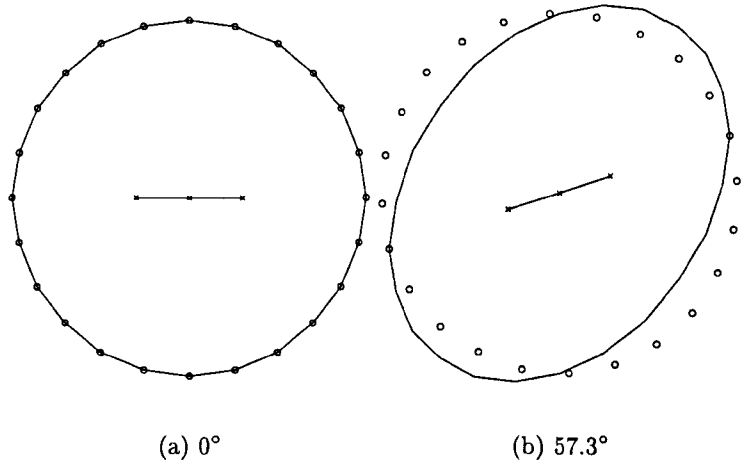


Figure 3.2: A circle of points rigidly rotated by bar using the IPS scheme (from [49]).

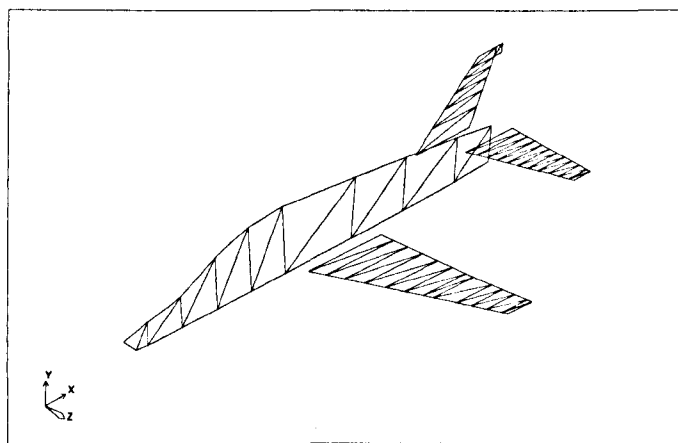


Figure 3.3: The Hawk structural model.

3.2.3 Sparse Structural Models

In general the static and dynamic behaviour of a structure can be adequately modelled using a sparse grid compared with the grid density required for the aerodynamics. However for a smooth transformation of the deformed structure it is sometimes necessary to increase the number of structural elements. Increasing the number of structural elements also increases the size of the transformation matrix increasing the memory requirements. A good transformation scheme should be able to perform smooth transformation using sparse structural grids. One such case was the Hawk aircraft which was investigated by Woodgate et al. [67]. Here the structural model of the Hawk aircraft as used in the industrial flutter certification process was used for CFD based predictions. The structural model is relatively sparse with just 78 elements for the complete aircraft (see Figure 3.3). The problem with very sparse structural grid arises in the association of the fluid grid nodes with a suitable structural element. Section 3.4.1 addresses this issue for the CVT scheme.

3.2.4 Complex Geometries

To realise its potential as an aeroelastic simulation tool CFD based analysis needs to also be able to analyse these instabilities over complex full aircraft configuration. Transformation between the structural and fluid grids has been identified as one of the nontrivial issue. For complete aircraft configurations there is a need for a robust and accurate transformation scheme that can treat complex geometries without introducing holes at the component interfaces.

3.2.5 Memory Requirements

An important consideration for performing nonlinear aerodynamic based aeroelastic simulations on full aircraft geometries arises from the fact that such high fidelity simulations involve large CFD and structural grids. For example a typical grid for a full aircraft can have 1×10^4 fluid points on the surface ($n_a = 10^4$) and 200 structural points ($n_s = 200$). For the IPS and FPS methods described in Section 3.3 a matrix defining the transformation must be stored. The number of elements in this matrix is $9 \times n_a \times n_s$, which means around 18 million non-zero values. The BEM method requires even more memory. IPS, FPS and BEM defined in Section 3.3 are all global methods which means that the deformation of a fluid surface point depends on all the points on the structural grid and hence require large transformation matrices. Compared to that the CVT is a local method in the sense that the transformation of a fluid point depends on the 3 structural points alone and hence the memory requirements are insignificant.

3.2.6 Conservation of Energy

The transformed forces from the aerodynamic grid deform the structure, hence energy is extracted from the flow for performing this work. The deformed structure in turn changes the pressure distribution over the surface which once again effects the energy extracted from the flow. For accurate prediction of aeroelastic instabilities it is vital that the transformation scheme be conservative in force and deformation transformation. The CVT scheme by definition conserves the volume between the aerodynamic and structural grids. The principle of virtual work

is used to transfer forces. This is shown in Section 3.4.

3.3 Interpolation Schemes

Some of the popular interpolation schemes are briefly described here. This section is based on the MSc thesis of Rampurawala [68] and is reproduced here for the sake of completeness.

3.3.1 Infinite Plate Spline

The Infinite Plate Spline method developed by Desmarais and Harder [69] is a widely used form of spline methods. Consider an infinite plate on which the structural points are located, having deflections δz_i . The static equilibrium equation for the plate is given by

$$\mathcal{D}\nabla^4\delta z = q \quad (3.1)$$

where \mathcal{D} is the plate flexibility and q is the distributed load. The solution for plate deflection can be written as

$$\delta z(x, y) = a_0 + a_1x + a_2y + \sum_{i=1}^N \mathcal{F}_i r_i^2 \ln r_i^2 \quad (3.2)$$

where r_i is the distance of any point (x, y) on the plate from the structural point $(x_{s,i}, y_{s,i})$. To produce linear behaviour at infinity, the force and momentum satisfy

$$\begin{aligned} \sum \mathcal{F}_i &= 0 \\ \sum x_i \mathcal{F}_i &= 0 \\ \sum y_i \mathcal{F}_i &= 0 \end{aligned} \quad (3.3)$$

From the Equations 3.3 the coefficients \mathcal{F}_i are calculated for known displacements at the structural nodes. These are then back substituted into Equation 3.2 to determine δz for the unknown deflections at the aerodynamic grid points. Here all the aerodynamic grid points are assumed to lie in the same plane as the structural grid. If the structural and aerodynamic points do not lie on the same surface then they are projected onto a neutral plane. The deflections for the projected aerodynamic points are calculated and then the original offset is added to the projected points to recover the deflected aerodynamic points.

3.3.2 Finite Plate Spline

This method was developed by Kari Appa [70] and applied by Guruswamy and Byun [71] to a fighter aircraft wing. The method makes use of a virtual surface (VS) which lies between the structural and fluid grids. The VS is discretisation into finite elements which are not necessarily the same elements as on the structural grid. A set of constraints are established such that the deformed VS is forced to pass through the deformed structural surface nodes. Consider m aerodynamic points at which displacements are needed due to displacements at n structural points. For any element the displacement at any point in the element is given by

$$r = \Omega \mathbf{n} \quad (3.4)$$

where Ω is the shape function of the element at a point used to interpolate the displacements within an element in terms of the nodal degrees of freedom \mathbf{n} . The vector \mathbf{n} can be related to the global displacement vector \mathbf{q} by the connectivity matrix \mathbf{A} , hence the i th element can be stated as

$$\mathbf{n}_i = \mathbf{A}_i \mathbf{q}. \quad (3.5)$$

Using the relation in Equation 3.4, the displacement vector for structural constraint points can be written after assembly, as

$$\mathbf{q}_s = \Psi_s \mathbf{q} \quad (3.6)$$

where

$$\Psi = \begin{bmatrix} \Omega_1 A_1 \\ \Omega_2 A_2 \\ \vdots \\ \Omega_n A_n \end{bmatrix}. \quad (3.7)$$

Similarly the displacement vector \mathbf{q}_a at the aerodynamic points in terms of the global displacement vector \mathbf{q} can be written as

$$\mathbf{q}_a = \Psi_a \mathbf{q} \quad (3.8)$$

where Ψ_a is the displacement mapping matrix from the VS to the fluid surface grid. To force the VS to pass through a given set of displacements \mathbf{q}_s the penalty method of constraints (as described in [72]) gives the equilibrium state of the structure.

$$[\mathbf{K} + \delta \Psi_s^T \Psi_s] \mathbf{q} = \delta \Psi_s^T \mathbf{q}_s \quad (3.9)$$

where \mathbf{K} is the stiffness matrix of the VS, Ψ_s is the displacement mapping matrix of the VS to the structural grid, and δ is a penalty parameter. Solving for \mathbf{q} and substituting in Equation 3.8, the displacements at the fluid surface grid points can be expressed as

$$\mathbf{q}_a = \mathbf{T} \mathbf{q}_s \quad (3.10)$$

where

$$\mathbf{T} = \Psi_a (\delta^{-1} \mathbf{K} + \Psi_s^T \Psi_s)^{-1} \Psi_s^T \quad (3.11)$$

3.3.3 Inverse Isoparametric Mapping

The isoparametric mapping technique is widely used in FEM analysis to transform state variables like displacement, stress and loads from structural grid points to the aerodynamic grid points. In this approach the same shape function (\mathbf{N}) is used to interpolate the aerodynamic grid point and to approximate the structural deformation. The isoparametric mapping is from a local coordinate (ξ, η) to a global coordinate system (x, y) . The mapping of an aerodynamic point is defined by the shape functions for a structural element within which it lies. Consider an aerodynamic point lying in a quadrilateral structural element (Figure 3.3.3). The local coordinates for such a point can be defined as

$$x = \sum N_i(\xi, \eta) x_i \quad 1 \leq i \leq 4 \quad (3.12)$$

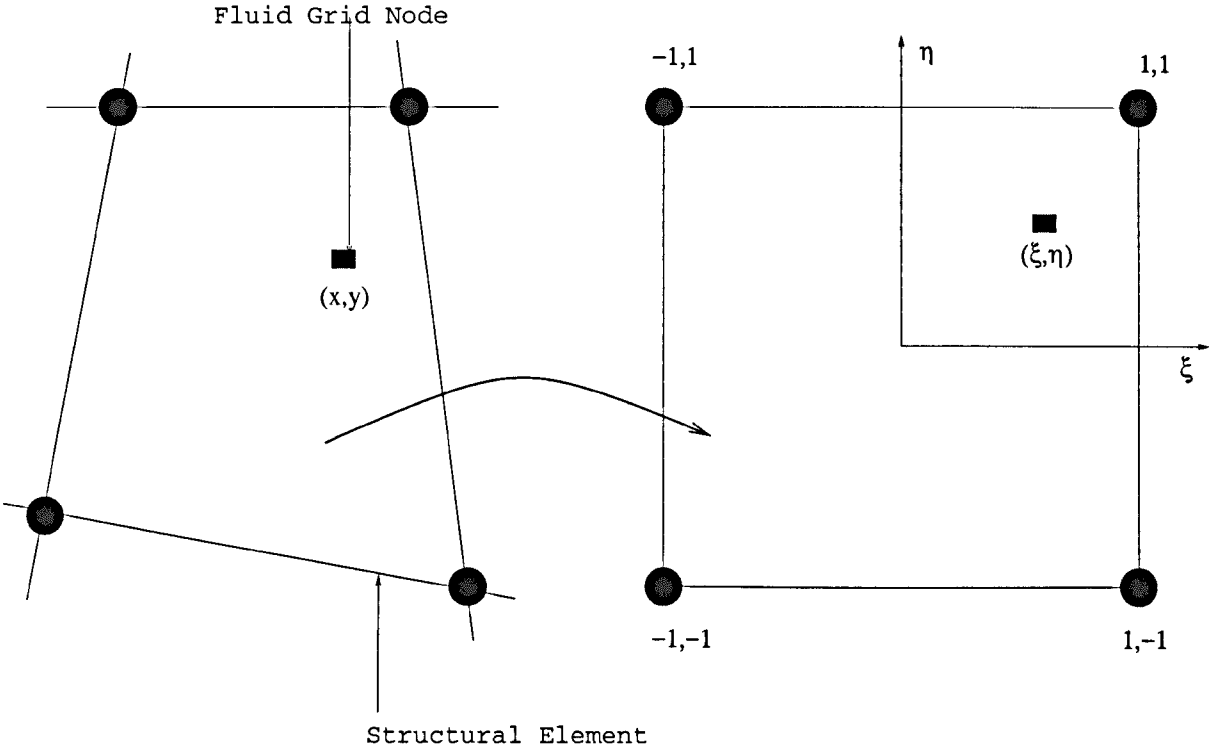


Figure 3.4: Isoparametric Transformation

$$y = \sum N_i(\xi, \eta) y_i \quad 1 \leq i \leq 4 \quad (3.13)$$

where

$$\begin{aligned} N_1(\xi, \eta) &= 1/4(1 - \xi)(1 - \eta) \\ N_2(\xi, \eta) &= 1/4(1 + \xi)(1 - \eta) \\ N_3(\xi, \eta) &= 1/4(1 + \xi)(1 + \eta) \\ N_4(\xi, \eta) &= 1/4(1 - \xi)(1 + \eta) \end{aligned} \quad (3.14)$$

After calculating the global transformed aerodynamic coordinates the local coordinates (ξ_m, η_m) of the aerodynamic points on the deformed structural grid are calculated as follows. An arbitrary line PQ is defined such that it lies on the aerodynamic point M and on an element node P. The line transforms into P'Q' through inverse mapping. The equation for the line P'Q' can be written as

$$A\xi^2 + B\xi + C = 0 \quad (3.15)$$

where the coefficients are constants calculated from the shape functions and the coordinates-ordinates of the elemental nodes [73]. Once the local coordinates-ordinates for the transformed aerodynamic grid point (ξ_m, η_m) are calculated then the transformed planar displacements (u, v) are obtained by isoparametric mapping

$$u = \sum_{i=1}^n N_i(\xi, \eta) u_i \quad 1 \leq i \leq 4 \quad (3.16)$$

$$v = \sum_{i=1}^n N_i(\xi, \eta) v_i \quad 1 \leq i \leq 4. \quad (3.17)$$

The aerodynamic loads can be distributed by using the (ξ, η) values. This form of transformation is accurate but suffers from a drawback that the aerodynamic points and the structural points must lie on the same surface.

3.3.4 Boundary Element Method

The transformation methods described earlier work on the fluid surface grid and structural grid. Chen and Jadic [74] proposed a BEM solver based on the full three dimensional equilibrium equations that would effectively transfer loads and displacement between the structural and fluid grids. In this approach the fluid surface grid is considered as an elastic homogeneous body with the fluid points as the nodes of the external boundary and the structural grid nodes are the internal points of the body as shown in Figure 3.5. A minimum strain energy requirement results in the universal spline matrix \mathbf{S} that relates the force and displacement vectors between the CFD and CSD grids as

$$\mathbf{u}_a = \mathbf{S}\mathbf{u}_s \quad (3.18)$$

$$\mathbf{f}_s = \mathbf{S}^T \mathbf{f}_a \quad (3.19)$$

where \mathbf{u}_a and \mathbf{f}_a are the fluid grid node displacements and loads, and \mathbf{u}_s and \mathbf{f}_s are the displacement and loads on the structural grid nodes. The universal spline matrix \mathbf{S} is obtained as follows. The usual BEM approach is to obtain an integral form of the equilibrium equation relating the internal displacement with the displacement and loads at the boundary Γ . The equilibrium equation in terms of displacements in tensor notations is written [75] in the form

$$[1/(1 - 2\nu)]u_{j,jl} + u_{l,jj} = 0 \quad (3.20)$$

where ν is the Poisson's ratio. The result of Equation 3.20 is known as the Somigliana's identity [75] and is written as

$$u_k^i + \int_{\Gamma} p_{lk}^* u_k d\Gamma = \int_{\Gamma} u_{lk}^* p_k d\Gamma \quad (3.21)$$

The superscript i refers to an internal point and superscript * refers to a Kelvin solution. The boundary of the body Γ is discretised into boundary elements and now Equation 3.21 can be written in the matrix form as

$$\mathbf{u}_s + \mathbf{H}_{bi}\mathbf{u}_a = \mathbf{G}_{bi}\mathbf{p} \quad (3.22)$$

where \mathbf{p} are the surface loads and the subscript bi refers to the boundary-interior influences. For the points on the boundary the relation between the displacement and the loads is given by

$$\mathbf{H}_{bb}\mathbf{u}_a = \mathbf{G}_{bb}\mathbf{p} \quad (3.23)$$

Here bb refers to the boundary-boundary influence. Substituting for \mathbf{p} from Equation 3.23 in Equation 3.22 we have

$$\mathbf{u}_s = \mathbf{B}\mathbf{u}_a \quad (3.24)$$

where

$$\mathbf{B} = \mathbf{G}_{bi}\mathbf{G}_{bb}^{-1}\mathbf{H}_{bb} - \mathbf{H}_{bb} \quad (3.25)$$

Equation 3.24 can be used only if the number of internal points (the structural grid) is equal to the boundary points (fluid grid), but in practice the structural grid is almost always coarser than the fluid grid. To obtain the universal spline matrix a minimisation of strain energy approach was used. The strain energy function ϵ can be obtained as

$$\epsilon = \mathbf{u}_a^T \mathbf{R}_a \mathbf{p} \quad (3.26)$$

where \mathbf{R}_a is the matrix containing the areas of the boundary elements. Substituting for \mathbf{p} in Equation 3.26 we have

$$\epsilon = \mathbf{u}_a^T \mathbf{A} \mathbf{u}_a \quad (3.27)$$

where

$$\mathbf{A} = \mathbf{R}_a \mathbf{G}_{bb}^{-1} \mathbf{H}_{bb} \quad (3.28)$$

A Lagrange multiplier technique is applied to minimise the strain energy. An objective function is defined as

$$\mathbf{F} = \mathbf{u}_a^T \mathbf{A} \mathbf{u}_a - \lambda^T (\mathbf{u}_s - \mathbf{u}_{s,given}) \quad (3.29)$$

where λ is the Lagrange multiplier and $\mathbf{u}_{s,given}$ are the given values of the displacements. By minimising the function in Equation 3.29 such that

$$\frac{\partial \mathbf{F}}{\partial \mathbf{u}_a} = 0 \quad (3.30)$$

with the constraints

$$\mathbf{u}_s = \mathbf{u}_{s,given} \quad (3.31)$$

we get an expression for the universal spline matrix \mathbf{S} as

$$\mathbf{u}_a = \mathbf{S} \mathbf{u}_s \quad (3.32)$$

3.4 The Constant Volume Tetrahedron

The description of the CVT scheme given here is based on the MSc thesis of Rampurawala [68]. The CVT scheme is a transformation technique proposed in Goura [49]. It is a 3D scheme using a combined interpolation-extrapolation approach for the transfer of the deformation variable. The structural grid is discretised into triangular elements and each fluid surface grid point ($\mathbf{x}_{a,l}$) is first associated with a triangular element Δ consisting of grid points ($\mathbf{x}_{s,i}$, $\mathbf{x}_{s,j}$ and $\mathbf{x}_{s,k}$). The position of $\mathbf{x}_{a,l}$ is given by the expression

$$\mathbf{c} = \alpha \mathbf{a} + \beta \mathbf{b} + \gamma \mathbf{d} \quad (3.33)$$

where $\mathbf{a} = \mathbf{x}_{s,j} - \mathbf{x}_{s,i}$, $\mathbf{b} = \mathbf{x}_{s,k} - \mathbf{x}_{s,i}$, $\mathbf{c} = \mathbf{x}_{a,l} - \mathbf{x}_{s,i}(t)$ and $\mathbf{d} = \mathbf{a} \times \mathbf{b}$. Here the term $\alpha \mathbf{a} + \beta \mathbf{b}$ represents the location of the projection of $\mathbf{x}_{a,l}$ onto Δ and $\gamma \mathbf{d}$ is the component out of the plane of Δ , as shown in Figure 3.6. In the above the values of α , β and γ are calculated as

$$\alpha = \frac{|\mathbf{b}|^2(\mathbf{a} \cdot \mathbf{c}) - (\mathbf{a} \cdot \mathbf{b})(\mathbf{b} \cdot \mathbf{c})}{|\mathbf{a}|^2|\mathbf{b}|^2 - (\mathbf{a} \cdot \mathbf{b})(\mathbf{a} \cdot \mathbf{b})} \quad (3.34)$$

$$\beta = \frac{|\mathbf{a}|^2(\mathbf{b} \cdot \mathbf{c}) - (\mathbf{a} \cdot \mathbf{b})(\mathbf{a} \cdot \mathbf{c})}{|\mathbf{a}|^2|\mathbf{b}|^2 - (\mathbf{a} \cdot \mathbf{b})(\mathbf{a} \cdot \mathbf{b})} \quad (3.35)$$

$$\gamma = \frac{(\mathbf{c} \cdot \mathbf{d})}{|\mathbf{d}|^2} \quad (3.36)$$

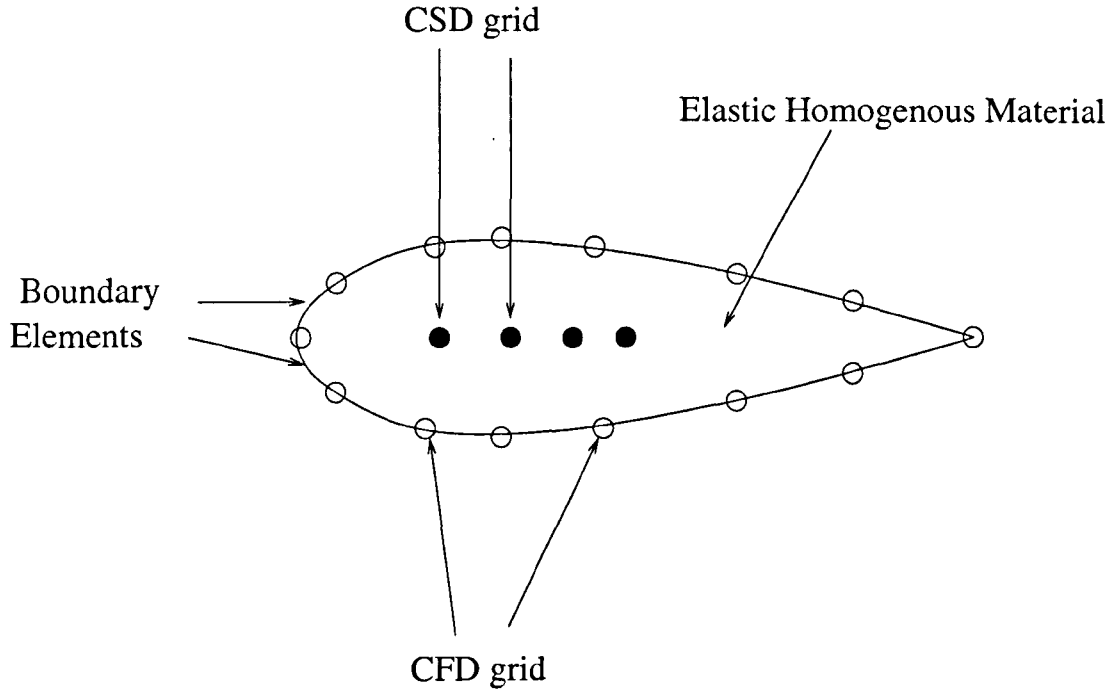


Figure 3.5: BEM treatment of an aerofoil

the volume of the tetrahedron is given by

$$V = \frac{\mathbf{a} \cdot (\mathbf{b} \times \mathbf{c})}{4} \quad (3.37)$$

Equation 3.33 gives a non-linear relationship between the fluid and structural locations which can be linearised in the structural displacements to give

$$\delta \mathbf{x}_{a,l} = \mathbf{A} \delta \mathbf{x}_{s,i} + \mathbf{B} \delta \mathbf{x}_{s,j} + \mathbf{C} \delta \mathbf{x}_{s,k} \quad (3.38)$$

$$\begin{aligned} \mathbf{A} &= \mathbf{I} - \mathbf{B} - \mathbf{C} \\ \mathbf{B} &= \alpha I - \gamma \mathcal{U} \mathcal{V}(\mathbf{b}) \\ \mathbf{C} &= \beta I + \gamma \mathcal{U} \mathcal{V}(\mathbf{a}) \\ \mathcal{U} &= I - \frac{2}{d^2} \mathcal{D}(\mathbf{d}) \mathcal{S}(\mathbf{d}) \end{aligned} \quad (3.39)$$

$$\mathcal{V}(\mathbf{z}) = \begin{pmatrix} 0 & -z_3 & z_2 \\ z_3 & 0 & -z_1 \\ -z_2 & z_1 & 0 \end{pmatrix} \quad (3.40)$$

$$\mathcal{D}(\mathbf{z}) = \begin{pmatrix} z_1 & 0 & 0 \\ 0 & z_2 & 0 \\ 0 & 0 & z_3 \end{pmatrix} \quad (3.41)$$

$$\mathcal{S}(\mathbf{z}) = \begin{pmatrix} z_1 & z_2 & z_3 \\ z_1 & z_2 & z_3 \\ z_1 & z_2 & z_3 \end{pmatrix} \quad (3.42)$$

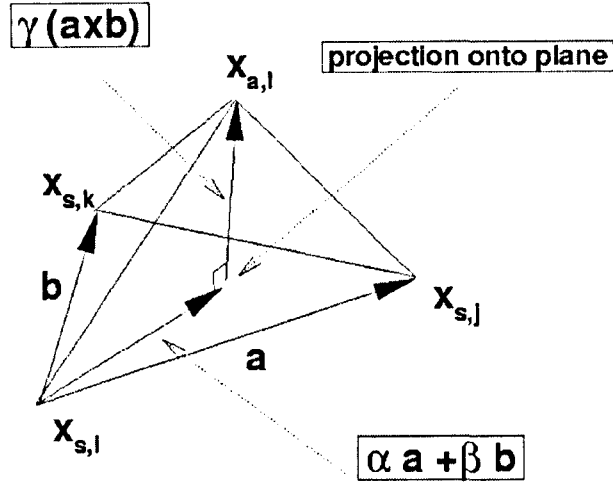


Figure 3.6: The Constant Volume Tetrahedron (from [67])

It was found in [49] that the linearisation error introduced can significantly effect the static and dynamic responses computed. Therefore, the matrices \mathbf{A} , \mathbf{B} and \mathbf{C} are updated every time the surface is moved so that the linearisation can be considered as being about the latest fluid and structural positions. The values of the transformed deflections have to be interpreted accordingly. This method is found to give geometrically identical results to using the full nonlinear method. The cost of computing the matrices is very small compared to the flow solution itself. There is a linear relationship for each application of the transformation, and the principle of virtual work is then used to give the force transformation. Denoting the linear relationship defined by Equation 3.38 as

$$\delta \mathbf{x}_a = S(\mathbf{x}_a, \mathbf{x}_s) \delta \mathbf{x}_s, \quad (3.43)$$

the condition of the conservation of forces for the transformation can be stated as

$$\delta \mathbf{f}_s^T \mathbf{x}_s = \delta \mathbf{f}_a^T \mathbf{x}_a = \delta \mathbf{f}_a^T S \mathbf{x}_a \quad (3.44)$$

hence the force transformation is given as

$$\delta \mathbf{f}_s = S^T \delta \mathbf{f}_a. \quad (3.45)$$

3.4.1 Selection of the Structural Elements

The structural models used for aeroelastic predictions can be in many cases extremely coarse [67]. The lack of structural elements means that the method used to associate fluid points with

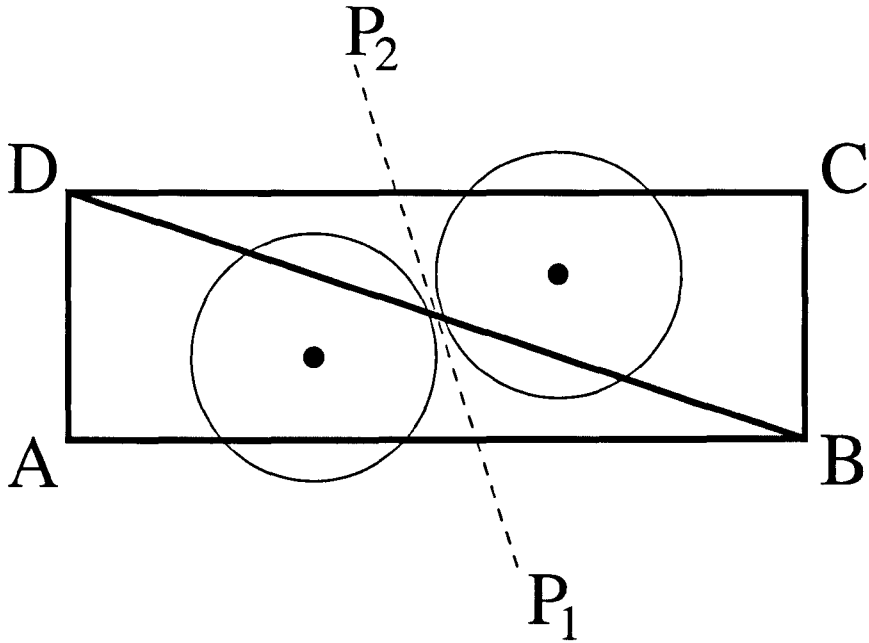


Figure 3.7: Search domains when using the triangle centroids to map fluid points onto triangles

a triangle Δ becomes critical. This mapping is done as a preprocessing step and is provided as input required for the time marching calculation. The method used for cases with reasonably fine structural grids was to select the triangle which minimises the distance between the projection of the fluid point and the centroid of the structural triangles. On very coarse structural grids the situation shown in Figure 3.7 arises. The line P_1P_2 shows the transition between Δ_{ABD} and Δ_{BCD} when nearest centroids are used. This method of association means extrapolation is used, for example near corner D of Δ_{ABD} when it is preferable to use linear interpolation within triangle Δ_{ABD} . To keep extrapolation to a minimum the following modification was made.

For each triangle in the structural model we calculate the area of the j th triangle ABC and the sum of the areas of triangles APB , BPC , and APC where P is the projected point $\mathbf{x}_{p,i}$, as shown in Figure 3.8. The difference in the sum of the three triangles containing the projected point and the original triangle is defined as

$$X_{\Delta_j} = |\Delta_{ABC} - \Delta_{APB} - \Delta_{BPC} - \Delta_{APC}| \quad (3.46)$$

The minimisation of X_{Δ_j} is used to associate Δ_i to point $\mathbf{x}_{f,i}$ and since X_{Δ_j} is zero if the projected point is inside the triangle this also minimises the number of displacements calculated using extrapolation. Figure 3.3 shows a coarse structural model of the Hawk aircraft used for predicting flutter in [67]. Figure 3.9 shows the difference between the two methods of association when used to transform one of the structural modes of the Hawk aircraft.

3.4.2 1D Constant Volume Tetrahedron

For structural components modelled as 1 dimensional beams (eg. the fuselage in many models) the CVT transformation does not work without some modification. In the original CVT, to form a tetrahedron 3 structural points forming a triangle are required. For an undeformed 1D

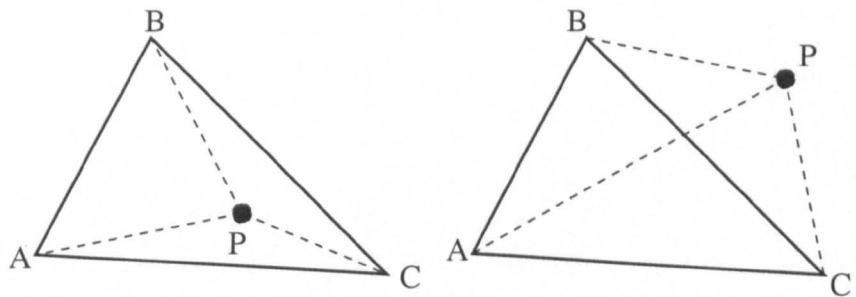


Figure 3.8: Search cases when placing projected points into triangles.

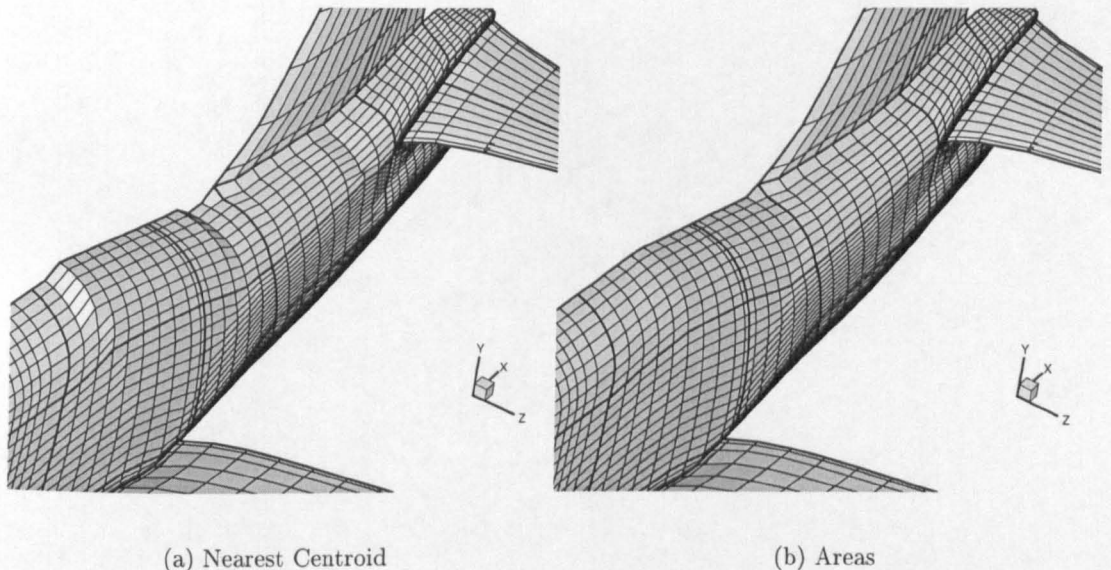


Figure 3.9: Difference in the transformed surface due to search method used. The surface gradient is smoother and conforms better to the original geometry when using the Areas method in Figure (b) than when using the Nearest Centroid method in Figure (a).

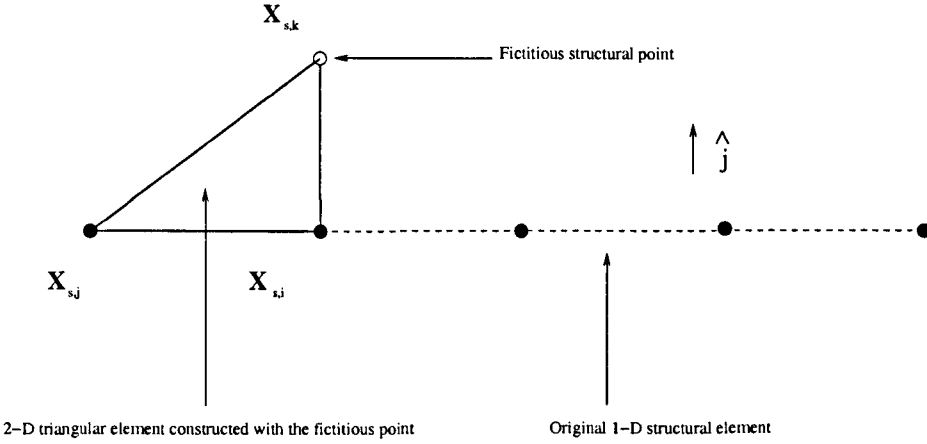


Figure 3.10: The 1D CVT fictitious point

beam element this is not possible as the structural points do not form a plane. One possible solution would be to create a structural triangle by adding in a fictitious point close to one of the structural nodes so that the two nodes of the beam element along with the fictitious point forms a triangular element. When the structure deforms the displacement of this fictitious point is calculated as equal to the displacement of the real structural point closest to it i.e. it undergoes only translation without adjusting the relative position to the bending of the fuselage. A fictitious third point for the structural grid was introduced for each 1D beam element. This point had the same x and z coordinates as one of the two points forming the 1D element. The y coordinate of the fictitious point has a unit more than that of the original point. Figure (3.10) shows the 1D structural element formed by the points $\mathbf{x}_{s,j}$, $\mathbf{x}_{s,i}$ and the fictitious structural point $\mathbf{x}_{s,k}$.

$$\mathbf{x}_{s,k} = \mathbf{x}_{s,i} + \hat{\mathbf{j}} \quad (3.47)$$

where $\hat{\mathbf{j}}$ is a unit vector in the direction of the y -axis. The triangular element formed is then used in the conventional CVT technique as described in section 3.4. This technique gives pure translation to the fluid points . No rotation is introduced, consistent with the motion of the points on the beam (refer Figure (3.11)). Consider the deformation of the node $\mathbf{x}_{s,i}$ which can be written as

$$\mathbf{x}_{s,i}^1 = \mathbf{x}_{s,i}^0 + \delta\mathbf{x}_{s,i} \quad (3.48)$$

where the superscript 1 and 0 represent the deformed and undeformed states of the structural nodes. The deformed fictitious node can then be calculated as

$$\mathbf{x}_{s,k}^1 = \mathbf{x}_{s,k}^0 + \delta\mathbf{x}_{s,i} \quad (3.49)$$

3.5 Full Aircraft Transformation

The preceding sections have dealt with the basic formulation of the CVT which can be used for simple stand alone geometries like the wing. A version of the CVT which can do the transformation for the complete aircraft with the minimum of manual intervention and which

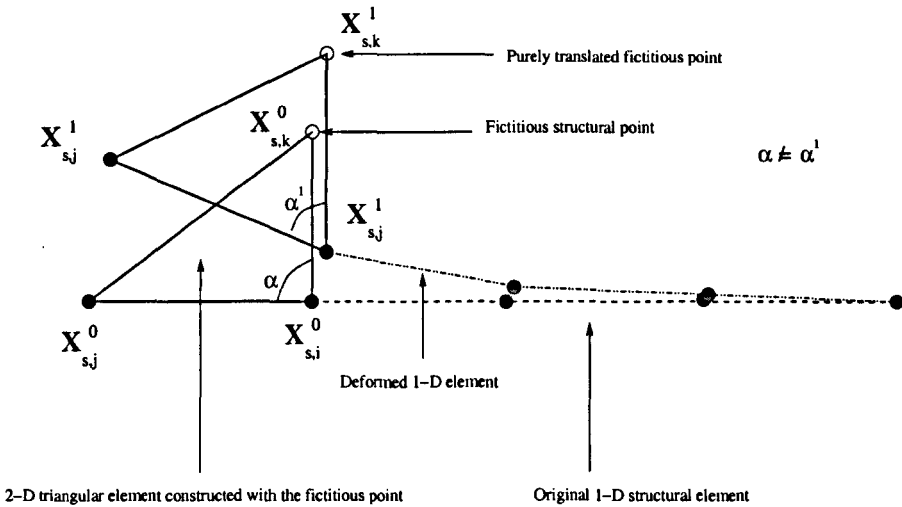


Figure 3.11: Translation of the 1D CVT element

preserves the surface mesh, particularly at junctions between components is described in the current section. The insight for the method is provided by the paper of Melville [76] which treats the aircraft components in a hierarchy.

The first stage of the method is to partition the fluid and structural points into levels associated with components. The primary component is the fuselage. The fluid and structural grid points on the fuselage are therefore designated as being of level 1. Next, the wings, horizontal stabiliser and the vertical fin are connected to the fuselage and the fluid and structural grid points on these components and the fuselage are designated level 2. The idea of the hierarchy is that level 2 points have a primary motion due to the fact that they are connected to the fuselage and a secondary motion due to their own elasticity. Extra components attached to the wing, such as pylons and control surfaces would be designated level 3, with their primary motion being due to the fact that they are attached to the wing.

At this stage a number of subsets of points have been defined for the fluid and structural grids, with one subset for each level. Denote the set of aerodynamic points in level m as \mathcal{A}^m and the structural points as \mathcal{S}^m . The lowest level contains all of the points in the respective grids and level $m - 1$ is a subset of level m .

The first stage for the CVT as described above is to associate each fluid point with three structural points. This is done in practice by defining a triangularisation of the structural grid and then associating the point with a triangle as described in section 3.4.1. This mapping can be done over the structural points in each level as well, defining mappings for each level. In the full aircraft case the level one mapping will have all points in the fluid grid driven only by points on the fuselage. The level 2 mapping will have the fuselage and the level 2 components like the wings, tail and the fin being driven by the respective structural components where as the level 3 components like pylons and control surface will be mapped by the level 2 components they are attached to. Level 3 mapping is equivalent to the original CVT method applied to all grid points without restriction. Consider a full aircraft case having the fuselage, the wings, the flap attached to the wings, the pylon attached to the wing, the fin, the rudder and the tail plane as components. Figure 3.12 shows the schematic of the 3 levels of transformation that lead to

a final transformation discussed later on. The transformation of a large generic aircraft with engine is demonstrated in Section 3.8. A problem with the mapping arises at junctions between components. For example at the wing/fuselage junction nodes that are not on the fuselage are being driven by a different transformation from those actually on the junction, which are driven by the fuselage. This leads to a small but disastrous distortion of the grid in the junction regions. Using the level one mapping treats all points in a consistent way and maintains the grid quality in the junction regions as a result. However, the level one mapping misses all effects introduced by the elasticity of the non-fuselage components, since these structural components are not used to drive the fluid surface grid. A new method is therefore needed to correctly transform the complete deformation while avoiding the problems at junctions. The basis for the method is the observation that the level one and two transformed mode shapes on level two components in regions close to the fuselage are almost identical. Similarly the level two and three transformed mode shapes on level three components in regions close to the level two components are also almost identical. This follows from the observation of Melville [76] that the fuselage drives the wing motions and this effect is dominant close to the wing root as opposed to any wing alone elastic effects. Similarly the wing/fin drives the pylon/control-surface motions and this effect is also dominant close to the junction. The method therefore blends the level one, two and three transformed fluid points, giving priority to the level one transformation as we approach the fuselage (in general the level m transformation is given priority as the level m component is approached). This means that in the junction region the fluid grid is transformed from the upper level structural model rather than individual components.

Denote the transformed deflection for a fluid point $\mathbf{x}_{a,l}$ using the m th level mapping as $\delta\mathbf{x}_{a,l}^m$. The blending used to give the final transformed displacement is given as

$$\delta\mathbf{x}_{a,l} = \sum_{m=1}^n w_{m,l} \delta\mathbf{x}_{a,l}^m. \quad (3.50)$$

The weights for the blending $w_{m,1}$ must add to one. To define the values of the weights for level m we need to consider the distance from the components associated with that level. Define the nearest distance of the point $\mathbf{x}_{a,l}$ to all of the points in level m by $d_{m,l}$. It is a simple matter to calculate $d_{m,l}$ by searching over the fluid points defined in level m for the nearest point. If $\mathbf{x}_{a,l}$ actually belongs to level m then $d_{m,l} = 0$. For a case with three levels (see Section 3.8) the weights for blending the two levels of transformation are computed from

$$w_{1,l} = e^{-10d_{1,l}} \quad (3.51)$$

$$w_{2,l} = 1 - w_{1,l} \quad (3.52)$$

For the third level component the weights for blending the three levels are computed as follows

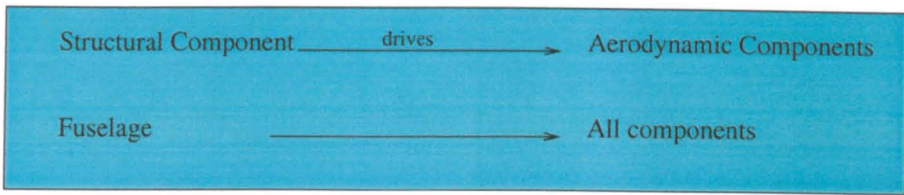
$$w_{1,l} = e^{-10d_{1,l}} \quad (3.53)$$

$$w_{2,l} = e^{-10d_{2,l}} \quad (3.54)$$

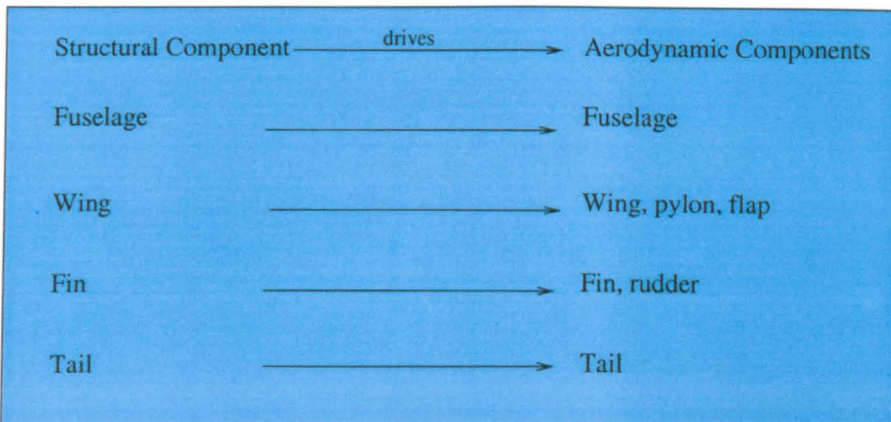
$$w_{3,l} = 1 - w_{1,l} - w_{2,l} \quad (3.55)$$

For points on the fuselage the entire weight will be put on the fuselage driven transformation, for points close to the fuselage most weight will be given to the fuselage driven transformation

Level 1 Mapping



Level 2 Mapping



Level 3 Mapping

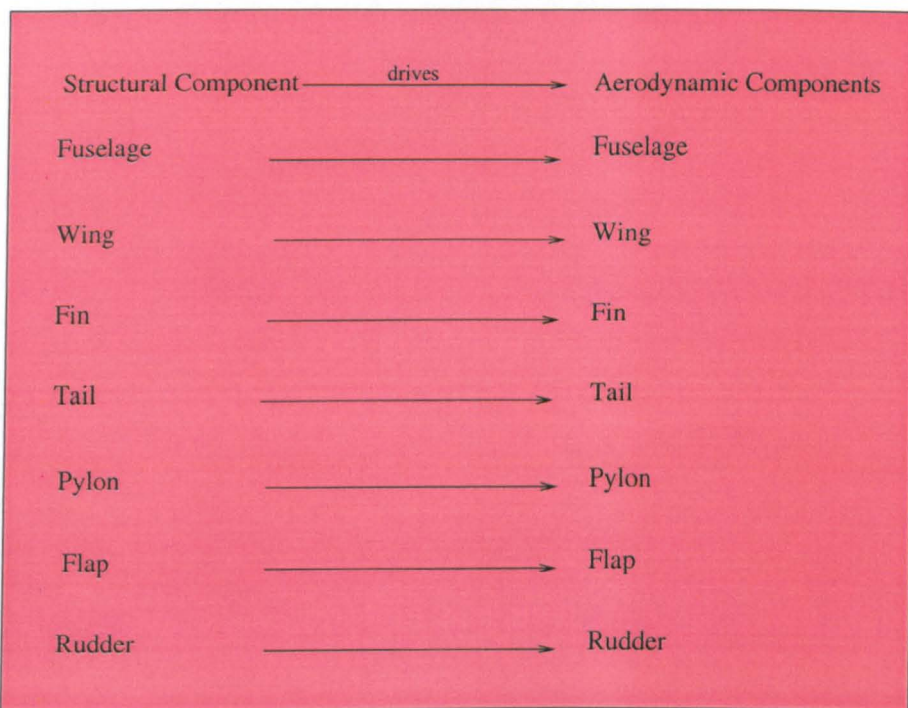


Figure 3.12: The 3 levels of mapping for a complete aircraft

and otherwise most weight is given to the level two component driven transformation. The exponential function e^{-10d} contains the blending parameter $-10d$ and is found to be suitable for most test cases but some experimentation with functions and parameters for other cases may be required. The effect of this parameter on aeroelastic stability is made evident in Chapter 3. Moreover this parameter is also used to get a smooth blending at control surface inboard and outboard edges.

The cost of computing the original CVT transformation is small and the cost of applying the new multi-level scheme is also small. On cost grounds there is an objection to using the exponential function in the weighting but the weights are calculated as part of a preprocessing step so this is insignificant.

3.6 Control Surface Transformation

The wing trailing edge control surfaces are usually modelled structurally as plates hinged at its leading edge. The inboard and outboard edges of the control surfaces are free and not blended into the wing. Computational simulations involving moving control surfaces are still not common mainly due to the difficulty in treating the grid over and around the control surfaces. The free edges of the flap cause a geometrical discontinuity along the wing span which is difficult to treat within the framework of a multiblock code. There are a number of ways a 3D flap can be modelled in a multiblock environment as listed in Figure 3.13 and are briefly described in the subsequent sections.

3.6.1 Transpiration

According to how the flap edges are modelled the flap treatment can be broadly classified into two categories, blended and flap with free edges. The blended edge treatments are more common due to simplicity and ease of implementation.

Of the blended treatments transpiration is one of the oldest methods and is easy to implement as it does not require deformation of the volume grid. This method is a means to manoeuvre the flow solver into seeing a deflection of the surface when in fact there is none [43]. The basic idea as described in [43, 77] is summarised here. If the variation in the surface normals is known, from a FEM solver for example, then this can be directly applied to the CFD grids through a modification of the existing surface normals. A change in the orientation of the surface is brought about by changing the velocity boundary conditions of the affected nodes. The change in boundary condition comes in form of additional fluid velocity outside of the existing surface elements. This additional velocity affects the way the unsteady flow solver resolves the flow tangency boundary conditions as shown in Figure 3.14. Here the $\mathbf{V}_{\text{Original}}$ is the original tangential velocity with normal $\hat{\mathbf{n}}$. In a moving control surface this surface normal changes to a new value $\hat{\mathbf{n}}_{\text{New}}$. In steady the flow tangency boundary condition is expressed as

$$\mathbf{V} \cdot \hat{\mathbf{n}} = 0 \quad (3.56)$$

this condition simply states that the velocity normal to the body must be zero. For the dynamic

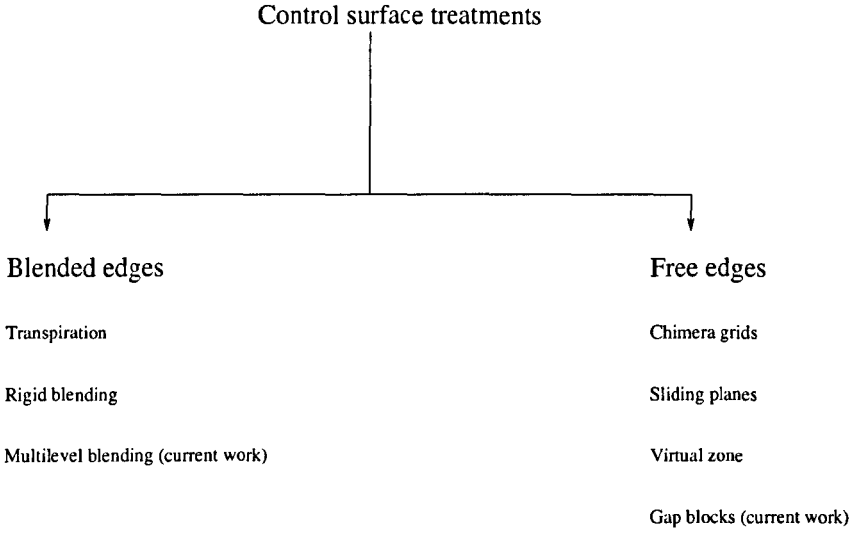


Figure 3.13: Different types of control surface treatment in CFD analysis.

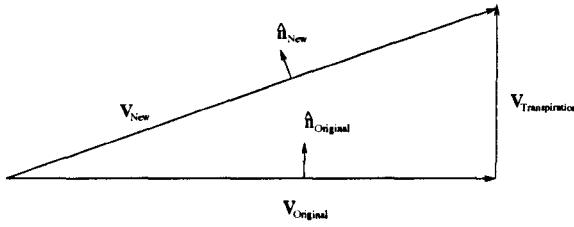


Figure 3.14: Application of the transpiration velocity

case the equation for flow tangency condition is expressed as

$$\mathbf{V} \cdot \hat{\mathbf{n}} = \mathbf{V}_b \cdot \hat{\mathbf{n}} \quad (3.57)$$

and means that the velocity normal to the surface just be equal to the velocity of body normal to itself. Hence it ensures that no flow can pass through the surface. It should be noted that \mathbf{V}_b is not equal to $\mathbf{V}_{\text{Transpirational}}$ in Figure 3.14.

3.6.2 Rigid blending

One of the simplest techniques is the blending of inboard and outboard edges of the flap with the wing surface. The blending does cause a deviation from the proper representation of the flap geometry but for most cases with small amplitude rotations of the flap this method is reasonably accurate. By rigid blending it is meant that there is no control on the length of the blended region. The blended region includes the cells of the flap edges which get deformed as the flap moves. Rigid flap blending has been used for both forced flap and aerodynamically driven flap simulations. .

3.6.3 Multilevel blending

Multilevel blending is a method developed for aeroelastic analysis of complex configurations and is described in Section 3.5. The method ensures grid smoothness at the component interfaces. This method is useful when the two components at the interface deform in different directions causing gaps. An oscillating flap attached to the wing at the hinge can be treated as a two component configuration and the multilevel blending can be used to blend the flap edges with the wing. The blending is easily implemented in the simulations while maintaining a reasonable grid quality, even for very large flap deflection angles (see Chapter 5). The blending of inboard and outboard flap edges is carried out using a three level hierarchical blending scheme described in Section 3.5. For the flap this means that the inboard and outboard edges are driven by the wing and the flap nodes adjacent to the edge nodes are driven by a combination of wing and flap deformations. The extent of the influence of the fin/fuselage on the flap depends on the blending parameter and hence the choice of the blending parameter controls the extent of blended length of the flap. Figure 3.18 is a schematic that illustrates the effect of blending on a two component system such as the flap and wing. The choice of the blending parameter depends on the extent of mismatch at the component interface. A very large mismatch will require a smaller absolute value of the blending parameter which means a large area of the lower hierarchy component will be influenced by the higher hierarchy component. A larger value will limit this influence to a smaller area of the lower hierarchy component. The effect of the blending parameter on the aeroelastic response on a rudder-fin system has been investigated in Chapter 6.

3.6.4 Chimera grids

Chimera or overset grids can be used effectively for the treatment of control surfaces in aeroelastic simulations. The flap definition is maintained and the gaps at the interface can be modelled accurately using overset methods. They involve generation of two sets of grids. As described in reference [44] the main grid or mother grid is constructed over the whole domain except around the region of the flap. The secondary or child grid is constructed in the region around the flap. The child grid is completely enveloped by the mother grid and there exists a region where the two grids overlap. During a dynamic aeroelastic simulation the physical properties from the child grid are interpolated to the mother grid through the overlapping region, the flow computations are performed in the whole of the mother grid and the calculated physical properties are interpolated to the interior of the child grid through the overlapping region and the cycle repeated.

3.6.5 Virtual zones

The virtual zone technique is an attractive method for treatment of control surfaces. The edge definition of the flap is maintained and the gap between the flap and wing is accurately modelled. Reference [41] describes the methodology of virtual zones for control surfaces. The virtual zones are zones of zero thickness which are introduced at the flap and wing edges to act as an interface for the interpolation of physical properties between the moving and stationary grids.

3.6.6 Gap blocks

Another option for modelling the flap is through the introduction of small gaps between the inboard/outboard flap edges and the wing. When the flap is deflected along its hinge the cells in these gap blocks are sheared. A flap modelled in this way maintains its geometric details but there is a penalty to be paid in computational time as the grid quality inside the sheared gap blocks is poor. Both the methods of flap treatment have been used in Chapters 4 and 5.

3.7 Assessment of Control Surface Treatments

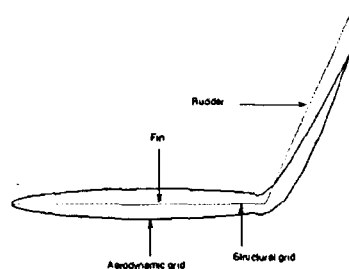
In the current work blending and the flap with free edges having gap blocks at the interface are used in the simulations. The effect of blending on the aeroelastic response has not been assessed in the literature. In the subsequent sections the issues related to blending of control surfaces are assessed with the aid of examples

3.7.1 Control Surface Transformation-Rudder

The blending of the rudder is easily implemented in the calculation while maintaining a reasonable grid quality, even for very large flap deflection angles. The blending of inboard and outboard flap edges is carried out using a three level hierarchical blending scheme which is an extension of the two level scheme previously described. For the rudder this means that the inboard and outboard edges are driven by the fin and the rudder nodes adjacent to the edge nodes are driven by a combination of wing and flap deformations. The extent of the influence of the fin/fuselage on the flap depends on the blending parameter,[51] hence the choice of the blending parameter controls the extent of blended length of the flap. Figure 3.16 shows the effect of the blending parameter on the shape of the flap.

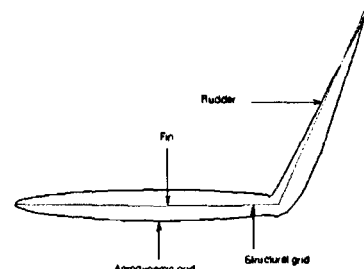
Figure 3.15 shows the slice taken through the fin-rudder deformed in the rudder deflection mode. The position of the slice taken is indicated out in Figure 3.17. The cross section of the fin-rudder fluid grid is driven by the structural grid that lives inside it. The rudder section of the fluid grid does not exactly follow the structural grid because of the influence of fin deformation over its own deformation brought about by the hierarchical blending. Figure 3.18 is a schematic that illustrates the effect of blending on a two component system such as the rudder and fin. The choice of the blending parameter depends on the extent of mismatch at the component interface. A very large mismatch will require a smaller absolute value of the blending parameter which means a large area of the lower hierarchy component will be influenced by the higher hierarchy component. A larger value will limit this influence to a smaller area of the lower hierarchy component. The effect of the blending parameter on the aeroelastic response on a rudder-fin system can be seen from Figure 3.19. A single rudder deflection mode is included in this analysis and the rudder is blended with the fin using blending parameters of -10d and -30d. As there is no possibility of coupling of modes the deflection should damp down to zero after a while, but as it can be seen from Figure 3.19 the simulation with the smaller value of blending results in the generalised velocity diverging away. It damps down to zero when a larger blending parameter is used. For the current work a blending parameter of -30d is used for all the calculations.

Transformation of the 1st mode using a blending parameter of -10d



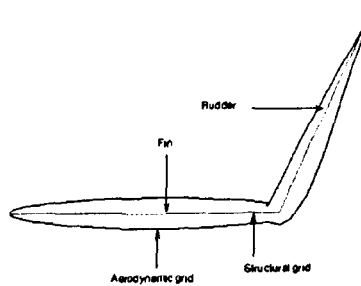
(a)

Transformation of the 1st mode using a blending parameter of -20d



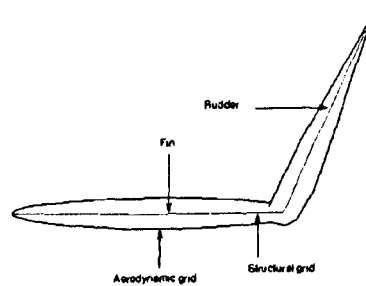
(b)

Transformation of the 1st mode using a blending parameter of -30d



(c)

Transformation of the 1st mode using a blending parameter of -40d



(d)

Figure 3.15: Dependence of the transformed mode shape on the value of blending parameter

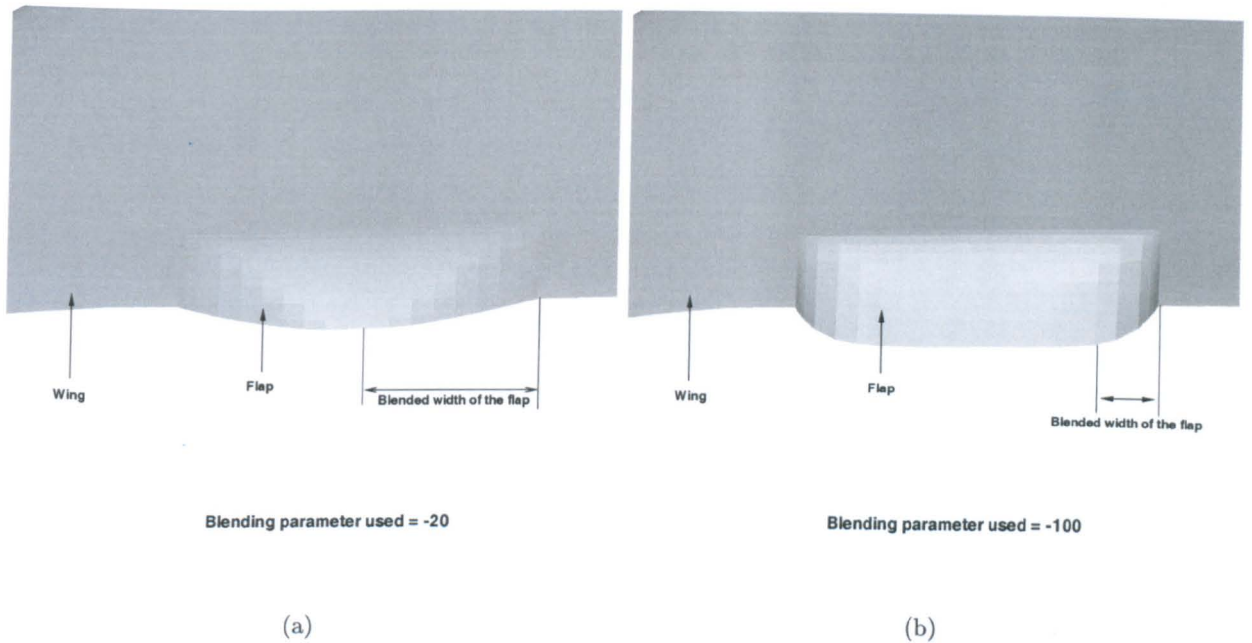


Figure 3.16: Transformed flap mode using two different values of blending parameter

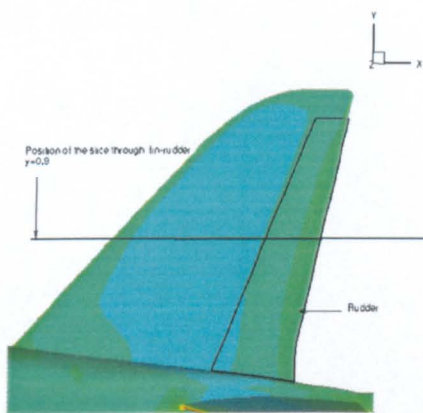


Figure 3.17: Position of the slice on the fin-rudder

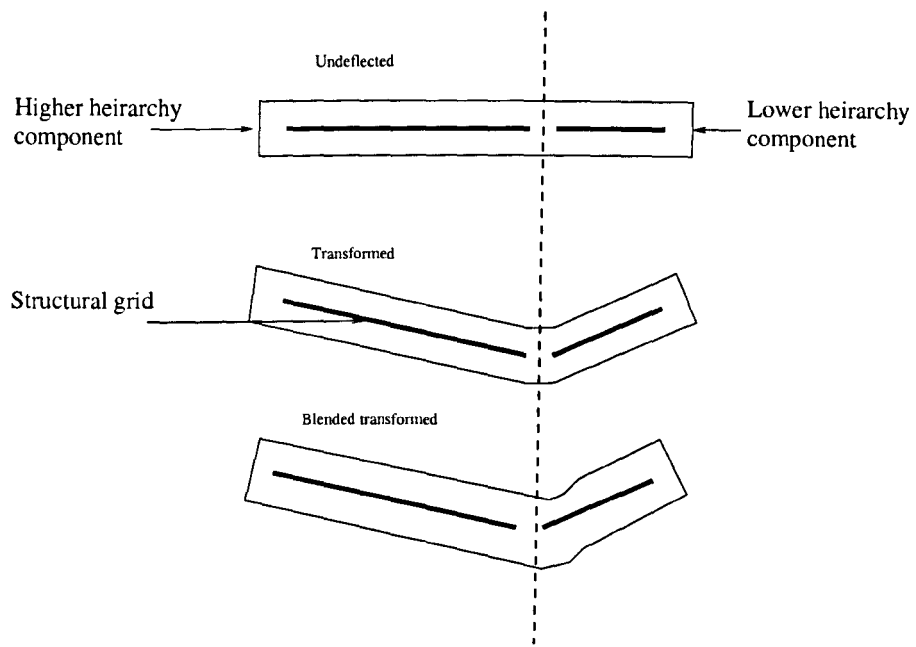


Figure 3.18: Effect of blending on a two component system

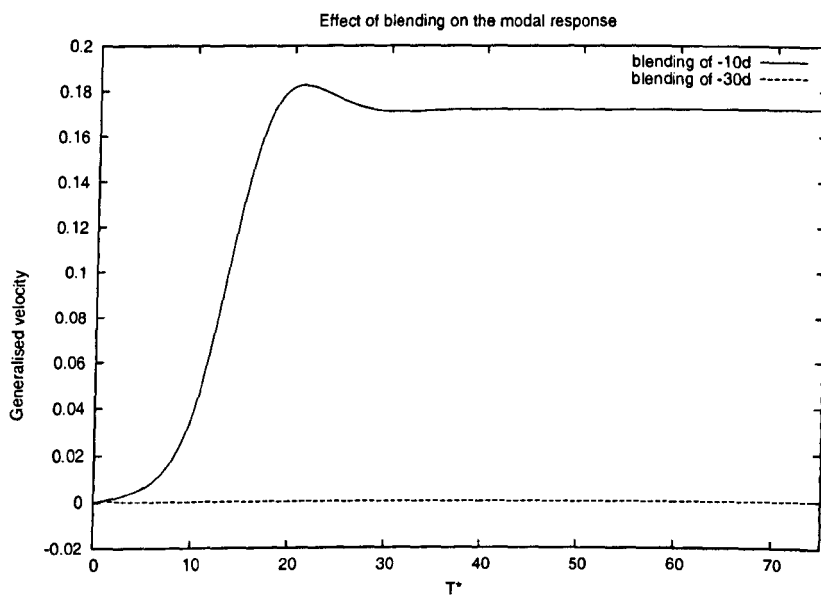


Figure 3.19: Difference in the modal response when using two different blending parameters at Mach 0.3.

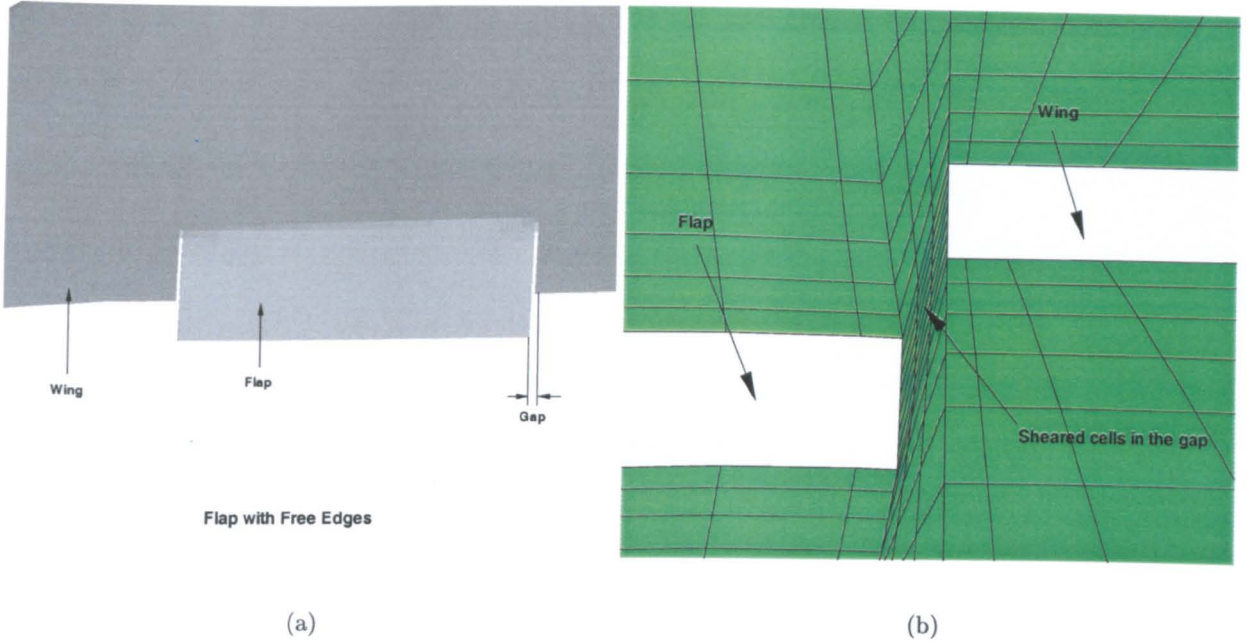


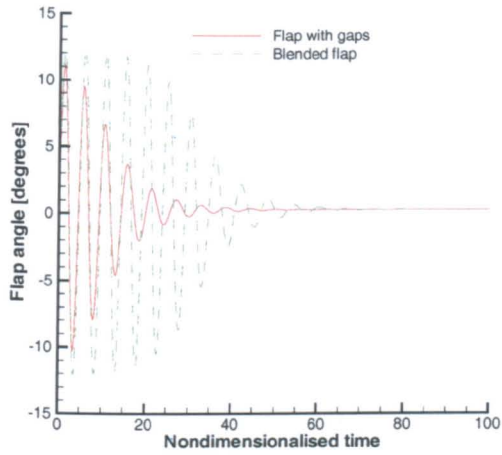
Figure 3.20: Transformed flap mode of a flap with free edges

3.7.2 Comparison of Flaps with Blended and Free Edges

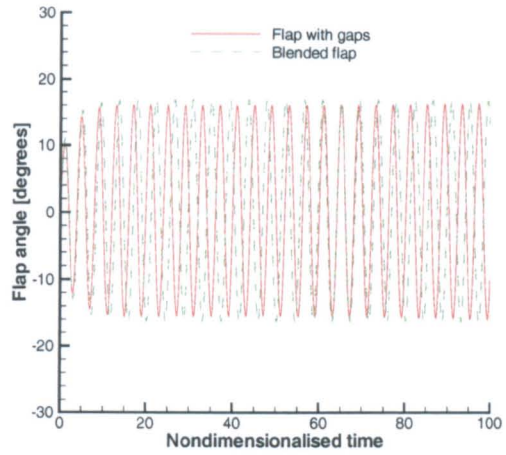
The blending of the flap edges with the wing using multilevel blending is very simple but the effect of the blending on the structural response needs to be assessed. It was shown in the preceding section that the choice of the blending parameter is important. However it will be seen from the test cases analysed in the subsequent chapters that if the correct blending parameter is used the difference between the aeroelastic responses from flaps with free edges and blended flaps is negligible. The flap with free edges in the current work is modelled by introducing gaps between the flap edges and wing. When the flap is deployed the grid in the gap shears as shown in Figure 3.20. Though this type of flap modelling is more accurate as the local flow features around the flap edges are resolved more time is required for the flow to converge in the sheared grid.

Figure 3.21 from Chapter 5 shows the flap response in a buzz simulation of flaps with free and blended edges. It can be seen that the response is very similar though the amplitude for the flap with blended edges is marginally greater than the flap with free edges on account of larger surface area. The flap with free edges has a slightly greater frequency.

Figures 3.22 and 3.23 from Chapter 4 show the real and imaginary components of the unsteady surface pressure distribution on the BACT test case. Here the flap is oscillated at a frequency of 5 Hz and an amplitude of 2.02° . Flap with blended and free edges are used and it is seen that unsteady pressure distribution is identical. It should be noted that the flap blending in the forced flap cases in the current work does not involve the multilevel mapping instead the blending is performed on the CAD geometry as explained in Chapter 4.

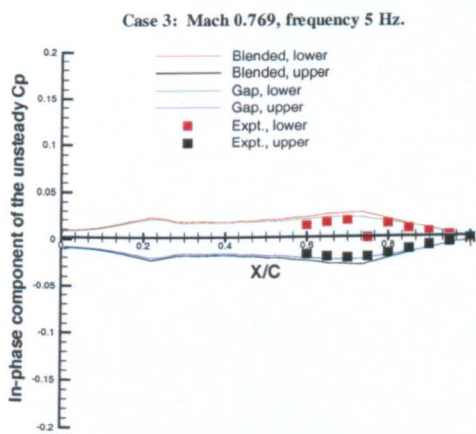


(a) Euler calculation, Mach 0.9, $k = 0.778$ and dynamic pressure = 26.468 kPa

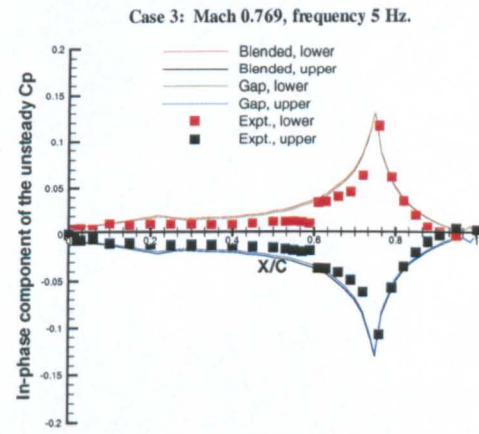


(b) Euler calculation, Mach 0.98, $k = 0.778$ and dynamic pressure = 26.468 kPa

Figure 3.21: Flap response of blended and free flaps at different Mach numbers with a blending parameter of 100



(a) In-phase component at 40% span



(b) In-phase component at 60% span

Figure 3.22: BACT Case 3 unsteady Cp values using blended flap and flap with gaps. $M = 0.769$, Re. No. 3.96 million, flap amplitude = 2.0° , FOF 5 Hz.

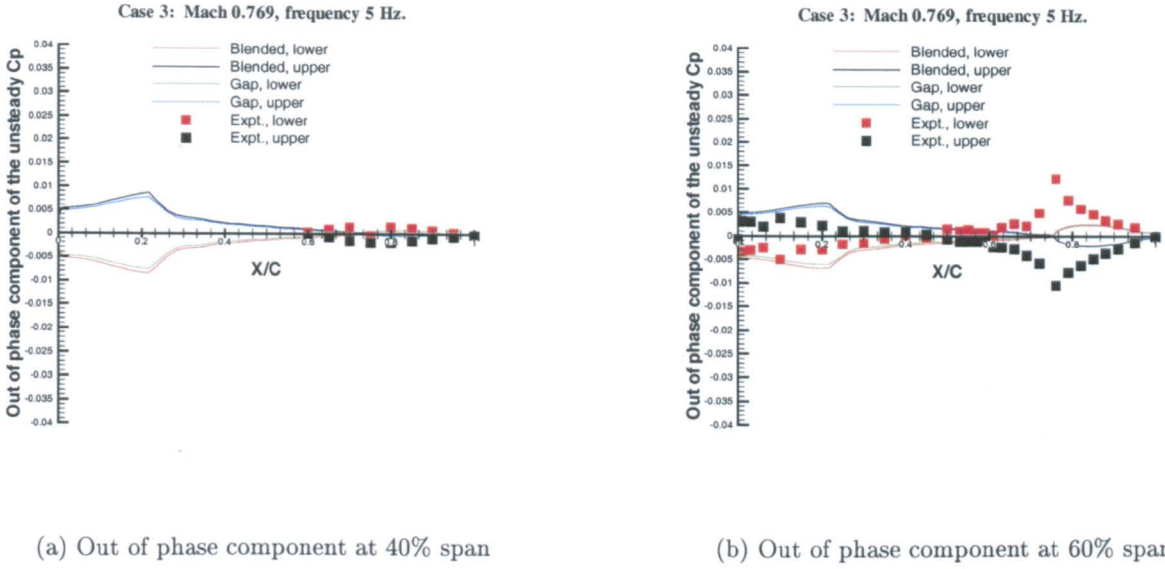


Figure 3.23: BACT Case 3 unsteady Cp values using blended flap and flap with gaps. $M = 0.769$, Re. No. 3.96 million, flap amplitude = 2.0° , FOF 5 Hz.

3.8 Multi-component Test Case

The mapping of the aerodynamic grid to the structural grid is one of the central steps in the aeroelastic calculations. In the current work the mapping is done as a preprocessing step before performing the coupled calculations. Figure 3.24 shows the various components that are assembled for a typical aeroelastic calculation. The mapping block in the figure involves the identification of the triangular element to which each surface aerodynamic point is anchored to, and the calculation of the distance of each point on the lower hierarchy fluid component from the nearest point on an upper hierarchy. This is written down in a mapping file which is used for the CVT and component blending scheme as described in Sections 3.4 and 3.5. Once the mapping file is obtained, the transformation needs to be visually inspected for each mode of the structure. This can be done by forcing the structure to statically deform in each mode without actually performing the fluid calculations. These calculations do not have any physical meaning except for mimicking the surface grid transformation of the individual mode shapes during the actual calculations.

The Generic Large Aircraft (GLA) test case has been adapted from the AIAA Drag Prediction Workshop. It is a relatively complex geometry for nonlinear aeroelastic calculations as there are 3 levels of hierarchy. The first level is the fuselage to which the wing is attached. Here the deformation of the wing root depends on the fuselage, hence it is classified into a second hierarchy component. The pylon is attached to the wing, and at the wing-pylon junction the deformation is due to the wing and hence the pylon is classified as the a third hierarchy component. The engine nacelle however is classified into a second level component since the deflection at the junction between the nacelle and the pylon is due to the nacelle and not the pylon. Moreover as the engine is at a distance from the fuselage the influence of the fuselage on the nacelle is negligible on account of the exponential blending parameter described in Section 3.5. Figure 3.25 shows the hierarchical classification of the structural components of the aircraft.

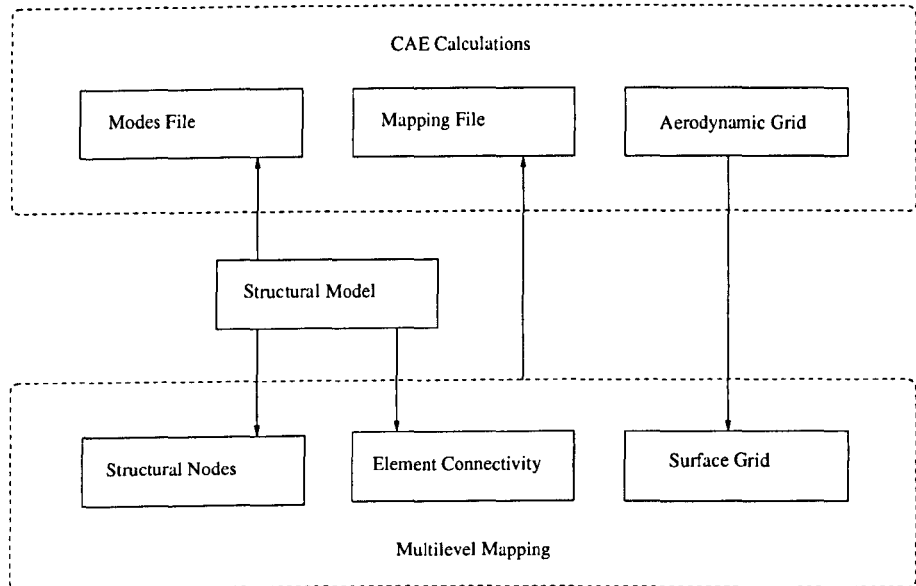


Figure 3.24: Components of an aeroelastic calculations

The process for structural classification has the following steps

- The structural nodes for each component are extracted from the FEM modelling tool.
- The extracted grid points are then triangulated using a Delaunay triangulation. The output from this is connectivity data in a file with each element consisting of the line numbers of the 3 nodes from the nodal file. A component label is given to each triangular element, in the current case, 1 for fuselage elements, 0 for wing, 2 for pylon and the 3 for the nacelle.
- The nodal files and the corresponding labelled element connectivity files are assembled into a single node file and a single connectivity file.

Like the elements of the structural components the nodes lying on the surface of the aerodynamic grid of the various components are also labelled. However the labelling is done during the grid generation step itself. The nodes on the fuselage of the aerodynamic grid are labelled as 50001, on the wing 50000, on the pylon 50002 and on the nacelle 50003. An aerodynamic surface grid file contains the nodal coordinates along with the labels. The linking of the elements of the structural components to the nodes of the corresponding components on the aerodynamic grid is done in a small file. This file classifies the components into their respective hierarchies. For the current case the linking is as follows

```

4
1 50001 1
0 50000 2
2 50002 3
3 50003 2

```

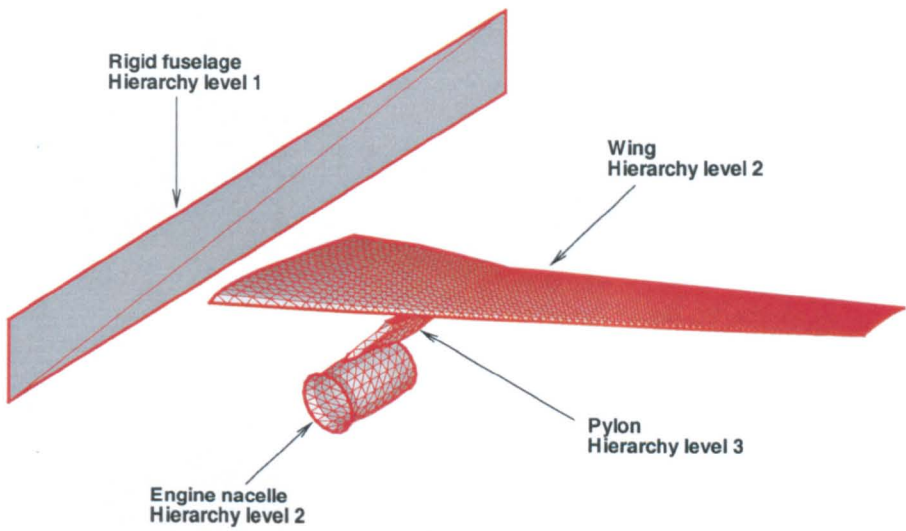
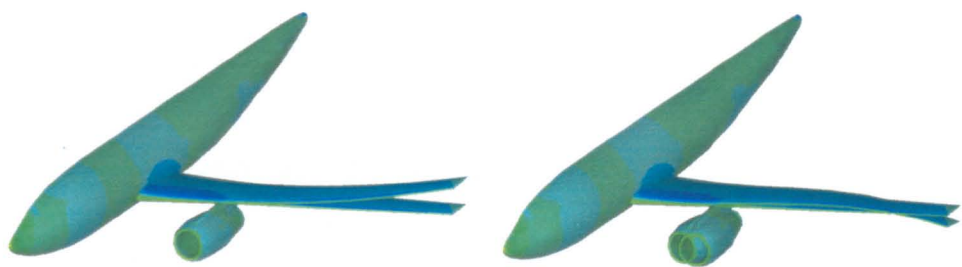
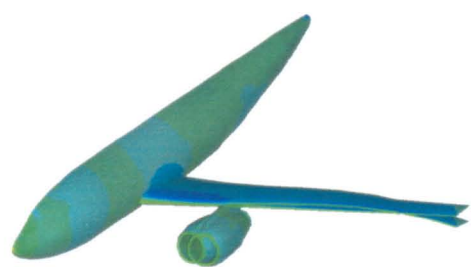


Figure 3.25: Division of components into hierarchical levels

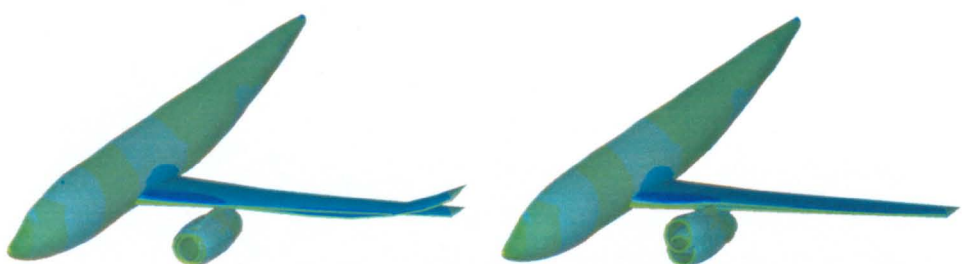
The first line indicates the number of components the geometry contains. The first column specifies the structural component label, the second column specifies the corresponding aerodynamic component it is linked to and finally the third column specifies the hierarchy level of the component. The linking file along with the labelled structural elements file and the labelled aerodynamic surface grid is used for the mapping. For each aerodynamic surface grid point the mapping utility searches for the nearest structural element of the fuselage in the level 1 mapping. In the second level it searches for the nearest fuselage element for the aerodynamic grid points on the fuselage and for the rest of the components it searches for the nearest second hierarchy component structural elements. Finally in the third level the utility searches for the nearest structural element of each component from the aerodynamic point on that corresponding component. This information is written down in the mapping file to be used by the transformation scheme during the coupled calculations. However before the mapping file is used the mapping is inspected by forcing the aerodynamic surface grid to deform in each structural mode to be used in the calculation. The transformed mode shaped of the first 6 modes of the GLA are shown in Figure 3.26. From visual inspection in the plotting tool TECPLLOT these were found to be smooth and maintained the grid quality at component interfaces.



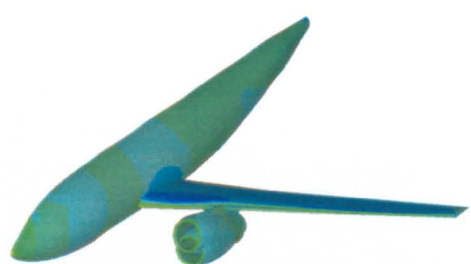
(a) Mode 1 0.56 Hz



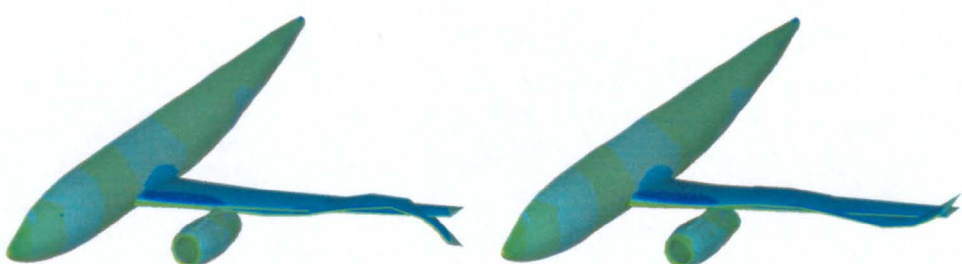
(b) Mode 2 1.65 Hz



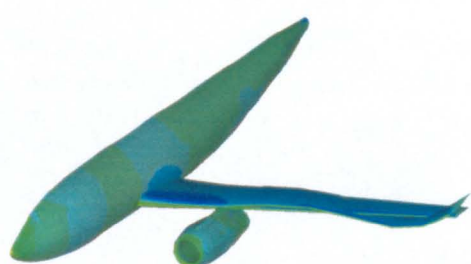
(c) Mode 3 1.93 Hz



(d) Mode 4 2.69 Hz



(e) Mode 5 3.63 Hz



(f) Mode 6 4.23 Hz

Figure 3.26: Transformed mode shapes of the GLA.

Chapter 4

Validation for Forced Flap Motions

4.1 Introduction

On flexible wings a control surface can induce twisting of the wing, which in extreme cases can lead to a control surface reversal. This phenomenon occurs when the deformation of the wing due to control surface deflection is large enough to have the opposite aerodynamic response to that intended, limiting the maximum operational amplitude of control surfaces. It is important that control surfaces are free of any structural or aerodynamic instabilities. Prediction of structural deformation due to control surface deflection is important to prevent the aircraft encountering such phenomenon. Another instability encountered is at transonic Mach numbers when the shock oscillates over the trailing edge control surface. This can lead to shock induced instabilities of the control surface and is an issue for supersonic transport aircraft with thin trailing edge flaps. The lack of space at the trailing edge in these configurations prevent adequate constraints to be applied to the control surface. The study of shock oscillation over the control surface is important in these cases.

One of the first computational forced flap oscillation studies was performed by Bharadvaj on the F5 and HARW wing configurations [39]. His computational analysis used the transonic full potential equations to calculate the unsteady loads due to the forced flap oscillations. The control surface deflections were brought about by an equivalent body velocity approach that changes the boundary conditions to model the effect of a moving control surface. The viscous effects were modelled through an interactive inverse boundary layer and the transpiration velocity approach. In both the wings were assumed to be rigid and hence the aeroelastic deformations were not calculated. Forced flap oscillations were performed over the F5 wing and a clipped delta wing by Obayashi and Guruswamy using the RANS code ENSAERO [40]. The control surface deflections were modelled by shearing the grid at the control surface-wing interface for both the cases. The wings were treated as rigid.

Obayashi *et al.* analysed a full span rigid arrow wing with symmetric and anti-symmetric oscillating control surfaces[78]. Reynolds-averaged thin layer Navier-Stokes equations were used in this study and the interaction of the primary vortex, the wake vortex and the flap oscillations at moderate angles of attack was demonstrated. The results were validated against wind tunnel experiments. Klopfer and Obayashi developed and implemented a virtual zone technique for the treatment of oscillating control surfaces. The technique uses intermediate virtual zones to act as an interface between the control surface and wing edges. This was applied to a clipped

delta wing and the computed results were validated against experiments[41] Unsteady pressure distribution due to an oscillating trailing edge control surface was calculated over a 55° delta wing by Karlsson[79]. Results for the transonic case were calculated using a linear aerodynamics based method, a transonic full potential method and an Euler equation based code EURANUS and were compared with the experimental results. Once again the model considered was rigid. Tamayama et al. [80] performed a 2D forced flap oscillation calculations on the NAL-SST wing profile. The main object of the study was to investigate the shock motion at higher transonic flows due to flap oscillations. A 2D RANS code with a thin layer assumption for the boundary layer was used. The wing profile of the 2D case was same as the one used in the current work. A 3D forced flap oscillation computational study in transonic flow was performed by Utaka and Nakamichi [44] on the NAL-SST configuration. The wing was modelled as elastic and unsteady pressure was compared against the experiments. The dynamic deformation was however not validated. A chimera grid approach was used to model the control surface and the Euler equations were used to model the flow.

The BACT wing has a rich database for the validation of aeroelastic and aeroservoelastic computations. Computations for unsteady pressure prediction have been performed on the BACT case by Schuster for the case with oscillating trailing edge control surface [42]. This case is also studied in the current chapter for the purpose of validating the CFD code. The BACT wing is rigid and hence the pressure unsteadiness brought about by the flap oscillations alone. As the structural deformations are absent there is no flow unsteadiness due wing bending. This simplifies the problem in the sense that errors due to aero-structural coupling are absent and hence makes it a good case for validating the forced flap oscillation methodology.

A transpiration boundary condition was applied to treat the oscillating flap by Cole et al. to simulate a Benchmark Active Control Technology (BACT) case [43] and the unsteady pressure distribution compared with the experiments. Flutter suppression and alleviation by Active Control Technology (ACT) [81, 77] and prediction of control surface reversal due to wing flexibility [82] has been the motivation for many of computational aeroservoelasticity simulations.

As all aircraft wings are flexible up to some extent, a more representative case is of an oscillating control surface on a flexible structure. The unsteady pressure distribution over the wing due to control surface oscillations results in dynamic structural deflections. Moreover the Flap Oscillating Frequency ω_F may resonate with the natural frequency of vibration of the structure causing large deformations. Such a simulation is performed in the current study on a flexible supersonic configuration along with a forced flap oscillation simulations on the BACT wing case.

The Japan Aerospace Exploration Agency (JAXA)¹, as part of the Japanese SST program, is developing an experimental Supersonic Transport model and a wind tunnel model of this was tested in the transonic regime for unsteady pressure and dynamic deformation [33, 83]. The purpose of the experiment was to accumulate verification data for the validation of aeroelastic codes and active control technology. The experimental data from this work is used here.

In this chapter we try to computationally predict the dynamic deformation and pressure distribution that are brought about by the forced oscillation of the control surface in transonic flows. Development of this ability is a step towards computational analysis of control surface

¹formerly National Aerospace Laboratory

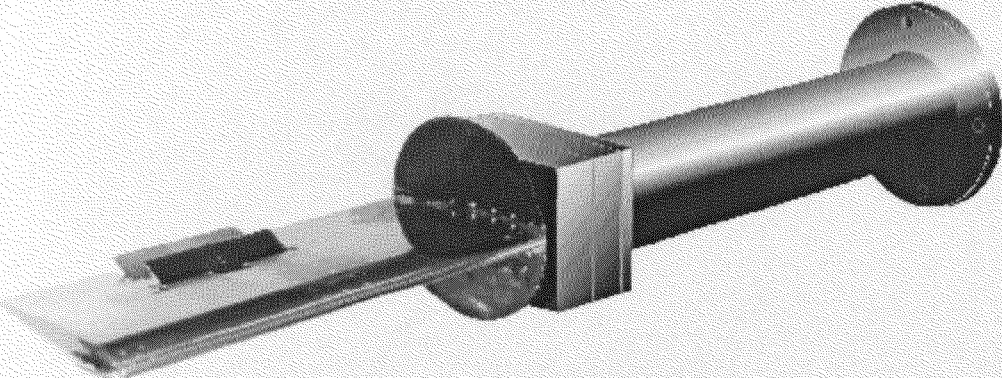


Figure 4.1: The BACT wind tunnel model with its upper spoiler and trailing edge control surface deflected.

instabilities on aircraft. Apart from validation of the aeroelastic methodology an important outcome of this study is the assessment of the effect of a blended control surfaces on the aerodynamics of the wing. This is an issue which needs to be addressed as there is not much information available in the literature regarding the effect of control surface treatment on the aero-structural response.

4.2 The Experimental Models

4.2.1 The BACT Wing

The Benchmark Active Control Technology wing model was developed at NASA Langley as part of the Benchmark Model Program. It is a simple generic rectangular wing with a NACA 0012 wing profile. It has upper and lower surface spoilers and a trailing edge control surface which can be oscillated for use in flutter suppression and dynamic response excitation. There have been a large number of experiments performed on this model over the years including the identification of the flutter boundary when the model is mounted on a Pitch and Plunge Apparatus (PAPA), steady and unsteady control surface effectiveness studies and measurement of dynamic response of a flexible system due to control surface excitation. The experiments on forced trailing edge control surface oscillations used in the current work were performed by Bennett *et al.* [84] using a wide range of parameters including Mach numbers, flap oscillation frequencies (ω_F), angles of incidence, flap deflection angles and spoiler deflection angles. Figure 4.1 shows the BACT apparatus on a rigid mount with the upper spoiler and control surface deflected. The BACT wing is considerably stiff and hardly exhibits any structural deformation due to the forced motion of the flap. Figure 4.2 shows the locations of the pressure sensors at 40% and 60% span. The sensor array at 60% span runs across the flap.

A total of 3 experimental cases have been selected for the validation study. Details of the experiments are given in Table 4.1. Case 1 and Case 2 are static whereas Case 3 involves forced flap oscillations.

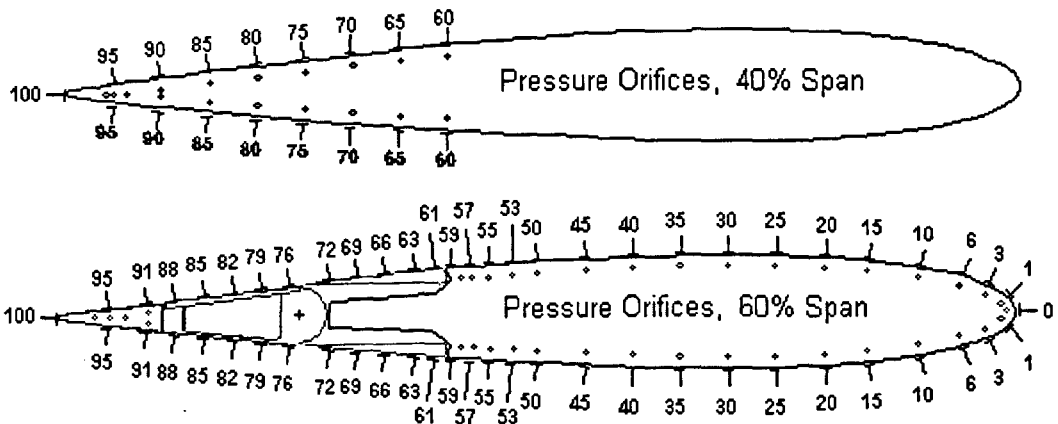


Figure 4.2: Locations of the pressure sensors at 40% and 60% span of the BACT wing.

	Incidence	Mean flap angle	Mach number	ω_F (Hz)	Flap amplitude
Case 1	-4.02°	0°	0.769	0	0°
Case 2	0.03°	5.0°	0.769	0	0°
Case 3	0°	0°	0.766	5	2.02°

Table 4.1: Experimental details of the BACT cases selected for current computations.

	Incidence	Mean flap angle	Mach number	ω_F (Hz)	Flap amplitude
Case1	0.0°	0.0°	0.8002	10	1.203°
				15	1.312°
				20	1.116°
				25	1.004°
Case2	-2.0°	0.0°	0.8009	10	1.567°
				15	1.448°
				20	1.229°
				25	1.091°
Case3	-4.0°	5.0°	0.9007	5	1.844°
				10	1.756°
				20	1.284°

Table 4.2: Conditions of the SST cases selected for computations.

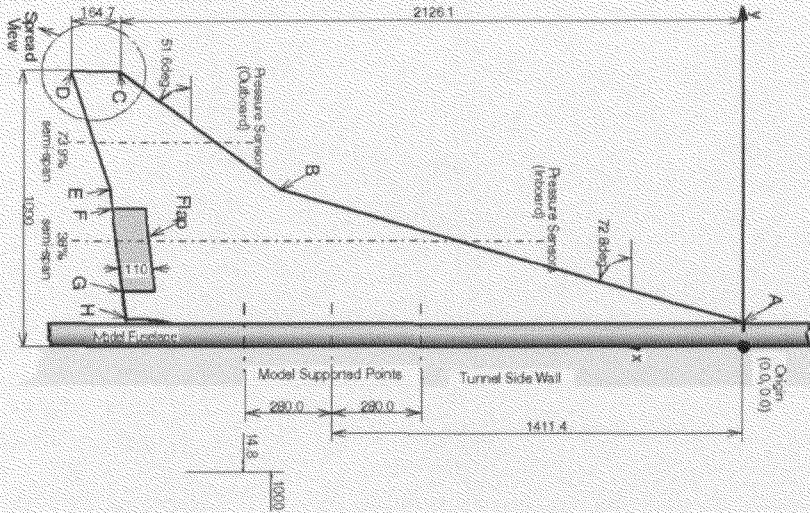


Figure 4.3: Dimensions of the SST wind tunnel model.

4.2.2 The NAL SST Arrow Wing

Computational validation of the second test case is based on the transonic aeroelastic experiments performed at NAL [33]. One of the motivations for the experiments was to generate a set of results against which aeroelastic codes could be validated. For this reason, along with the unsteady pressure distribution over the wing, the dynamic deformation and unsteady force coefficients were also measured.

The SST arrow wing is a cranked double delta with a root chord of 2.103 metres. A half model is used in the experiments with a semi-span of 1 metre. The section profile is a NACA 0003. The inboard delta has sweep angle of 72.8° and the outboard a sweep of 51.6° . The trailing edge flap starts at 20% half-span and terminates at 50% half-span. The flap chord is 0.11 metres. Figure 4.3 shows the dimensions of the experimental model in millimetres. Experimental data is available for a range of Mach numbers between 0.79 and 0.91, angles of attack of 0° , -2° and -4° , flap mean angles of 0° , -5° and 5° and Flap Oscillating Frequencies(ω_F) of 5 Hz, 10 Hz, 15 Hz, 20 Hz, 25 Hz and 30 Hz.

FEM data in the form of a structural grid and computed natural modes of vibration are provided in the paper [33]. A brief description of the structure of the experimental model is presented in an earlier paper by Tamayama [83]. The wing structure is made up of a 7 mm thick aluminium plate with holes drilled out to make it flexible. It was found in the experiments that the frequency of the first wing bending mode increased from 9.79 Hz in vacuum to around 15 Hz at Mach 0.8 [83]. As the frequency of this mode lies in the vicinity of the forced ω_F (5 Hz-30 Hz), and as the frequency of the next natural mode is higher (40.25 Hz) almost all the deformation of the structure is due to the first wing bending mode. It was observed in the experiments that this mode stiffened in the flow and coupled with the ω_F of 15 Hz. This means that the maximum wing dynamic deformations occur at a ω_F of 15 Hz.

It was found in the current study that the FEM model provided in the paper presenting the experimental results [33] did not resonate with the ω_F of 15 Hz. To examine this an aeroelastic simulation was performed with the given FEM model and the flow conditions described in the experiment [83]. A small impulse was given to the wing and the frequency of the oscillation was

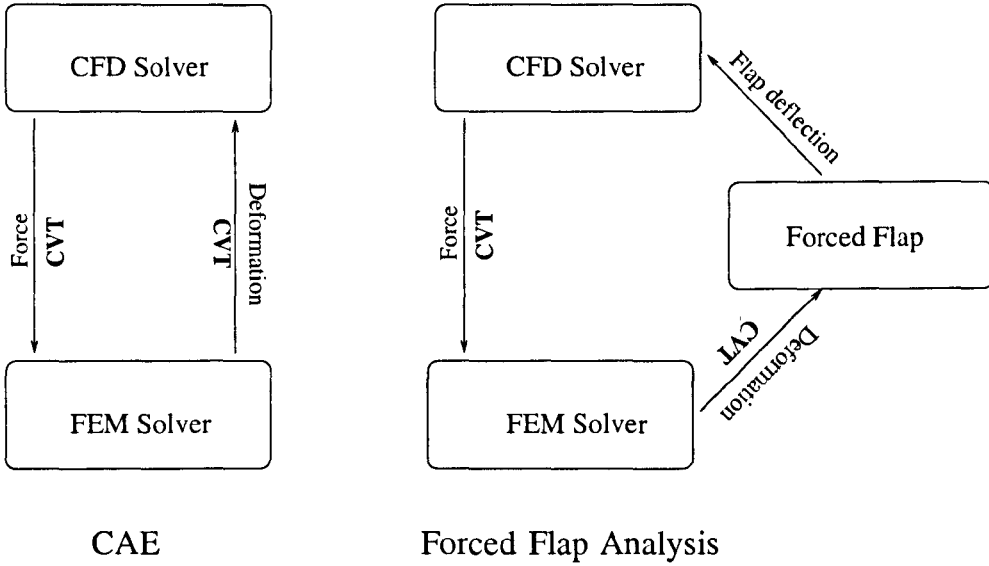


Figure 4.4: A typical CAE loop showing the coupling of structural and fluid solver. An intermediate step that models the forced motion of the flap is added in the current study.

measured. At Mach 0.8 and a dynamic pressure of 23.35 kPa the frequency of the first wing bending mode increased from 11.09 Hz (in vacuum) to 12 Hz lower than the 15 Hz quoted in the experiments. A stiffer model was constructed with the frequency of the first bending mode greater than the one obtained from the GVT. The new stiffer model resonates with a ω_F of 15 Hz as in the experiments.

Table 4.3 shows the generalised mass and frequencies of the first 3 modes of the original FEM model the new stiffened model and the frequencies obtained from the GVT. Figure 4.8 shows the structural grid and the first three modes of the stiffened model transformed onto the surface grid. The wing deformations are primarily in the y direction and the y-coordinate contours are plotted in the figure. The first three natural modes are included in the aeroelastic calculations.

4.3 Aeroelastic Modelling

The CFD code PMB solves the Euler and Navier-Stokes equations on the fluid grid and calculates the aerodynamic force on the geometry surface. The predicted aerodynamic force is then transferred to the structural grid using the Constant Volume Tetrahedron (CVT) transformation scheme. The modal FEM solver incorporated in PMB calculates the structural response and transfers the deformation information to the fluid grid using the CVT. An intermediate step to the above loop for the forced flap calculations is the inclusion of forced motion of the flap geometry. Every real timestep the flap geometry is moved by a certain angle and consequently there is a redistribution of pressure over the wing. The FEM solver is coupled to the fluid solver in pseudo time hence the structural response takes into account the pressure redistribution due to the forced motion while calculating the deformation before moving onto the next real timestep. Figure 4.4 shows a typical CAE loop and a forced flap loop that includes wing flexibility. If the wing is assumed to be rigid then the FEM solver is omitted from the loop to get a purely sinusoidal oscillation of the flap. When including the wing flexibility it is important

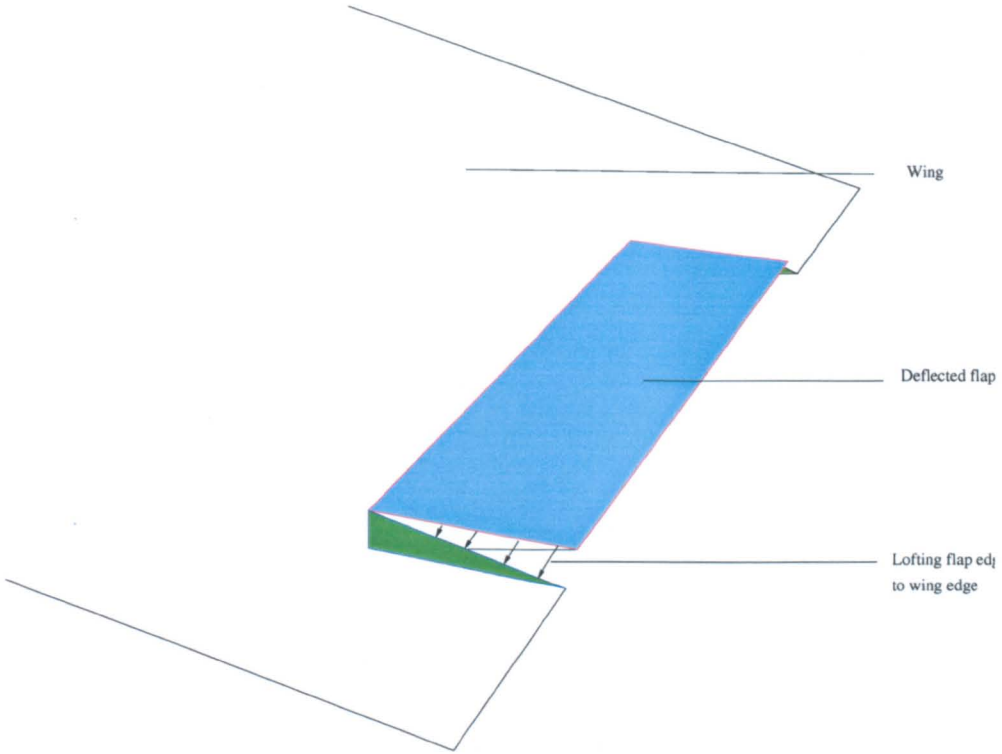


Figure 4.5: Blending of the flap edge with the wing.

that the reduced frequency of the forced flap motion is calculated in a consistent manner with the structural reduced frequencies.

4.3.1 Flap Grid Treatment

In the current work blended flaps and flaps with free edges are used for simulations. The flap blending is performed on the CAD model by simply lofting the flap edge curves with the wing trailing edge curves to create a blended surface as shown in the schematic in Figure 4.5. The flap with free edges is constructed by introducing small gaps between the flap edge and the wing in the CAD model. A single block is then used to grid space in inside this gap. Figure 4.7 shows the close-up of the two types of flap edge modelling. The flaps in the figure are deflected by an angle of 1.4° and the surface pressure contours are plotted along with the surface mesh. The gaps at the flap edges are 0.5% of the flap width and they decrease the effective surface area of the flap by 1%. For the forced flap oscillation cases three sets of geometries are constructed. The first is the one with 0° flap deflection. The second and third have the flap deflected at $\pm 5^\circ$. Surface grids are generated on these three geometries. A flap mode shape is obtained by subtracting the coordinates of the surface grids of the geometry with flap deflected at -5° from the geometry with flap deflected at 5° . In unsteady CFD calculations the forced flap oscillation is brought about through the sinusoidal variation of the scaled flap mode shape with time. The flap mode shape contributes to the wing shape in a similar way to the structural mode shapes except that the modal coordinate is applied rather than computed from the structural model. The surface grid deformations $\delta \mathbf{x}_f$ are therefore obtained from the equation

$$\delta \mathbf{x}_s = A \sin \omega t \phi_f \quad (4.1)$$

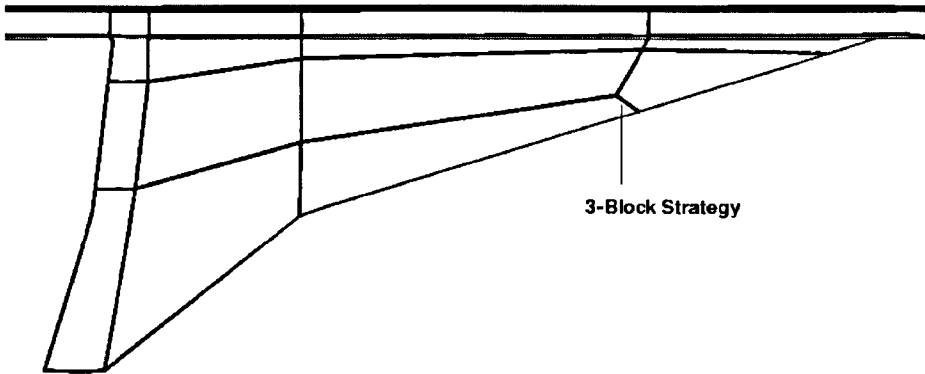


Figure 4.6: The 3-block strategy to avoid collapsed cells at the leading edge of wing root.

where A is the amplitude of the flap oscillation, ϕ_f is the flap mode shape and ω is the frequency of the applied motion. The surface deflections due to structural modes are transformed from the structural grid and the new wing surface grid is calculated by summing the applied and structural contributions. The volume grid is recalculated by using transfinite interpolation of displacements of the surface grid deflections. The deformation of the surface grid requires a recalculation of the volume grid. This is performed with a Transfinite Interpolation (TFI) scheme that deforms the grid inside the blocks containing the deforming surface grid. This flap oscillation scheme independent of the aeroelastic module. Hence it is possible to calculate the aerodynamic quantities over the body surface with an oscillating flap assuming the body to be rigid.

4.3.2 CFD Grids

The BACT Wing

To model the effect of gaps at the flap edges two different grids have been used in this study. The first is a RANS grid with blended flap edges. The wall spacing is $1 \times 10^{-6}c$ and has 800 thousand cells. The second grid is a RANS grid with free flap edges. A small gap of the width 2 % of the flap span is introduced between the flap edge and the wing. This gap has a wedged shaped grid block in the flow domain. The rest of the topology and wall spacings are as for the blended edge. The blocking topology of the grids has a C-type blocking over the wing leading edge and a H-type blocking at the trailing edge. The wing tip which is a rotated aerofoil half profile and block face over the tip is collapsed into an edge.

NAL SST Arrow Wing

To model the effect of gaps and viscosity a total of 4 different grids has been used in this work. The RANS grid has 15 cells to resolve the boundary layer. The wall spacing is $1.8 \times 10^{-6} c$. The RANS calculations are performed only with blended flaps as there are problems with grid quality when gaps are introduced at flap edges. A C-Type grid topology is used over the wing

leading edge, the wing tip and also around the fuselage. The blocks at the trailing edge are of H-Type. The wing geometry is basically a slender delta wing on the inboard side and a collapsed triangular block is avoided at the leading edge tip by using a 3-block strategy as shown in Figure 4.6. Points are clustered around the trailing edge and the flap region where a shock is likely to develop and move. There are 14 cells in the chord-wise direction and 28 in the span-wise direction on the flap. The size of the RANS grid is 800 thousand cells. The blended flap Euler grids have the same topology as the RANS grid. The fine Euler grid has 1.6 million cells. There are 24 cells in the chord-wise direction and 50 span-wise. The wall spacing is 1×10^{-3} c. A coarse grid is obtained from the fine grid by removing every alternate grid point in all the three directions. The coarse Euler grid has 200 thousand cells. The grid used for flaps with gaps is the same as the coarse Euler grid for blended flaps but with two extra blocks in the gaps between the flap edges and the wing.

4.4 BACT Results

The steady cases 1 and 2 show a good comparison with the experiments as seen in Figures 4.9 and 4.10. Figure 4.9 shows results using blended gap treatments. The modelling of the gap has practically no effect on the local pressure distribution at 40% and 60% even when the wing is at an angle of -4.02° and a Mach number of 0.769, which is mildly transonic for this wing profile. Figure 4.10 shows the comparison between computed and experimental results for Case 2 using blended flaps alone, and a good agreement is obtained. Figure 4.11 shows the mean computed and experimental pressure coefficients for the unsteady Case 3 at 40% and 60% span. A good mean comparison is an important indicator of the correctness of unsteady input parameters like flap oscillation amplitude and reduced frequency. The blended flap and flap with gap treatment results show that the differences between the two are minor for this case.

Figures 4.12 and 4.13 show the in-phase and out of phase components of the unsteady pressure coefficient. These are the real and imaginary components obtained by performing a Fourier analysis on the pressure time history. In the current analysis the flap is oscillated for 4 cycles and a Fourier analysis is performed on the last cycle when a periodic state is reached. 200 time intervals per cycle of flap oscillation are used. The transient vanishes during the first cycle itself and the aerodynamic response in time is a smooth sinusoidal curve. The majority of the response is in phase with the flap oscillations and a small percentage is out of phase as can be seen from Figures 4.12 and 4.13. The computed Cps compare well with the experiments for both blended and flap with gap treatments.

4.5 SST Results

It is observed for the rigid BACT case that the transient dies after the first cycle with a ω_F of 5 Hz. This was not found to be the case when flexibility is included in the study of the SST wing. The duration of the transient can be between 6 to 40 cycles of the flap oscillation. Figure 4.14 shows the modal response of the first wing bending mode against non-dimensionalised time for Case 1. At the ω_F of 15 Hz there is coupling of the first structural mode and the flap oscillations, resulting in large deformation of the structure. The transient response is generally longer for

higher ω_F .

It is observed that the structural response is sensitive to the size of the timestep at the ω_F where the coupling with the structural modes takes place (which is 15 Hz for the current case). Figure 4.15 shows the generalised coordinate of the first mode plotted against non-dimensionalised time at Mach 0.8 and the ω_F of 15 Hz and 25 Hz respectively with two different timesteps. The timestep refinement from 0.15 to 0.06 makes no difference at the ω_F of 25 Hz. However the amplitude of oscillation considerably increases at the ω_F of 15 Hz when the timestep is decreased from 0.14 to 0.08 and is then insensitive when the timestep is further reduced to 0.04.

The unsteady pressure and deformation were obtained by taking a FFT of these values during the last cycle of the flap after a periodic state is reached. The unsteady pressure was recorded on the upper surface at 38% and 74% wing span locations as shown in Figure 4.16. At 38% span the flap hinge is located at 90.5% of local chord and distinct peaks on the unsteady pressure can be seen aft of this point at all ω_F . The dynamic deformation is obtained along a line originating at the wing root which is at 8% semi-span including the fuselage, and 80.7% of the root chord. The line makes an angle of 113° with the x-axis.

Figure 4.17 shows the magnitude of the unsteady pressure, and deformation in metres, on a coarse grid using the Euler equations. Blended flap edges are used in this simulation. The computed unsteady pressure and deformation compare well with measurements at the resonant ω_F of 15 Hz. The position and magnitude of the pressure peaks over the flap at 38% semi-span are well predicted for all ω_F . There is a considerable increase in the pressure unsteadiness at 74% semi-span which decreases from leading edge to trailing edge at the resonant frequency. This indicates the wing undergoing a twisting motion at the tip. The dynamic deformation magnitude peaks at the resonant ω_F frequency of 15 Hz. The phase angle of the unsteady pressure is compared for the resonant ω_F and the computed result has a lag almost 40° less than the experiments. It is found that although the timestep refinement has a large effect on the amplitude of the oscillations at the resonant frequency, it does not have much effect on the phase of the unsteady pressure or dynamic deformations.

The computational results for Case 1 obtained by using the original structural model are compared with the experiments in Figure 4.21. The wing tip undergoes the maximum dynamic deformation for all cases and ω_F . The deformation at the tip is plotted against the ω_F using the two FE models and compared with the experiments. It can be seen that the original model resonates with the ω_F of 10 Hz instead of 15 Hz and the dynamic deformation peaks at this value. It predicts the deformation accurately at ω_F of 10 Hz but under-predicts the deformation for all the other ω_F . The stiffened model has a much better comparison with the experiments and follows the experimental trend. The original model is also unable to predict well the unsteady pressure at 74% span location.

Computed results using the Euler equations for Case 2 are presented in Figure 4.18. A coarse grid was used for the calculations and blended flap edges are used. The unsteady pressure and deformation trends are similar to those observed in Case 1 and the computed results once again match the pressure unsteadiness well at all ω_F and both semi-span locations. In contrast to Case 1 the magnitude of the unsteadiness is higher. The computed dynamic deformation shows an increase of almost 20% with deformation at the tip increasing from 1 cm for Case 1 to 1.2

cm for Case 2 at the resonant frequency. As for Case 1 the computed pressure phase angle at the two span locations is under-predicted by 40° , though the experimental trend of the phase along the chord is reproduced well in the computations.

The angle of incidence is further decreased in Case 3 to -4° and the Mach number increased to 0.9007. The flap oscillates around a mean flap angle of 5° . At these parameters a strong shock develops just aft of the flap hinge on the upper surface of the wing. Figure 4.20 shows the inviscid steady surface pressure coefficient contours over the wing and pressure plot at the 38% semi-span location on a fine grid. The Euler equations usually predict the shock location downstream of the real location. For the Case 3 the flap oscillates around a mean deflection angle of 5° , which means that the shock for the flow modelled by the Euler equations predicts the shock oscillation over the flap, which may not happen in the real flow. This shock oscillation over the flap is the reason for the peak in the unsteady pressure magnitude at 38% semi-span location seen in Figure 4.19.

Figure 4.22 shows the pressure contours on plane through the cross section of the blended flap and the flap with free edge treatment. The cross sectional plane is at 58 % from the flap hinge as shown in the figure. The flow conditions are for Case 2 where the wing is at an angle of -2° . There were no noticeable differences observed in the pressure contours for the two type of flap treatments. To further assess the effect of the blended edges on the computed unsteady pressure and deformation an inviscid simulation is performed using flaps with free edges. Figure 4.23 compares the unsteady pressure and deformation for Case 2 at the ω_F of 15 Hz obtained from blended flap and flap with free edges. There is little difference seen in the computed results though the blended flap predicts a slightly bigger dynamic deformation on account of it having a larger flap surface area.

The NAL-SST arrow wing has a thin section profile and for this reason the flow remains attached for most cases and for all ω_F . Viscous effects are not observed in the simulations at low angles of incidence and the computed unsteady pressure and deformation using RANS are similar to the Euler results . Figure 4.24 shows the computed results from the viscous simulation for Case 1. At 38% semi-span the pressure peak over the oscillating flap is under-predicted though the location of the peak matches the experiment. The unsteady pressure at 74% semi-span and the dynamic deformation is similar to the inviscid calculations. At flow conditions where the shock does not reach the control surface it is found that the inviscid results are similar to RANS. For cases where the shock does reach the control surface, as in Case 3, viscous calculations are required to predict the shock location accurately. The shock induced separation over the oscillating control surface causes pressure redistribution and could have an effect on the structural response. Case 3 remains to be simulated using the RANS equations.

4.6 Conclusion

Unsteady viscous and inviscid forced flap oscillation simulations were performed on the flexible NAL-SST arrow wing and the rigid BACT wing using a range of ω_F . A good comparison is obtained of the steady and unsteady surface pressures with the experiments for the BACT case. The pressure unsteadiness is in-phase with the flap oscillations as the Fourier processed out-of-phase component is very small compared to the in-phase component. The predicted

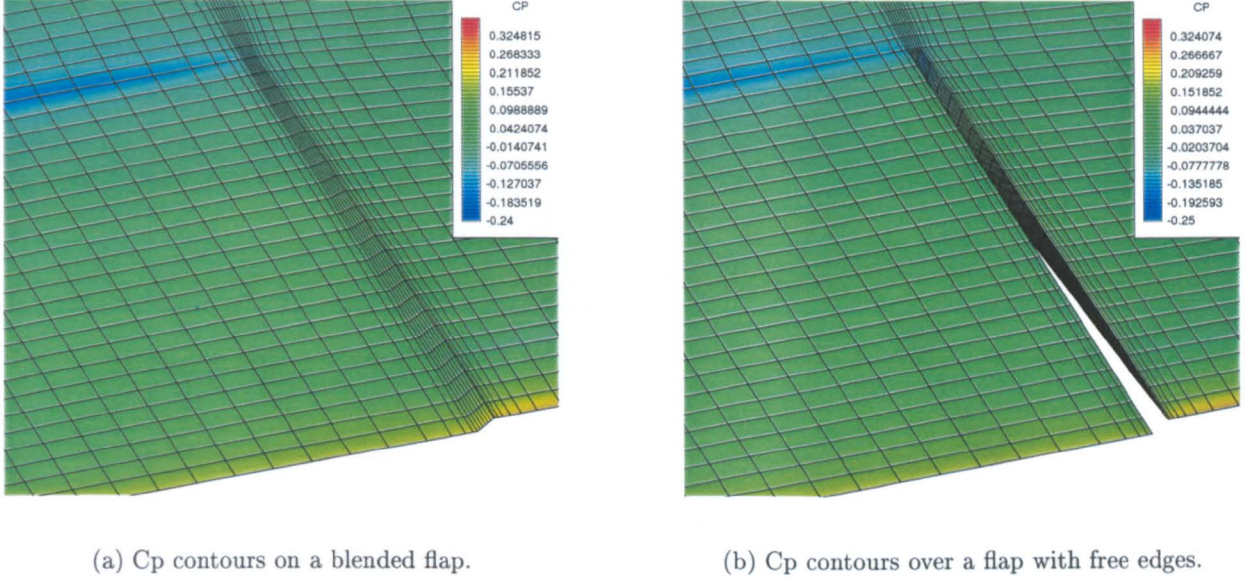
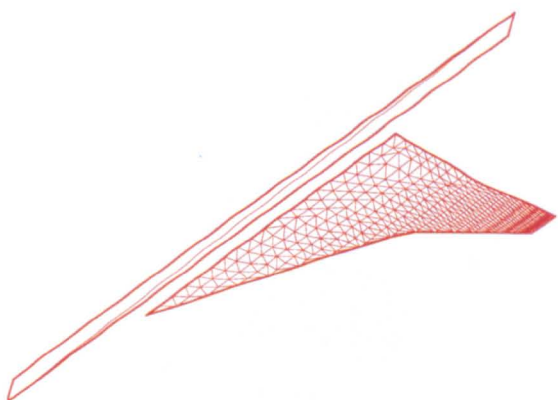


Figure 4.7: The two types of modelling of the flap edges on the BACT and SST wings.

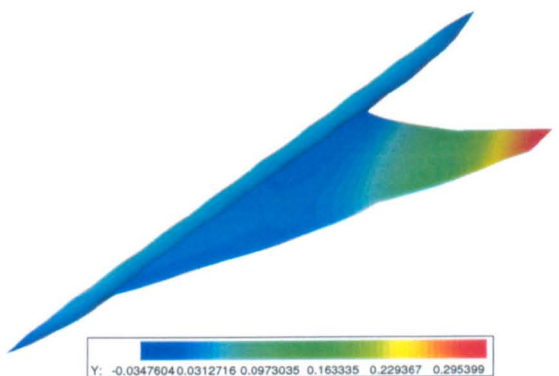
Mode	Natural Frequencies (Hz)		
	GVT	FEM - Original	FEM - Stiffened
Mode 1 - First wing bending	9.79	11.09	12.44
-	-	41.65	-
Mode 2 - First wing twisting	40.25	44.00	51.65
Mode 3 - Second wing bending	47.91	56.26	58.32

Table 4.3: Natural frequencies of the experimental and FEM models of the SST configuration.

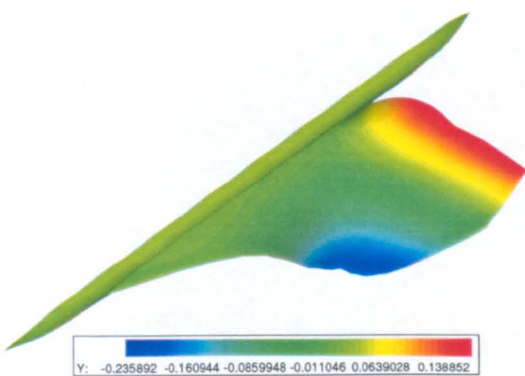
dynamic deformation of the SST compares well with the experiments at the resonant frequency and a reasonable comparison for unsteady pressure distribution was obtained for all frequencies. Viscous effects were found to be negligible and inviscid predictions were as accurate as viscous for the case with 0° incidence. It is concluded that Euler equations can accurately predict the unsteady pressure for transonic Mach numbers where the shock remains well ahead of the control surface hinge. The effect of blended flap edges on the prediction of pressure distribution and deformation of wing was found to be insignificant when compared with flaps with free edges. The FEM structural model was stiffened to allow the resonance to take place at ω_F of 15 Hz. Future work could include a detailed FEM model that takes into account the structural nonlinearities.



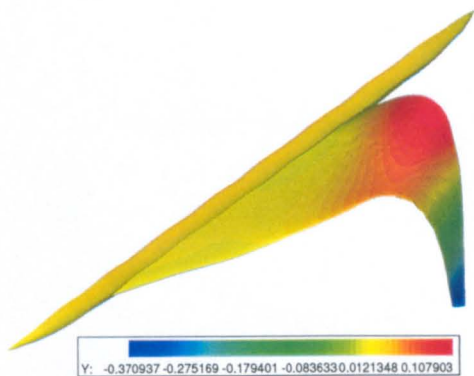
(a) Structural model



(b) Mode 1 - 12.44 Hz



(c) Mode 2 - 51.65 Hz



(d) Mode 3 - 58.32 Hz

Figure 4.8: The structural model and transformed mode shapes used in the flexible SST simulations.

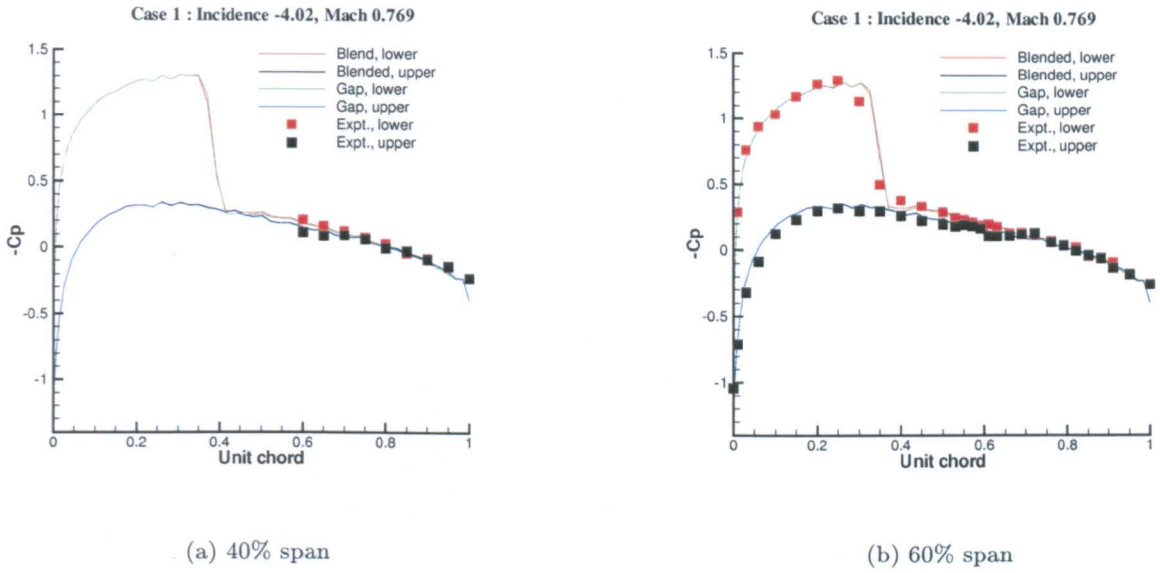


Figure 4.9: BACT Case 1 steady C_p values using blended flap and flap with gaps. $M = 0.769$, Re. No. 3.96 million, $\alpha = -4.02^\circ$

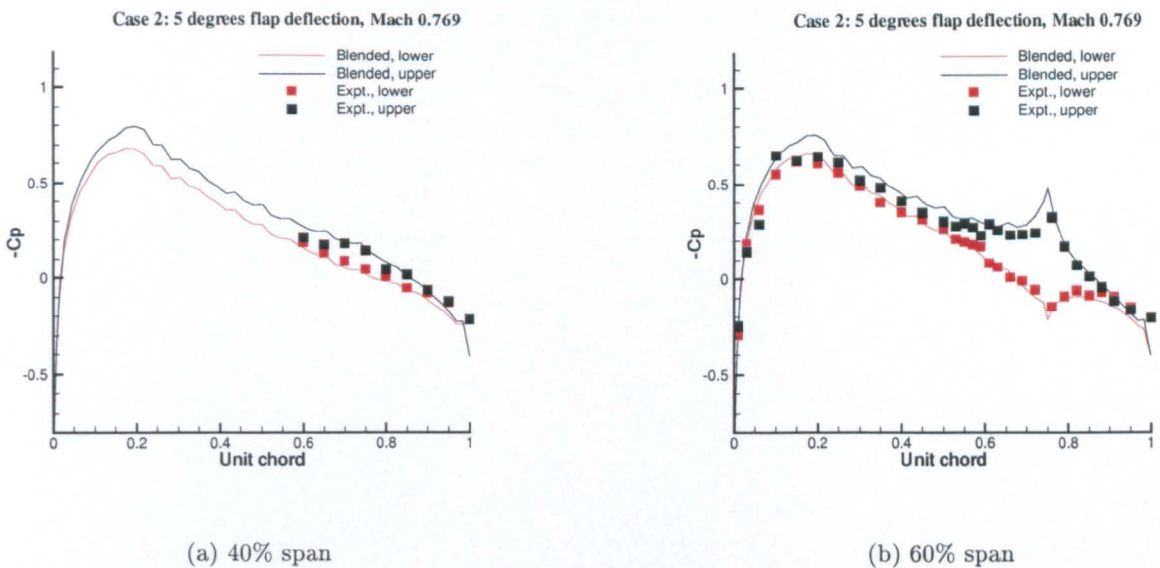


Figure 4.10: BACT Case 2 steady C_p values using blended flap. $M = 0.769$, Re. No. 3.96 million, flapangle = 5.0°

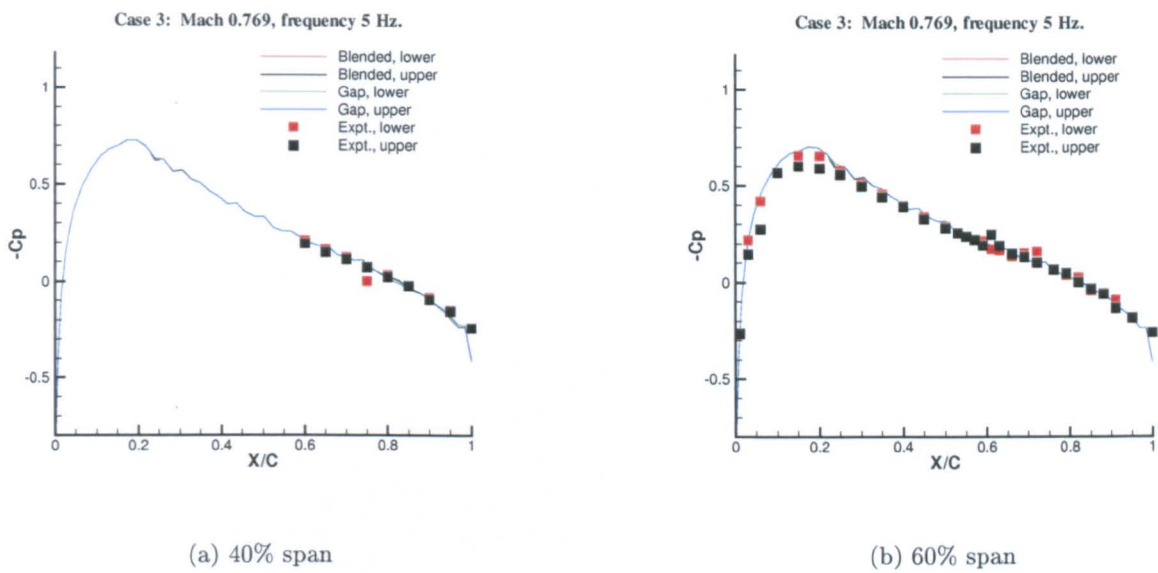


Figure 4.11: BACT Case 3 mean Cp values using blended flap and flap with gaps. M = 0.769, Re. No. 3.96 million, flap amplitude = 2.02°

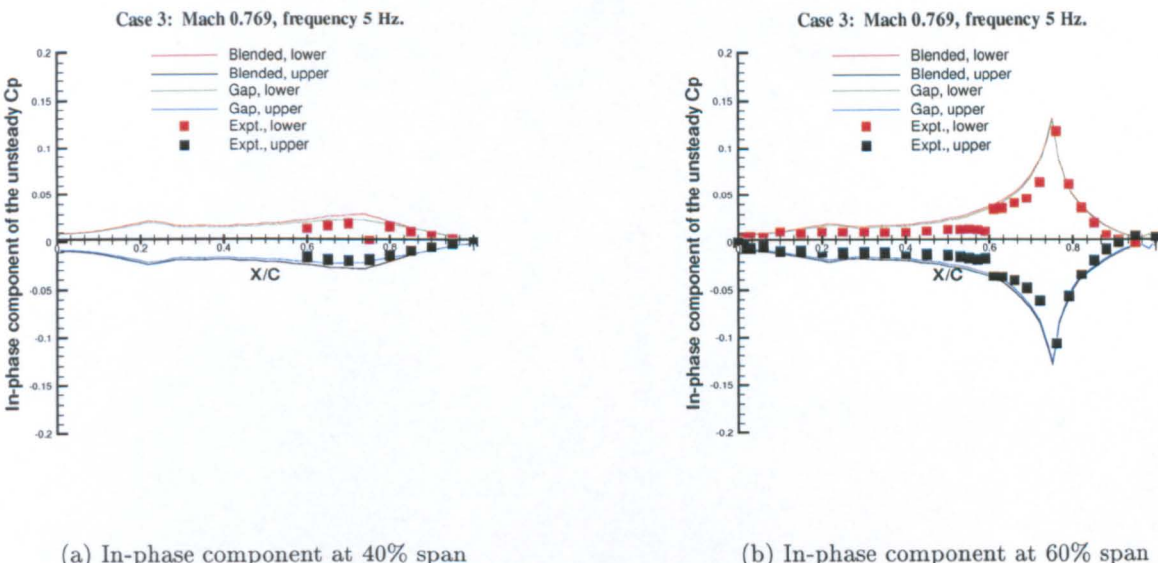
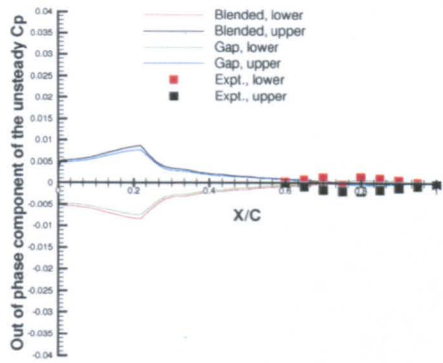
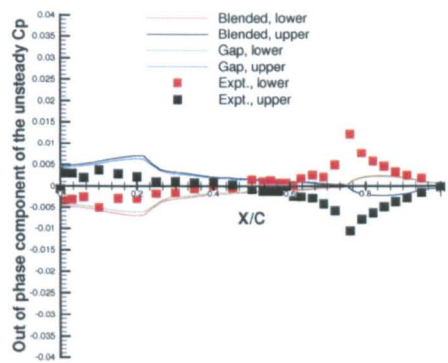


Figure 4.12: BACT Case 3 unsteady Cp values using blended flap and flap with gaps. M = 0.769, Re. No. 3.96 million, flap amplitude = 2.0°, ω_F 5 Hz.

Case 3: Mach 0.769, frequency 5 Hz.



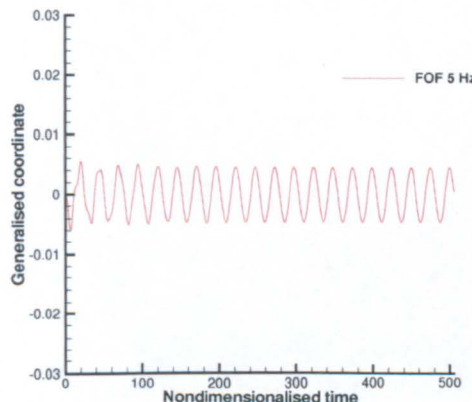
Case 3: Mach 0.769, frequency 5 Hz.



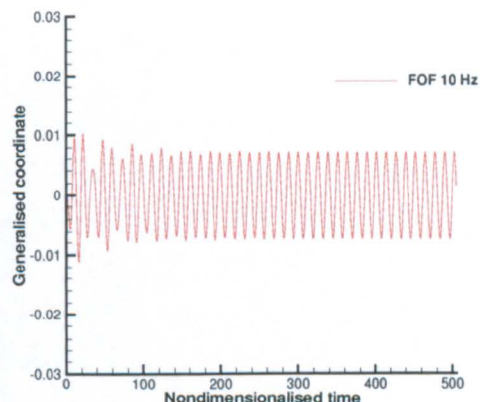
(a) Out of phase component at 40% span

(b) Out of phase component at 60% span

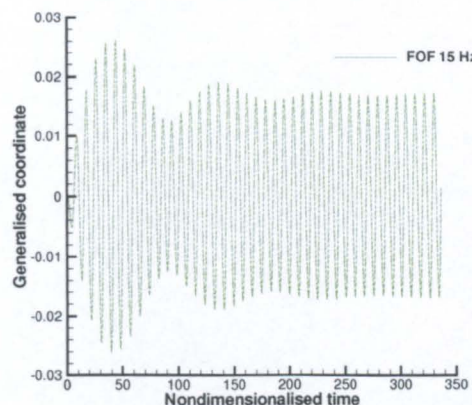
Figure 4.13: BACT Case 3 unsteady C_p values using blended flap and flap with gaps. $M = 0.769$, Re. No. 3.96 million, flap amplitude = 2.0° , ω_F 5 Hz.



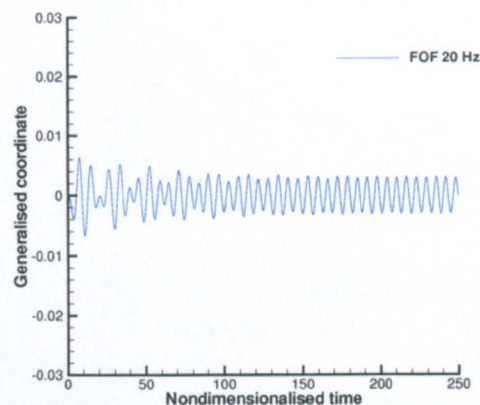
(a)



(b)

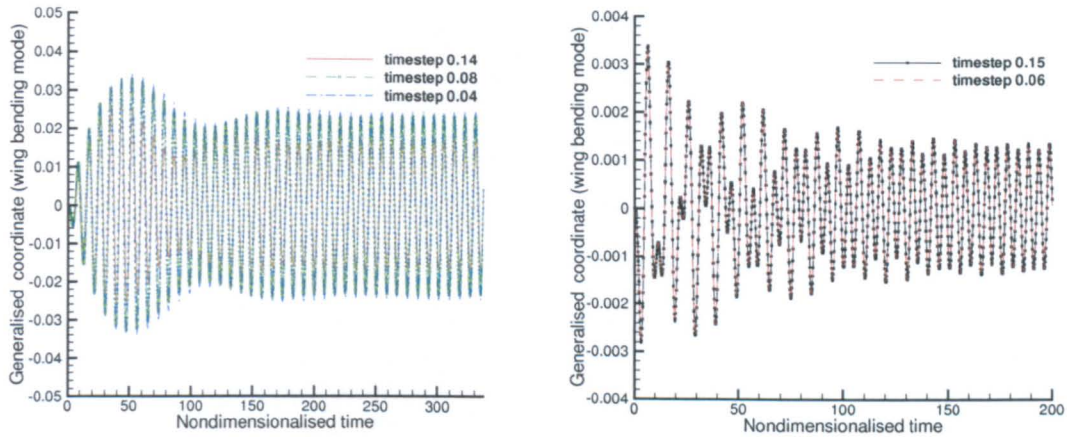


(c)



(d)

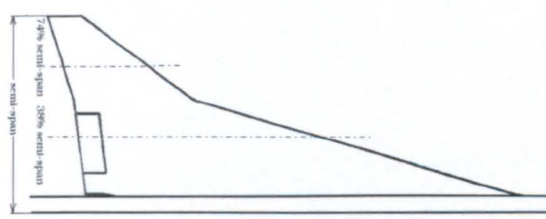
Figure 4.14: Wing bending response to different flap frequencies.



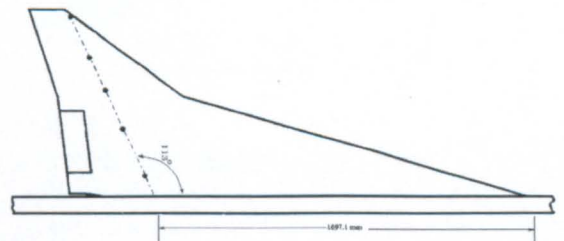
(a) At ω_F of 15 Hz amplitude increases with decreasing timestep.

(b) At ω_F of 25 Hz amplitude remains unchanged with decreasing timestep.

Figure 4.15: Sensitivity of the modal response to the timestep at the resonance ω_F of the SST, Case 1, Euler simulation.

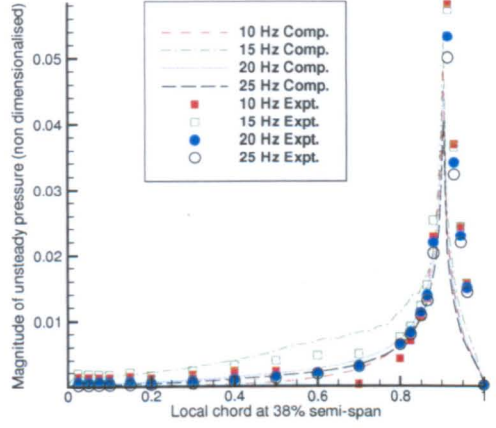


(a) Location of unsteady pressure transducers.

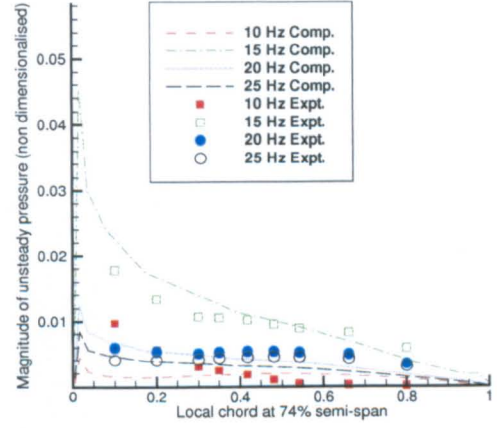


(b) Location of optical targets to measure dynamic deformation.

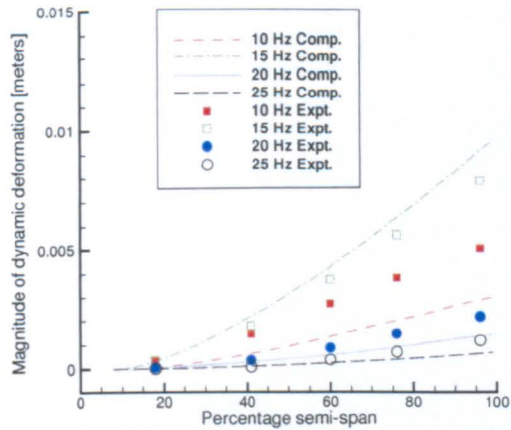
Figure 4.16: Location of measurement points in the SST experiments.



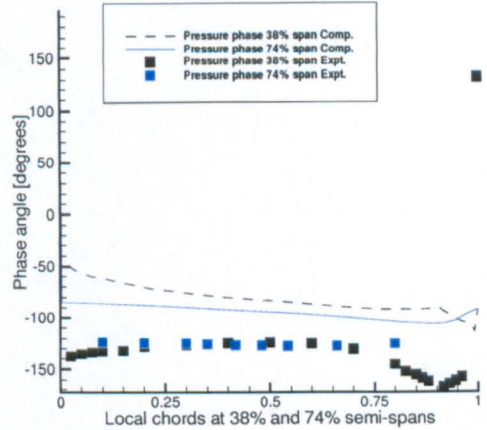
(a) Unsteady pressure at 38% semi-span location.



(b) Unsteady pressure at 74% semi-span location.

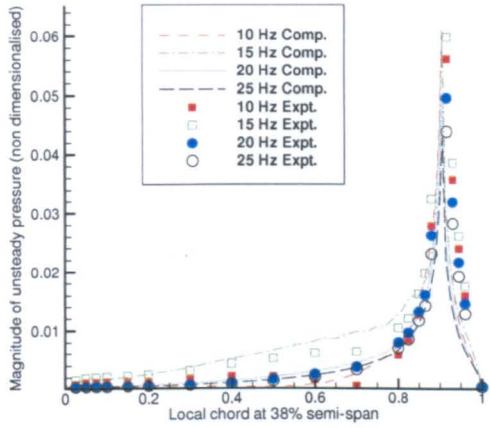


(c) Unsteady deformation along the span (see Figure 4.16).

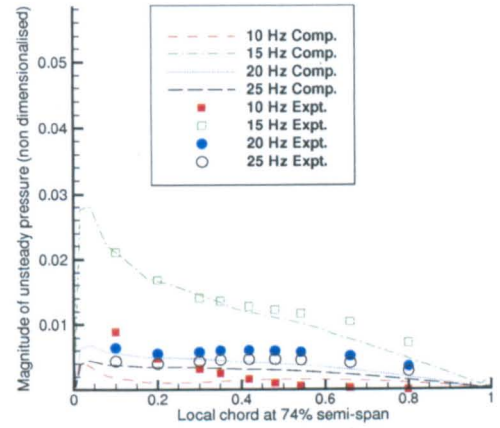


(d) Pressure phase lag at the ω_F of 15 Hz

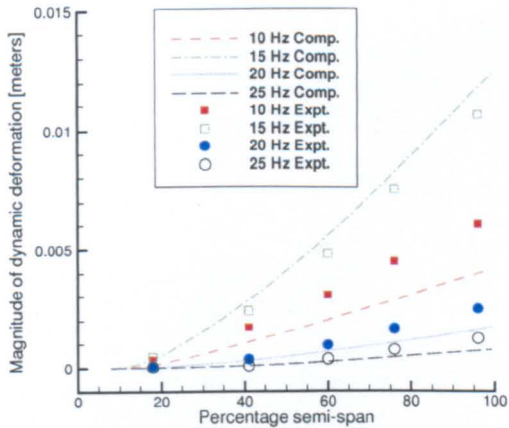
Figure 4.17: Unsteady pressure and deformation plots for SST Case 1 computations on a coarse grid using Euler equations.



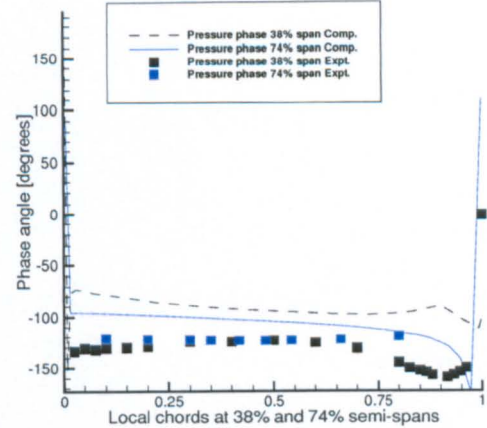
(a) Unsteady pressure at 38% semi-span location.



(b) Unsteady pressure at 74% semi-span location.

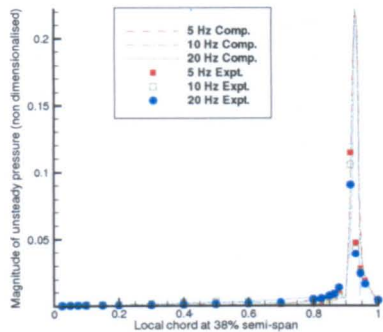


(c) Unsteady deformation along the span (see Figure 4.16).

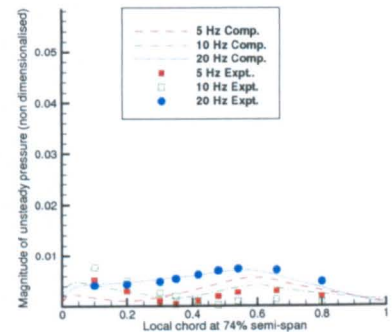


(d) Pressure phase lag at the ω_F of 15 Hz.

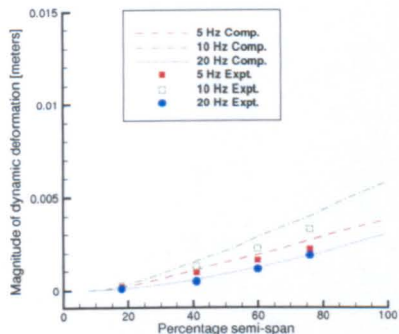
Figure 4.18: Unsteady pressure and deformation plots for the SST Case 2 computations on a coarse grid using Euler equations.



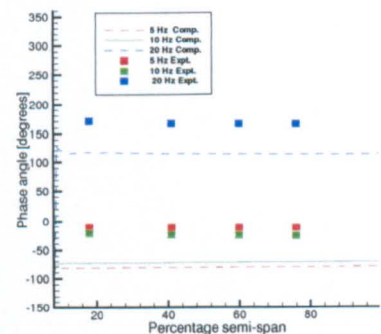
(a) Unsteady pressure at 38% semi-span location.



(b) Unsteady pressure at 74% semi-span location.

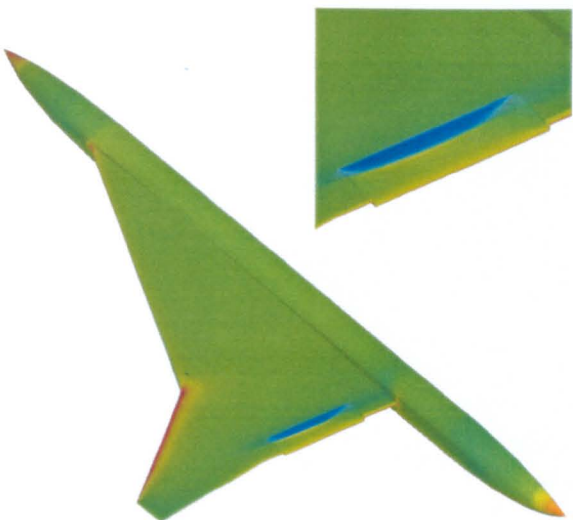


(c) Unsteady deformation along the span (see Figure 4.16).

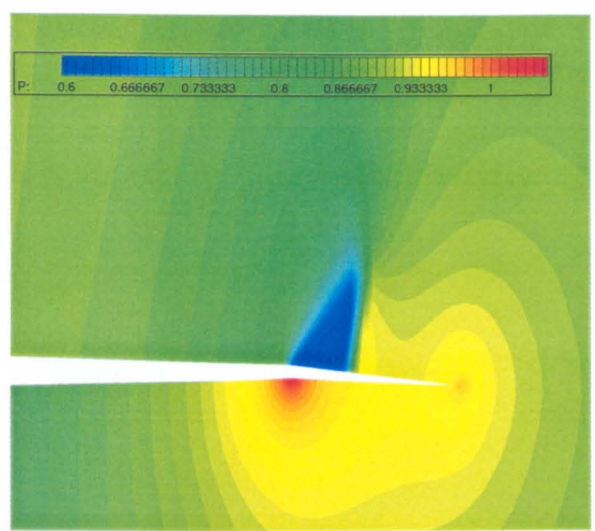


(d) Deformation phase lag at the ω_F of 5 Hz, 10 Hz and 20 Hz.

Figure 4.19: Unsteady pressure and deformation plots for the SST Case 3 computations on a coarse grid using Euler equations.

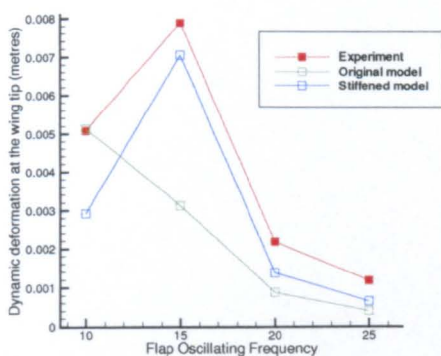


(a) Surface Cp contours.

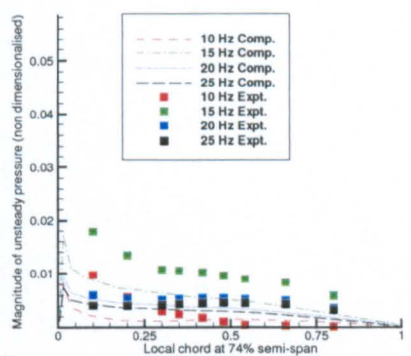


(b) Steady pressure at 38% semi-span location.

Figure 4.20: Steady inviscid pressure contours for the SST Case 3. The region of low pressure at the flap leading edge has supersonic flow.

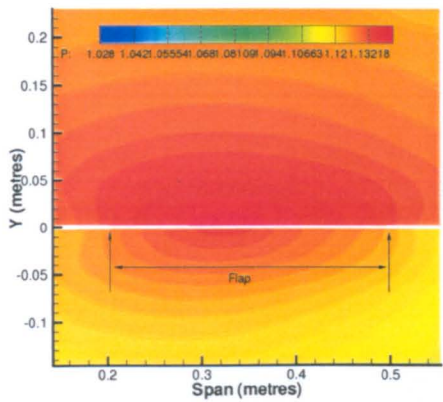


(a) Comparison of dynamic tip deformation with different FEM models.

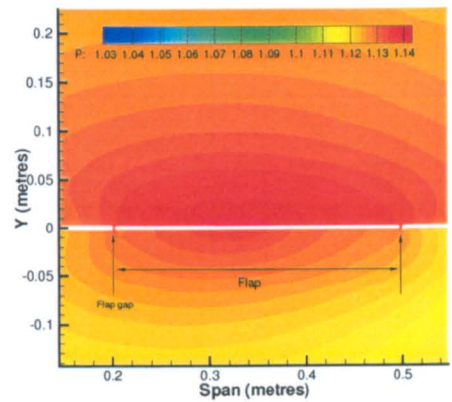


(b) Unsteady pressure at 74% semi-span location.

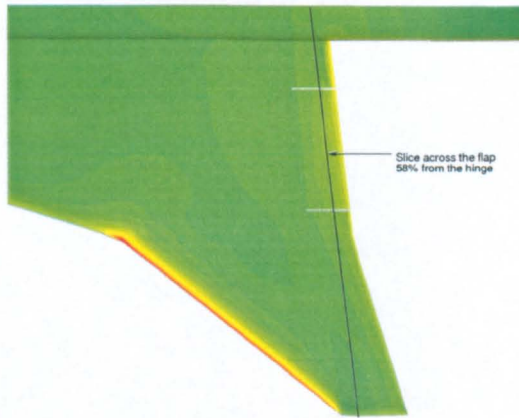
Figure 4.21: Comparison of unsteady pressure and deformation results between the original and the new stiffened structural models of the SST.



(a) Flap with blended edges.

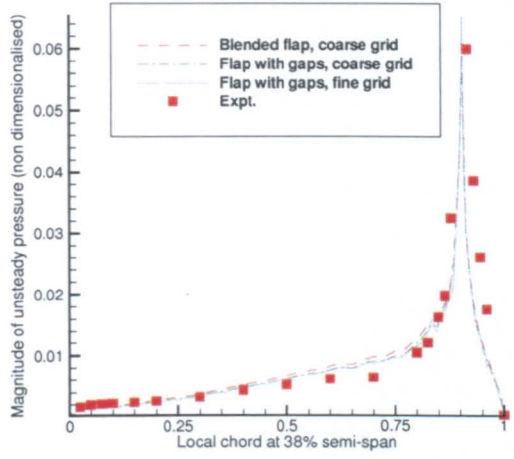


(b) Flap with free edges.

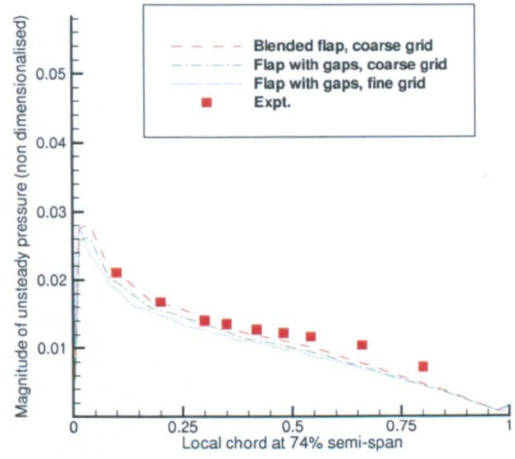


(c) Position of the plane at 58 % from the flap hinge.

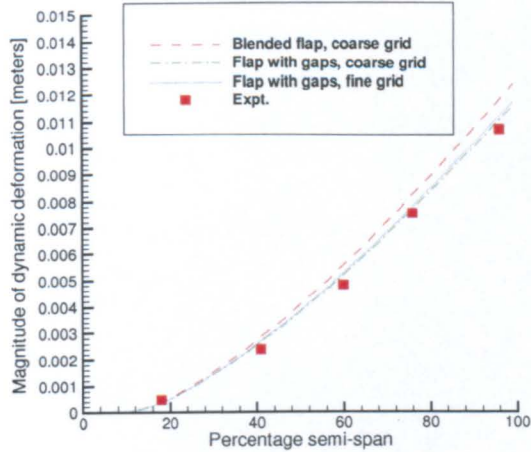
Figure 4.22: Pressure contours through a plane 58 % from the flap hinge. Steady state Euler calculations for Case2.



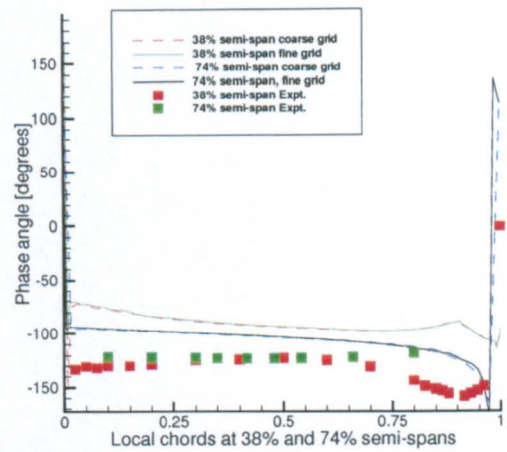
(a) Unsteady pressure at 38% semi-span location.



(b) Unsteady pressure at 74% semi-span location.

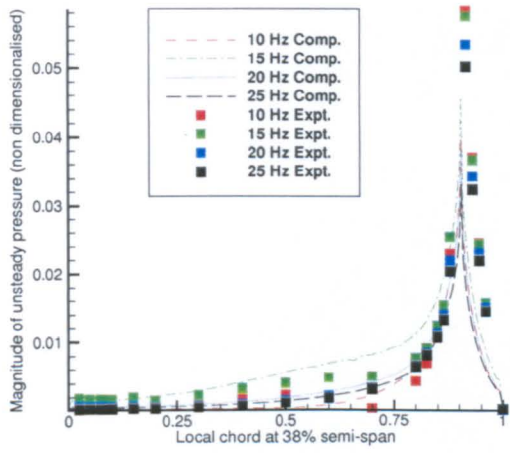


(c) Unsteady deformation along the span (see Figure 4.16).

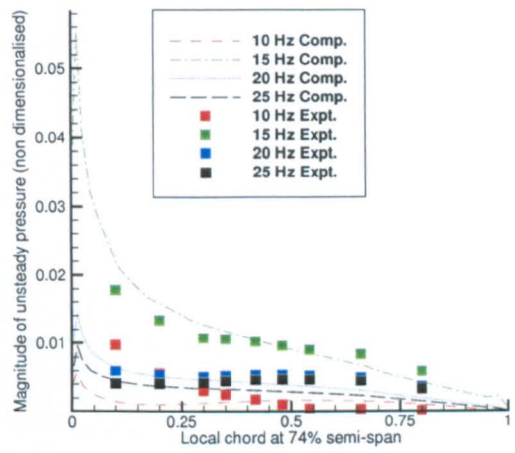


(d) Pressure phase lag of fine and coarse grids with ω_F of 15 Hz.

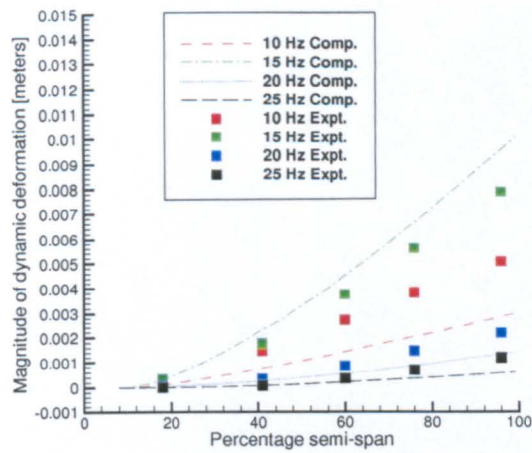
Figure 4.23: Unsteady pressure and deformation plots for the SST Case 2 computations on a coarse and fine grids using flaps with gaps and at ω_F of 15 Hz using the Euler equations.



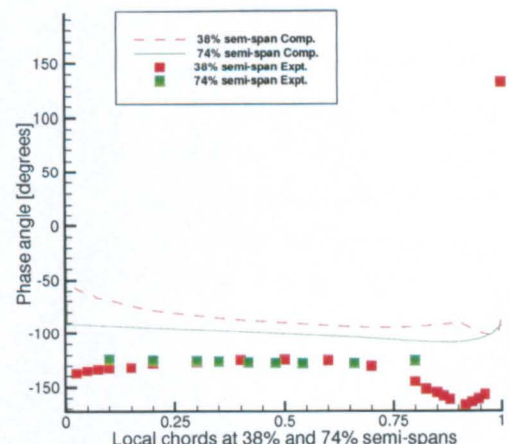
(a) Unsteady pressure at 38% semi-span location.



(b) Unsteady pressure at 74% semi-span location.



(c) Unsteady deformation along the span (see Figure 4.16).



(d) Pressure phase lag the ω_F of 15 Hz.

Figure 4.24: Unsteady pressure and deformation plots for the SST Case 1 computations using the RANS equations.

Chapter 5

Control Surface Instability

5.1 Introduction

In recent years Computational Aeroelasticity (CAE) has advanced to a point where flutter boundaries for complete aircraft configurations can be predicted, even in the difficult transonic flow regime [76, 85, 86, 67]. Along with simulations of classical aeroelastic instabilities like flutter and divergence, an interesting area of CAE application is the prediction of control surface instabilities like buzz. Extensive work on numerical simulations of buzz has not been undertaken. This is mainly because by the time the computational tools were in place for such an undertaking, buzz ceased to be an issue in modern aircraft. The advent of hydraulic actuators reduced the chance of control surfaces developing oscillation about its hinge, when compared with flaps on older aircraft with mechanical spring loaded fixtures.

Experimentally there were a number of important studies in the 60s and 70s exploring the buzz phenomenon[4, 87, 88]. The popular classification of buzz in the literature was defined by Lambourne[4]. During the course of his experiments he found that there are 3 main types of buzz possible on a trailing edge flap, which he called Types A, B and C. Type A buzz occurs when the shock stands somewhere ahead of the flap hinge line and interacts with the boundary layer and the flap motion. The limit cycle oscillation is brought about by the synchronisation of the shock strength and motion, the flow separation and the angular flap motion. As the control surface moves it alternately weakens or strengthens the shock, causing separation and re-attachment of the flow. The separated flow in turn creates a hinge moment at the flap leading edge which makes the flap undergo oscillation. The Type A buzz is limited to thick aerofoils, and is rarely seen in aerofoils with less than 10% camber[3]. Shock induced flow separation is the primary requirement for Type A buzz to occur. Type B buzz is when the shock crosses the hinge line and translates over the control surface. The driving mechanism here is the unsteady hinge moment from the pressure pulse created by the shock motion. The hinge moments involved in Type B buzz are greater than in Type A and are much more difficult to alleviate. In terms of numerical simulation, Type B buzz can be simulated using the Euler equations. Although there can be flow separation over the flap in Type B buzz, which can effect the amplitude and frequency of the buzz, the actual onset of buzz is not influenced by viscous effects [3]. Type C buzz occurs when the shock has crossed the whole length of the control surface and is attached to the trailing edge. This type of buzz occurs in supersonic flows and is thought not to involve flow separation.

Until now there have been few numerical simulations of buzz described in the literature. One of the first such studies was performed by Steger [36] who carried out a 2D buzz simulation on a P-80 wing using an implicit finite difference code capable of solving the RANS equations. The P-80 aircraft was already known to suffer from buzz problems during flight testing and this was further investigated in the NASA Ames wind tunnel by Erickson and Stephenson [89]. Steger was able to match the computed results with the experiments, and also measured the effect of viscosity on buzz simulations. It was found that for a certain Mach number the oscillations in an inviscid calculation would die down after an initial kick but that the oscillations in viscous simulations would result in a limit cycle[36]. At a higher Mach number the inviscid simulation would diverge whereas the RANS simulation would still predict a limit cycle. Hence he deduced that viscosity had an effect of both preserving and mitigating the oscillations.

Fuglsang *et al.* [90] solved a buzz problem on the fin-rudder section of T-45 Goshawk aircraft through steady CFD simulations. By analysing the flow field using CFD around the flow parameters where buzz was known to arise, a solution using two parallel shock strips was developed. Shock strips are raised sections that are stuck on the wing to move the shock forward of its original position. The strips were successful in alleviating buzz in the T-45 flight envelope.

Bendiksen numerically investigated a type of buzz instability that relies purely on the interaction between the shock and flap motion, which he termed non-classical buzz[3]. He showed that for certain cases, especially for thin aerofoil sections, the flow separation does not play an important role in maintaining a limit cycle oscillation. A buzz boundary traced from inviscid calculations compared well with experiments [3]. Recently the non-harmonic motion of the shock over an aerofoil with a harmonically oscillating flap[80] and 3D aileron buzz calculated using the thin layer RANS equations were shown[38].

The Japan Aerospace Exploration Agency¹ (JAXA) has been developing scaled powered and non-powered Supersonic Transport models as part of their objective to acquire and establish advanced aircraft integration technology. The first non-powered model from this program was launched in Woomera, Australia in 2002. As with all supersonic configurations this model had thin, low aspect ratio wings with little possibility of flow separating over the wing at moderate angles of attack within the flight envelope. However at high transonic and low supersonic conditions a strong shock develops where a trailing edge flap/aileron might be situated. Due to the thinness of a supersonic wing it is difficult to have stiff hinges or powered actuating systems for the trailing edge flap. This means that the shock motion over the flap can interact with the one degree of freedom flap motion by feeding energy to it and causing undamped flap oscillations that grow in time. As the wings used for supersonic aircraft are usually thin, analysis for Type B buzz is of most relevance. The flap in the current work is modelled as having blended edges and free edges. Chapter 3.18 describes these two type of treatments in detailed. The aeroelastic response from the two types of modelling are compared here.

5.1.1 Test Case Description

The geometry of the configuration is described in an RTO report [91]. The section profile is the NACA 0003 and the wing is a cranked double delta. A fuselage swell near the wing trailing

¹formerly National Aerospace Laboratory (NAL)

Mode	Frequency (Hz)- Model 1	Frequency (Hz)-Model 2
Wing bending	10.39	10.44
Flap Oscillation	16.202	-
Wing Torsion	44.24	44.13
Second Wing Bending	53.89	50.23
Second Wing Torsion	89.06	88.80

Table 5.1: Natural frequencies of the model

edge, which was present in the experimental model to house the flap oscillation mechanism, is eliminated from the CAD model. The wing tip is modelled by rotating the aerofoil at the tip.

5.1.2 The Structural Model

The structure of the SST was modelled as a 2D plate in **NASTRAN** with the aid of the **PATRAN** preprocessor. The flap is modelled as a separate plate attached to the main wing through springs (See Figure 5.1). Two structural models were constructed using the same material and geometric properties. The difference between the two models is in the value of the spring stiffness at the flap hinge. The spring stiffness constant in Model 1 is adjusted so that it gives a flap frequency of 16.2 Hz which is within the realistic frequency range of a mechanically constrained trailing edge control surface. The spring stiffness constant of the hinge in Model 2 is set to a very high value so that the flap is constrained and the flap mode is eliminated. The first computed natural mode of vibration is a wing bending mode that has a frequency similar to previously published values[91]. Table 5.1 gives the details of the natural frequencies of the 2 models used in the buzz and flutter calculations. The second natural mode of Model 1 is the flap oscillation mode which is used for buzz simulations. The first 5 natural modes were used for flutter calculations for the case with the flap having a low hinge spring attachment stiffness and the first 4 natural modes were used in flutter calculations for the case with a high hinge spring attachment stiffness. By increasing the stiffness of the flap hinge the flap oscillation mode was eliminated at the same time maintaining the shape and frequencies of other modes. The wing structure is made up of 550 triangular elements and the flap has 20 elements. The fuselage structure consists of two triangular elements that are clamped rigid.

5.1.3 CFD Grids

To model the effect of gaps and viscosity a total of 4 different grids have been used in this work. The viscous grid has 15 cells to resolve the boundary layer. The wall spacing is 1.8×10^{-6} chord lengths. The viscous calculations are performed only with blended flaps to avoid problems with grid quality when gaps are introduced at flap edges. A C-Type grid topology is used over the wing leading edge, the wing tip and also around the fuselage. The blocks at the trailing edge are of H-Type. The C-Type blocks wrap around the rounded leading edge and the tip ensuring orthogonal cells which otherwise would not be possible with an H-H Type of blocking. The wing geometry is basically a slender delta wing on the inboard side and a collapsed triangular block is avoided at the leading edge tip by using a 3-block strategy as shown in Figure 5.2. Points

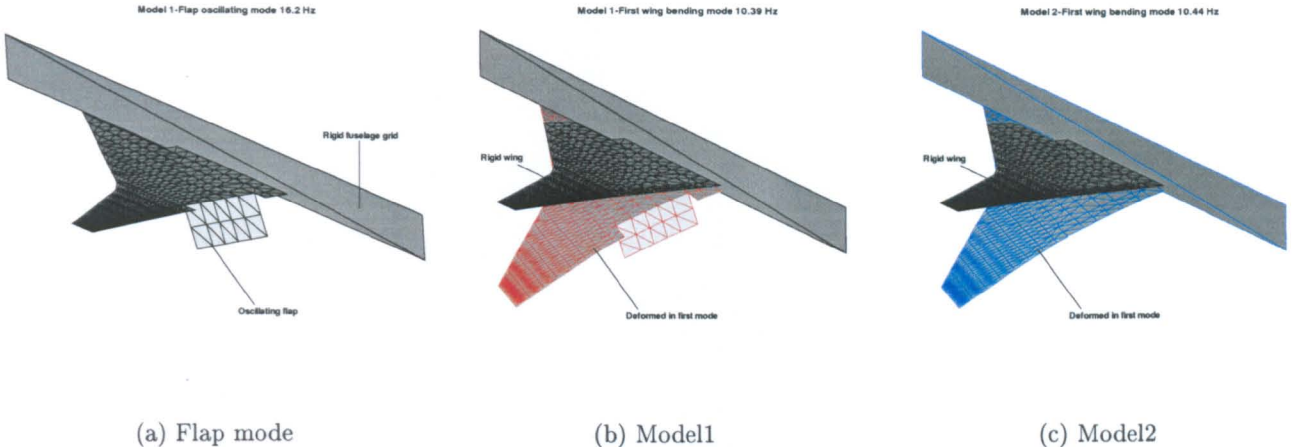


Figure 5.1: Structural models with the flap oscillation mode and the first wing bending mode

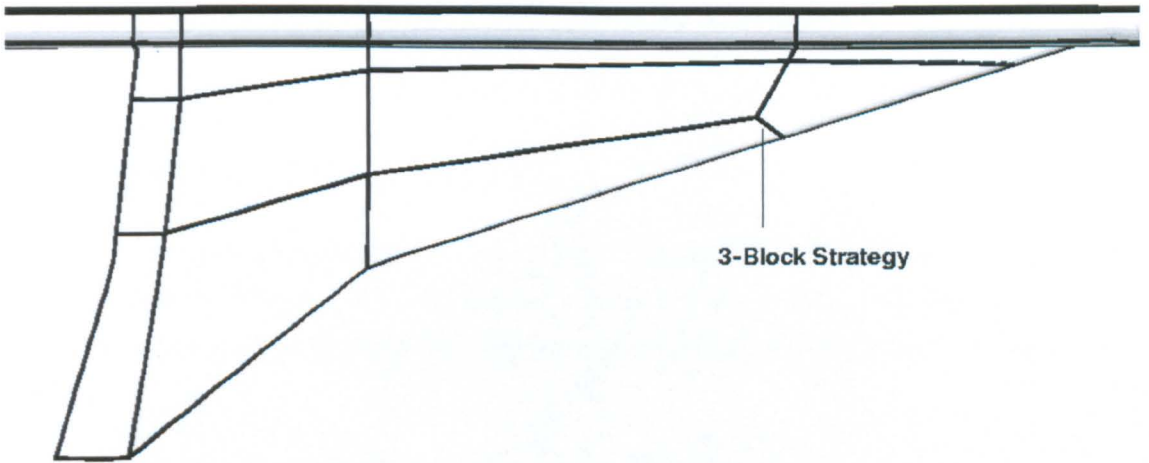
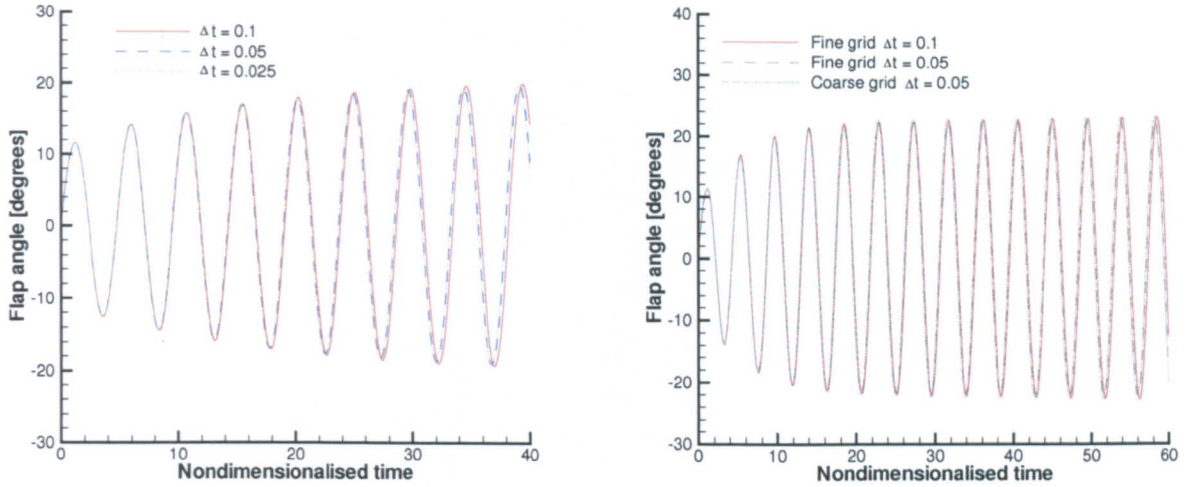


Figure 5.2: 3-block strategy to prevent a collapsed point at the leading edge of the wing root

are clustered around the trailing edge and the flap region where the shock is likely to develop and move during the buzz simulation. There are 14 cells in the chord-wise direction and 28 in the span-wise direction on the flap. The size of the viscous grid is 800k cells. The grid is capable of accurately resolving the flow in the region of interest but at the same time is small enough to allow rapid turn around for the unsteady calculations. The blended Euler grids have the same topology as the viscous grid. The fine Euler grid has 1.6 million cells. There are 24 cells in the chord-wise direction and 50 span-wise. The wall spacing is 1×10^{-3} chord lengths. A coarse grid is obtained from the fine grid by removing every alternate grid point in all the three directions. The coarse Euler grid has 200k cells. The grid used for flaps with gaps is the same as the coarse Euler grid for blended flaps but with two extra blocks inside gaps between the flap edges and the wing.



(a) RANS calculation, Mach 0.987, $k = 0.778$ and dynamic pressure = 26.468 kPa

(b) Euler calculation, Mach 0.95, $k = 0.778$ and dynamic pressure = 26.468 kPa

Figure 5.3: Timestep and grid refinement calculations

5.2 Results and Discussions

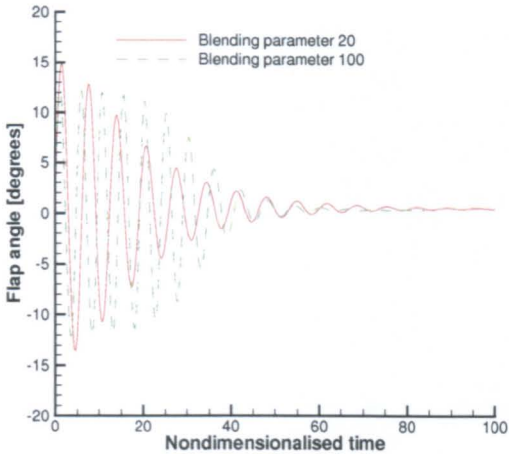
The steady and unsteady results for a case with a forced flap motion have been validated with the experiments in Chapter 4. The current chapter deals with a flap that is driven by the unsteady aerodynamics and unlike the previous case experimental results are not available for validation.

5.2.1 Grid and time-step refinement study

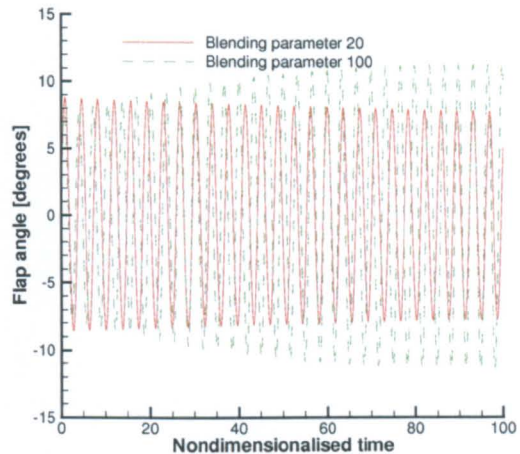
A timestep refinement study was performed on the RANS case at Mach 0.987. At a freestream velocity of 275m/s the reduced frequency of the response is 0.778. Figure 5.3(a) shows the time traces of the modal response using timesteps of 0.025, 0.05 and 0.1. As can be seen the curves of timesteps 0.025 and 0.05 almost overlap each other and maintain the frequency and the amplitude. Hence a timestep of 0.05 is used for all the buzz simulations in the current study. Figure 5.3(b) shows the modal response at Mach 0.95 using the Euler calculations on fine and coarse grids with timesteps of 0.05 and 0.1. Once again the modal response curves overlap each other. The results indicate the coarse Euler grid with a timestep of 0.05 are able to adequately predict the flap response.

5.2.2 Dependence of buzz on flap blending

This section concerns the effect of the blending parameter [51] on the onset of buzz. Again a coarse Euler grid is used to assess this effect as we are concerned with the variation in the predicted buzz Mach number with a change in the blending parameter. In the first case a low blending value of 20 and in the second a higher value of 100 is used. The larger the value of the blending parameter the more the transformed fluid grid conforms to the structural grid at



(a) Euler calculation, Mach 0.9, $k = 0.778$ and dynamic pressure = 26.46 kPa



(b) Euler calculation, Mach 1.1, $k = 1.42$ and dynamic pressure = 7.85 kPa

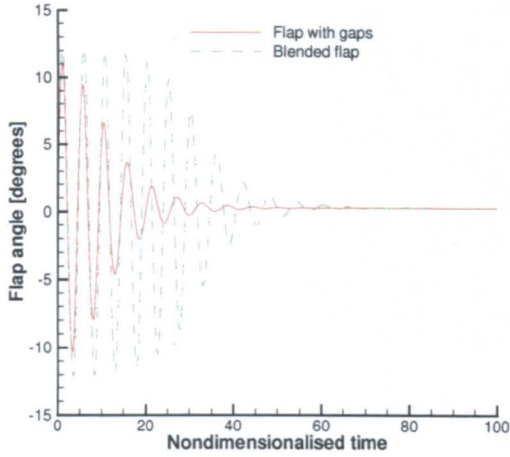
Figure 5.4: Flap response at different values of blending parameter

Mach No.	0.9	0.91	0.92	0.93	0.95	0.98	1.1	1.2	1.3	1.4
Euler blended	No	No	Yes	Yes	Yes	Yes	Yes	Yes	No	-
Euler gap	No	No	No	Yes	Yes	Yes	Yes	Yes	No	-
Viscous	No	-	No	-	Yes	Yes	Yes	Yes	Yes	Maybe

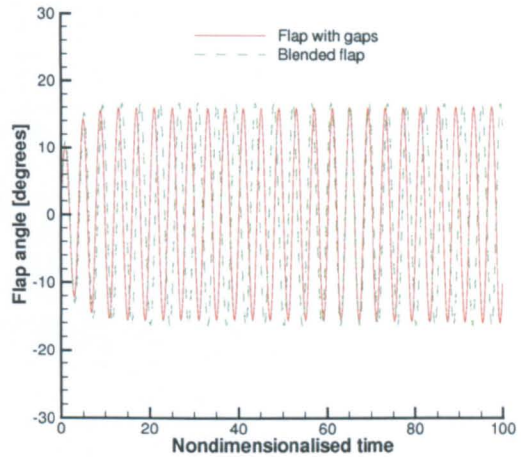
Table 5.2: Buzz prediction at various Mach numbers by different models

the given transformed mode. For the flap mode where the flap nodes move relative to the wing nodes the blending parameter acts as a damper limiting the motion of the flap. This damping effect decreases with the increasing value of the blending parameter. Also a higher blending parameter maintains a sharper shape at the flap edge. Figure 5.4 shows the flap angle against time for the two values of blending parameter. The flap modelled with a blending parameter of 20 has, in general, a more restrained response both in amplitude and in frequency.

To assess the influence of blending gaps are introduced at the inboard and outboard edges. The total width of both gaps combined is 1% of the flap span. The cells in these gaps are sheared as the flap moves from its mean position. It takes longer to converge due to poor grid quality of the sheared cells, and hence increases the overall computation time by almost 50%. In terms of prediction of the Mach number at which buzz occurs the two types of flap treatment give similar results. Table 5.2 shows the occurrence of buzz at different Mach numbers as predicted by different simulation methods. The angle of incidence for all the cases is 0.6° and the Reynolds number for the viscous case is 21.42 million. The maximum amplitude of flap rotation arises at Mach numbers 0.91 - 0.93 with flap rotation angles approaching 25° . The amplitude of the flap angle for the blended case is larger than the flap with free edges as seen in Figure 5.5. This is because the blended flap has more surface area for the shock driven unsteady aerodynamics to



(a)



(b)

Figure 5.5: Flap response of blended and free flaps at different Mach numbers

act on and hence more force is transferred to the structural grid resulting in larger deformations.

A conclusion that can be drawn from Table 5.2 with respect to Euler and RANS calculations is the dependence of Type-B buzz on the shock prediction. As the Euler equations predict the shock aft of RANS modelled flows for a given angle of incidence and Mach number, and hence the Mach number at which the RANS equations predict the onset of Type-B buzz is higher. It was found for the current case that the location of the shock predicted by the Euler equations at Mach 0.98 is the same as the location predicted by the RANS equations at Mach 0.987. Figure 5.6 shows the pressure contours for the inviscid case at Mach 0.98 and the viscous case at Mach 0.987. The slice is taken at 38.4 % span and the shock locations for both the cases is at approximately 95.7% local chord. The angle of incidence is 0.6° .

5.2.3 Dependence of buzz on the initial impulse

It is known that control surface buzz is sensitive to the initial disturbance. In cruise conditions this displacement of the control surface can be brought about by atmospheric turbulence or sudden changes in dynamic pressure along the flight path. Depending on the magnitude of the displacement angle of the control surface and the Mach number, a shock can develop over either the upper or lower side of the control surface. Figures 5.7 through 5.9 show unsteady pressure contours through a cycle of oscillation that is growing in amplitude. This is for an inviscid solution on the fine grid with the wing at an incidence of 0.6° and at a Mach number of 0.95. The slice is taken through 32 % wing span which intersects the flap at 40 % span. The coupled calculation is initiated by perturbing the flap velocity. Depending on the angle the flap reaches following the initial perturbation and the Mach number, the shock can either move far aft of the flap or remain near the flap leading edge. The strength and position of the displaced shock on the flap decides whether the system will enter an LCO or if the initial perturbation will

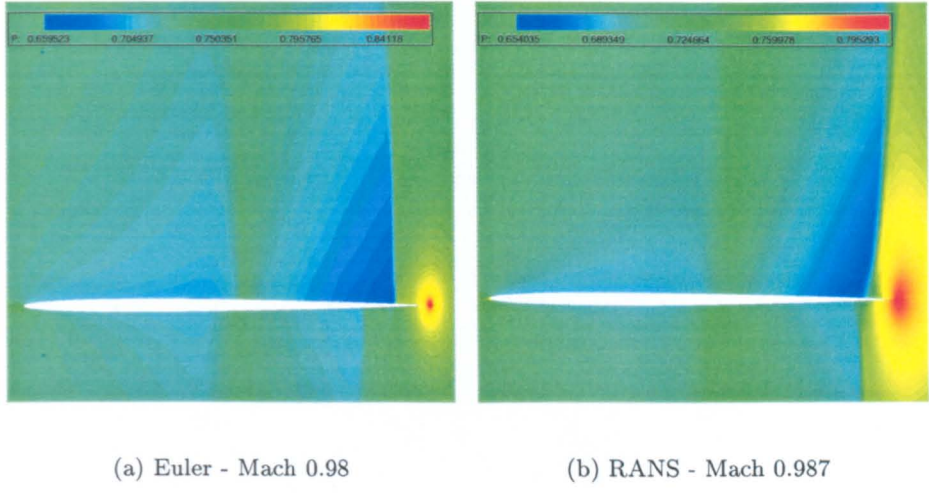
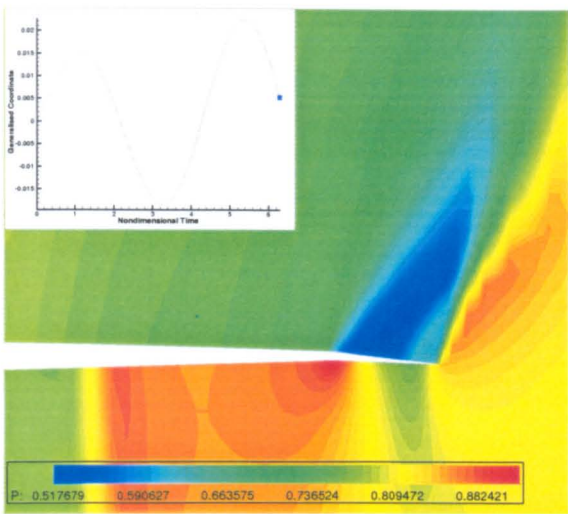


Figure 5.6: Steady pressure contours for Euler and RANS cases at a slice taken at 38.4% span.

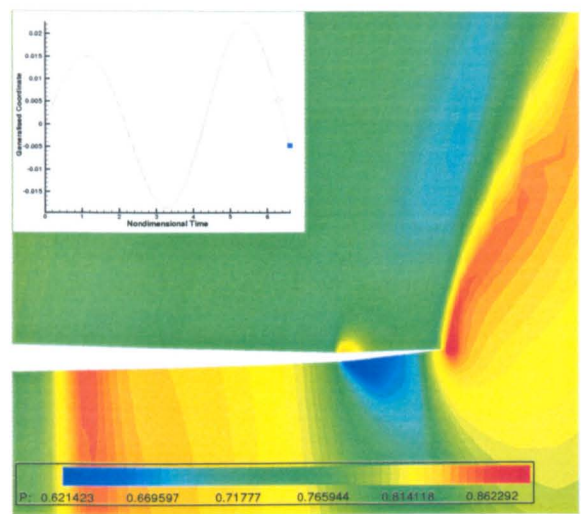
die down. Hence the buzz onset depends both on the Mach number and the size of the initial perturbation at a given incidence.

Consider a case where a large initial perturbation is applied as shown in Figures 5.7 through 5.9. The side with the shock has an area of higher free stream velocity and hence lower dynamic pressure than the opposite side. This pressure difference across the control surface creates a hinge moment that pulls the control surface towards the opposite side weakening the shock. Due to the inertial forces and the lag in the aerodynamic response the control surface continues its motion resulting in the formation of a shock on the opposite side. This cycle continues locking the system into a limit cycle oscillation due to the motion of the shock over the control surface. Figure 5.11 shows the same case but with a low initial perturbation. Here the initial impulse is not strong enough for the flap to deflect to a required angle for a strong shock to develop over the control surface. Hence the hinge moment created is too weak for the LCO to ensue. Figure 5.12 shows the dependence of buzz to the initial aerodynamic impulse at different Mach numbers. It can be seen that for low transonic cases, where the shock is not very aft of the hinge line, buzz is dependent on the initial perturbation, but for high transonic and supersonic cases even a small impulse can result in buzz. This phenomenon was also observed in 2D simulations by Bendiksen[3]. Steger found that buzz was dependent on the initial position of the flap[36] and this is consistent with Bendiksen's explanation of the non-classical buzz as direct consequence of shock motion on the flap as the initial position of the flap shifts the location of the shock towards the trailing edge .

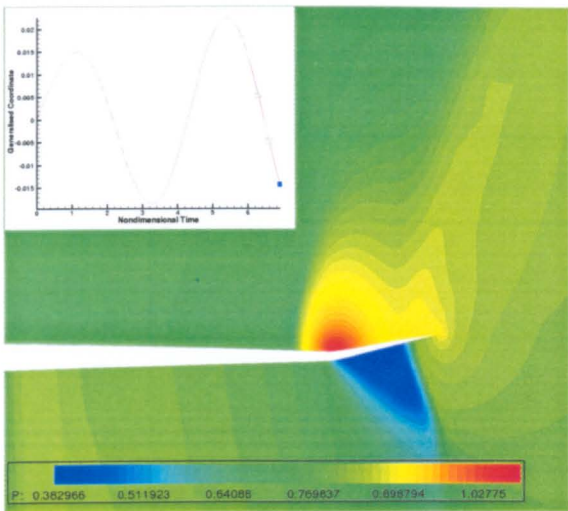
The results in Figure 5.12 are from calculations performed on a coarse grid using Euler equations. As viscous effects are not modelled the instability here is brought about purely due to the motion of the shock. However the dependence on the initial impulse is also observed in RANS simulations. Figure 5.13 illustrates the variation of the normal force on the upper and lower surfaces of the flap with angular motion of the flap when given a high initial perturbation at Mach 0.95. This simulation is performed using the Euler equations. The static force and deflection have been subtracted from the plotted results. It can be seen that there is a phase



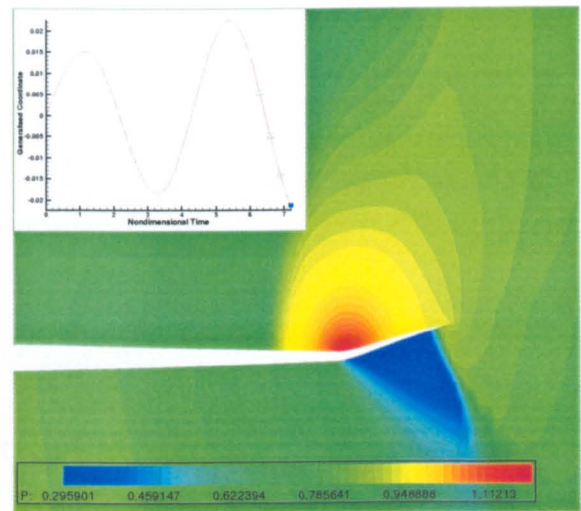
(a)



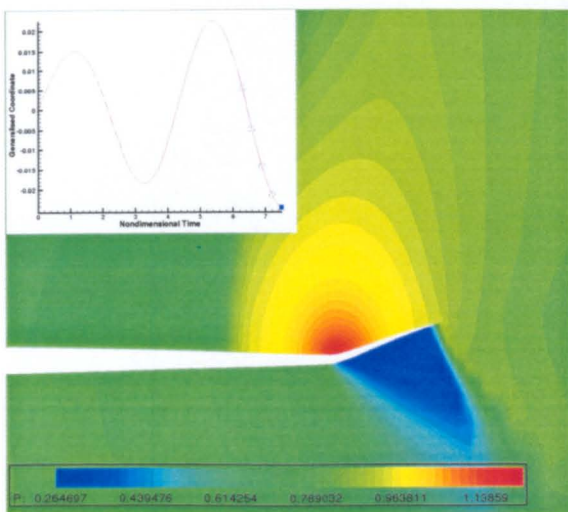
(b)



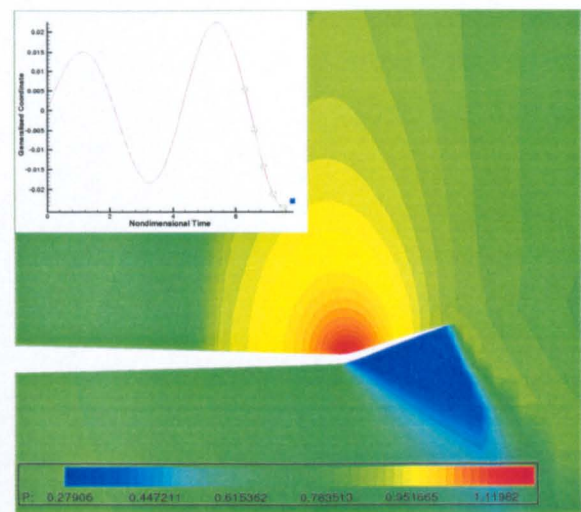
(c)



(d)

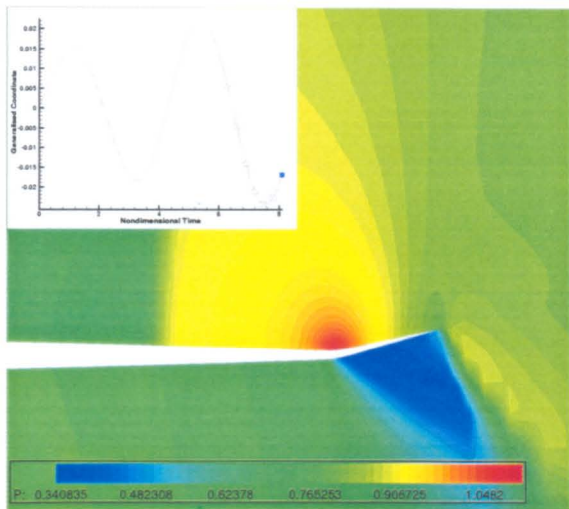


(e)

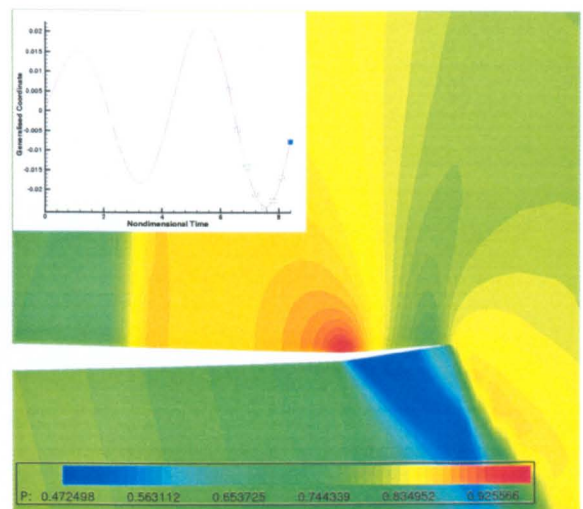


(f)

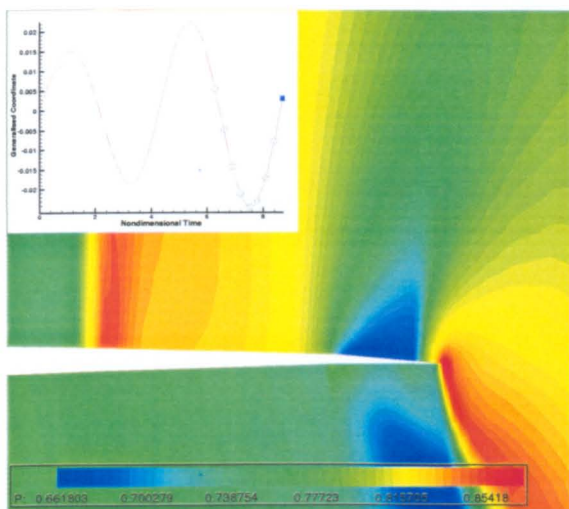
Figure 5.7: Unsteady pressure contours during a single buzz cycle (P.T.O.)



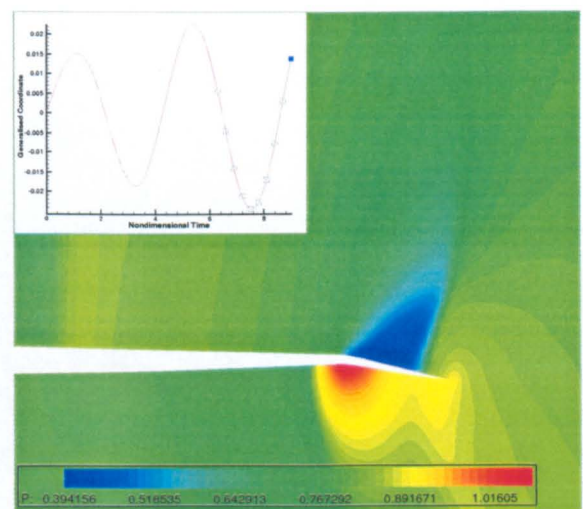
(a)



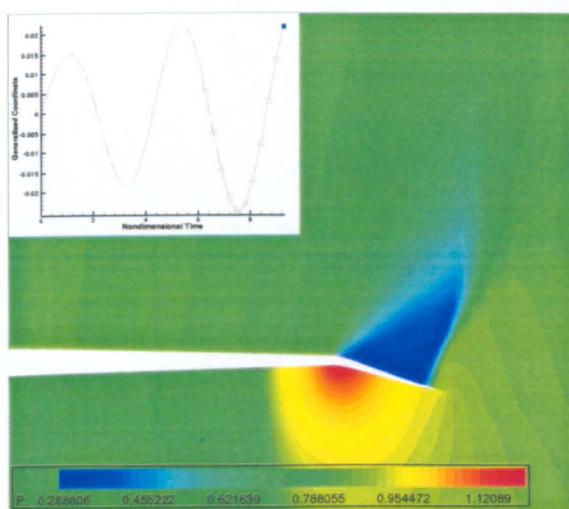
(b)



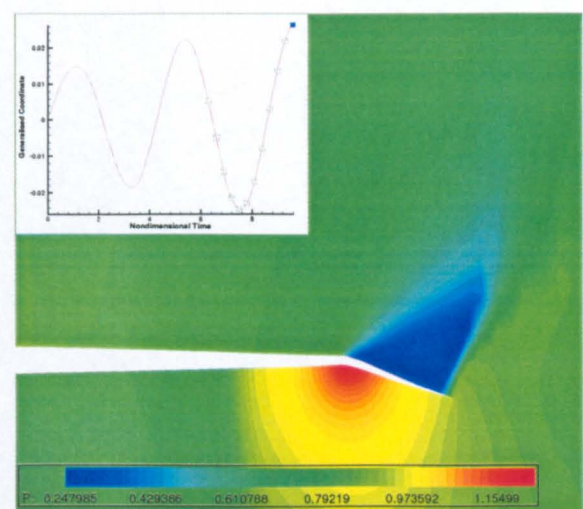
(c)



(d)

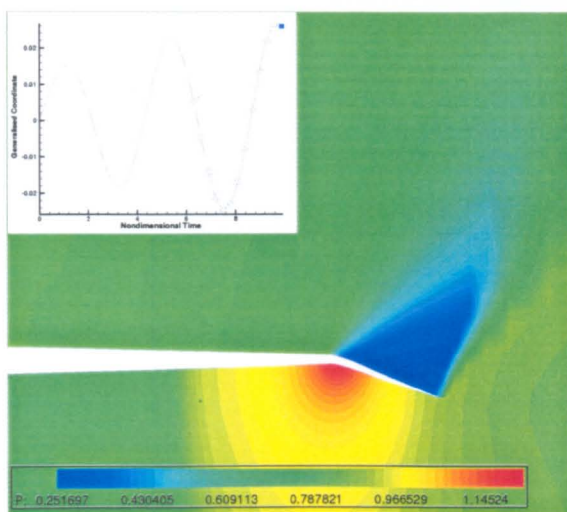


(e)

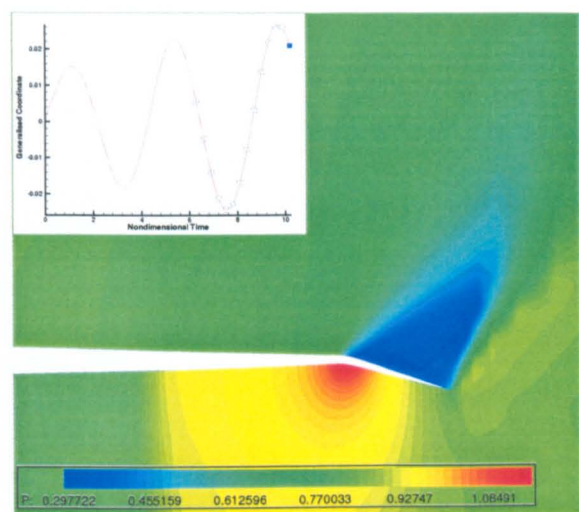


(f)

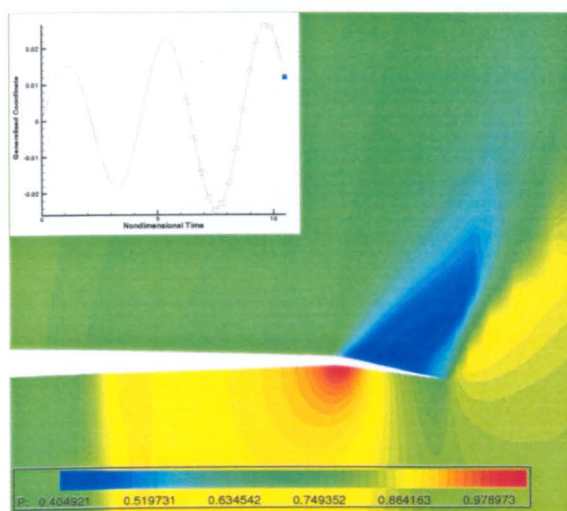
Figure 5.8: Unsteady pressure contours during a single buzz cycle (P.T.O.)



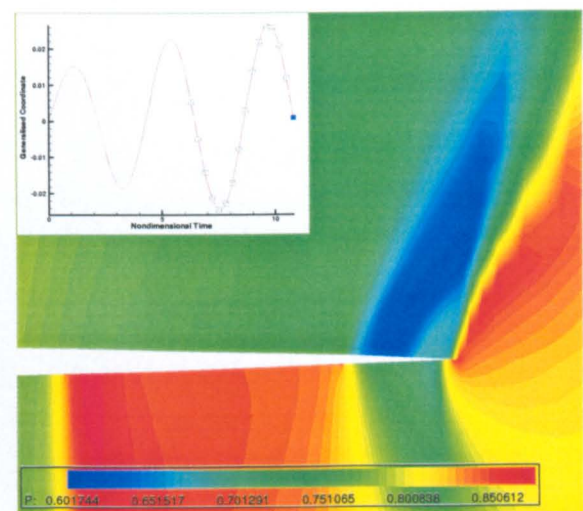
(a)



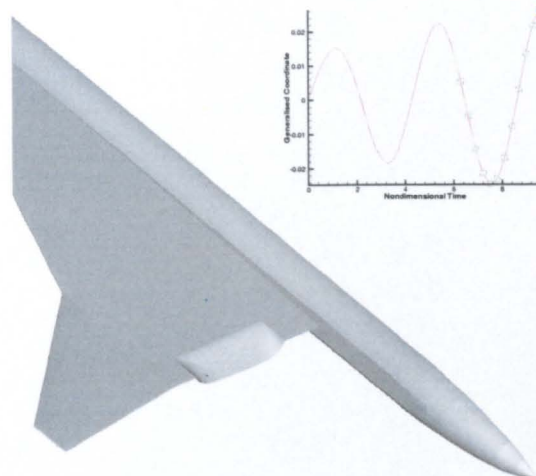
(b)



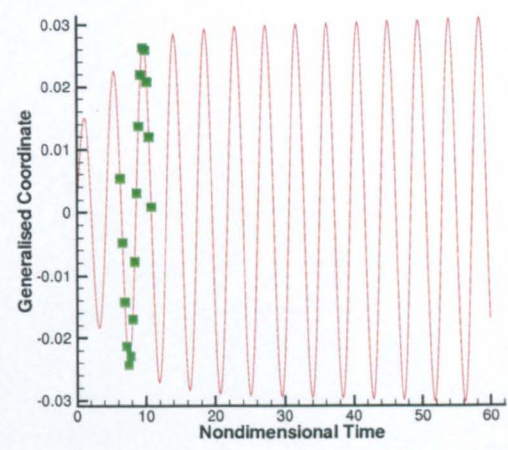
(c)



(d)



(e)



(f)

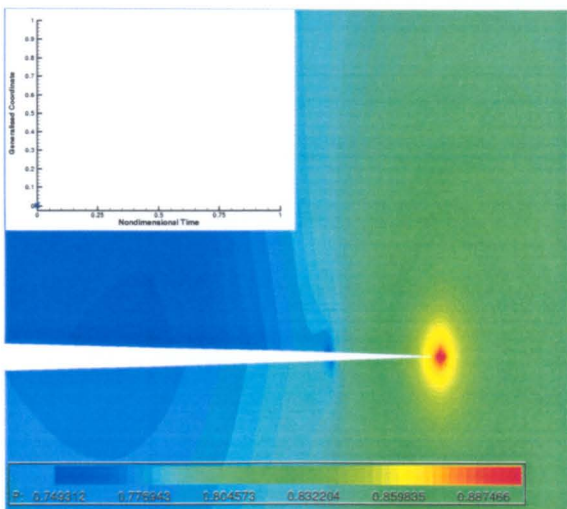
Figure 5.9: Unsteady pressure contours during a single buzz cycle (concluded).

lag between the force on the flap and the flap motion which grows initially. The phase lag in aerodynamic force on the flap in the Euler case is due to the alternate strengthening and weakening of the shock on the flap end is self sustaining provided the initial perturbation results in a large enough phase difference. In contrast Figure 5.14 shows the same case but with a smaller initial perturbation. The shock driven phase difference between the force and the flap motion here is not large enough for the buzz to occur and keeps getting smaller until the the flap and the force are in-phase and the oscillations die down. Figure 5.15 shows the plot the force against flap motion plots while using the RANS equations at Mach 0.95 when given a large initial perturbation. Here too we get a control surface buzz however the amplitude is much lower than from the Euler simulation as the shock predicted by the RANS equations is weaker. Also, as the unsteady force on the flap is a consequence of the shock strength it is almost half of what is predicted by the Euler simulations for the same Mach number and the angle of attack. Figure 5.16 shows the force and flap motion plot at Mach 0.95 using RANS equations but with a smaller initial perturbation. Here to we see a buzz developing though not as rapidly as the similar case using Euler equations.

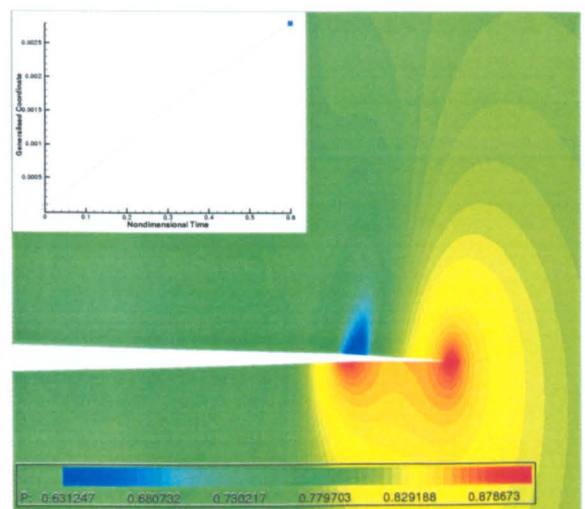
5.2.4 Dependence of buzz amplitude and frequency on Reynolds numbers

It was shown experimentally [88] that for lower values of reduced frequency the LCO amplitude was sensitive to the Reynolds number. Figure 5.17 shows the time traces of the flap amplitude for constant reduced frequencies and dynamic pressure at two different values of Reynolds number. Both the cases in Figure 5.17(a) and Figure 5.17(b) have the same dynamic pressure but different reduced frequencies which is achieved by adjusting the freestream density. For both cases the amplitude and the buzz frequency increase slightly with an increase in the Reynolds number. Although it was shown [88] that the sensitivity to Reynolds number changes was only at low values of reduced frequency, it was observed in the current work that amplitudes were sensitive to the Reynolds number even for higher values of reduced frequency. In the previous work viscous effects are more pronounced on account of the thicker aerofoil profile and bigger flap to wing chord ratio.

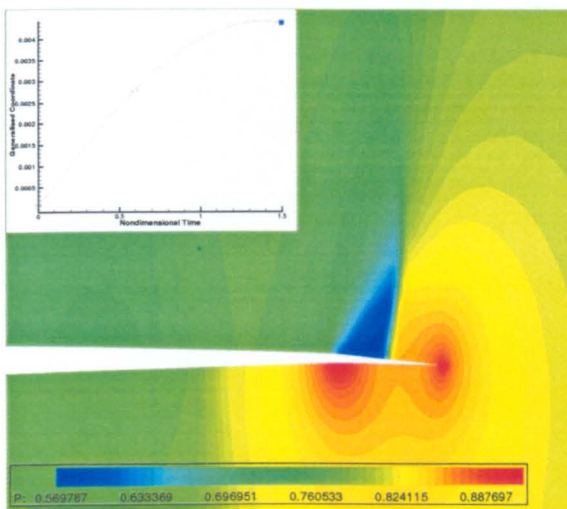
In the current case the flow, at a Reynolds number of 21.42 million, is attached along the entire chord of the wing except at larger flap deflection angles when a separation bubble forms at the flap trailing edge. Figure 5.18 shows the instantaneous pressure contours when the flap is at 0° for two cases with Reynolds number of 3 and 21 million respectively. In both the plots the flap has finished two cycles but the shock location for the case with Reynolds number of 21 million is much aft than the case with the Reynolds number of 3 million. This is because the separation bubble, the size of which decreases with increasing Reynolds number, pushes the shock towards the leading edge. This decreases the moment across the flap hinge and hence reduces the buzz amplitude. Figure 5.19 shows the flow streamlines at Mach 0.987 for the two cases.. The instantaneous flap angle is 10.83° for both cases but the snapshots are taken at different time levels as the frequency and amplitude of the buzz oscillations change with the Reynolds number. A separation bubble can be seen for the case at Reynolds number of 3 million and is absent for the case with Reynolds number of 21 million. The separation is shock induced and plays a part in influencing the buzz characteristics.



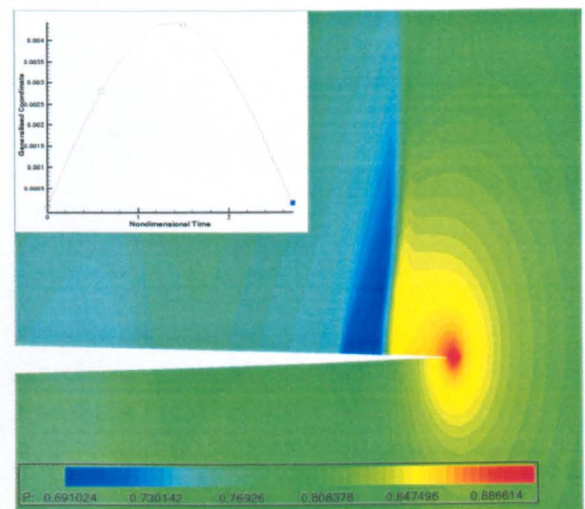
(a)



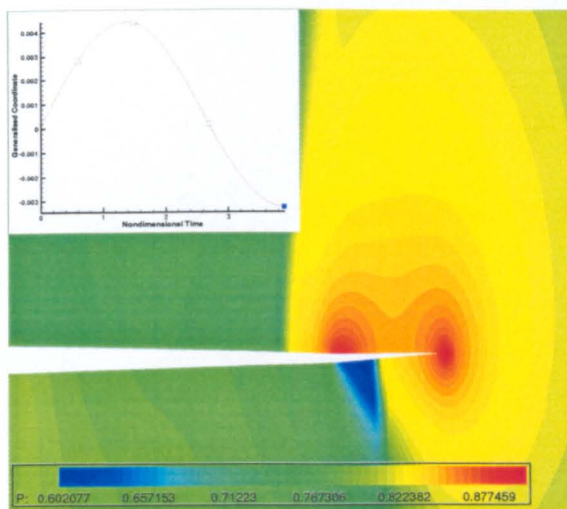
(b)



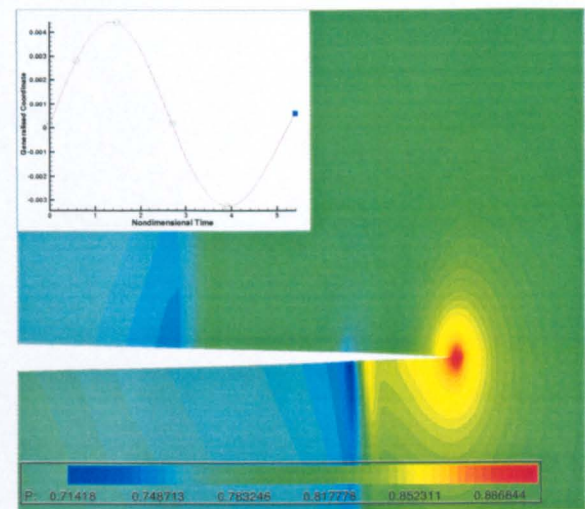
(c)



(d)

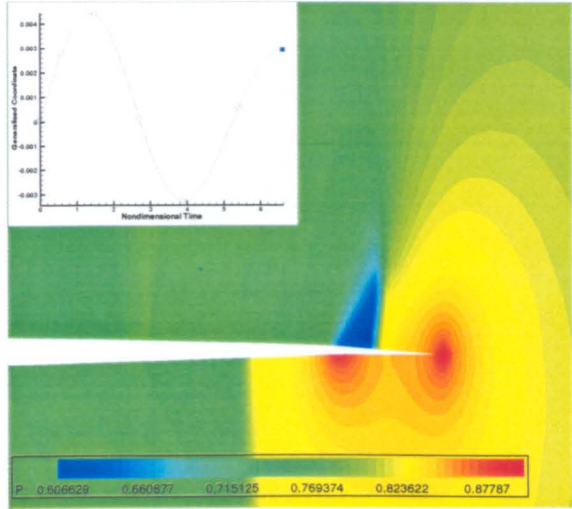


(e)

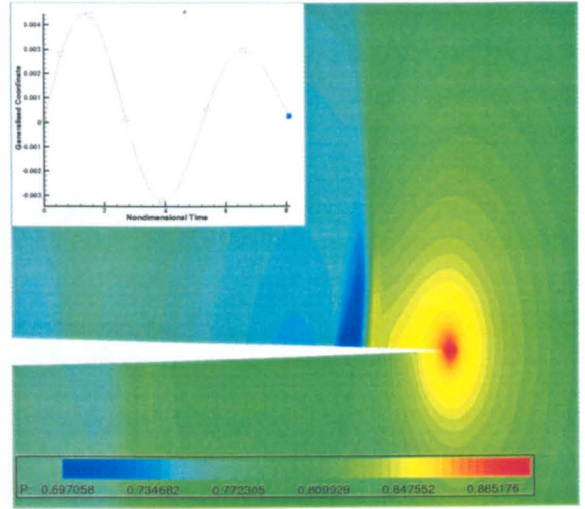


(f)

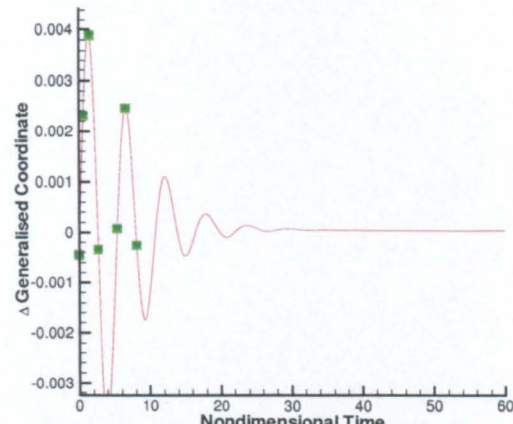
Figure 5.10: Unsteady pressure contours of a decaying buzz cycle (P.T.O)



(a)

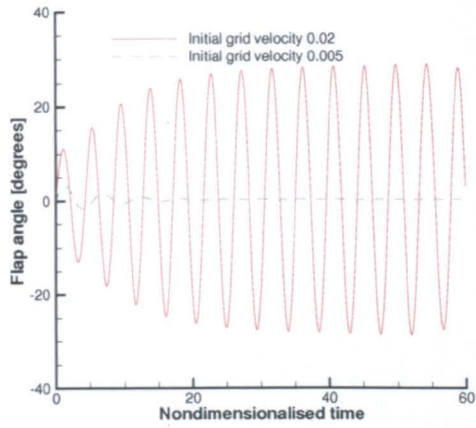


(b)

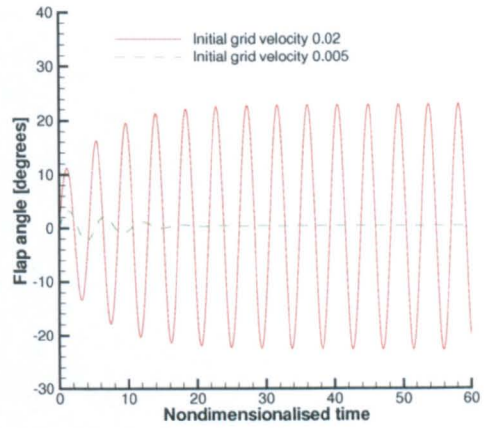


(c)

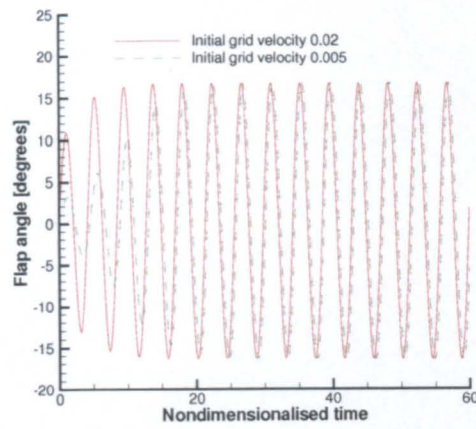
Figure 5.11: Unsteady pressure contours of a decaying buzz cycle (concluded).



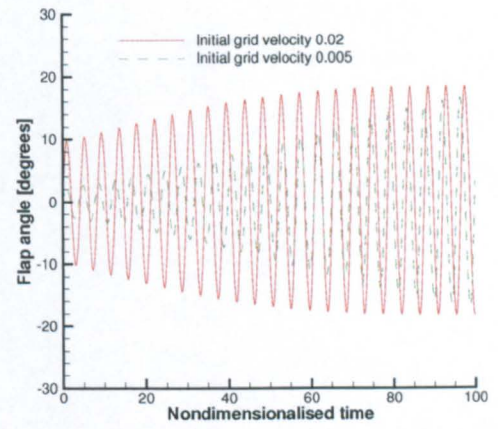
(a) Euler calculation, Mach 0.93, dynamic pressure 21.8 kPa



(b) Euler calculation, Mach 0.95, dynamic pressure 26.4 kPa

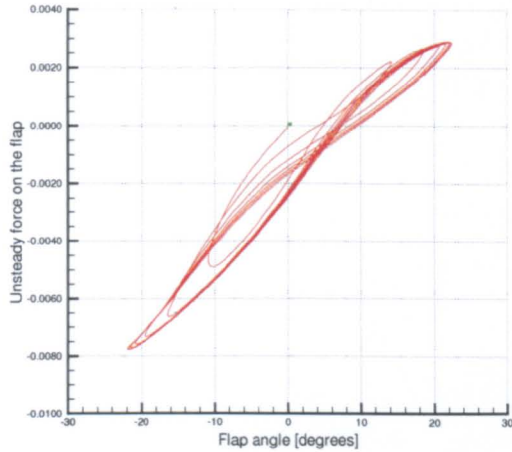


(c) Euler calculation, Mach 0.98, dynamic pressure 26.4 kPa

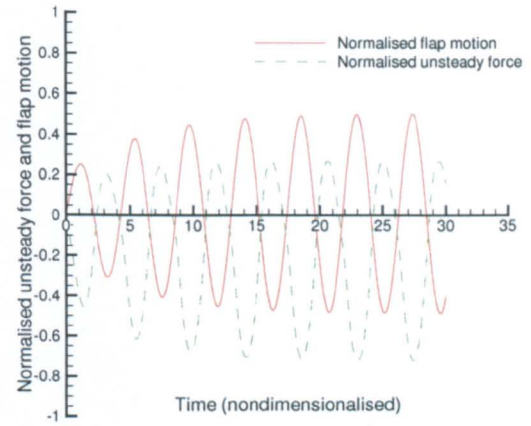


(d) Euler calculation, Mach 1.1, dynamic pressure 26.4 kPa

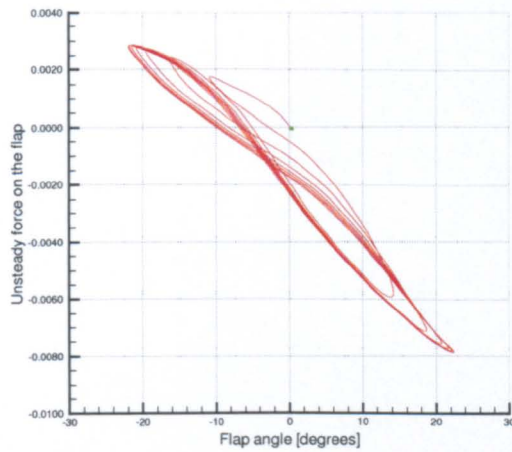
Figure 5.12: Dependence of buzz on initial impulse at Mach numbers 0.9 - 0.95



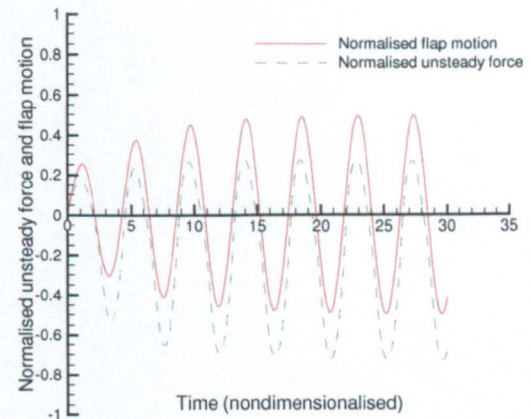
(a) Flap upper surface



(b) Flap lower surface

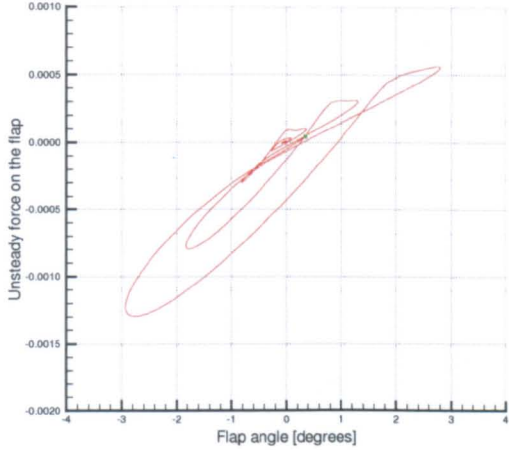


(c) Flap upper surface

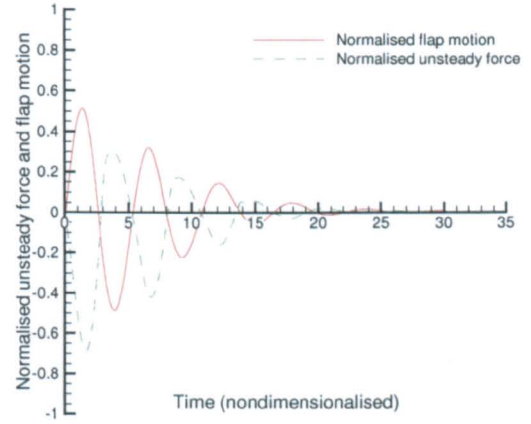


(d) Flap lower surface

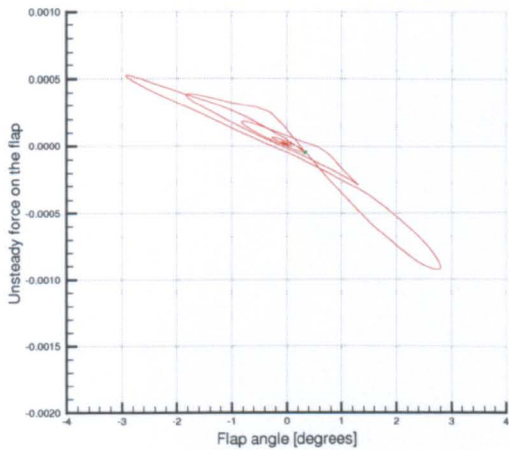
Figure 5.13: The unsteady force and flap motion when given large initial perturbation. Unsteady force values are taken on the flap upper and lower surfaces. Euler simulation at Mach 0.95 and dynamic pressure 26.4 kPa.



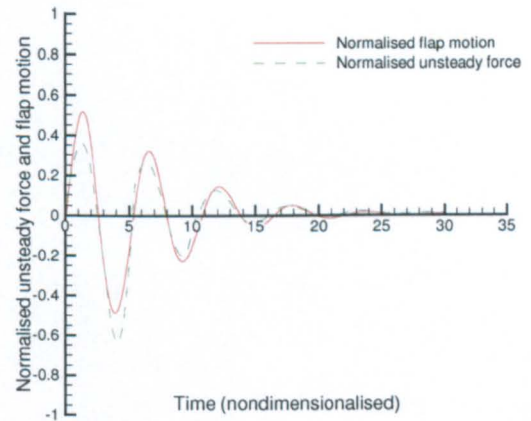
(a) Flap upper surface



(b) Flap upper surface

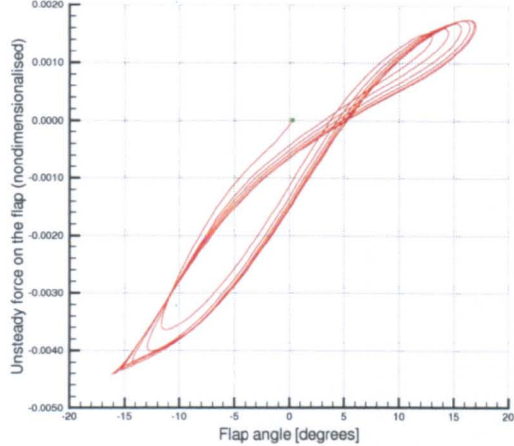


(c) Flap lower surface

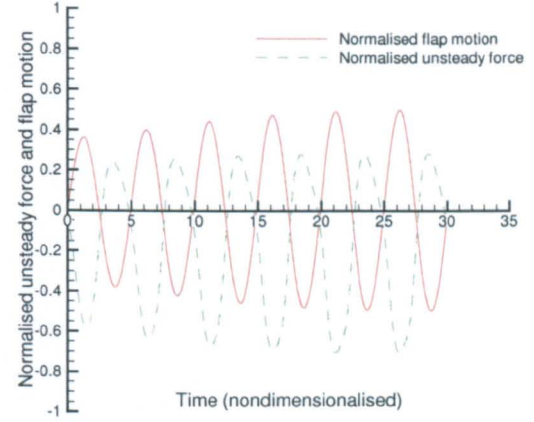


(d) Flap lower surface

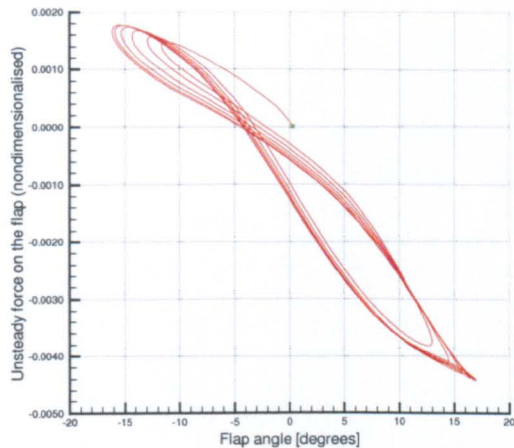
Figure 5.14: The unsteady force and flap motion when given small initial perturbation. Unsteady force values are taken on the flap upper and lower surfaces. Euler simulation at Mach 0.95 and dynamic pressure 26.4 kPa.



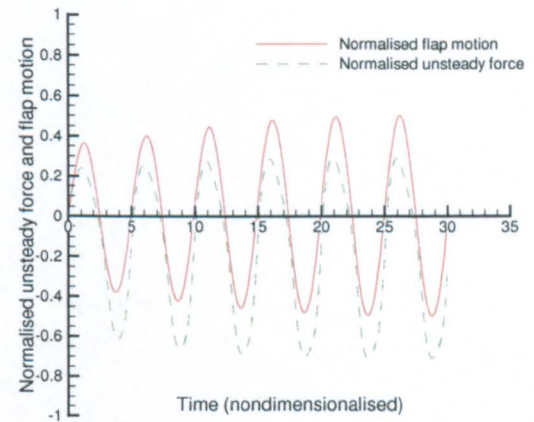
(a) Flap upper surface



(b) Flap upper surface

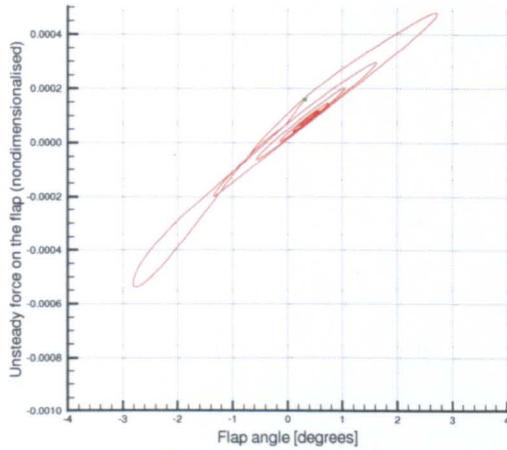


(c) Flap lower surface

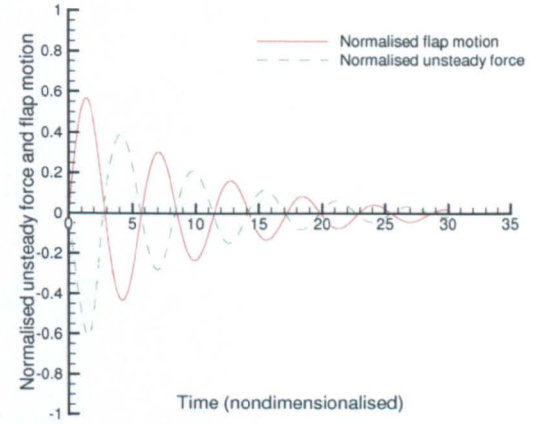


(d) Flap lower surface

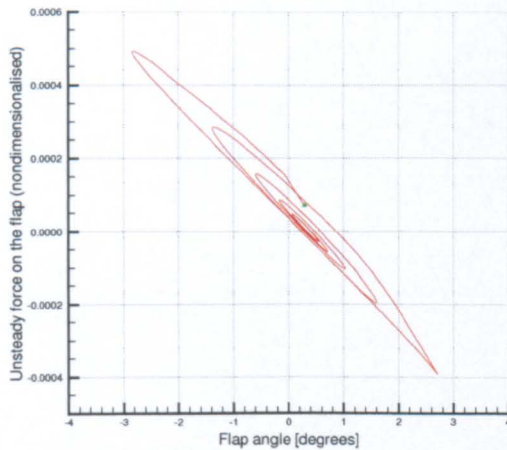
Figure 5.15: The unsteady force and flap motion when given large initial perturbation. Unsteady force values are taken on the flap upper and lower surfaces. RANS simulation at Mach 0.95 and dynamic pressure 26.4 kPa.



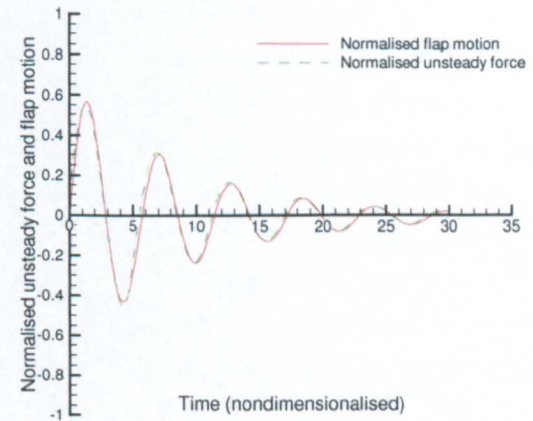
(a) Flap upper surface



(b) Flap upper surface

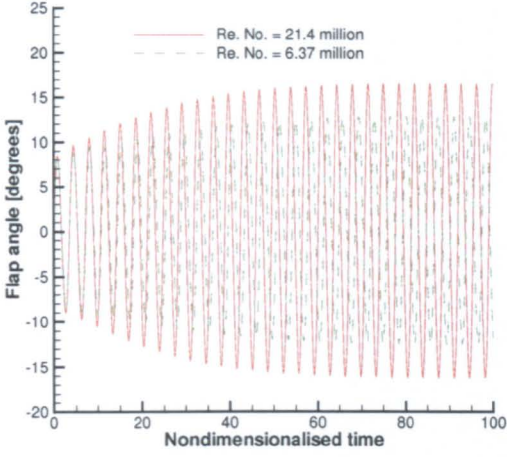


(c) Flap lower surface

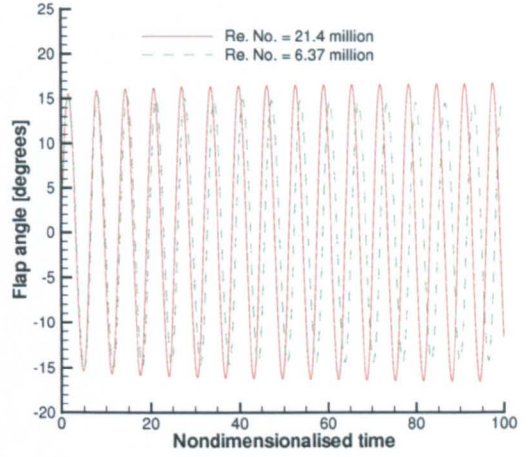


(d) Flap lower surface

Figure 5.16: The unsteady force and flap motion when given small initial perturbation. Unsteady force values are taken on the flap upper and lower surfaces. RANS simulation at Mach 0.95 and dynamic pressure 26.4 kPa.



(a) RANS calculation, Mach 0.987, $k = 1.427$ and dynamic pressure = 7.875 kPa



(b) RANS calculation, Mach 0.987, $k = 0.778$ and dynamic pressure = 7.875 kPa

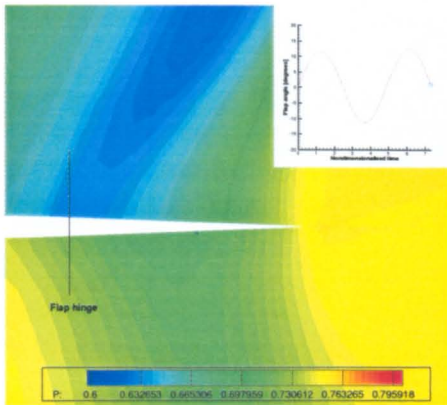
Figure 5.17: Dependence of buzz amplitude and frequency on the Reynolds number

5.2.5 Dependence of buzz amplitude on structural damping

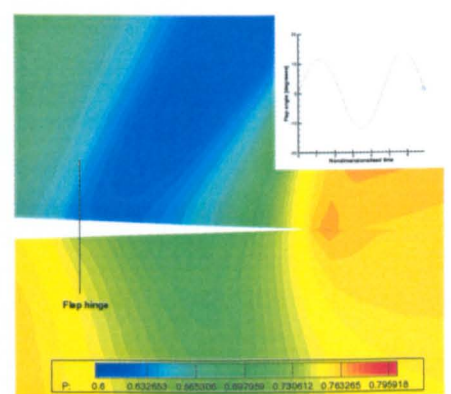
Control surfaces can have mechanical dampers to restrict oscillations and reduce the structural response. The effect of damping on buzz is measured here by varying the damping values at Mach 0.98 for Euler and 0.987 for RANS simulations. Percentage damping is the value of the damping constant C in Equation 2.51 multiplied by 100. The damping term in Equation 2.51 produces an opposing force linearly proportional to the speed of the control surface motion. Figure 5.20 shows the buzz amplitude against percentage structural damping for the Euler case at Mach 0.98 and incidence of 0.6° . The amplitude steadily decreases until it dies suddenly at a structural damping of 24%. The amplitude of oscillation at 23% damping is 5.977° . In contrast to Euler simulations the buzz amplitude is much more sensitive to damping in viscous simulations. Figure 5.20(b) shows the amplitude against damping for the viscous case at Mach 0.987. The slope of amplitude versus damping is much more steeper and 13% damping is enough to kill buzz completely.

5.2.6 Linear and CFD based flutter results for Model1 and Model2

The aeroelastic effect of the oscillating flap when attached to the wing trailing edge is computed in this section. Linear calculations are performed using **NASTRAN**. The wing and the flap are included in the analysis with a total of 486 aerodynamic panels to calculate the aerodynamics. The Doublet Lattice Method is used in the subsonic flows and ZONA51 for supersonic flows. The first 5 natural modes including the flap mode of vibration are used in the aeroelastic analysis of Model 1 (See Section 5.1.2) whereas the first 4 natural modes are used for the aeroelastic analysis of Model 2. Figure 5.21 shows the flutter boundary of the two models calculated by

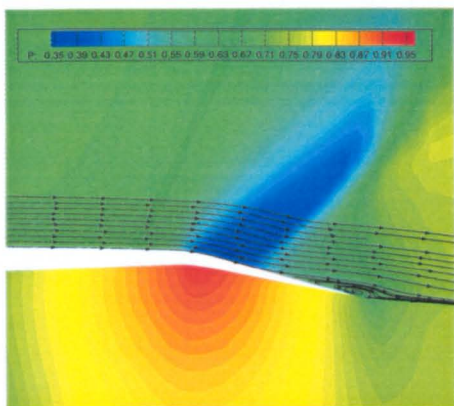


(a) Reynolds number 3 million

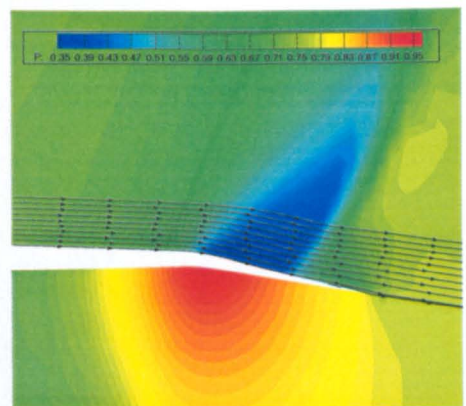


(b) Reynolds number 21 million

Figure 5.18: Shock locations for cases at Mach 0.987, RANS simulation.

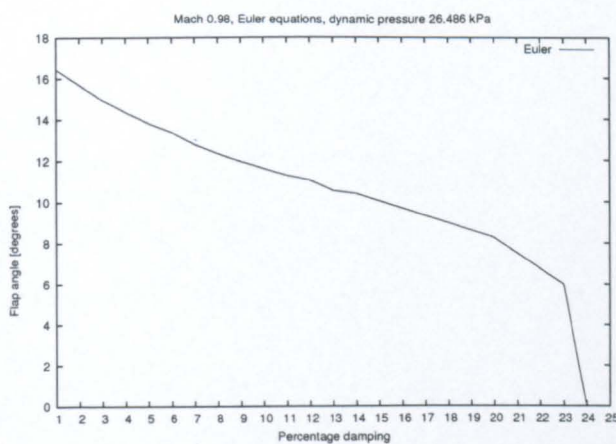


(a) Reynolds number 3 million

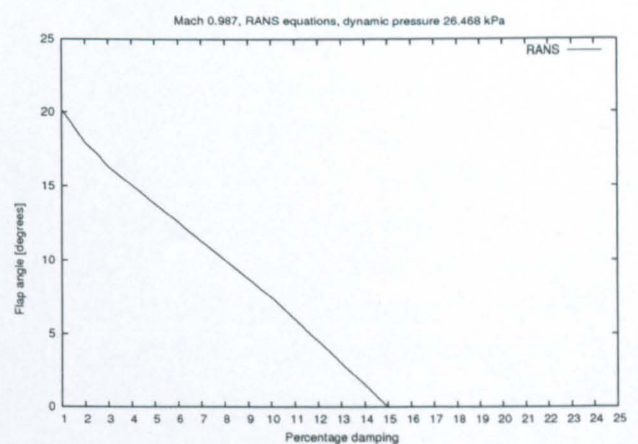


(b) Reynolds number 21 million

Figure 5.19: Separation on the flap along a buzz cycle. Instantaneous flap angle of 10.83° , RANS simulation.



(a)



(b)

Figure 5.20: Effect of damping on buzz amplitude

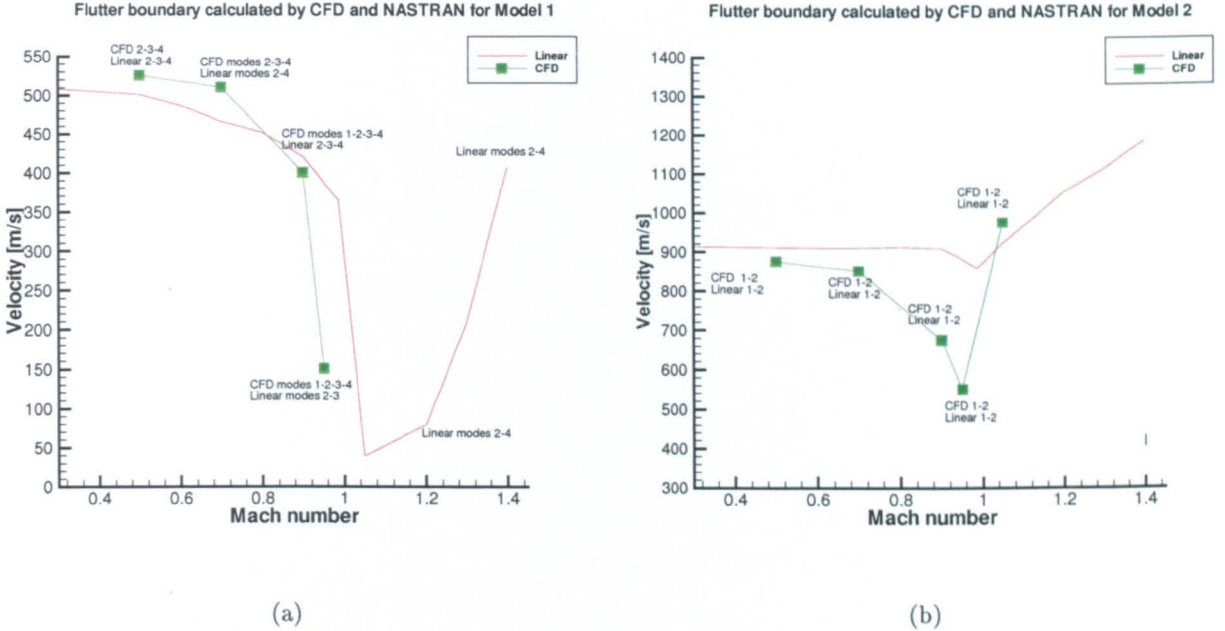


Figure 5.21: Flutter boundary along with the interacting modes calculated by NASTRAN and PMB

linear methods and CFD.

The flutter velocity calculated by NASTRAN for Model 1 has a big dip at Mach 1.05 and then increases. As the linear models are not able to predict shocks, this dip remains unexplained. The behaviour of Nastran at Mach 1.05 in predicting the flutter velocity is very similar to what was observed in Chapter 3 with the Hawk model. This re-enforces the conclusion that linear based aeroelastics tools are unable to predict flutter between Mach numbers 1.0 and 1.1 for cases with trailing edge control surface. One possibility is that linearised supersonic theories give negative damping for an aerofoil pitching along its leading edge at low supersonic Mach numbers. In the current case the flap is oscillating along its leading edge (the hinge line) and this might be the reason for the spurious flutter velocities of the wing between Mach numbers 1.05 and 1.4. The flutter velocities calculated by CFD on a coarse grid and using the Euler equations match the linear results in the low subsonic regions. There is a dip at Mach 0.9 due to the shock formation over the wing which is not predicted by NASTRAN. After Mach 0.95 the shock moves over the control surface and the oscillations due to buzz dominate the aeroelastic response. As buzz is shock driven the oscillations persist at even very low velocities (as low as 100 m/s). It was shown in Section 5.2.3 that the onset of buzz is sensitive to the initial impulse given to the flap. It was also shown that for the current case the buzz does not occur when the initial impulse is small at Mach 0.95. Hence it is possible to couple the wing bending and wing torsion mode by giving a small impulse to the wing bending mode at Mach 0.95 without exciting the flap mode. This is the reason a flutter velocity could be extracted at Mach 0.95 but not at higher Mach numbers where there is onset of buzz at a small impulse to the flap mode.

To understand the dominance of shock effects at the upper transonic flow, Figure 5.22 shows the modal response of the 5 modes of Model 1 at the Mach 0.95 and dynamic pressure of 5.4 kPa. The freestream velocity is 125 m/s which is below the critical flutter velocity. When the initial impulse is given to the first wing bending mode the oscillations are damped. However when the impulse is given to the flap mode the wing starts to undergo a limit cycle oscillation involving all the modes. Figure 5.22(f) shows the modal response of all the modes at Mach 1.05. Here the wing undergoes limit cycle oscillation of all the modes even though the initial impulse was given to the first wing bending mode.

The flutter velocities calculated for Model 2 where the flap is held rigid shows a normal wing behaviour in both **NASTRAN** and CFD simulations. **NASTRAN** is unable to predict the transonic dip which is captured by CFD. Also the big dip in the flutter velocity predicted by **NASTRAN** when the flap is allowed to move in Model 1 is absent. A reasonable match between the CFD and linear results is obtained at subsonic and supersonic Mach numbers. As compared to Model 1 the flutter velocities are much higher which underscores the significance of the aeroelastic effects of control surfaces on the wing structure.

5.3 Limitation of Linear Aerodynamics

The linearised aerodynamics used in **NASTRAN** is based on potential flow theory which assumes the flow to be inviscid and incompressible and for unsteady flow it is assumed to be gusting harmonically. This means it is unable to predict shock which is the main driver for buzz and buzz induced flutter instability as we saw in the preceding sections. **NASTRAN** uses the Doublet Lattice Method (DLM) in the subsonic and the ZONA51 in the supersonic flows and brief theoretical formulations can be obtained in the **NASTRAN** User's Guide [92] and also the **ZERO** Theoretical Manual [93]. Due to their inability to predict shocks the DLM based aeroelastic analysis tends to over predict the flutter onset velocity usually between Mach numbers 0.7 and 0.95 depending on the wing profile. For Mach numbers greater than 1 **NASTRAN** uses the ZONA51 which is a method based on the linearised supersonic theory outlined by Jones [94][95]. ZONA51 is basically an improvement of the Potential Gradient Method (PGM) proposed in [95] in the sense that it has reduced demands for the number of panels for higher reduced frequencies and low supersonic Mach numbers (between Mach 1.0 and 1.2) which were required in the PGM. However for the version of ZONA51 used in **NASTRAN** there still is a discrepancy at low supersonic Mach numbers. The reason behind this is well known for most of the linearised supersonic theories and is due to the term $\sqrt{M^2 - 1}$ used during the calculation of the oscillatory lift. The Jones's supersonic theory calculates the localised lift on each rectangular panel of the wing as

$$\tilde{l}(x, y) dx dy = c^2 \beta \tilde{l}(x', y') dx' dy' \quad (5.1)$$

where the \tilde{l} is the local lift, x, y are the dimensional space coordinates, c is the reference length, and x', y' are the nondimensionalised coordinates. The nondimensional local lift $\tilde{l}(x', y')$ is calculated thus,

$$\tilde{l}(x', y') = 2\pi \left(\frac{\rho U^2}{\beta} \right) \left[\frac{\delta \Phi}{\delta x'} - i \frac{k}{\beta} \Phi \right] e^{-ik' M x'} \quad (5.2)$$

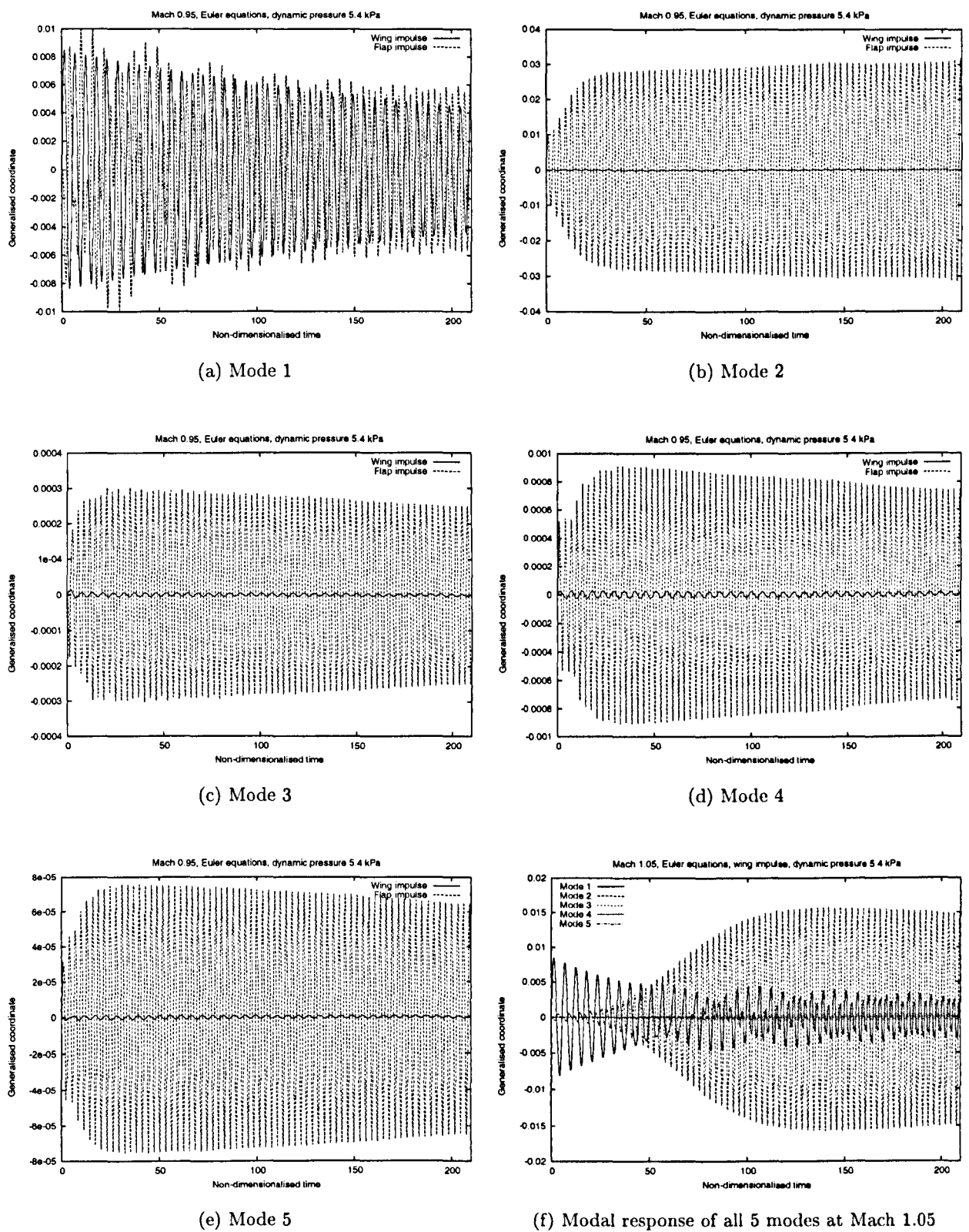


Figure 5.22: Domination of shock induced aeroelastic response at higher transonic Mach numbers

where the ρ is the air density, U is the free stream velocity, β is $\sqrt{M^2 - 1}$, Φ is the modified potential difference above and below the aerodynamic panel and is given by $\Phi \equiv \frac{\Phi_{\text{above}} - \Phi_{\text{below}}}{2\pi}$, k is the reduced frequency given by $\frac{k=2\pi f c}{U}$ where f is the frequency of the mode, k' is the modified reduced frequency and is defined as $k' = \frac{kM}{\beta}$ and finally M is the Mach number. In equation 5.2 it can be seen that as the Mach number approaches 1 the term $\frac{1}{\beta}$ approaches infinity rendering the lift calculation invalid. Physically it has the effect of increasing the value of the reduced frequency and since the number of panels used to resolve the flow is proportional to the reduced frequency theoretically a very large number of panels are required for flow analysis at Mach numbers approaching 1 to get meaningful results. Further developments of ZONA51 have been made with reformulation of calculation of the unsteady lift that has solved this limitation at low supersonic Mach numbers [45] and is implemented in the ZAERO package [93]. However these developments are not incorporated in the original ZONA51 methodology used in NASTRAN which is the linear tool used in the current work. It should also be noted that that the inclusion of the control surface rotation mode is the source of instability at the low supersonic Mach numbers and it this might be due to the negative damping observed in supersonic linear analysis for aerofoils undergoing pitch oscillations about its leading edge [3]. An exact explanation of this phenomenon in NASTRAN requires details of ZONA51 which is unavailable in literature.

5.4 Conclusions

A method for simulation of 3D buzz was demonstrated. Apart from the prediction of the instability boundary, buzz parameters like amplitude, frequency and effect of damping were also measured using the Euler and RANS equations. Buzz simulations using the Euler equations were performed on blended flaps and flaps with free edges and the flap response was found to be similar. A strong dependence of the buzz onset on the initial impulse was observed. From inviscid simulations it was concluded that although they can predict the onset of buzz, they cannot accurately predict the buzz parameters like amplitude and frequency. Flow separation over the oscillating flap has an influence on these parameters and hence viscosity effects need to be modelled. Consistent with experimental observations the amplitude of LCO predicted by the RANS equations was found to be sensitive to the Reynolds number and the reduced frequency of the flap.

The effect of control surface on the flutter of the wing was investigated and it was found to reduce the flutter velocity significantly even at subsonic flows as compared to a wing without a control surface. In transonic and supersonic flows the shock induced oscillations of the flap dominate the aeroelastic response of the wing dictating the frequency of oscillations. Along with the linear flutter results on the SST from it is concluded that linear methods are unable to predict flutter between Mach numbers 1.0 and 1.1 for cases with trailing edge control surface. Though it is shown here that CFD based time marching analysis is able to predict the instabilities due to aerodynamic nonlinearities it remains computationally expensive. Reduced Order Model (ROM) techniques like Proper Orthogonal Decomposition (POD), Volterra theory and Hopf Bifurcation method for unsteady aerodynamics maintain the fidelity of the modelled aerodynamics at the same time lower the computational degrees of freedom present in the numerical model [96]. These have been used to determine the flutter boundaries of wings and aerofoils in transonic

flow [97, 96] with computational times two orders of magnitude lesser than that of time marching analysis [97].

The present work has looked into time marching simulation of a thin section wing where the flow is more or less attached at all Mach numbers and at low incidence angles. Future work can include geometries with thicker sections where the flow is detached when it reaches the flap hinge line.

Chapter 6

The Hawk Aircraft¹

6.1 Overview

It is noted here that due to the proprietary nature of the work the scales on all plots and figures in Chapter 6 have been blanked. However there is no validation against experiments performed in this chapter with most of the plots being qualitative in nature. The comparison of the flutter boundaries in Chapter 6 using linear and CFD methods serve to establish the qualitative differences in the behaviour of the instability boundary at transonic Mach numbers.

An aeroelastic analysis of the Hawk aircraft is carried out on configurations with increasing geometric complexity. This enables an understanding to be built up of the issues related to time marching analysis of realistic configurations, and to assess the influence of the various simplifications. Flutter boundaries based on linear methods are calculated for each case and compared with the CFD based analysis. It is noted here that due to the proprietary nature of the work the scales on all plots and figures in the current chapter have been blanked. However there is no validation against experiments performed in this chapter with most of the plots being qualitative in nature. In the subsonic region the comparison acts as a validation for the CFD as linear methods have proven robust in this region. However, at transonic and lower supersonic freestream Mach numbers the comparison highlights the limitations of the linear methods due to an inability to predict shocks. Moreover at freestream Mach numbers between 1 and 1.2 the linear methods have difficulty in representing trailing edge control surfaces. This is made evident in comparison with the CFD based results.

One of the most interesting aspects of the current work is the investigation of the Hawk fin-rudder configuration. Its relevance is accentuated by the fact that transonic buzz responses of the rudder have been reported in the literature in flight tests on the T45 Goshawk trainer aircraft in the U.S [90]. However detailed unsteady calculations have never been reported and recommendations for such a study have been made [98, 90]. This behaviour is easily resolved through the use of shock strips [90], but presents a good confidence building test case for the CFD capability

The structural models used have been obtained from the original models developed by BAE SYSTEMS for flutter clearance, with minor modification in the form of boundary conditions applied to the aircraft components. These applied boundary conditions alter the modal behaviour

¹This chapter is reproduced with the kind permission of BAE SYSTEMS plc 2006. This contains information which is proprietary to BAE SYSTEMS.

marginally. The original structural model of BAE SYSTEMS used for linear aeroelastic analysis is a half model. Section 6.4.2 describes the preprocessing of the antisymmetric modes from this half model before they can be used for CFD based simulations.

To lay foundations for the analysis of more complex configurations, a detailed study of the Hawk wing is reported first in Section 6.2. This includes grid and time refinement studies along with a comparison with linear results. The results from this study have been reported in [67] and naturally lead on to cases with a trailing edge control surface. Section 6.3 brings in a trailing edge flap and assesses its effect on the flutter velocity. The flap is a combat configuration with a deflection angle of 12.5° . This configuration is of interest because there is no simple procedure for including static angles of flap deflection in *Nastran* Aeroelastic Analysis (the “linear” method used) where the flap angle is always assumed to be 0° . Section 6.4 introduces the fin-rudder configurations for the investigation of rudder buzz. There are three configurations studied here, the Body-Fin-Rudder (B-F-R), Body-Fin-Rudder-Tail (B-F-R-T) and Body-Fin-Wing-Rudder-Tail (B-F-W-R-T). The steady pressure distribution on the fin-rudder at five span-wise locations has been compared with calculated values obtained at BAE SYSTEMS for a geometry including a detailed aircraft geometry including the Radar Warning Receiver (RWR). The receiver, due to its size and location, might have an influence in suppressing the shock induced instability. Finally some conclusions are drawn in Section 6.5

6.2 The Hawk Wing

This section describes the analysis of the Hawk wing [67]. To place the overall study of the Hawk on a firm basis, an evaluation of the CFD results for this is required. In the absence of experimental data the best check is to match up the CFD results with linear predictions in the subsonic range. A detailed grid and time step study has been done. These results for the Hawk wing only lay the basis for the studies of more complex configurations later in the chapter. For the clean wing it is established from the linear results that the flutter mechanism is a wing bending-torsion interaction.

6.2.1 CFD Setup

A series of grids which have an O-O topology was generated. The footprint of the blocks on the surface geometry is shown in Figure 6.1 along with the surface grid itself. The block topology leads to a large number of points on the wing surface. It will be shown below that grid independent solutions are obtained on this family of grids. It is noted that this sort of topology around the trailing edge is not good at preserving wakes, but the current calculations are inviscid so this is of no concern. For the wing only grid, there are 845,000 points on the fine level, with 11,565 points on the wing surface. The medium and coarse levels have 114,000 and 16,600 points in the volume grid and 2919 and 744 points on the wing surface respectively.

The concentration of points in the wing tip region allows a grid converged solution to be obtained. Flutter speed predictions on the different grid levels are shown in Section 6.2.3. All the calculations were run on a cluster of 2.5 GHz PC’s running under Linux and connected by 100 Mbit Fast Ethernet. For the wing only case driving the residual down 6 orders for a steady

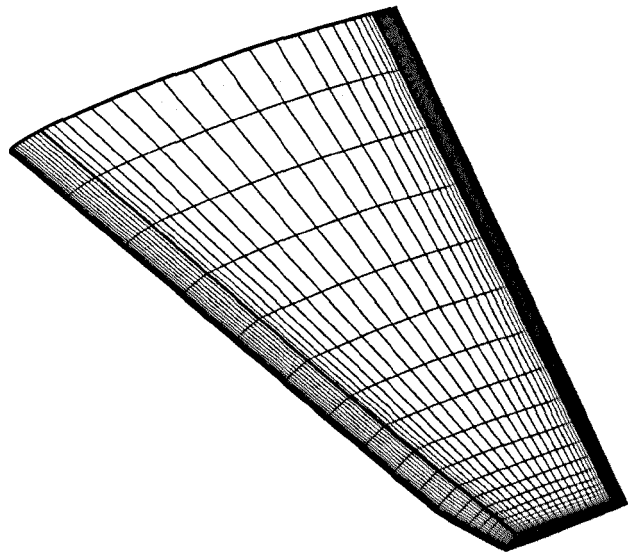


Figure 6.1: Surface topology and grid for the Hawk wing only configuration.

calculation, the times were 44 seconds, 35 minutes and 60 minutes on 1, 1 and 8 processors for the coarse, medium and fine levels respectively.

6.2.2 The Structural Model

The structural model used was supplied by BAE SYSTEMS. This is version 6 of the model used in the company's flutter clearance procedure and was constructed in **Nastran**. Extra interpolation nodes were added to the wing to aide the transformation in the CFD calculations. Figure 6.2 shows the original model. The various components of the aircraft are modelled as one dimensional beams (CBAR entries in **Nastran**). For example the wing is modelled by a one dimensional beam representing the wing flexural axis. The elemental nodes of this beam have lumped masses (CONM2 entries in **Nastran**) representing the real aircraft mass and inertia distribution. Massless rigid bar (RBAR entries in **Nastran**) elements are attached perpendicular to the flexural axis beam and connect to nodes at leading and trailing edges. These nodes serve the purpose of relating the rotation and translation of the flexural axis to the aerodynamic panels. Figure 6.3 shows a close up of the wing flexural axis with the rigid bars which relate the deformation at wing leading and trailing edges. The tailplane, fin and control surfaces are constructed in similar fashion. The fuselage is also a beam model but without the aerodynamic panels. In the present study wing tip missile, stores and wing fuel are not included in the baseline test case.

The transformation proves inaccurate when based on the arrangement of bars in the original model. For this reason a number of intermediate nodes were added between the leading and trailing edges and the flexural axis by way of rigid bars. Also as the control surfaces were not included in the current study, extra nodes were added along the trailing edge to represent the deformation there. It should be noted that these modifications do not change the structural properties of the model and hence the modal response remains identical to the original model.

Figure 6.4 shows the leading and trailing edge rigid bars and the addition of the extra intermediate bars. The components are attached to their respective parent geometry through spring attachments (CELAS2 entries in **Nastran**). This provides some control over the modal frequencies of the individual components. Hence the control surfaces are attached to the wing and the vertical fin through stiff springs, and the wing and fin themselves are attached to the fuselage through springs. Table 6.1 gives the spring stiffness values of different components. The pitching axis of the structural model is the y-axis here. For CFD calculations the z-axis forms the pitching axis and hence the structural model axes are transformed later to conform to CFD requirements. The control surfaces and their masses are included in the structural model but their response is not considered in the aeroelastic calculations. Hence although the presence of control surfaces effects the wing modes, the deformation of the control surfaces themselves is not included in the wing alone analysis. Table 6.2 gives the frequencies and description of the first 10 modes.

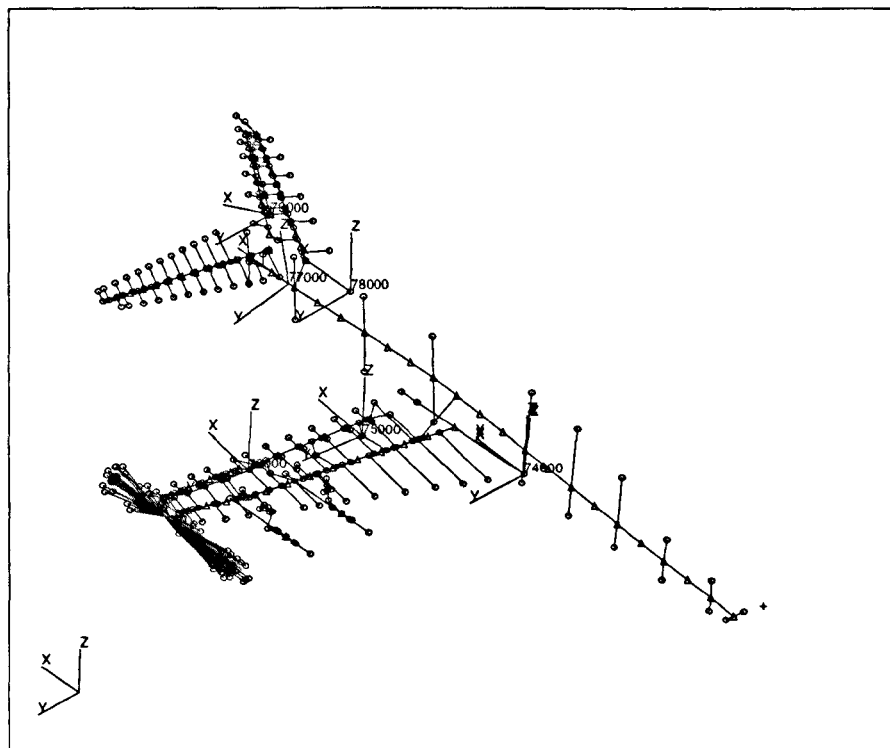


Figure 6.2: Hawk structural model.

6.2.3 Results

A rigid steady state calculation was used to initialise the static aeroelastic calculation, which in fact converged rapidly since a very small deformation was observed. Then, a non zero generalised velocity for the first mode was set and the time marching calculations started. The response for different values of dynamic pressure was obtained and the airspeed at which stability is lost was inferred from the growth or decay of these responses. Structural damping value of 0% was used in the **Nastran** and the CFD calculations. A detailed time step convergence study was carried out and negligible differences between using 50 time steps per flutter cycle and smaller time steps were observed on all grids and at all Mach numbers. Hence, this time step was

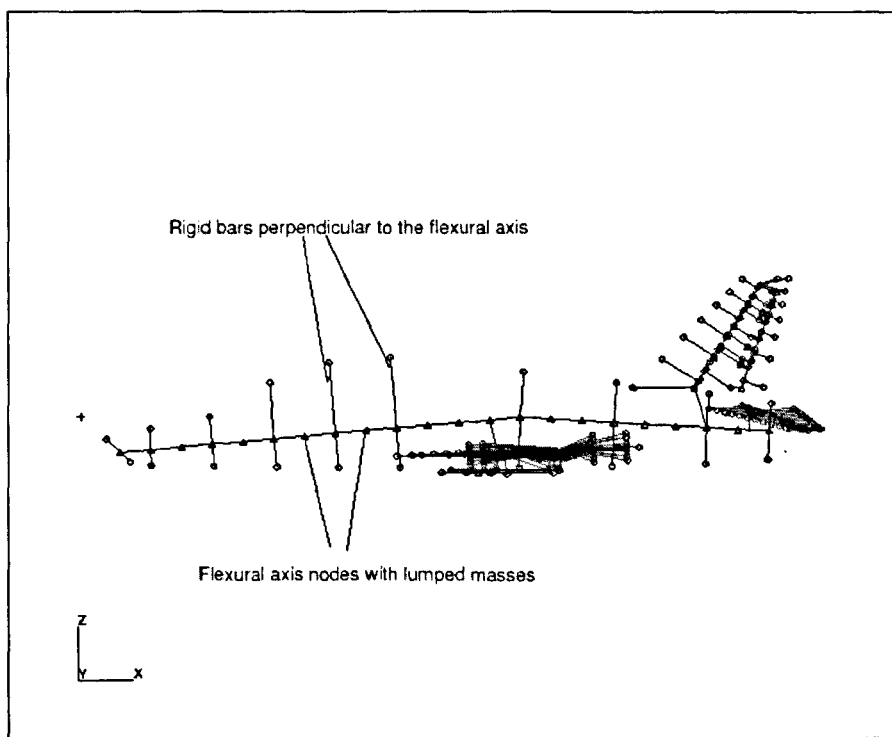
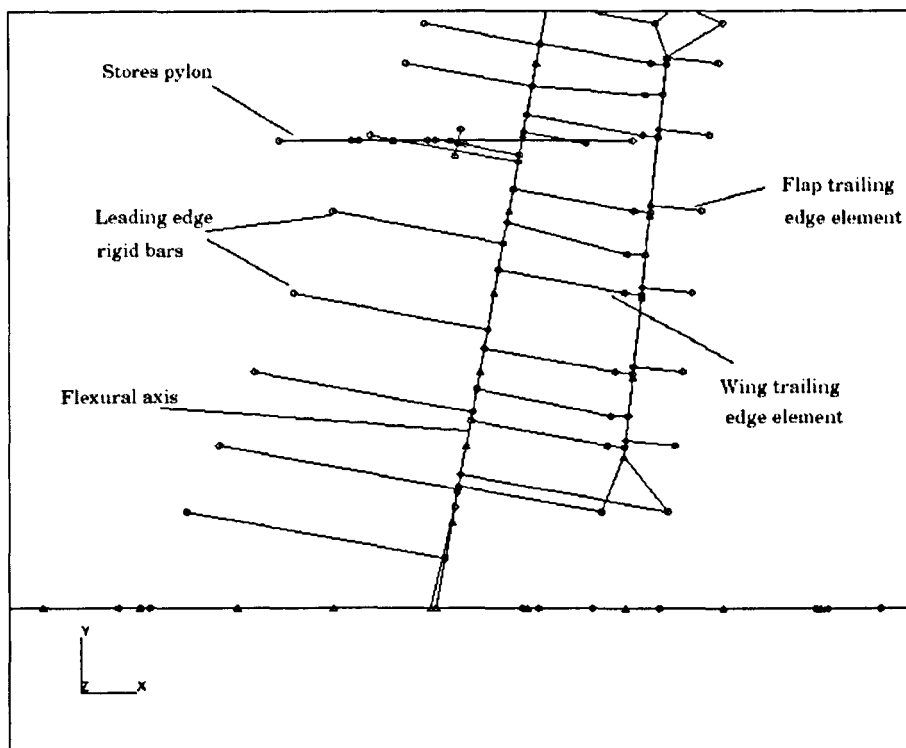


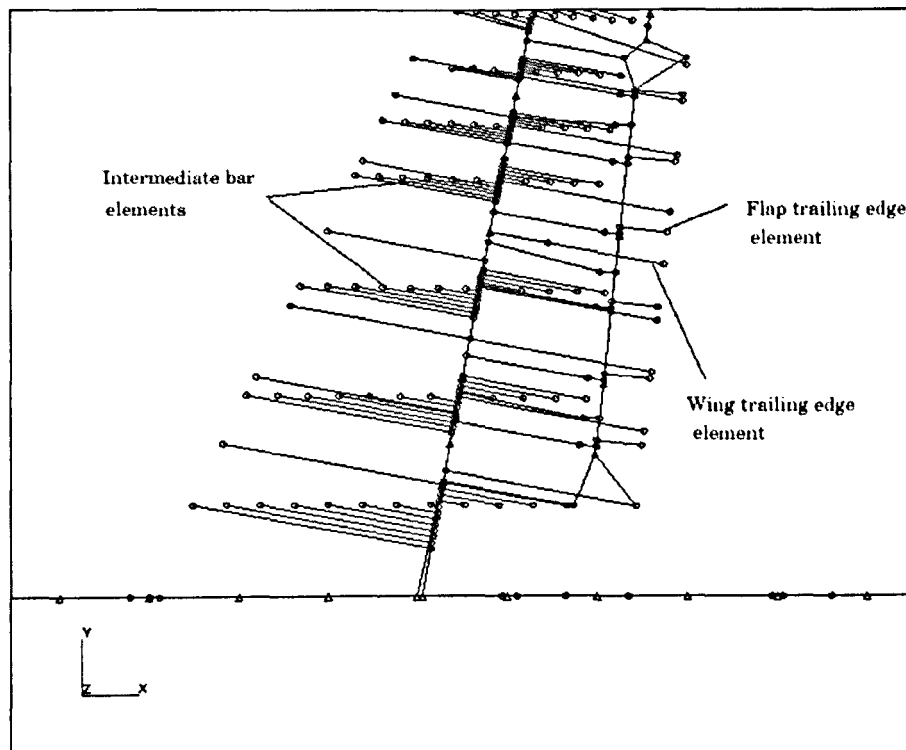
Figure 6.3: Fuselage flexural axis with attached rigid bars

Component	T_x (N/m)	T_y (N/m)	T_z (N/m)	R_x (Nm/rad)	R_y (Nm/rad)	R_z (Nm/rad)	Mass (Kg)
Wing	-	-	6×10^8	5×10^6	5.5×10^8	-	504.321
Tail	-	-	1.1×10^7	2×10^6	6×10^5	2×10^6	45.85
Fin	-	1×10^{12}	-	1×10^{12}	-	1×10^{12}	33.115
Rudder	-	-	-	-	-	1.348×10^3	9.24
Flap	-	-	-	-	131.2×10^3	-	14.58
Aileron	-	-	-	-	24.7×10^3	-	8.16
Fuselage	-	-	-	-	-	-	2017.664

Table 6.1: Values of spring constants and masses of each component



Leading and trailing edge bars on the original Hawk wing model



Leading and trailing edge bars on the modified Hawk wing model

Figure 6.4: Hawk wing finite element model

Frequency [Hz]	Mode description
12.4257	1 st wing bending
14.429	1 st fuselage vertical bending
22.129	1 st tail bending
32.455	2 nd fuselage vertical bending
37.870	1 st wing torsion
44.112	2 nd wing bending
50.552	2 nd tail bending 3 rd fuselage vertical bending
55.840	2 nd wing torsion due to flap rotation mode
60.583	3 rd wing torsion due to aileron rotation mode
64.466	3 rd tail torsion

Table 6.2: Modal frequencies and description for the symmetric model

used. At a given Mach number the flutter point was identified by interpolating between the two closest values of the dynamic pressure where the structural response diverges and damps down respectively. The flutter speed was identified this way at a series of freestream Mach numbers on the wing only grids and the results are compared in Figure 6.5 with the linear results for the full configuration. First, the wing only results show convergence between the results on the medium and fine grids, at both a low subsonic and a transonic freestream Mach number. The medium grid and linear results are in close agreement for all Mach numbers below a supersonic freestream, when the CFD generated results show a significant rise in the flutter speed as the shock wave reaches the trailing edge. In this case there is no evidence of a significant flutter dip. This was thought to be because the Hawk structure is fairly stiff. To test this the structural model was weakened by reducing the elastic modulus by an order of magnitude. The comparison between the linear and CFD predictions on the medium grid is shown in Figure 6.6. In this case the CFD generated speeds dip below the linear predictions in the transonic range. For a single response calculation the CPU times were 1 hour on a single processor, 9 hours on 1 processor, 16 hours on 8 processors on the coarse, medium and fine grids respectively.

6.3 Wing with Flap

Wing bending-torsion flutter is unlikely to be a concern for an aircraft since this is precluded by strength requirements. Problems are more likely to involve the behaviour of a control surface, store or nacelle. In this section a combat flap is included on the wing to increase the realism and exercise the control surface treatment. The three cases of the wing with flap which are analysed are shown in Table 6.3. The flap in the combat configuration is deflected 12.5° about an axis below the wing. In linear aeroelastic simulations the combat flap configuration cannot be modelled easily. This is because of the requirement of the linear unsteady method (*Nastran Aeroelastic Analysis*) that the flow be in the x-direction at all times. This means that a wing or a flap cannot have an angle of incidence. Thus a second geometry was constructed with the flap

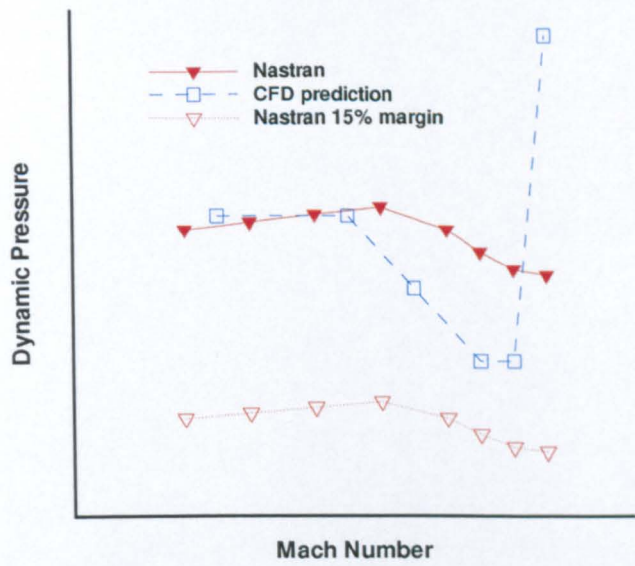
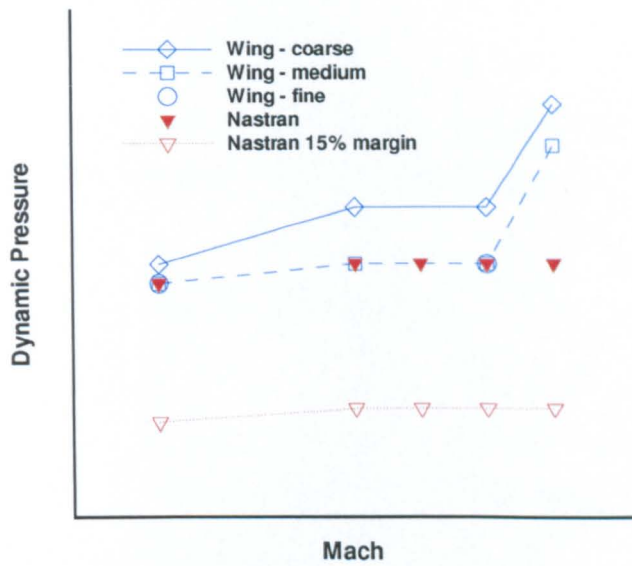


Figure 6.5: Qualitative comparison between the flutter boundaries on the Hawk aircraft predicted on the Hawk aircraft using the linear method and the wing-only configurations for the original structural model [67].

Case	Flap angle	Flap in structural model
Combat flap	12.5°	Yes
Wing with flap	0°	Yes
Wing	0°	No

Table 6.3: The three cases of the Hawk wing with flap. Note that even though the flap structural model is excluded in the third case the flap mode is retained.

at 0° deflection. CFD based aeroelastic analysis is performed for these two cases and compared with results from **Nastran**. The combat flap configuration on the aircraft is deployed in certain manoeuvres only and has constraints on the flight speeds within which it can be deployed. These flight speeds are limited to subsonic Mach numbers and shock induced instabilities on the combat flap configuration in transonic flows are of academic interest only.

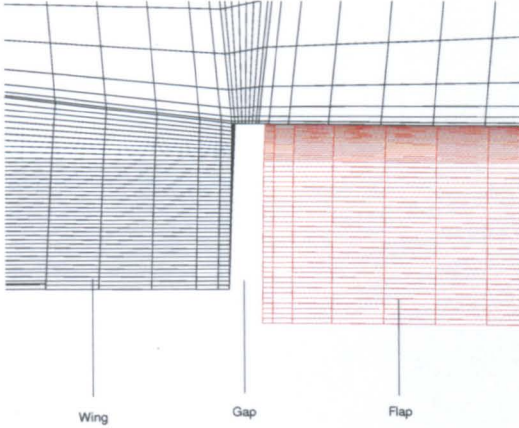
A blended flap is used for the simulation of the wing with flap at 0°. It was shown in Chapters 4 and 5 that the aeroelastic predictions of the blended flaps are comparable to the flap with free edges, however they slightly underpredict the flutter velocity due to the larger aerodynamic surface area of the blended region. As the aircraft flies with the flaps undeployed at the full range of Mach numbers the aeroelastic predictions on this case are of practical interest.

Finally simulation is performed using the blended flap grid but excluding the flap structural nodes. This is done by mapping the the aerodynamic nodes of the flap to the wing structural grid. This can be done by switching the 2 level transformation to a 1 level transformation where all the aerodynamic nodes are driven by the wing structural model alone (See Chapter 3). Practically this has the same effect as excluding the flap rotation from the aeroelastic calculations, although the structural influence of the flap modes on the wing motion will still be present. The purpose of analysing this case is to measure the increase in the flutter velocity when the control surface rotation is excluded.

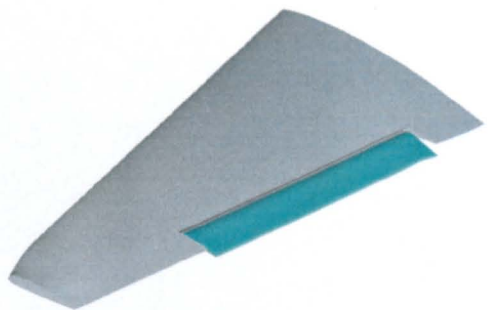
6.3.1 CFD Setup

The geometry of the Hawk wing with a combat flap was constructed by merging the two geometries using the **EZ-Cad** package of **ICEMCFD**. First all the components from the complete aircraft CAD model were deleted except the wing, which was left intact. Then the combat flap, obtained separately from BAE SYSTEMS in the form of a large number of coordinates, was imported into **EZ-Cad** as points. A space for the flap to live inside the wing was created by cutting out the sections of the wing around the flap. A gap of approximately 2% of the flap span was left between the flap edge and the wing. A small groove was created ahead of the flap leading edge to conform to the original geometry which has a similar cavity as shown in Figure 6.8. CFD simulations have shown that a twin vortex system sits inside this cavity as seen in Figure 6.9. Discussions with engineers from BAE SYSTEMS established that aerodynamically this cavity does not have much influence on the flow over the flap and can be completely eliminated for current purposes. However for the purpose of maintaining a smooth grid over the flap leading edge a shallow cavity was retained.

Figure 6.10 shows the blocking strategy used to block the wing with a free unattached flap.



(a) Gap between the wing and flap.



(b) The combat flap definition.

Figure 6.7: The flap on the Hawk wing.

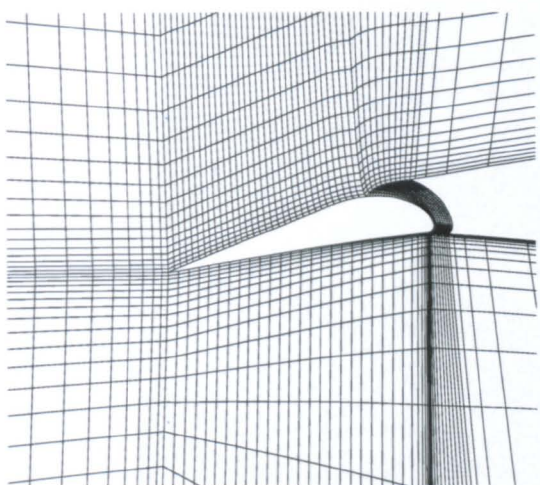
A C-H blocking over the wing and a separate C-H block over the flap ensures a smooth grid over the entire geometry. A 3-block strategy is used on the wingtip and the inner edge of the wing in the wing-flap gap. This type of blocking avoids grid singularities on geometries where a plane collapses into a line or a point. The grid has 827,300 points and a coarse grid was extracted by removing every alternate point in the three directions, and has 117,800 points. There are 22,000 points on the wing and flap surface on the fine level and 5,500 on the coarse level. A wall spacing of $10^{-3}c$ where c is the hawk wing root chord, is used for the simulations.

For the case with the flap at 0° the blocking used is similar to the one used for the wing alone case in Section 6.2. Additional flap blocks are added to define the flap edges over the wing. The flap edges are assumed to be blended with the wing. There are 3255 points on the wing and flap surface and 119,808 in the volume grid on the coarse level.

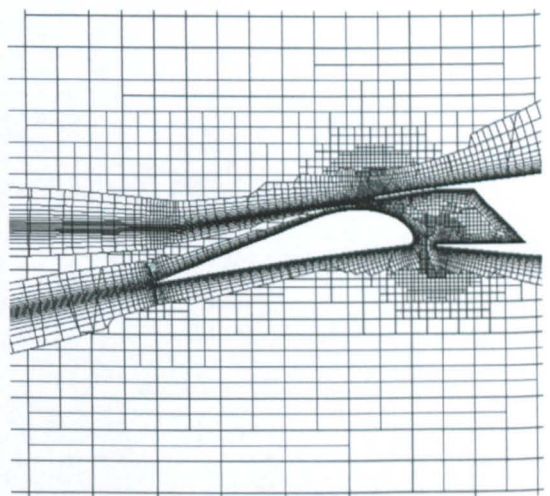
6.3.2 Structural Model

The structural model used here has been derived from the Hawk structural model described in Section 6.2.2. The wing root is constrained in all of the six degrees of freedom to isolate the wing and the flap modes from the rest of the aircraft structure. The flaps and the aileron are attached to the wing though only the flap nodes are used in the simulation. The deformation in the aileron mode is not confined purely to the aileron. The wing and the flap deform also in this mode but not to the same magnitude as the aileron. Hence, even though aileron structural nodes are excluded from the mapping, the aileron mode itself is included. The first six modes are used for the analysis which includes the first wing bending, the first wing torsion and the flap rotation mode. For the sake of simplicity higher frequency modes have been excluded from the calculations.

The flap is attached to the wing at three hinge points. One of the hinges is spring loaded, representing the actuator stiffness which is assumed constant. Due to the smaller dimensions of the control surfaces as compared to the major components of the aircraft the control surface



(a) Flap definition in the current work. The cavity is ahead of the flap leading edge is shallow.



(b) The original **SOLAR** from BAE SYSTEMS [99]

Figure 6.8: Cross section of the Hawk wing with combat flap configuration from the current work and the grid from BAE SYSTEMS simulation using **SOLAR**.

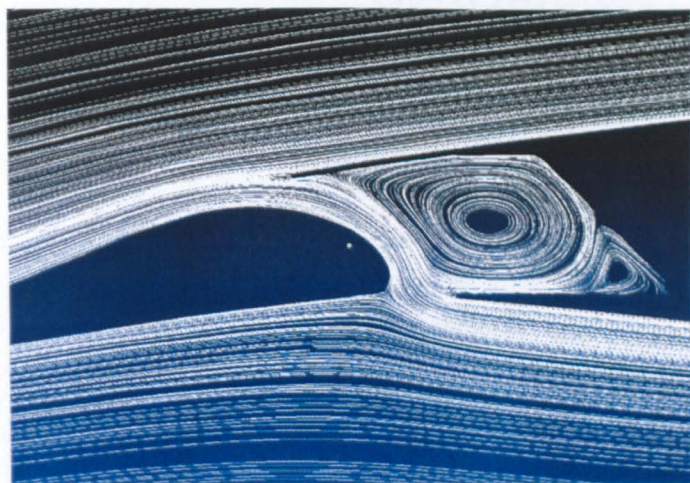
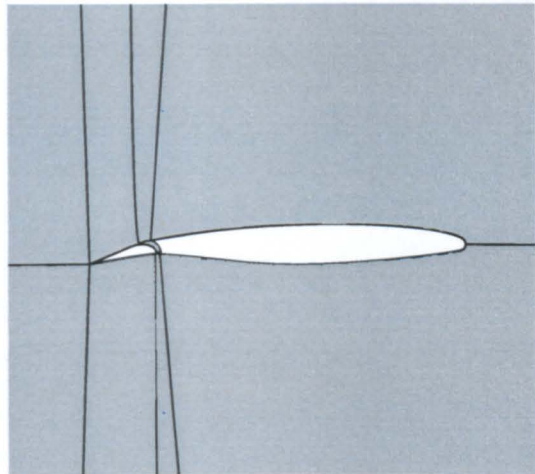
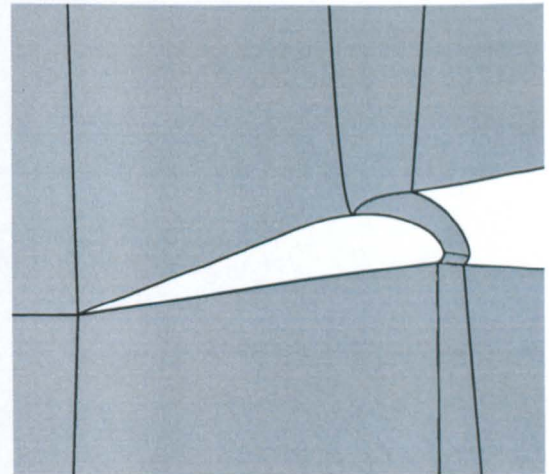


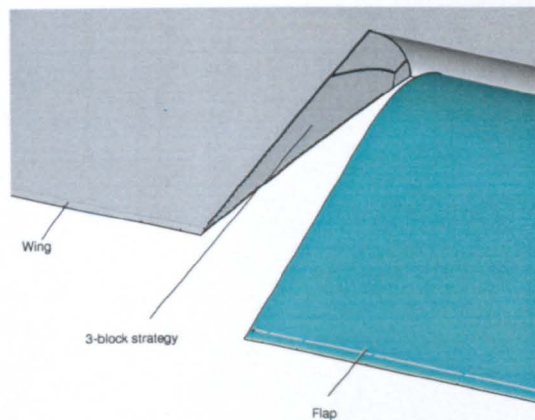
Figure 6.9: A vortex system sitting inside the flap groove in the **SOLAR** solution.



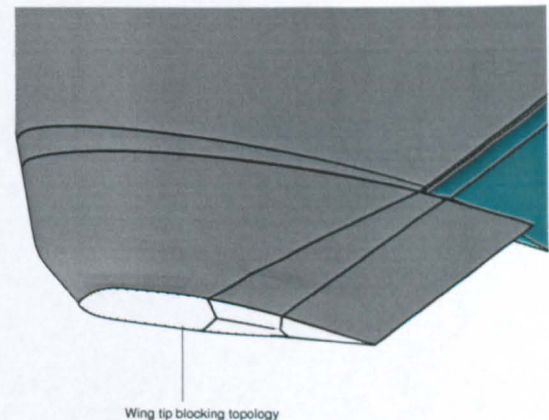
(a) A C-H-type blocking over the wing.



(b) A C-H-type blocking over the flap.



(c) 3-block strategy on the inner edge of the wing at the wing-flap junction.



(d) Wing tip blocking topology.

Figure 6.10: Block topology used for the gridding of the Hawk wing with flap case.

	Frequency (Hz)	Description
Mode 1	12.8	First wing bending
Mode 2	37.9	First wing torsion
Mode 3	44.1	Second wing bending
Mode 4	55.7	Flap rotation
Mode 5	60.5	Wing tip twist (aileron rotation mode with the aileron structural nodes not included in the aeroelastic calculations)
Mode 6	70.0	Second wing torsion

Table 6.4: Natural frequencies and mode description of the Hawk wing with flap case.

deformation modes have relatively higher frequencies. However the control surface rotation modes depend on the hinge spring stiffness and are important for aeroelastic instabilities. The flap and the wing structural nodes are mapped to the flap and wing fluid nodes using a 2-level mapping as described in Chapter 3. The natural frequencies and mode description for the structural model are given in Table 6.4.

6.3.3 Results

The flight envelope within which the combat flap configuration is deployed is limited to subsonic Mach numbers and the results presented here for transonic Mach numbers are purely of academic interest. The simulated flight conditions are outside the flight envelope and the results are not applicable to the real aircraft. The objective here is to simulate the shock induced effects on a deployed flap and to assess the effect of the deployed flap on the flutter boundary. Figure 6.11 shows the flutter boundaries for the combat flap configuration predicted using **Nastran** and CFD. The comparison is reasonable at subsonic Mach numbers. At a certain transonic Mach number the CFD prediction shows a large drop in the flutter velocity which is due to a small amplitude limit cycle oscillation of the flap. In contrast **Nastran** predicts a peak in the flutter velocity at this Mach number. Moreover the **Nastran** method breaks down at low supersonic Mach numbers due to the limitations of the linearised supersonic aerodynamic theory explained in Chapter 5. The amplitude of the oscillations in the CFD based simulation depends on the dynamic pressure. However the decrease in the amplitude is asymptotic and a finite amplitude exists even at very low values of the dynamic pressure (see Figure 6.12).

A cross section through the wing-flap shows a well defined shock standing at the wing trailing edge inducing a strong separation over the entire flap surface (see Figure 6.13). The unsteady separated flow over the flap drives the flap to result in a LCO. The frequency of the oscillations was found to be very high suggesting that the instability is driven mainly by the unsteadiness in the flow. For matched conditions at transonic Mach numbers the frequency of oscillations was twice the natural frequency of the flap oscillations. Currently the timestep used in the simulation is based on the highest structural frequency and a smaller timestep based on flow unsteadiness scales is required to accurately resolve the amplitude and frequency of the oscillations. The shock here stands ahead of the flap hinge hence according to Lambourne's classification [4] it can be termed as a Type A buzz. The instability caused by separated flow has been termed as

classical buzz by Bendiksen [3]. It is interesting to note that in the paper Bendiksen describes nonclassical buzz or “inviscid buzz” as a phenomenon where separation is not involved. Mainly he assumes that viscous effects are necessary to model the flow separation. In the current case the separation is caused by a combination of the sharp trailing edge of the wing, a strong shock and the deflected flap. Separation of the boundary layer is not involved. It is seen here, that like the simulation of the nonclassical buzz in Chapter 5, a qualitative evaluation of classical buzz is possible using the Euler equations. However for accurate results with regards to amplitude of oscillations and frequencies modelling of the viscous effects is necessary. Once again it should be stressed that the aircraft does not fly at transonic Mach numbers with a combat flap configuration due to the structural constraints.

Figure 6.14 shows the flutter boundary for the wing with flap at 0° deflection. The linear boundary here is the same as for the combat flap configuration. It is seen that the buzz instability is absent from the CFD results. It is also seen that there is no shock induced separation on the flap hinge observed in the combat flap configuration (see Figure 6.15). Absence of a separation bubble together with the fact that no LCO was observed in the case with 0° flap deflection at transonic Mach number suggests that a mean flap angle greater than 0° is necessary for the Type A buzz to occur. The flutter boundary compares reasonably with the linear results in the subsonic region. The CFD analysis predicts a shallow transonic dip which is not present in the Nastran results. As in all cases analysed so far the linear method predicts a large drop in the flutter velocity at low supersonic Mach numbers.

Finally Figure 6.16 shows the flutter boundary for the case when the flap structural nodes and hence the flap rotation is excluded from the analysis. The flutter velocity increases to almost twice when compared to the flap cases. The transonic dip seen in the case with the flap is absent here as in the wing alone case in Section 6.2. This is due to the fact that the modes and the structural behaviour are similar to the wing alone case. The general increase in the flutter velocities as seen in Figure 6.17 for all Mach number underscores the importance of the control surface modes to the aeroelastic response. The difference in the flutter velocities for the case without the flap and the cases with flap is due to the differences in the structure model. The flap cases have the flap rotation mode which is absent in the wing alone case. The transonic dip due to the shock induced LCO in the combat flap configuration is absent in the case with flap at 0°. The differences in the predicted aeroelastic response between these two cases at transonic Mach numbers is due to the different aerodynamics.

6.4 Rudder Cases

The behaviour of the fin-rudder is investigated in this section. One of the motivations for this study comes from a difficulty with obtaining realistic results with the rudder rotation mode at low supersonic Mach numbers in linear aeroelastic calculations. A CFD based study is performed in this section to investigate the aeroelastic response at a range of Mach numbers including the low supersonic Mach numbers. The configuration considered has various degrees of complexity. The interference effect of different components on the pressure distribution over the fin and rudder is investigated. The fin bending and torsion occur in the antisymmetric modes of the

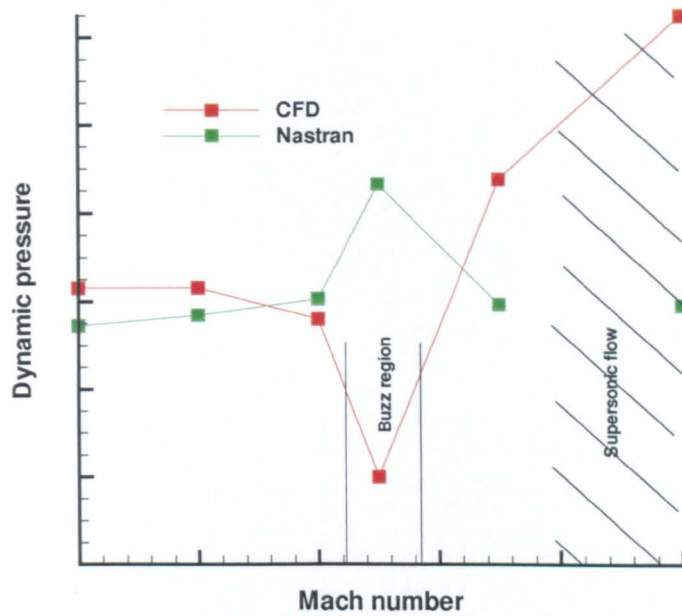


Figure 6.11: Qualitative comparison of flutter boundaries for the Hawk wing combat flap configuration using linear and CFD methods.

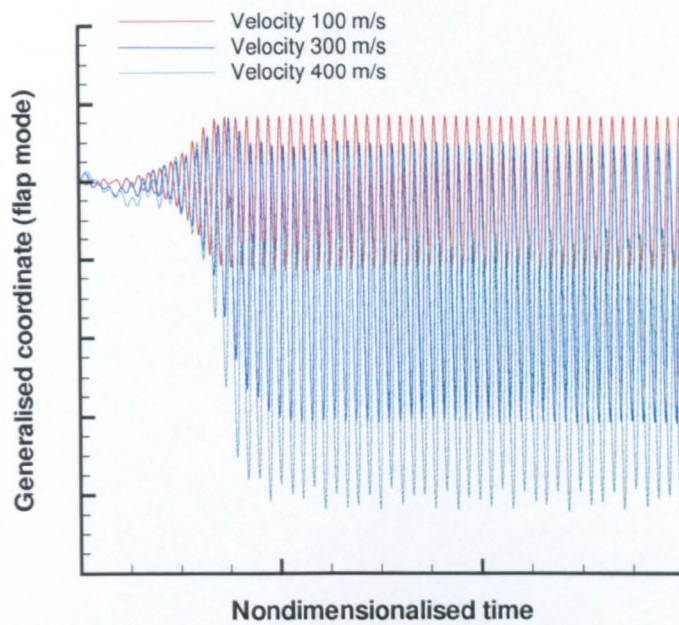


Figure 6.12: Limit cycle oscillations of the combat flap configuration on the Hawk wing at a transonic Mach number.

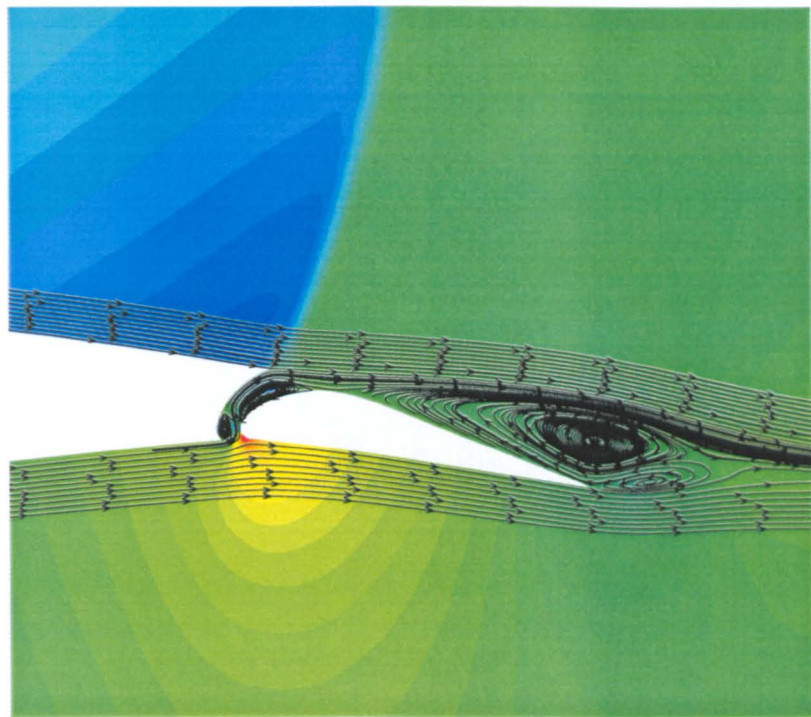
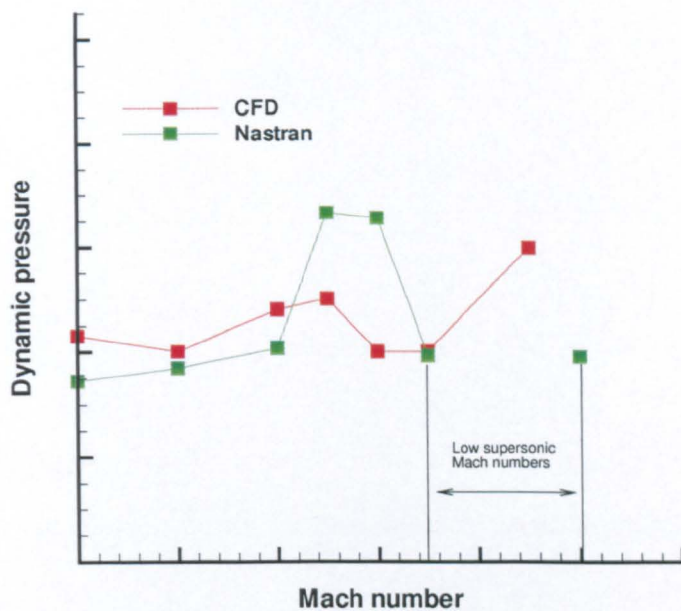


Figure 6.13: Shock induced separation at the flap hinge at transonic Mach number.



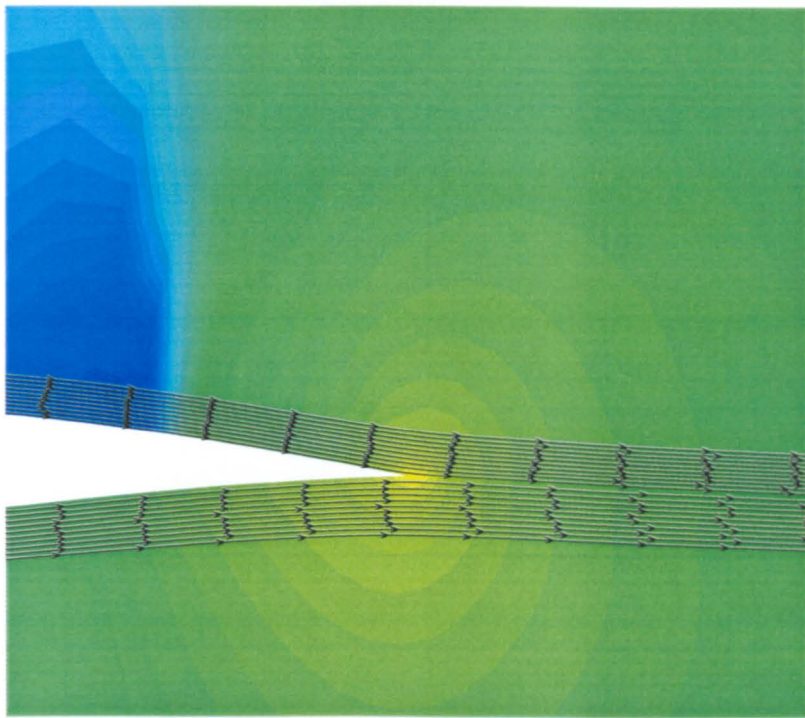


Figure 6.15: Attached flow all along the flap at transonic Mach number when the flap is undeployed.

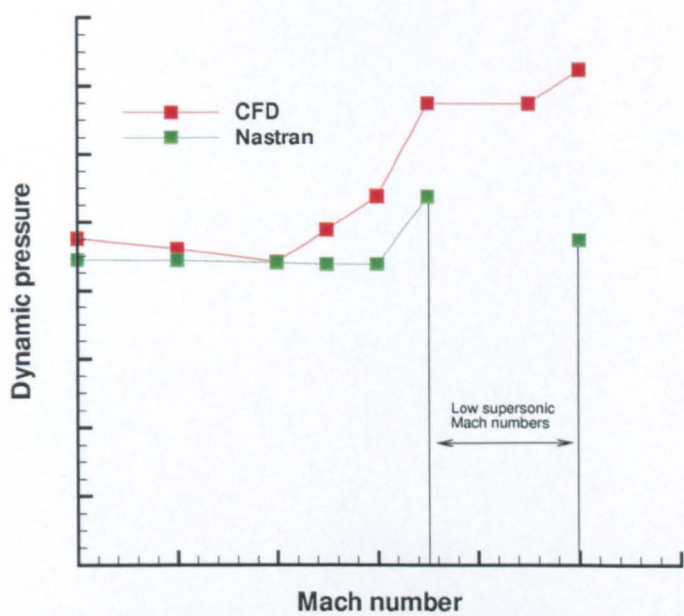


Figure 6.16: Qualitative comparison of flutter boundaries using linear and CFD methods of the Hawk wing with the flap and aileron aero-structural relations replaced by a full planform wing arrangement.

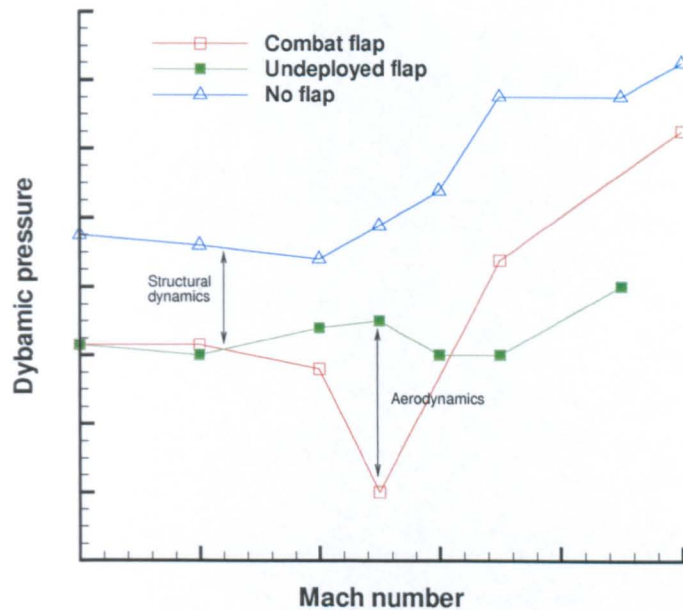


Figure 6.17: Qualitative comparison of the flutter boundaries for the Hawk combat flap case, the Hawk wing with 0° flap deflection and the Hawk wing with the full planform wing replacing the separate flap grid using CFD.

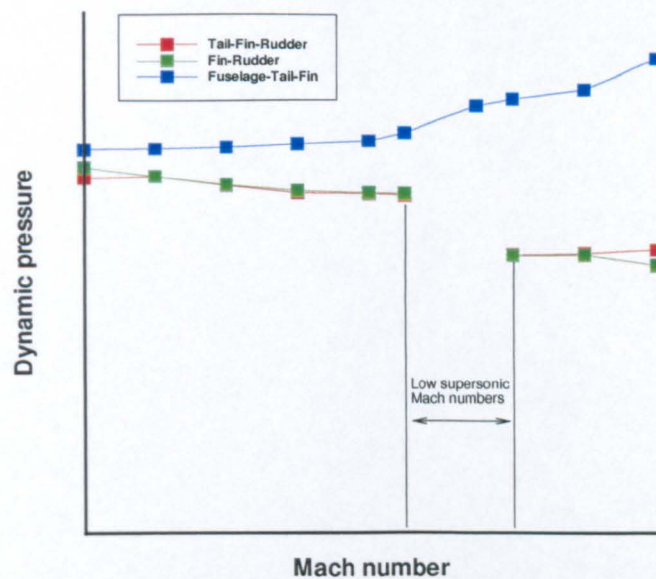


Figure 6.18: Qualitative flutter boundaries of the Hawk tail-fin-rudder, fin-rudder and fuselage-tail-fin cases using linear aeroelastic analysis.

aircraft, and hence these are used for the calculations. Figure 6.18 shows the flutter boundary of the Hawk model as predicted by **Nastran** using antisymmetric modes of vibrations. The tail, fin and rudder are included in this simulation. In an attempt to simplify the structural response only the fin and the rudder were allowed to vibrate with all other components constrained.

Further interest in this particular case arises from development flights of the T-45A Goshawk Aircraft, the Hawk variant in use with the US Navy. During its early development the Goshawk fighter trainer was reported to experience the phenomenon known as rudder buzz [90]. Uncontrollable rudder oscillations were described at Mach 0.9 at 10, 000 and 30, 000 feet and at Mach 0.95 at 20, 000 feet. The oscillations were attributed to a shock induced instability and were successfully eliminated by the use of shock strips [90]. The location of the shock was computationally predicted through steady simulations by Fuglsang *et al.* [90] using a Body-Fin-Rudder geometry. It will be seen below that the interference due to the wing has an effect on the prediction of the shock on the fin and the prediction of shock induced instability. This case is a useful test to extend the CFD based analysis. Whilst the buzz phenomenon is straightforward to resolve [90], for the simulation of moving control surface and shock provide a challenge.

6.4.1 CFD Setup

The constraining of the structural model everywhere except for the fin and the rudder effectively eliminates the structural interaction of the components which though not directly responsible for known flutter instabilities do modify the modal responses of individual modes. However the aerodynamic interference of the components has an effect on the pressure distribution especially at transonic and supersonic Mach numbers. The interference effect is investigated by performing static and dynamic simulations on configurations with different levels of complexity. The following subsections describe the CFD setup of the different configurations.

Body-Fin-Rudder Case

As stated in Section 6.4 the T-45A Aircraft experienced rudder buzz during a development flight test programme at Mach 0.95 at 20, 000 feet [90]. The oscillations were assumed to be shock induced and a steady state CFD analysis was performed on the Body-Fin-Rudder (B-F-R) configuration to locate the position of the assumed shock. A strong shock was predicted at Mach 0.95 just ahead of the rudder hinge on the B-F-R configuration using a RANS based CFD code TLSN3D. The instability observed in the flight test at Mach 0.95 was attributed to this. In the current work a similar B-F-R configuration is analysed. A grid was constructed with 540,000 points and the wall spacing of $10^{-3}c$ (where c is the wing root chord). The blocking consists of an O-type block over the fuselage and an H-type over the fin and rudder as shown in Figure 6.19. There are 9500 points on the surface of the aircraft. It was found that viscous effects were minimal over the fin and did not alter the predicted location of the shock significantly and only the inviscid calculations are performed for the rest of the cases.

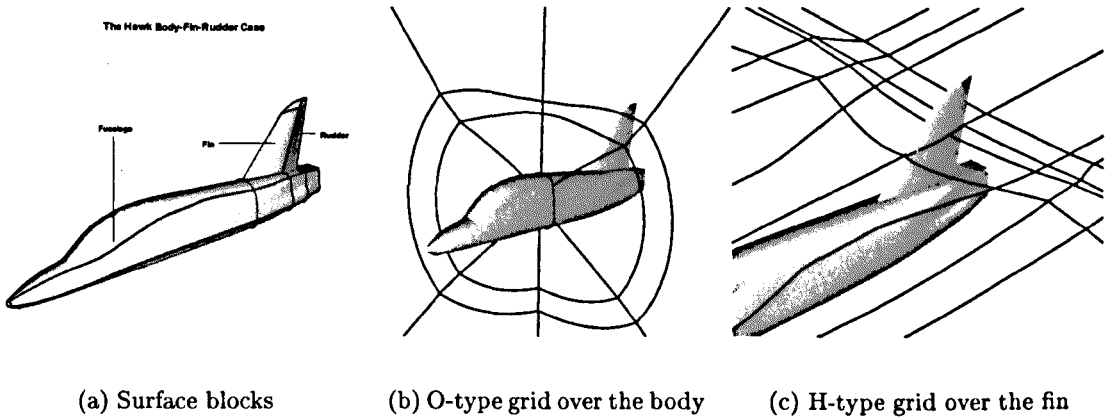


Figure 6.19: The blocking topology of the Body-Fin-Rudder test case

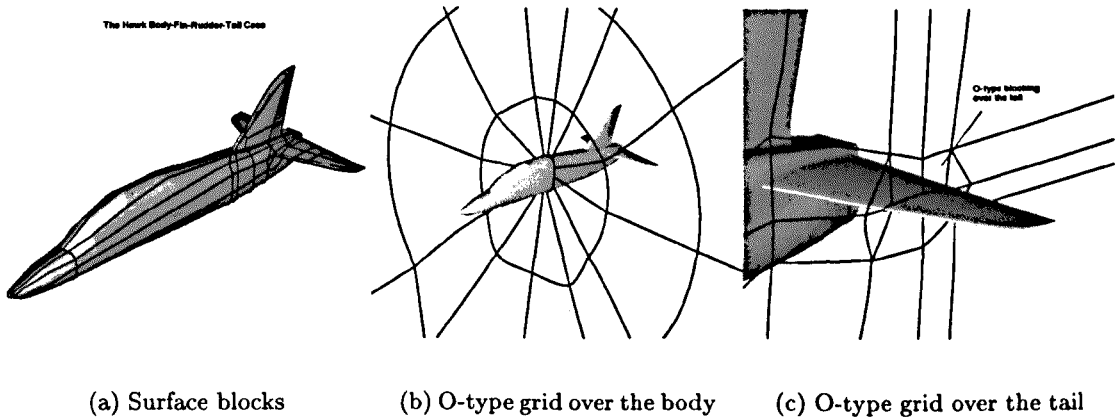


Figure 6.20: The blocking topology of the Body-Fin-Rudder-Tail test case

Body-Fin-Rudder-Tail Case

After analysing the results of the B-F-R case (see Section 6.4.4) it was felt that a more detailed representation of the aircraft may be required in order to get realistic aerodynamic results over the fin and the rudder. This is important as an interaction between the fin-rudder structure and the oscillating shock is observed in the unsteady simulation. To improve on the flow predicted over the fin the interference effects from the adjacent aircraft components may need to be included. Hence the tailplane was added to the simulated geometry. The Body-Fin-Rudder-Tail (B-F-R-T) case has an C-H blocking over the fin-rudder and an O-block over the tail and the fuselage (see Figure 6.20). The wall spacing is $10^{-3}c$ and the size of the coarse and fine grids are 300 thousand and 2 million points respectively.

Body-Fin-Wing-Rudder-Tail Case

When the tail was included in the simulation the steady pressure distribution changed to a very large extent. This gave an indication that at transonic Mach numbers the interference of other components has a very big impact on the pressure distribution. Recognising this the wing was

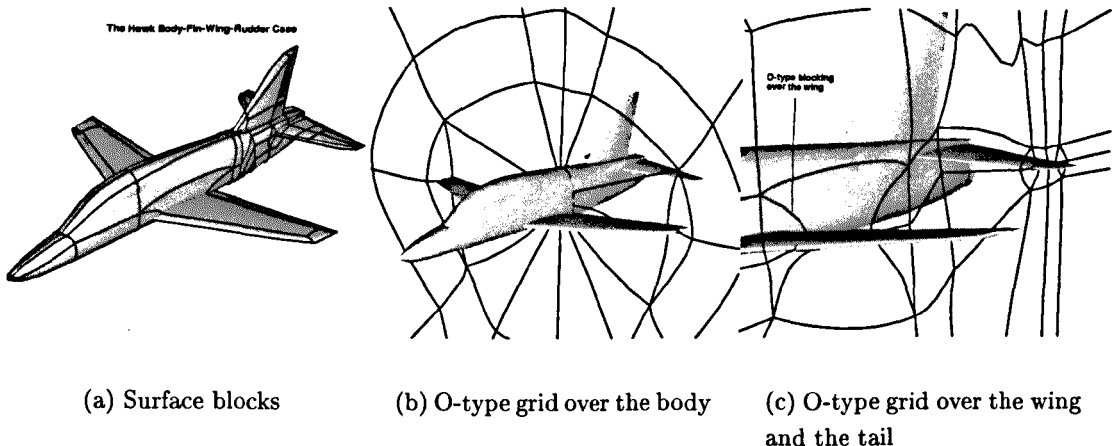


Figure 6.21: The blocking topology of the Body-Fin-Wing-Rudder-Tail test case

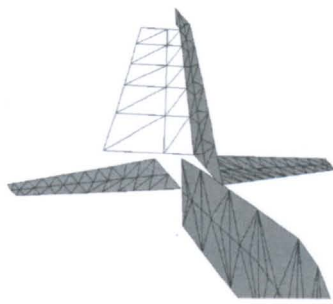
	Frequency (Hz)	Description
Mode 1	18.8	Rudder rotation
Mode 2	22.3	First fin bending
Mode 3	62.2	First fin torsion
Mode 4	71.3	Second wing bending

Table 6.5: Natural frequencies and mode description of the Hawk fin-rudder structural model.

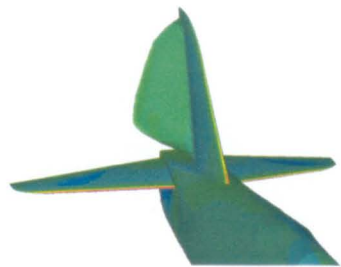
also included in the simulation to model the component interference. It should be noted that the engine bulge on the fuselage and the radar on the fin have been not included in this simulation. The blocking is an extension of the B-F-R-T grid and consists of an O-block over the fuselage, the tail and the wing whereas the fin-rudder has a C-H blocking. The size of the grids are 310 thousand and 2.1 million points for coarse and fine levels respectively.

6.4.2 The Structural Model

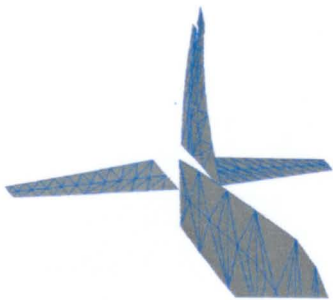
For our purpose all the nodes except those modelling the fin and rudder are constrained in all of the six degrees of freedom. Hence the whole aircraft except the fin and rudder is kept rigid. Modal analysis is performed and the first 4 natural modes of vibration of the fin-rudder are extracted from the **Nastran** output file and converted into the format required by the flow solver using a parser utility. The structural nodes required for the representation of the aircraft are extracted from the **Nastran** output file and labelled for the multi-level transformation using an extraction utility. The extracted structural nodes are triangulated using an open source software **TRIANGLE**. The first four natural modes are used in the analysis. Table 6.5 gives the natural frequency of these modes. One of the important issues in a CFD based aeroelastic analysis is the transformation between the structural and the fluid grids. Before commencing the unsteady calculations the transformation is checked by visually inspecting the statically deformed modes. Figure 6.22 shows the forced modal deformation on the structural grid and the corresponding transformed modes on the fluid grid of the B-T-F-R case.



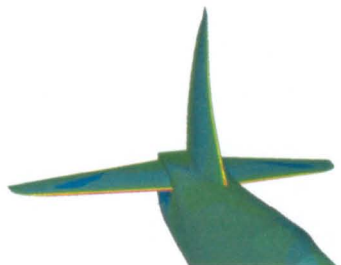
(a) Mode 1 - structural



(b) Mode 1 - fluid



(c) Mode 2 - structural



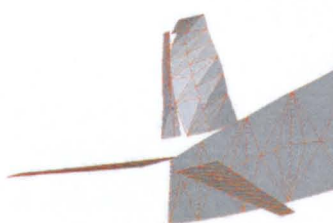
(d) Mode 2 - fluid



(e) Mode 3 - structural



(f) Mode 3 - fluid



(g) Mode 4 - structural



(h) Mode 4 - fluid

Figure 6.22: The structural mode shapes are transformed on to the fluid surface grid to visually verify the accuracy of the transformation. A medium fluid grid of the B-F-R-T case is used for the visualisation.

Mirroring of Modes

The treatment of antisymmetric modes for aeroelastic analysis requires some explanation. In our analysis we consider only the translation of the structural nodes and ignore the rotational components. An aircraft is predominantly symmetric along the fuselage centre-line in the pitching plane (the xy plane, see Figure 6.23). This means that for the calculation of the aerodynamic force over the aircraft body in a flow without a crosswind, a half body representation of the aircraft is enough to predict the relevant aerodynamics. In terms of structural response an aircraft can have 3 types of modes. The first are the symmetric modes, which are such that the motion of any point on the structure is mirrored in the symmetry plane (the x-y plane in the CFD case). The components lying on the x-y plane, like the fin and the rudder deform in the x and y direction and do not deflect in the z direction. The second type of possible modes are the antisymmetric modes. These are such that the motion of any point is 180° out of phase with the motion of its mirror image point in the x-y plane. Nodes in the CFD x-y plane have no motion in the x or y directions, however they can move in the CFD z direction. The third type of modes are the asymmetric modes. The deformation of points in these modes is independent of the motion of the mirror image points in the x-y plane. It should be noted that both symmetric and antisymmetric modes can be obtained from a half-model by applying appropriate boundary conditions to the structural nodes lying in the plane of symmetry but asymmetric modes cannot be identified from a half-model.

To extract symmetric modes the nodes lying in the symmetry plane should be constrained by:

$$z = 0.0 \quad Tx = 0.0 \quad Ty = 0.0$$

To extract anti-symmetric modes the constraints should be

$$x = 0.0 \quad y = 0.0 \quad Tz = 0.0$$

Here x, y and z are the displacements and Tx, Ty and Tz are the rotations along x, y and z axes respectively. These constraints are for the CFD coordinate system (see Figure 6.23) which is different from coordinate system of FEM model shown in Figure 6.2

The current section involves the analysis of the anti-symmetric modes of the fin-rudder configuration. In the linear analysis of the problem a half model of the configuration is used. The structural model of the components lying in the x-y plane like fin, rudder and the fuselage are modelled with half the weight of the full structure. The aerodynamic panels for these components are the same as those for symmetric components. An entry in the Nastran analysis deck specifies the plane of symmetry which is x-z for the FEM model. Nastran recognises the aerodynamic panels lying on the symmetry plane and the aerodynamic loads calculated on these panels are exactly half of what would normally occur on a completely modelled aircraft. For CFD based aeroelastic calculations the full structural and aerodynamic models are required for antisymmetric modes of the components lying in the symmetry plane. CFD does not recognise the symmetry plane for aeroelastic deformations unlike Nastran. Moreover the deformations are in the direction perpendicular to the symmetry plane and hence a complete model is required. For symmetric modes of components lying on the symmetry plane a half model of the aircraft

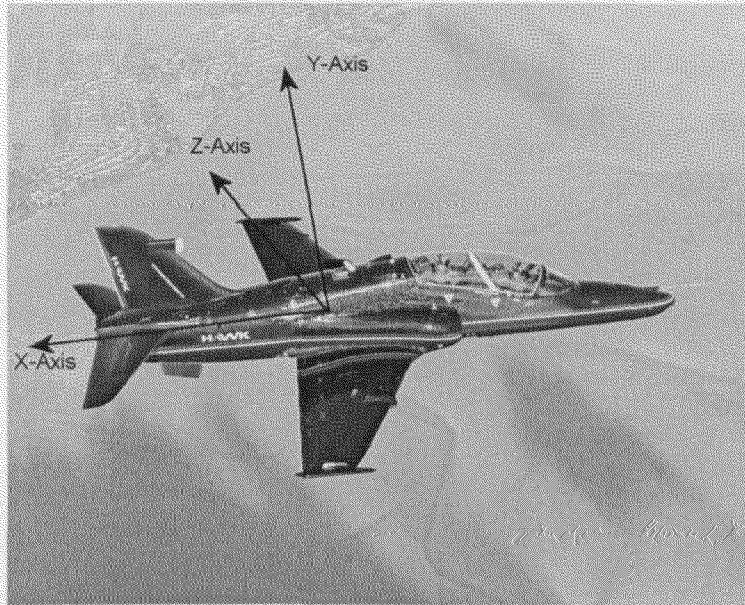


Figure 6.23: Axes definition of the aircraft as used in the current work

can be used since the deformations in these modes are not in the direction perpendicular to the symmetry plane.

The coupled solver uses mass generalised modes for aeroelastic analysis. The mass generalisation is performed by **Nastran** while calculating the natural modes hence they can be used directly for aeroelastic calculations without performing any additional pre-processing. The mass generalisation of the natural modes is given by the equation

$$[\phi_i]^T \mathbf{M} [\phi_i] = 1 \quad (6.1)$$

where ϕ_i is the i^{th} mode shape and the \mathbf{M} is the mass matrix of the structure. The mirroring of the structural nodes and its modes increases the number of elements in the given mode shape by 2 and hence the mirrored mode shapes now satisfy

$$[\phi_i^F]^T \mathbf{M} [\phi_i^F] = 2 \quad (6.2)$$

where ϕ^F is the mode shape of the full structural model. To mass generalise the modes of the mirrored model the mode shapes should be scaled by $\sqrt{2}$ and hence

$$\left[\frac{\phi_i^F}{\sqrt{2}} \right]^T \mathbf{M} \left[\frac{\phi_i^F}{\sqrt{2}} \right] = 1 \quad (6.3)$$

The following steps are taken to convert a half model and its modes to a full model valid for CFD based aeroelastic calculations. The FEM grid and modal data are available in the .f06 file as part of the **Nastran** output.

1. Extract the required structural nodes of the half model from the .f06 file.
2. Extract the modal data corresponding to the extracted nodes from the .f06 file.

	Incidence	Mach number
Case 1	1.1°	0.88
Case 2	-0.3°	0.94

Table 6.6: Steady cases used for comparison with SOLAR.

3. Transform the y and z components of the structural coordinates to conform to the CFD requirements i.e. the pitching axis is the z-axis and the structural starboard wing transforms to the CFD port wing.
4. Mirror the structure by duplicating all the nodes, except the ones in the CFD x-y plane, and multiplying the z-coordinate of the duplicated nodes by -1.
5. Multiply the pitching component (y-component) of the mirrored modes by -1 if the extracted modes are anti-symmetric.
6. Divide all of the modal deflections by $\sqrt{2}$.

6.4.3 The Complete Hawk Model

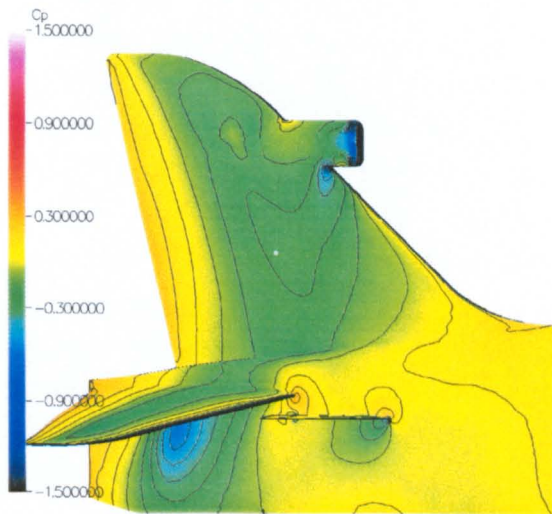
Steady Euler results obtained by the SOLAR code for the complete Hawk configuration [99] were provided by BAE SYSTEMS. The geometry used for the calculation is a detailed one and includes smaller components like the radar on the fin, the lateral fins and the Side Mounted Under Roof Fins (SMURFs). The steady pressure distribution on the fin was extracted from these calculations and are used here for comparison. The main objective for these comparisons is to investigate the interference effect of the components on the pressure distribution at transonic Mach numbers. Figure 6.24 shows the pressure distribution over the fin.

6.4.4 Results and Discussions

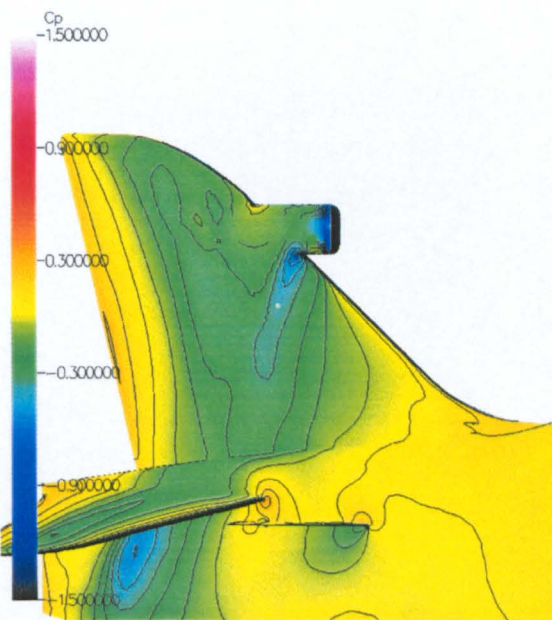
One of the reasons for studying the Hawk fin-rudder case using unsteady CFD based aerodynamics was to investigate the transonic buzz observed at Mach 0.95 during a flight test on the T45 aircraft [90]. As this occurs at upper transonic freestream Mach numbers and involve a trailing edge control surface it is important to first evaluate the shock position which possibly influences/excites the rudder rotation mode. It was seen in Chapter 5 that the shock location is the main parameter for control surface buzz and hence accurate shock prediction is of primary importance.

Steady Results

There are no experimental surface pressure data available for the comparison with the computed results and hence the next best option was to compare the results from the current work with CFD based results obtained from BAE SYSTEMS [99]. Table 6.6 shows the conditions for the two cases used for comparison and Figure 6.24 shows the surface pressure contours on the fin for the two cases. The absence of a shock on the fin is noticeable. Surface pressure cuts were obtained on the fin at five horizontal locations shown in Figure 6.25. The Cp values are compared



(a) Euler calculation, Mach 0.88, Incidence
 1.1°



(b) Euler calculation, Mach 0.88, Incidence
 -0.3°

Figure 6.24: Surface pressure plots on the fin of the complete Hawk configuration [99].

for three cases of increasing geometric complexity B-F-R, B-F-R-T and the B-F-W-R-T cases. Figures 6.26 to 6.30 show the plots of these comparisons. It can be seen that for both Case 1 and Case 2 there is an absence of a noticeable shock along the five span-wise locations. This absence is due to the fact that as the flow accelerates over the wing resulting in a strong shock over the wing surface. The shock reduces the velocity of the flow reaching the fin and hence a strong shock does not develop over the fin. The tail too has a limited interference effect which alters the flow velocity over the fin. In Figures 6.26 to 6.30 it can be seen that the B-F-W-R-T case compares closest to the BAE SYSTEMS results mainly due to the fact that the wings diffuse the shock over the wing. The B-F-R case is seen to predict a strong shock on the rudder hinge. This can cause the corresponding unsteady simulation to predict a shock induced instability which would not be realistic as the shock exists due to inadequate modelling of the geometry. Another interesting feature of the comparisons is the hump that can be seen between 10 and 10.2 metres on the X-axis and between 2.2 and 2.4 metres semi-span in Figures 6.28 and 6.29. This is attributed to the radar attached to the fin (see Figure 6.24). This geometrical feature is not modelled in the current work though it seems to influence the pressure distribution over the fin. From these results it is also seen that the full B-F-W-R-T case comes closest to the completely modelled geometry and predicts a relatively strong shock which can induce the control surface instability.

The computational work done on the by Fuglsang *et al.* [90] to investigate the rudder buzz incident in the flight test of the T45 aircraft used a simplified configuration of the aircraft ignoring all the components except the body, fin, and rudder. Figure 6.31 shows the surface pressure plots taken from reference [90] at 41% and 68% semi-span at Mach 0.95. These plots clearly predict the presence of a strong shock near the rudder hinge. A similar calculation was performed on the current B-F-R configuration which also predicts a strong shock near the rudder hinge. However we know from the surface pressure comparison with the full model that this shock will not actually exist on the real aircraft due to the interference effects. An engineering solution to address the rudder buzz was based on the steady calculations performed on this simplified geometry and included the placement of shock strips before the rudder hinge. Shock strips are raised surfaces or “humps” that are used to accelerate the flow and cause a premature shock ahead of the location where a shock would normally occur. Finally Figures 6.33 and 6.34 show the surface pressure contours on a cross-sectional plane through the fin at Mach 1.05 for the B-F-R, the B-F-R-T and the B-F-W-R-T cases. A strong shock before the fin can be seen on the cross-sectional plane for the B-F-W-R-T case.

Dynamic Results

One of the aims of the aeroelastic study of the fin-rudder case was to investigate the region of low supersonic Mach numbers where the linear analysis does not provide meaningful results. Linear aeroelastic analysis is known to be inaccurate between Mach numbers 1 and 1.3 as shown in Chapter 5. A drop in the flutter velocity for all the cases at low supersonic Mach numbers was noticed in CFD based simulations, however this commences at transonic Mach numbers less than 1 where the linear analysis predicts an instability at a much higher flutter velocity. A flutter boundary was traced for the complete B-F-W-R-T configuration and compared with the linear analysis (see Figure 6.35). The drop in the flutter velocity is in transonic and lower

supersonic Mach numbers and is due the shock induced buzz instability. Figure 6.36 shows the variation of the shock strength at a span location of $y = 2.2$ metres. It can be seen that the shock increases in strength initially and but weakens as the Mach number increases.

In the subsonic region CFD predicts a lower flutter velocity than linear. This is because in the CFD analysis the flow accelerates over the wings and when it finally reaches the fin it is at a higher velocity than the freestream velocity. At upper supersonic Mach numbers the interference effect of the wing on the fin seem to reduce and a good comparison between linear and CFD based flutter velocity is obtained.

The effect of component interference was investigated by performing aeroelastic analysis on the B-F-R, B-F-R-T and B-F-W-R-T cases. As seen in the steady flow simulations the interference effects of the components has a major effect on the shock strength on the fin and hence the pressure distribution. Matched point analysis was performed at 10,000 feet and at Mach 0.97 on the three cases to investigate the presence of the buzz instability. Figure 6.37 shows the modal response of the rudder rotation mode. It is seen that for the complete B-F-W-R-T case the initial perturbation damps down in time. In Figures 6.33 and 6.34 the B-F-W-R-T case in comparison to the other two cases has the weakest shock. The B-F-R and the B-F-R-T cases do undergo buzz at Mach 0.97 due to the presence of the shock. It is seen that the amplitude of oscillation is greater for the B-F-R-T case as the presence of a tail changes the shock location to the rudder trailing edge (see Figure 6.38). Theoretically the buzz onset occurs much earlier for the B-F-R and B-F-R-T cases than the B-F-W-R-T cases. Figure 6.35 shows the dynamic instability boundary of the B-F-W-R-T case. In the subsonic region there is a flutter type instability, i.e. an undamped instability and not an LCO, predicted which compares reasonably with the linear method. Figure 6.39 shows the damped and undamped modal responses for two dynamic pressures at Mach 0.85. Unlike the LCO type instability the amplitude of the flutter oscillations keep growing until the calculations break down due severe grid distortions. A dip in the dynamic pressure develops with increasing Mach number and at a certain transonic Mach number the instability becomes an LCO type. The linear analysis is unreliable close to Mach number 1. However where linear results are acceptable there is a big difference between the boundaries predicted by CFD and the linear method at supersonic freestream Mach numbers. This is because the instability is shock induced and is beyond the prediction capability of linearised aerodynamics. Once the shock defuses at higher Mach number the linear and CFD predictions begin to match up. Figure 6.36 shows the pressure distribution on the B-F-W-R-T case at 2.2 metres span (see Figure 6.25) at range of Mach numbers. It can be seen that the shock is absent on the rudder at low transonic Mach numbers and the instability is of the “flutter” type. At upper transonic Mach numbers the shock strengthens on the rudder resulting in buzz. At upper supersonic Mach numbers the shock diffuses over the fin-rudder and buzz disappears.

6.5 Conclusions

The analysis in the current chapter has provided useful insights into the modelling of aeroelastic cases for the prediction of buzz type instabilities.

It was seen in the investigation of the combat flap configuration that at transonic numbers

Spanwise locations on the fin of the extracted Cp values

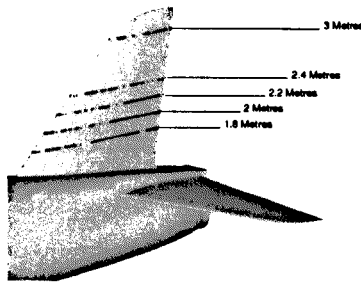


Figure 6.25: The span-wise locations on the fin of the Hawk where the Cp values have been extracted for comparison.

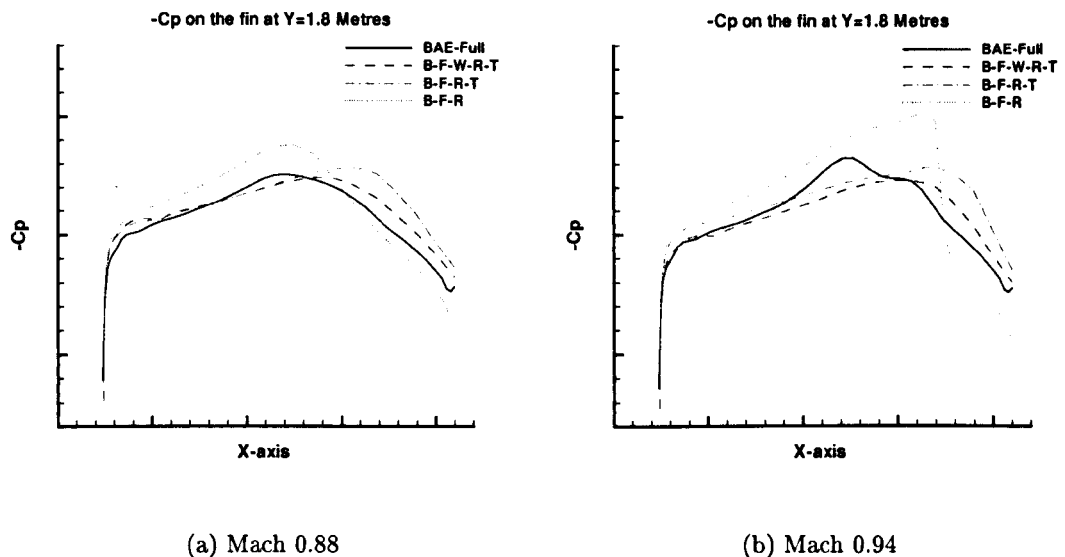


Figure 6.26: Surface pressure plots on the fin of the complete Hawk configuration at 1.8 Metres span

(but outside the flap envelope) there were instabilities involved which were beyond the capabilities of linear aerodynamics. It was also seen that the aeroelastic behaviour changes with the inclusion of a flap deflection angle which is also not currently simple to implement in Nastran. Finally it was demonstrated that a Type A buzz instability or the classical buzz instability can be predicted using the Euler equations due to a combination of a sharp wing trailing edge, the flap deflection and the shock at the trailing edge.

The aeroelastic investigation of the Hawk fin-rudder case highlighted the need for a detailed definition of the aircraft geometry in order to predict the buzz instability. The interference effects of the various components can either increase the buzz amplitude like in the B-F-R-T case or damp it out completely as in the B-F-W-R-T case. As the buzz boundary is sensitive to the shock location and the shock location itself is influenced by the presence of other components a detailed aircraft geometry is essential for the accurate prediction.

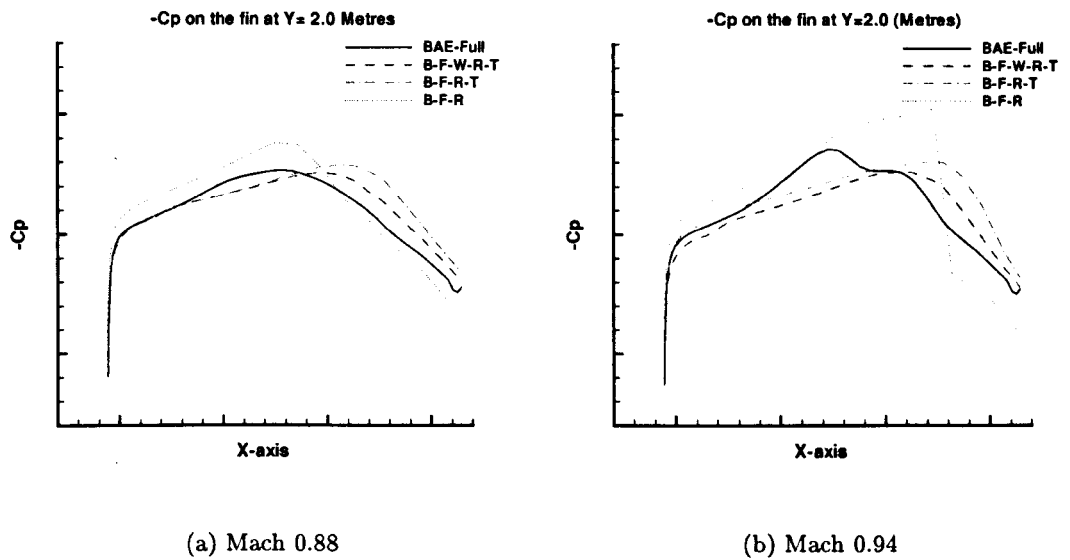


Figure 6.27: Surface pressure plots on the fin of the complete Hawk configuration at 2 Metres span

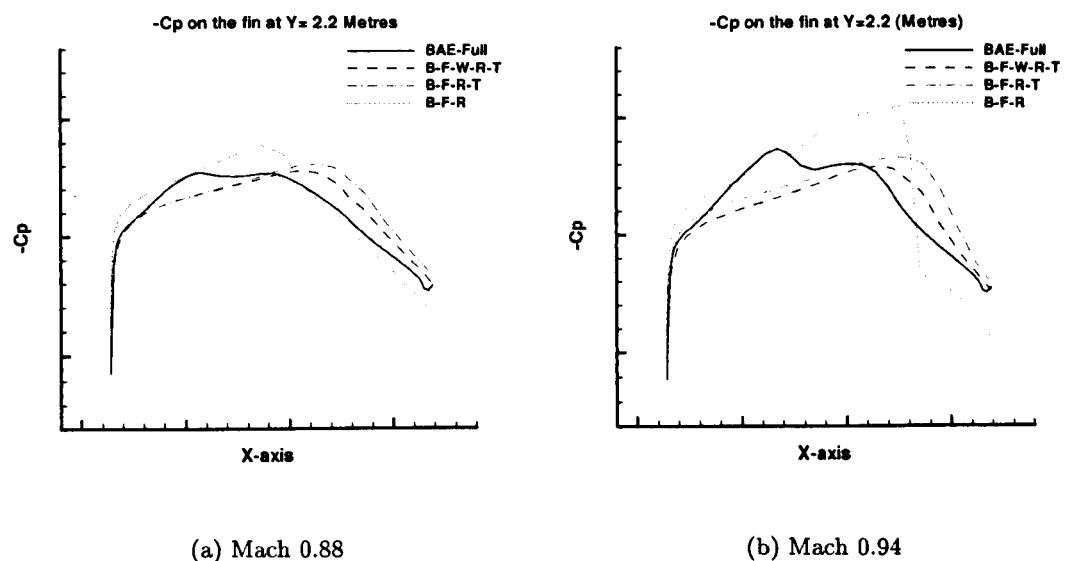


Figure 6.28: Surface pressure plots on the fin of the complete Hawk configuration at 2.2 Metres span

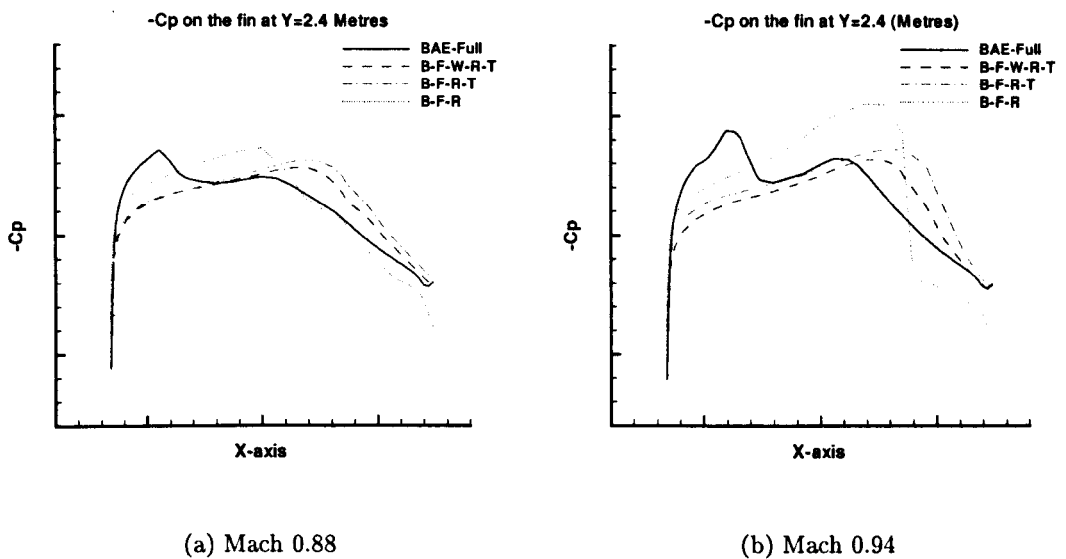


Figure 6.29: Surface pressure plots on the fin of the complete Hawk configuration at 2.4 Metres span

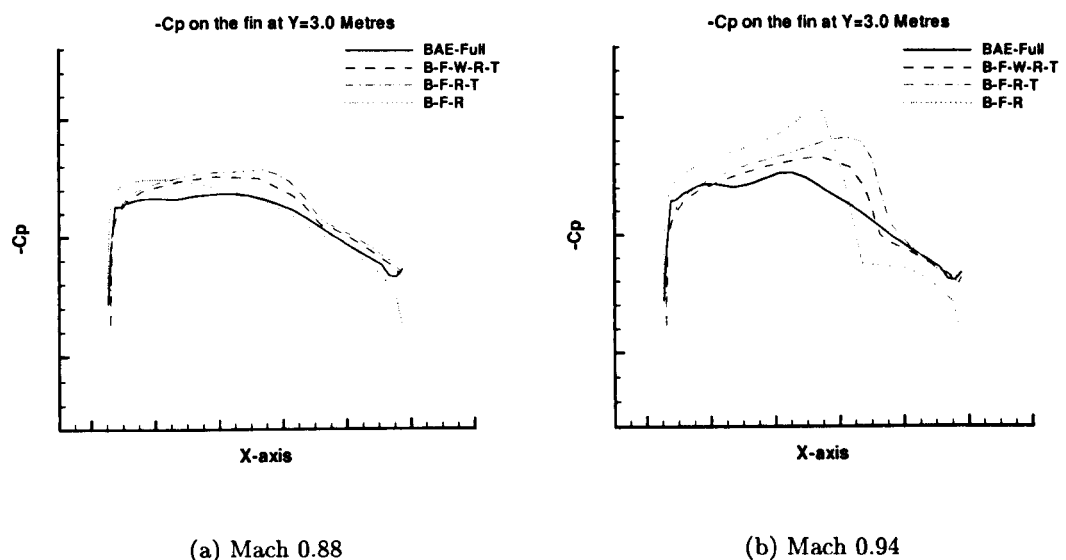


Figure 6.30: Surface pressure plots on the fin of the complete Hawk configuration at 3 Metres span

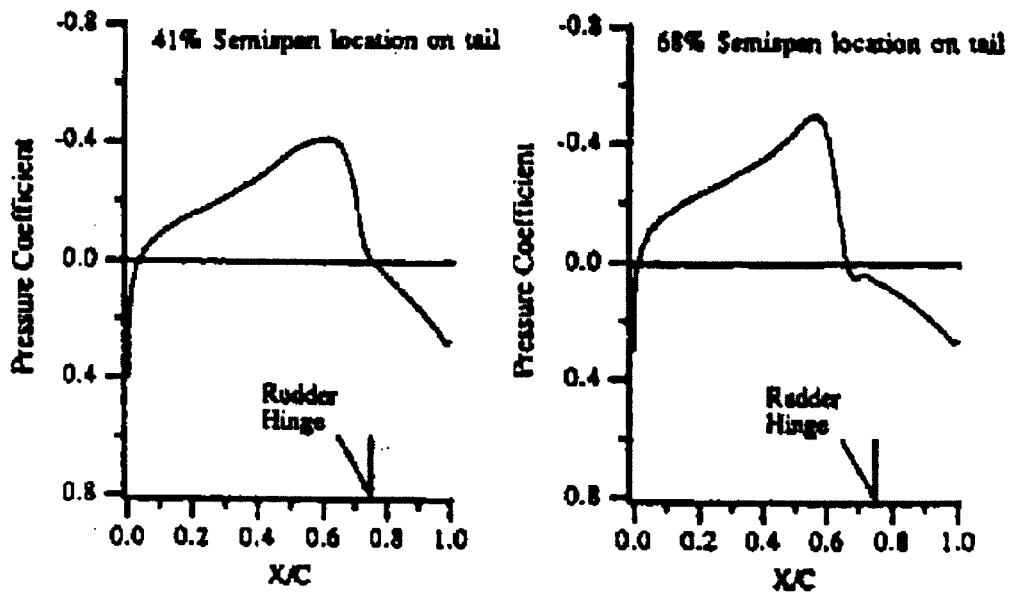
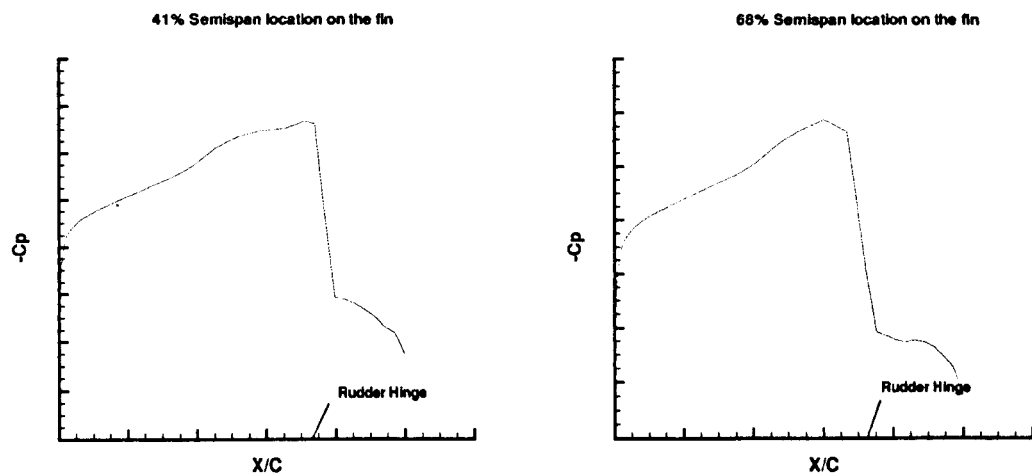


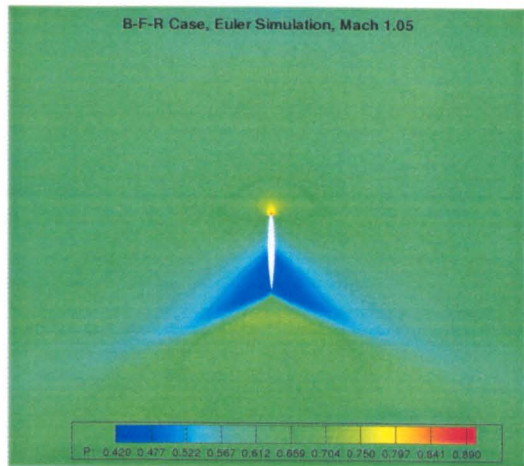
Figure 6.31: The surface pressure plots for Goshawk as predicted in reference [90] using RANS equations at Mach 0.95 and incidence 0° for the B-F-R case. Note that the “tail” refers to the vertical tail i.e. fin.



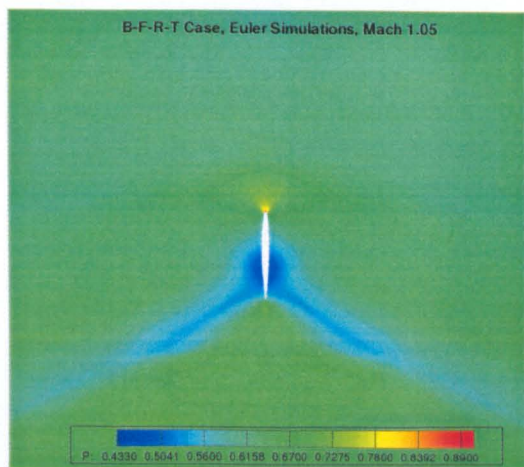
(a) Mach 0.95, Euler simulation, 41 % semi-span.

(b) Mach 0.95, Euler simulation, 68% semi-span

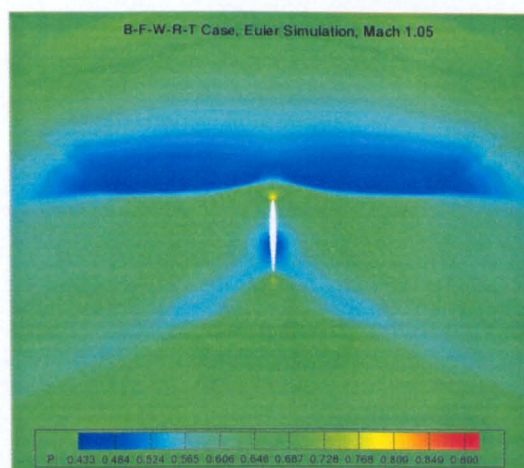
Figure 6.32: Surface pressure plots predicted at Mach 0.95 and incidence 0° for the Hawk B-F-R case.



(a) The B-F-R case at Mach 1.05



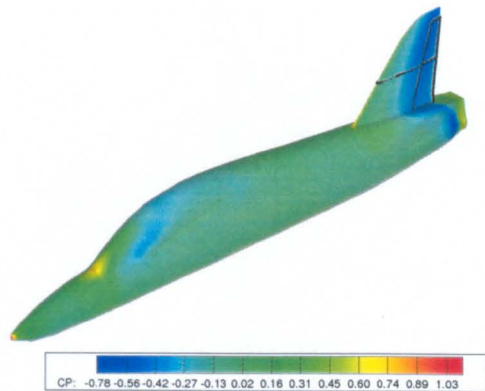
(b) The B-F-R-T case at Mach 1.05



(c) The B-F-W-R-T case at Mach 1.05

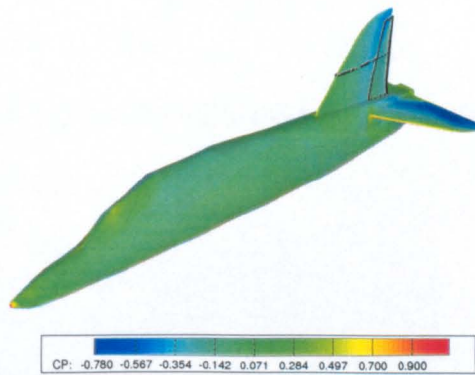
Figure 6.33: Hawk steady pressure contours at Mach 1.05 for increasing level of geometric complexity showing the gradual formation of shock ahead of the fin. Cases (a) and (b) without the wing show a shock over the rudder.

B-F-R Case, Euler Simulation, Mach 1.05



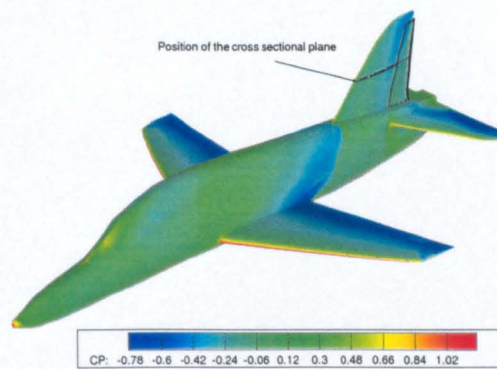
(a) The B-F-R case at Mach 1.05

B-F-R-T Case, Euler Simulation, Mach 1.05



(b) The B-F-R-T case at Mach 1.05

B-F-W-R-T Case, Euler Simulation, Mach 1.05



(c) The B-F-W-R-T case at Mach 1.05

Figure 6.34: Hawk steady surface pressure contours at Mach 1.05 for cases with increasing level of complexity.

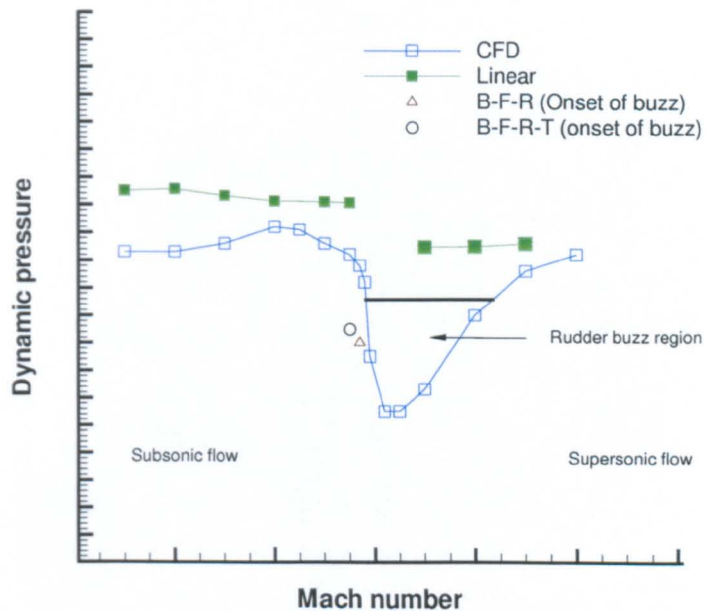


Figure 6.35: Qualitative flutter boundaries for the Hawk B-F-W-R-T case.

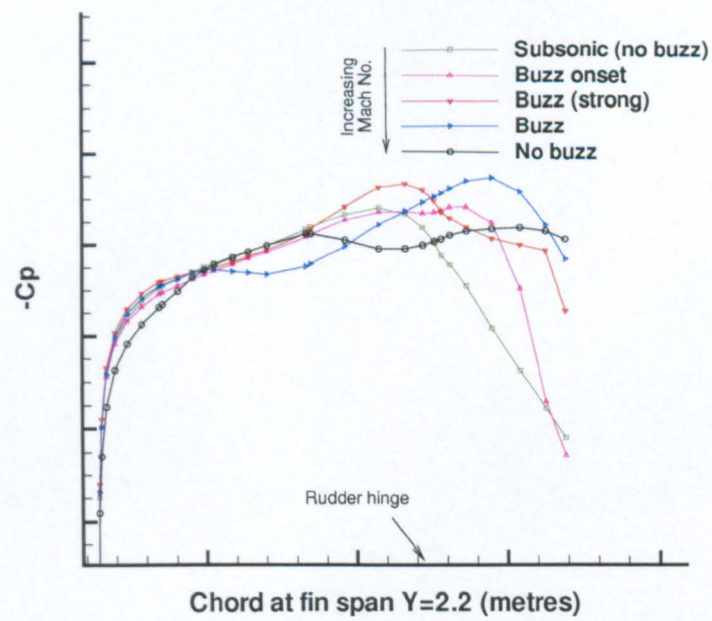


Figure 6.36: Cp plot at 2.2 metres fin span at increasing Mach numbers showing the strengthening and the gradual weakening of the shock across the fin span with for the Hawk B-F-W-R-T case.

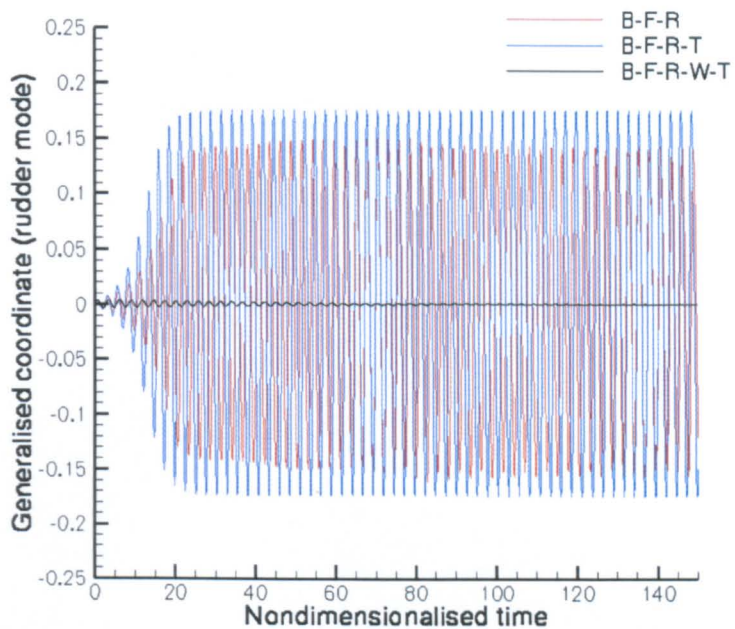


Figure 6.37: Match point analysis at 10,000 feet. Rudder rotation response of the Hawk B-F-R, B-F-T-R and B-F-W-T-R cases at Mach 0.97 and dynamic pressure of 45.89 kPa.



(a) The shock location for the Hawk B-F-R case at Mach 0.97

(b) The shock location for the Hawk B-F-R-T case at Mach 0.97

Figure 6.38: Shock location on the Hawk B-F-R and B-F-R-T cases.

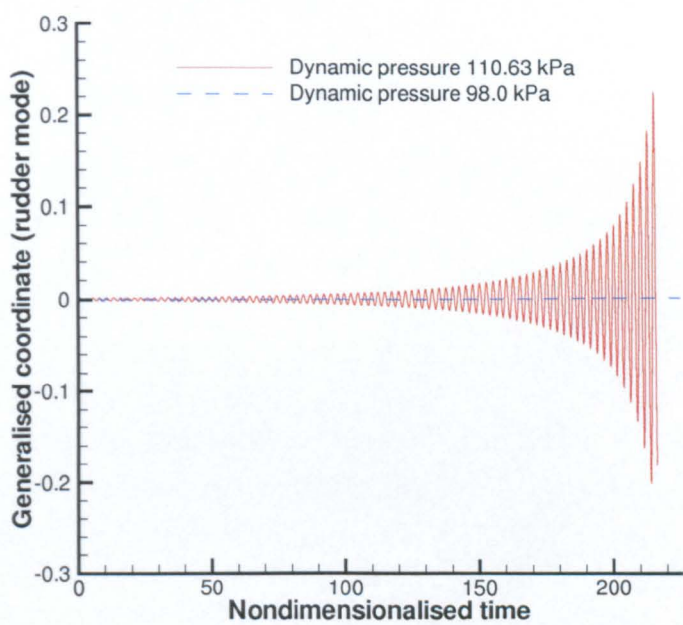


Figure 6.39: Damped and undamped modal responses at Mach 0.85 for the Hawk B-F-W-R-T case.

Chapter 7

Conclusions

A methodology for treatment of control surfaces on complex geometries for CFD based aeroelastic analysis has been developed and tested on a number of cases. A summary of the work performed is given in the following sections.

7.1 Treatment of Control Surfaces

A method has been developed and tested to treat aircraft control surfaces in unsteady CFD simulations. The control surface edges are blended into the wing using the multilevel hierarchical blending approach developed for complete aircraft geometries. There is no extra input required for this except for the value of the blending parameter which dictates the blended length of the control surface. Forced flap oscillations and aerodynamically driven trailing edge control surfaces have been simulated using this method.

The validity of blended control surfaces have been determined by comparing the results with a flap treatment including edges for statically deployed , forced driven and aerodynamically driven flaps. The flap with free edges was found to give similar results but required almost 50% more computational time due to poor convergence in the sheared mesh in the gap region.

For aerodynamically driven flaps (buzz simulations) flap rotation angles of up to 20° were recorded with flaps with blended edges without encountering problems with convergence. This is mainly because the blended flaps maintain the grid fidelity for large angles of flap deflection.

7.2 Buzz Instability

Detailed unsteady 3D buzz simulations have been performed on a SST configuration. The flap treatment was first validated by comparing the predicted dynamic deformation and pressure distribution against experiments. Flaps with free edges and blended flaps were used for the validation and they gave similar results. The detailed validation of predicted dynamic deformation has not been reported in the literature for any test case and the results presented in this work are the first.

Characteristics of buzz observed in experiments have been reproduced computationally. It has been shown here that a Type B buzz boundary can be predicted as long as a correct estimation of the shock location is made. It has also been shown that viscosity has an extenuating effect on the buzz amplitude although it also maintains the low amplitude buzz oscillations

which are not predicted by the Euler equations. The buzz onset is dependent on the initial perturbation of the flap and is found to be independent of the dynamic pressure for the SST case and at upper transonic Mach numbers the oscillations are sustained even at very low Mach numbers indicating that buzz can occur at high altitudes. Increasing the hinge damping helps in decreasing the amplitude of oscillations and the decrease is asymptotic. The buzz amplitude was found to increase with increasing Reynolds number as shown in the experiments. It is concluded here that though the Euler equations can predict the buzz boundary the RANS equations are required for prediction of characteristics like frequency, amplitude and damping of oscillations.

Both blended and flaps with free edges were used for buzz simulations on the SST. It was observed that the aeroelastic response predictions were similar however localised flow phenomenon like the trailing edge vortices due to the flap edges were not resolved by the blended flaps. This is not an issue if the objective is only to predict the aeroelastic behaviour of the wing-flap.

The Hawk aircraft was analysed for rudder buzz instability. Geometries with increasing complexity were tested and buzz has been identified on incomplete geometries. It was found that buzz onset is sensitive to the shape and location of the shock. For the Hawk aircraft it was found that the addition of the tailplane changed the shock location and shape by making it parallel to the hinge and moving it aft towards the trailing edge. This brought down the buzz onset Mach number as compared to other cases. The sensitivity of the buzz onset to interference effects from other components and the span-wise shape shock on the wing-control surface calls into question the validity of buzz predictions using to 2D simulations.

7.3 Instability on Complex Geometry

A transformation methodology is now in place to enable aeroelastic evaluation of full aircraft configurations including nacelles, engines, missiles and control surfaces. The requirements for a successful transformation of deformation from structural grid to the fluid grid is the correct labelling and classification of the aircraft components. The hierarchical blending ensures that the correct matching up of the components at the component interfaces and also the blending of control surface edges. A parsing utility extracts the required modes of the components and writes them down in the format required by the flow solver. This has been used for the analysis of a number of complete aircraft test cases including a generic fighter aircraft, the Generic Large Aircraft and the Hawk cases.

It was found that the aerodynamic interference effects are important in the transonic flow region as they alter the shock location and behaviour. This was seen in the Hawk rudder buzz investigations where the addition of components increased and also decreased the buzz onset Mach numbers.

In almost all the cases with a trailing edge control surface it was found that the linear aeroelastic analysis failed between Mach numbers 1 and 1.2. A large drop in the flutter velocity is observed which is due to the limitations of the linearised supersonic theory.

The inclusion of the control surface aerodynamics and the corresponding control surface structural modes is very important to obtain realistic flutter velocities of the wing. This is because the flutter mechanism of the cases analysed here invariably involved the coupling of the control surface modes with one or more wing modes. This is true in all the freestream Mach

numbers. However a buzz instability can precede a flutter instability at transonic Mach numbers since buzz occurs even at low values of dynamic pressure.

It is shown by all the cases that have been analysed in this work that time marching aeroelastic analysis has the capability to accurately identify and understand the physics behind the instabilities. Detailed flow features and the structural deformations can be extracted at any moment of time. Moreover identification of instabilities like buzz which are beyond the modelling capabilities of linear methods can be done accurately. However due to the long run times, time marching methods cannot be a replacement for linear methods that are currently used in the industry. The use of CFD must be targetted at difficult flow regimes for eg. transonic Mach numbers (buzz) and high angle of attack flows (buffet).

7.4 CFD in Industry

One of the outcomes of the Partnership in Unsteady Modelling of Aerodynamics - Defence and Research Partnerships PUMA DARP sponsored work not discussed earlier in the thesis has been the close collaboration with the engineers at BAE SYSTEMS for the aeroelastic simulations on the Hawk aircraft. Structural models used for flutter clearance were released by the company for use in the CFD based aeroelastic analysis. In turn the engineers from the company were trained in the use of the CFD code for aeroelasticity. A library of cases has been set up at the BAE SYSTEMS facility in Brough. The coupled CFD cases have been setup in a manner that any changes in the structural model can be easily realised in the aeroelastic calculations with minimal preprocessing on behalf of the engineers. This is a significant step in increasing the confidence in CFD based simulations at production level and will encourage the use of CFD for investigation of future aeroelastic problems when and if they arise.

7.5 Future Work

Control surface freeplay is one of the important issues in the aircraft industry. Almost all control surfaces have some freeplay built in due to the manufacturing limitations. The standards prescribed by the aviation authorities are difficult to confirm with. It is felt that these regulations could be relaxed if there is more understanding of the aeroelastic response due to freeplay. CFD based analysis is an excellent tool to study this phenomenon. For the aeroelastic tool used in the current work it involves implementing a technique to treat the freeplay nonlinearity in the linear modal FEM solver that is coupled to the fluid solver. This can be an interesting extension of the current work which has already established the capability of the code to treat a control surface instability

In recent years aeroelastic tailoring of aircraft wings have become popular. Aeroelastic tailoring can be defined as controlled aeroelastic deformation of the wing structure in order to obtain beneficial aerodynamic handling of the wing. As the aeroelastic deformation needs to be controlled it requires Smart Material Actuators that can deform or morph the wing shape as required. The actuating mechanism can be costly and before a model is built it would be helpful to have an idea of the deformed shape and the rate of deformation that would give optimum aerodynamic performance. Time marching CFD simulations can provide predictions for this.

Controlled wing deformations and forced oscillations are possible as shown in the forced flap study earlier. The structural model can be tuned computationally to provide the best results and this can be used to guide the manufacture of the real wing.

An interesting application of the time marching CFD simulations are the loads and deformations on an aircraft in a manoeuvre. Military aircrafts can undertake rapid manoeuvres resulting in large aerodynamic and g loads on the wings. This can cause large deformations of the wings. A computational capability of predicting the loads and the deformations on an aircraft in a manoeuvre can help in the design of the wings and for calculating the operational limits of the aircraft. This can be a future extension of the current work.

Bibliography

- [1] L. Fornasier, H. Rieger, U. Tremel and E. van der Weide. Time-Dependent Aeroelastic Simulation of Rapid Manoeuvring Aircraft. AIAA paper 2002-0949, 2002.
- [2] W. Herbst. Future Fighter Technologies. *Journal of Aircraft*, 17(8):561–566, 1980.
- [3] O. Bendiksen. Nonclassical Aileron Buzz in Transonic Flow. *34th AIAA/ASME/ASCE/AHS/ASC Structures, Structural Dynamics and Materials Conference*, (AIAA Paper 93-1479), April 1993.
- [4] N. Lambourne. Control Surface Buzz. *Aircraft Research Council R & M*, No. 3364, 1964.
- [5] B. Lee, S. Price and Y. Wong. Nonlinear Aeroelastic Analysis of Airfoils: Bifurcation and Chaos. *Progress in Aerospace Sciences*, 35(3):205–334, 1999.
- [6] J. Bae, S. Yang and I. Lee. Linear and Nonlinear Aeroelastic Analysis of Fighter-Type Wing with Control Surface. *Journal of Aircraft*, 39(4):697–708, 2002.
- [7] E. Garrick and W. Reed. Historical Development of Aircraft Flutter. *Journal of Aircraft*, 18(11):898–912, 1981.
- [8] G. Hill. Advances in Aircraft Structural Design. *Anglo-American Aeronautical Conference, Brighton*, The Royal Aeronautical Society, September 1951.
- [9] F. Lanchester. Torsional Vibrations of the Tail of an Aeroplane. *Aircraft Research Council R & M*, No. 276(Part 1), 1916.
- [10] L. Bairstow and A. Fage. Oscillations of the Tail Plane and the Body of an Aeroplane. *Aircraft Research Council R & M*, No. 276(Part 2), 1916.
- [11] I. Keynes. Review of Aeroelasticity in the U.K. *DERA-Farnborough*, DERA/MSS/MSTR2 CR010456, 2001.
- [12] K. Schwartzmann. German Flutter Experience. *AVA Gottingen*, (46/J/5), 1947.
- [13] Accidents Investigation Subcommittee. Report on the Puss Moth Accidents. *Aircraft Research Council R & M*, No. 276, 1936.
- [14] A. Smith. Recent Flutter and Vibration Incidents (1954–1960). *RAE TM, Structures*(Second Addendum), 1961.

- [15] H. Templeton. Flutter Research at the Royal Aircraft Establishment. *AGARD Report 4*, September 1955.
- [16] NACA Subcommittee on Vibrations and Flutter. A Survey and Evaluation of Flutter Research and Engineering. *NACA*, (RM-56112), 1956.
- [17] J. Baldcock and C. Skingle. Flutter Technology in the United Kingdom - A Survey. *RAE TM*, (Structures 831), April 1973.
- [18] *Aviation Week*, December 1997.
- [19] A. Baumhauer and C. Koning. On the Stability of Oscillations of an Airplane Wing. *International Air Congress, London*, 1923.
- [20] R. Frazer and W. Duncan. The Flutter of Aeroplane Wings . *Aeronautical Research Committee R & M*, 1155, 1928.
- [21] T. Theodorsen. General Theory of Aerodynamic Instability and the Mechanism of Flutter. *NACA Report*, 496, May 1934.
- [22] T. Theodorsen and I. Garrick. A Theoretical and Experimental Investigation of the Flutter Problem. *NACA Report*, TR-865, September 1940.
- [23] R. Yurkovich. Status of Unsteady Aerodynamic Prediction for Flutter of High-Performance Aircraft. *Journal of Aircraft*, 40(5):832–842, 2003.
- [24] B. Smilg and L. Wasserman. Application of Three Dimensional Flutter Theory to Aircrafts. *U.S. Airforce Labs., Dayton, Ohio*, TR-4798, July 1942.
- [25] E. Albano and W. Rodden. A Doublet-Lattice Method for Calculating the Lift Distributions on Oscillating Surfaces in Subsonic Flows. *AIAA Journal*, 7:279–285, 1969.
- [26] W. Rodden, P. Taylor and S. Macintosh. Further Refinement of the Nonplanar Aspects of the Subsonic Doublet Lattice Lifting Surface Method. *ICAS*, 96-2.8.2, 1996.
- [27] W. Rodden, P. Taylor, S. Macintosh and M. Baker. Further Convergence Studies of the Enhanced Subsonic Doublet Lattice Oscillatory Lifting Surface Method. *International Forum on Aeroelasticity and Structural Dynamics*, 1997.
- [28] W. Rodden. The Development of the Doublet Lattice Method. *International Forum on Aeroelasticity and Structural Dynamics*, 1997.
- [29] R. Yurkovich, D. Liu and P. Chen. The State-of-the-Art of Unsteady Aerodynamics for High Performance Aircraft. *International Forum on Aeroelasticity and Structural Dynamics*, 2001.
- [30] P. Chen and D. Liu. A Harmonic Gradient Method for Unsteady Supersonic Flow Calculations. *Journal of Aircraft*, 22(5):371–379, 1985.
- [31] C. Borland and D Rizetta. Nonlinear Transonic Flutter Analysis. *AIAA Journal*, 20(11):1606–1615, 1981.

- [32] T. Forrester, E. Tinoco and N. Yu. Thirty Years of Development and Application of CFD at Boeing Commercial Airplanes, Seattle. *Computers & Fluids*, 34:1115–1551, 2005.
- [33] M. Tamayama, K. Saitoh, H. Matsushita and J. Nakamichi. NAL Arrow Wing with Oscillating Flap. In *Verification an Validation Data for Computational Unsteady Aerodynamics*, pages 295–318. RTO Technical Report–26, October 2000.
- [34] E. Livne and T. Weisshaar. Aeroelasticity of Nonconventional Airplane Configurations - Past and Future. *Journal of Aircraft*, 40(6):1047–1065, 2003.
- [35] M. Abzug and E. Larrabee. *Airplane Stability and Control- A History of Technologies that Made Aviation Possible*, volume Chapter 19. Cambridge University Press, England, U.K., 1997.
- [36] J. Steger and H. Bailey. Calculation of Transonic Aileron Buzz. *AIAA Journal*, Vol. 18(3):pp. 249–255, 1980.
- [37] C. Pak and M. Baker. Control Surface Buzz Analysis of a Generic NASP Wing. *42nd AIAA/ASME/ASCE/AHS/ASC/ Structures, Structural Dynamics and Materials Conference*, (AIAA Paper 2001–1581), 2001.
- [38] G. Yang and S. Obayashi. Aileron Buzz Simulation Using an Implicit Multiblock Aeroelastic Solver. *Journal of Aircraft*, Vol. 40(3):pp. 580–589, 2003.
- [39] B. Bharadwaj. Computation of Steady and Unsteady Control Surface Loads in Transonic Flow. AIAA paper 90–0935, 1990.
- [40] S. Obayashi and G. Guruswamy. Navier-Stokes Computations for Oscillating Control Surfaces. AIAA paper 92–4431, 1992.
- [41] G. Klopfer and S. Obayashi. Virtual Zone Navier-Stokes Computations for Oscillating Control Surfaces. AIAA paper 93–3363, 1993.
- [42] D. Schuster and R. Bartels. Benchmark Active Control Technology (BACT) Wing CFD Results. In *Verification an Validation Data for Computational Unsteady Aerodynamics*, pages 225–238. RTO Technical Report - 26, October 2000.
- [43] H. Cole and A. Andrew and K. Gupta. Application of the Transpiration Method for Aerovielastic Prediction Using CFD. AIAA paper 98–2071, 1998.
- [44] Y. Utaka and J. Nakamichi. Aeroelastic Analysis of an SST Wing with Trailing Edge Flap Using a Chimera Grid Approach. *42nd AIAA Aerospace Sciences Meeting and Exhibit*, (AIAA Paper 2004–1271), 2004.
- [45] D. Liu, D. James, P. Chen and A. Pototzky. Further Studies of Harmonic Gradient Method for Supersonic Aeroelastic Applications. *Journal of Aircraft*, Vol. 28(9):pp. 598–605, 1991.
- [46] W. Rowe, B. Winther and M. Redman. Unsteady Subsonic Aerodynamic Loadings Caused by Control Surface Motions. *Journal of Aircraft*, Vol. 11(1):pp. 45–54, 1974.

- [47] K. Roughen, M. Baker and T. Fogarty. Computational Fluid Dynamics and Doublet-Lattice Calculations of Unsteady Control Surface Aerodynamics . *Journal of Guidance, Control, and Dynamics*, Vol. 24(1):pp. 160–166, 2001.
- [48] K. Badcock, M. Woodgate and B. Richards. Elements of Computational Fluid Dynamics on Block Structured Grids using Implicit Solvers. *Progress in Aerospace Sciences*, 36:351–392, 2000.
- [49] L. Goura. *Time marching analysis of flutter using Computational Fluid Dynamics*. PhD thesis, University of Glasgow, 2001.
- [50] M. Sadeghi, F. Liu, K. Lai and H. Tsai. Application of Three-Dimensional Interfaces for Data Transfer in Aeroelastic Computations. *22nd AIAA Applied Aerodynamics Conference*, (AIAA Paper 2004-5376), August 2004.
- [51] K. Badcock, A. Rampurawala and B. Richards. Intergrid Transformation for Aircraft Aeroelastic Simulations. *AIAA Journal*, Vol. 42(9):pp. 1936–1939, September 2003.
- [52] J. Anderson Jr. *Computational Fluid Dynamics - The basics with applications*. Mechanical Engineering Series. McGraw-Hill International Editions, 1995.
- [53] K. Badcock, F. Cantariti and B. Gribben. *Theory Guide to PMB2D Version 3.1*. Department of Aerospace Engineering, University of Glasgow, 2000.
- [54] M. Allan. *A CFD Investigation of Wind Tunnel Interference on Delta Wing Aerodynamics*. PhD thesis, University of Glasgow, 2002.
- [55] D. Wilcox. Turbulence Modelling for CFD. *DCW Industries, Inc., La Cañada, California*, 1993.
- [56] S. Osher. and S. Chakravarthy. Upwind Schemes and Boundary Conditions with Applications to Euler Equations in General Geometries. *Journal of Computational Physics*, Vol. 50:447–481, 1983.
- [57] K. Badcock, X. Xu, L. Dubuc and B. Richards. *Preconditioners for High Speed Flows in Aerospace Engineering*, volume Vol. 5, pages pp. 287–294. Institute for Computational Fluid Dynamics, Oxford, U.K., 1996.
- [58] O. Axelsson. *Iterative Solution Methods*. Cambridge University Press, 1994.
- [59] F. Cantariti, L. Dubuc, B. Gribben, M. Woodgate, K. Badcock and B. Richards. Approximate Jacobians for the Solution of the Euler and Navier-Stokes Equations. Technical Report 5, Aerospace Engineering Report, University of Glasgow, Glasgow, UK, 1997.
- [60] A. Jameson. Time Dependent Calculations Using Multigrid, with Applications to Unsteady Flows Past Airfoils and Wings. (AIAA Paper 1991-1596), June 1991.
- [61] L. Dubuc, F. Cantariti, M. Woodgate, B. Gribben, K. Badcock and B. Richards. A Grid Deformation Technique for Unsteady Flow Computations. *International Journal for Numerical Methods in Fluids*, Vol. 32:pp. 285–311, 2000.

- [62] P. Thomas and C. Lombard. Geometric Conservation Law and its Application to Flow Computations on Moving Grids. *AIAA Journal*, Vol. 17:pp. 1030–1037, 1979.
- [63] G. Guruswamy. A Review of Numerical Fluids/Structures Interface Methods for Computations Using High-Fidelity Equations. *Computers & Structures*, Vol. 80:31–41, 2002.
- [64] M. Hounjet and J. Meijer. Evaluation of Elastomechanical and Aerodynamic Data Transfer Methods for Non-Planar Configurations in Computational Aeroelastic Analysis. *International Forum on Aeroelasticity and Structural Dynamics - Manchester*, June 1995.
- [65] M. Smith, C. Cesnik and D. Hodges. Evaluation of Some Data Transfer Algorithms for Non-contiguous Meshes. *ASCE Journal of Aerospace Engineering*, Vol. 13(2):52–58, September 2000.
- [66] M. Smith, D. Hodges and C. Cesnik. Evaluation of Computational Algorithms Suitable for Fluid-Structure Interaction. *Journal of Aircraft*, Vol. 37(2):282–294, 2000.
- [67] M. Woodgate, K. Badcock, A. Rampurawala, B. Richards, D Nardini and M. Henshaw. Aeroelastic Calculations for the Hawk Aircraft Using the Euler Equations. *Journal of Aircraft*, Vol. 40(4):pp. 1005–1012, 2005.
- [68] A. Rampurawala. Assessment of Inter-Grid Transformation for Complete Aircraft Aeroelastic Analysis. Master's thesis, University of Glasgow, 2002.
- [69] R. Harder and R. Desmarais. Interpolation Using Surface Splines. *Journal of Aircraft*, Vol. 9(2):189–191, February 1972.
- [70] K. Appa. Finite-Surface Spline. *Journal of Aircraft*, Vol. 26(5):495–496, 1989.
- [71] G. Guruswamy and C. Byun. Direct Coupling of Euler Flow Equations with Plate Finite Element Structures. *AIAA Journal*, Vol. 33(2):375–377, 1994.
- [72] K. Bathe. *Finite Element Procedures in Engineering Analysis*. Prentice Hall, 1982.
- [73] V. Murti and S. Valliappan. Numerical Inverse Isoparametric Mapping in Remeshing and Nodal Quantity Contouring. *Computers and Structures*, Vol. 22(6):1011–1021, 1986.
- [74] P. Chen and I. Jadic. Interfacing Fluid and Structural Models via Innovative Structural Boundary Element Method. *AIAA Journal*, Vol. 36(2):282–287, February 1998.
- [75] C. Brebbia and J. Dominguez. *Boundary Elements: An Introductory Course*. McGraw-Hill, 1992.
- [76] R. Melville. Nonlinear Simulation of F-16 Aeroelastic Instability. *AIAA Paper 2001-0570*, 2001.
- [77] H. Cole and A. Andrew and K. Gupta. CFD-Based Aeroservoelastic Predictions with Comparisons to Benchmark Experimental Data. AIAA paper 99-0766, January 1999.
- [78] S. Obayashi, I. Chiu and G. Guruswamy. Navier-Stokes Computations on Full Span Wing Body Configuration for Oscillating Control Surfaces. AIAA paper 93-3687, 1993.

- [79] A. Karlsson and B. Winzell. Unsteady Control Surface Pressure Measurements and Computations. AIAA paper 96-2417, 1996.
- [80] M. Tamayama, T. Weisshaar and J. Nakamichi. Unsteady Shock Wave Motions on a Thin Airfoil at Transonic Speeds Caused by an Aileron Oscillation. *International Forum on Aeroelasticity and Structural Dynamics - Amsterdam*, June 4-6 2003.
- [81] H. Ide and D. Ominsky. Simulation of Static and Dynamic Aeroelastic Behaviour of a Flexible Wing with Multiple Control Surface. AIAA paper 90-1075, April 1990.
- [82] D. Yeh. Aeroelastic Analysis of a Hinged-Flap and Control Surface Effectiveness Using the Navier-Stokes Equations. AIAA paper 95-02263, June 1995.
- [83] M. Tamayama and J. Nakamichi. Unsteady Aerodynamics Measurements on an Elastic Wing Model of SST. AIAA paper 97-0836, January 1997.
- [84] R. Bennett, R. Scott and C. Wieseman. Test Cases for the Benchmark Active Controls Model: Spoiler and Control Surface Oscillations and Flutter. In *Verification and Validation Data for Computational Unsteady Aerodynamics*, pages 201-224. RTO Technical Report-26, October 2000.
- [85] B. Prananta, J. Kok, S. Spekreijse, M. Hounjet and J. Meijer. Simulation of Limit Cycle Oscillation of Fighter Aircraft at Moderate Angle of Attack. *International Forum on Aeroelasticity and Structural Dynamics - Amsterdam*, June 4-6 2003.
- [86] C. Farhat, P. Geuzaine and G. Brown. Application of a Three-field Nonlinear Fluid-structure Formulation to the Prediction of the Aeroelastic Parameters of an F-16 Fighter. *Computers & Fluids*, Vol. 32(3):pp.3-29, 2002.
- [87] Y. Nakamura. Some Contributions on a Control Surface Buzz at High Subsonic Speeds. *Journal of Aircraft*, Vol. 5(2):pp. 118, 1968.
- [88] Y. Nakamura and L. Woodgate. Effects of Reynolds Number and Frequency Parameter on Control Surface Buzz at High Subsonic Speeds. *Aeronautical Research Council R & M*, No. 3702, 1972.
- [89] A. Erickson and J. Stephenson. A Suggested Method for Analyzing for Transonic Flutter of Control Surfaces Based on Available Data. *NACA RM A7F30*, 1947.
- [90] D. Fuglsang, L. Brase and S. Agarwal. A numerical study of control surface buzz using computational fluid dynamics methods. *10th AIAA Applied Aerodynamics Conference*, (AIAA Paper 92-2654), June 1992.
- [91] M. Tamayama, K. Saitoh, H. Matsushita and J. Nakamichi. NAL SST Arrow Wing with Oscillating Flap. *RTO Report*, RTO-TR-26 AC/323(AVT)TP/19, October 2000.
- [92] *Aeroelastic Analysis User's Guide*. MSC Software Corporation, 2001.
- [93] *Theoretical Manual*. ZONA Technology, 2003.

- [94] W. Jones. Supersonic Theory for Oscillating Wings of Any Planform. *British Aeronautical Research Council*, (R & M 2655), June 1948.
- [95] W. Jones. Unsteady Supersonic Aerodynamic Theory by Method of Potential Gradient. *15th AIAA Aerospace Sciences Meeting*, (AIAA Paper 77-155), January 1977.
- [96] D. Lucia, P. Beran and W. Silva. Reduced-order Modeling: New Approaches for Computational Physics. *Progress in Aerospace Sciences*, Vol. 40:pp. 51-117, 2004.
- [97]
- [98] R. Sowden. Assessment of the Results from the Ground Resonance Test and Recommendations for a Provisional Aircraft Flutter Clearance . *BRITISH AEROSPACE, Aerodynamic Technology Department*, BAe-BAE-RP-HWK-7178(1), September 1997.
- [99] N. Sellers. Personal Communication. *Senior Aerodynamicist, Aerodynamics Department, BAE SYSTEMS*, Brough, United Kingdom, 2005.

